Reaction Dynamics of $O(^3P)$ Atoms with Saturated Hydrocarbons

by

Florian Ausfelder

A thesis presented for the degree of Doctor of Philosophy

The University of Edinburgh

2002

Declaration

I hereby declare that the work presented in this thesis is entirely my own, except where due acknowledgement has been made to the work of others, and has not been presented previously, in whole or in part, for any other degree or professional qualification.

Some say the world will end in fire,

Some say in ice.

From what I've tasted of desire

I hold with those who favour fire.

but if it had to perish twice,

I think I know enough of hate

To say that for destruction ice

Is also great

and would suffice.

Robert Frost (1874-1963)

(New Hampshire, 1923)

Acknowledgements

The principal mention is deserved to go to Professor Ken McKendrick for his expertise, advice, generosity and patience. He always put up a brave face, for even the most outrageous questions or the latest disaster in the laboratory.

I would like to acknowledge Professor Robert J. Donovan for taking over as my supervisor and for finding some money for me from somewhere.

I would like to thank all the people who managed to work together with me in the laboratory, at Edinburgh and at Heriot-Watt University, in chronological order:

Dr Craig Murray, who managed to resist all of my "continental communist influence" and was fun to work with. Thanks for this time.

Dr David Henderson, for taking over the planning of the gas-liquid experiment. Good Luck, you will need it.

Dr Matthew L. Costen, for his brief and well-informed answers to questions. Never forget, lasers are human beings too.

Dr Stefan Himmelmann, for keeping me company at the lunches at HWU. Never trust a company that deals with explosives.

Hailey Kelso, who taught me the deeper meaning of handbags. Good luck for the rest of your time. You will get Robbie Williams in the end.

Hilary J. Crichton, for questions one would never dare to ask. Get yourself a personal heat gun.

Special thanks to the Stuart Mains, Ian Drummond, Alan Barton and Bill Stirling and everyone else at the workshops at Edinburgh and Heriot-Watt.

Furthermore, I would like to thank Dr Robert O. Gould for lavish meals and

discussions on "Gott und die Welt."

I had the pleasure to attend lectures in the European Institute, which constituted highlights in my academic career. Thanks to Dr Caitriona A. Carter, Andrew Scott and Dr Rachael Crauwfurd-Smith.

In addition to my working life I enjoyed the company of my flatmates, again in chronological order

Andrew, don't solve all the riddles of mathematics.

Friederike, please become more like your mother.

Nicola, what was I supposed to do with the botanical garden you left me with?

Jean-Louis, for helping me to understand French politics in the EU and many philosophical discussion. I hope you will get a microwave soon.

Silvia, Giuseppe, Simonetta, Pinuccia, Paola and Sara, the Italian connection, for bringing a taste of Mediterranean lifestyle in my existence.

Furthermore, I would like to thank my friends who made my stay in Edinburgh enjoyable, as there are Anna, Bärbel, David, Helen, Heli, Tom and Yukari. Of course, I also want to acknowledge my friends outside Edinburgh, some of them visited me, some didn't...

Last, but definitely not least I want to thank my sister and my brother, but especially my parents who always supported me in every situation of my life. It was a long way, but eventually their son manages to get out of university (well, sort of...). It is wonderful that you are there.

I have decided to omit the list of dishonourable mentions. It is available on request.

For my parents

Abstract

An intensive study of the dynamics of reactions $O(^3P)$ + hydrocarbons has been carried out. This work represents the first study to directly compare the effect of deuterating the hydrocarbon reactant. The reactions under investigation were

$O(^3P) + CH_4 \rightarrow OH\ X\ ^2\Pi_i\ (v'=0/1) + CH_3$ reaction (1)

$O(^3P) + cyclo\text{-}C_6H_{12} \rightarrow OH\ X\ ^2\Pi_i\ (v'=0/1) + cyclo\text{-}C_6H_{11}$ reaction (2)

$O(^3P) + CD_4 \rightarrow OD\ X\ ^2\Pi_i\ (v'=0/1) + CD_3$ reaction (3)

$O(^3P) + cyclo\text{-}C_6D_{12} \rightarrow OD\ X\ ^2\Pi_i\ (v'=0/1) + cyclo\text{-}C_6D_{11}$ reaction (4)

The $O(^3P)$ atoms were generated by laser photolysis of NO_2 at 266 nm. The OH / OD products were detected by laser induced fluorescence (LIF) on the $A\ ^2\Sigma^+ \leftarrow X\ ^2\Pi_i$ (1-0) and (2-1) bands for the vibrational ground state ($v'=0$) or the first vibrationally excited state ($v'=1$) respectively. The quantities derived from these measurements include the rotational distributions, the fine-structure propensities and the Λ-doublet preferences for these reactions. No OH ($v'=1$) from reaction (1) was observed, and an upper limit its yield of 0.03 of the production of the OH ($v'=0$) state derived. In comparison reaction (3) produced OD ($v'=1$) that was just detectable and the branching ratio for OD ($v'=1$) to OD ($v'=0$) was derived to be about 0.07. Both reactions of cyclohexane, (2) and (4) produce significant amounts of OH and OD in the first excited vibrational state in addition to the ground state. The rotational distributions for OH / OD ($v'=0$) for all reactions and OH / OD ($v'=1$) for reactions (2) and (4) were measured and analysed. Despite the opposite trend in exothermicities, the OH / OD ($v'=0$) products of reactions (1) and (3) have more energy in rotation than the respective products from reactions (2) and (4). The amount of energy channeled into the rotational motion of the product only depends

on the nature of the hydrocarbon, i.e. the nature of the C-H / C-D bond, but not on the isotope used. The lower spin-orbit manifold F_1 of the X $^2\Pi_i$ state of the OH / OD product is found to be favoured in all cases and its relative preference is found to be independent of the hydrocarbon molecule, vibrational level produced or isotope. The observed preference is well explained by an electronic surface coupling model which allows mixing of electronic surfaces if Ω and parity are conserved. As in previous experimental studies, no preference for either Λ-doublet was observed for any of the reactions. The overall data are consistent and provides further strengthening of the view of $O(^3P)$ + hydrocarbon reactions as a collinear abstraction mechanism. Additionally, experiments have been carried out to study the effect of vibrational excitation in reaction (1) by pumping the ν_3 asymmetric stretch mode in CH_4.

$$O(^3P) + CH_4\ (\nu_3,\ v{=}1) \rightarrow OH\ X\ ^2\Pi_i\ (v'{=}0/1) + CH_3 \qquad \text{reaction (5)}$$

No effect has yet been observed for reaction (5). In the case of total optical saturation, the relative reactivity of the vibrationally excited CH_4 (ν_3, v=1) would not be higher than a factor of 3 with respect to CH_4 in its vibrational ground state to be consistent with the observed signal-to-noise level. Furthermore, an investigation was carried out to identify the main products of the reaction of ground state oxygen atoms with acetonitrile.

$$H_3CCN + O(^3P) \rightarrow \text{Products} \qquad \text{reaction (6)}$$

The two main prospective channels produce OH or NCO, respectively. While neither OH or NCO was observed as a product of reaction (6), a relative upper limit in comparison to reaction (2) is given as 0.7±0.7% for the OH producing channel.

Table of Contents

List of Figures

List of Tables

Chapter 1: Introduction

1.1 General Introduction

The aim of reaction dynamics is to understand the path a chemical reaction takes to change the reactants into the products. It is at the very heart of chemistry, trying to establish the rules that govern a given chemical process.

Even though chemical reactions are constrained by the conservation of energy and angular momentum, they display an astonishing variety of different mechanisms. A chemical reaction is a delicate system of balance involving energy and angular momentum in its different forms. Trying to establish the accurate "balance sheet" for a given reaction, even as simple as $H + H_2$, is a very difficult task.

Experiments usually only manage to pin down a few details and the theoretical effort, even though huge progress has been made, is still struggling to keep up with the experimental work for all but the most basic reactions. In a few areas, experimental work and theoretical effort stimulate each other, pushing the border of understanding slowly forward.

The following study is set in one of these areas. In parallel with this experimental study, contemporary new calculations deepened the insight into the systems dramatically.

Far from having just a confirmative role, experiments provide the ultimate test for the calculations, and more importantly, also shed light on aspects not yet well understood theoretically.

1.2 Introduction to the reactions of oxygen atoms with saturated hydrocarbons

Reactions of oxygen atoms with hydrocarbons are of broad interest in many applied fields ranging from high temperature combustion processes, through atmospheric processes to degradation of plastics in near-earth orbiting spaceships. In addition they represent the simplest form of oxidation that can be imagined for an alkane.

The two lowest electronic states of the oxygen atom, $O(^3P)$, the electronic ground state, and $O(^1D)$, the first electronically excited state, which lies about 190 kJ mol^{-1} higher in energy, show very distinct behaviours. While the general reaction of oxygen atoms with a saturated hydrocarbon, where R denotes an alkyl group,

$$O + HR \rightarrow R + OH \qquad \text{reaction (1.1)}$$

remains valid for both cases the products are formed in very different ways.

In the case of $O(^1D)$, a large fraction of the reactive flux is thought to involve insertion of the incoming $O(^1D)$ atom into an existing bond to form a relatively long-lived H-O-R alcohol intermediate following reaction (1.2).

$$O(^1D) + HR \rightarrow [HOR] \rightarrow R + OH \qquad \text{reaction (1.2)}$$

In addition, if the hydrocarbon is not CH_4, C-C bond rupture may occur in competition with the C-O bond fission in the alcohol intermediate.

On the other hand, it is generally thought that the analogue reaction with a ground state oxygen atom $O(^3P)$ proceeds via a collinear H atom abstraction as shown in reaction (1.3).

$$O(^3P) + HR \rightarrow [O\text{--}H\text{--}R] \rightarrow OH + R \qquad \text{reaction (1.3)}$$

The extent to which these limiting pictures are supported by experimental data and theoretical calculations will be discussed in detail in the following sections.

For a long time most dynamical studies focussed on reaction (1.2) mainly because its energetics are very favourable. Reactions of class (1.2) tend to be hugely exothermic and essentially barrierless. The reaction rate, which is close to the gas kinetic limit [1,2,3,4], shows hardly any temperature dependence [5]. This makes reaction (1.2) easily accessible for experimental studies even for the parent molecule CH_4 which has the least favourable energetics. The reaction passes over a deep potential well which corresponds to the stable methanol molecule. Photolytically generated $O(^1D)$ provides, for example, an important mechanism for the oxidation of hydrocarbons in the atmosphere [6].

This is not the case for $O(^3P)$, however, for which the high barriers more than offset its greater abundance. Experimental work is hampered by the much less favourable energetics. Reactions of the type (1.3) have in general a significant barrier which increases in the order tertiary < secondary < primary < CH_4 and an exothermicity which changes in the opposite direction making the reaction of $O(^3P)$ with CH_4 even slightly endothermic. A compilation of the thermodynamic data can be found in reference [7]. A schematic representation of the reaction profile is shown in figure 1.1.

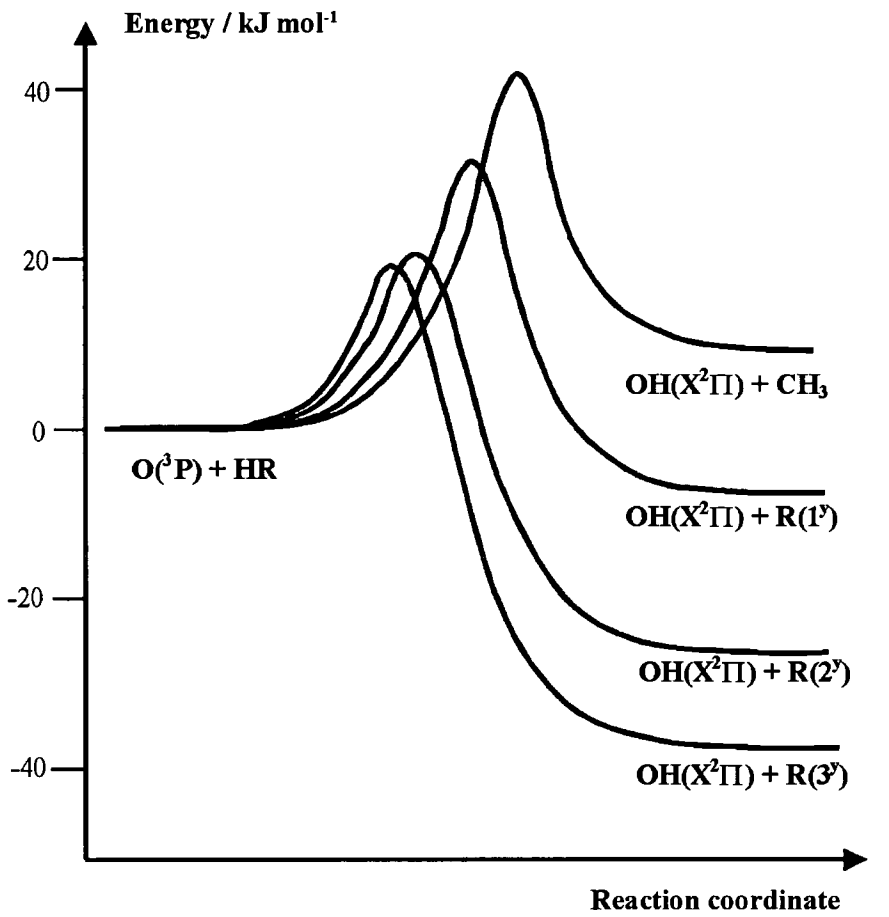

Figure 1.1: Schematic reaction profiles for $O(^3P)$ + saturated hydrocarbon reactions. Adapted from a similar diagram in [14].

Therefore the rates of reaction (1.3) tend to be very slow unless in an extreme environment like high temperature combustion. It is beyond the scope of this introduction to discuss the rates of reactions in detail, which can be found elsewhere [8,9,10,11].

It should be noted again that the main differences between $O(^3P)$ and $O(^1D)$ are the electronic configuration and the total energy. In reactions of oxygen atoms with hydrocarbons, the chemical identity and the kinematics are the same. The following sections will focus on the reactions of $O(^3P)$ with saturated hydrocarbons in the gas phase, but, where appropriate, the differences to the reactions with $O(^1D)$ will be highlighted.

1.3 Experimental studies of $O(^3P)$ + hydrocarbons

A standard approach to investigate a chemical reaction is the use of crossed molecular beams combined with "universal" mass spectrometric detection. While this method was used to study other reactions of $O(^3P)$ atoms [12,13], there are no reports on $O(^3P)$ + saturated alkane reactions using this technique. This is presumably the result of practical limitations.

The first successful investigation of the dynamics of $O(^3P)$ with hydrocarbon reactions was done in the ground breaking experimental study by Andresen and Luntz [14], using laser-induced fluorescence (LIF) to observe the OH product on the near-UV $A\ ^2\Sigma^+$-$X\ ^2\Pi$ band [15] spectroscopically.

This product-state-specific detection technique also is the foundation of nearly all later experimental work including this study. Andresen and Luntz combined LIF detection with molecular beam methods for preparing the reagents. The $O(^3P)$ atoms were generated by microwave discharge of O_2 and released in an effusive beam. The precursor gas stream contained a small fraction (typically ~3%) of H_2O, which enhanced $O(^3P)$ atom production. This effusive beam was crossed in the collision zone by a supersonic beam of the hydrocarbon seeded in either H_2 or He. The collision energy was controlled by varying the carrier gas and the temperature of the nozzle. It was verified by time-of-flight measurements using a chopper wheel.

A significant drawback of this method of $O(^3P)$ generation is OH production in the discharge. The non-reactive background signal had to be subtracted by recording the OH LIF signal on alternate shots with and without the hydrocarbon nozzle firing. There is no straightforward way to ensure "single collision" conditions in the reaction zone other than to limit the beam fluxes and have sufficient pumping capacity to maintain a low background pressure.

Andresen and Luntz [14] did choose a set of hydrocarbons, neopentane ($(CH_3)_4C$), cyclohexane (*cyclo*-C_6H_{12}) and isobutane ($(CH_3)_3CH$) to represent primary, secondary and tertiary hydrocarbons respectively. Deuterated isobutane ($(CH_3)_3CD$) was used to verify that the observed OH signal from non-deuterated isobutane was characteristic of reaction on the tertiary C-H bond, at least at low collision energies.

Whitehead's group [16] refined the experiment by replacing the effusive $O(^3P)$ beam with a supersonic expansion of microwave discharge-generated $O(^3P)$ in He. The translational energies of both the $O(^3P)$ and the hydrocarbon supersonic beam could be selected by choppers. The hydrocarbon beam was additionally equipped with a tuning-fork chopper to allow the necessary subtraction of the LIF signal from OH present in the $O(^3P)$ beam. A further series of hydrocarbons (including some unsaturated reagents) was examined.

The experimental work entered a new age with the introduction of pulsed laser photolysis of a suitable precursor to create $O(^3P)$ atoms. This allowed the creation of higher instantaneous densities of the transient $O(^3P)$ reagent as well as introducing a well-defined zero of time against which collisional relaxation of nascent product state distributions could be referenced.

On the other hand, the absence of a suitable diatomic precursor for $O(^3P)$ atoms and special steps to reduce the spread of thermal velocities of the precursor and reagent gases [17] means the method allows less control over the reagent collision energy distribution compared to chopped crossed-molecular beam experiments. Some relatively crude variation is possible through the choice of precursor and photolysis wavelength.

Nevertheless, the pulsed photolysis-probe setup has dominated all recent studies. A typical example of what is now achievable is the most recent experiment of this type by Tsurumaki *et al.* [18]. The schematic setup of this experiment is presented in figure 1.2.

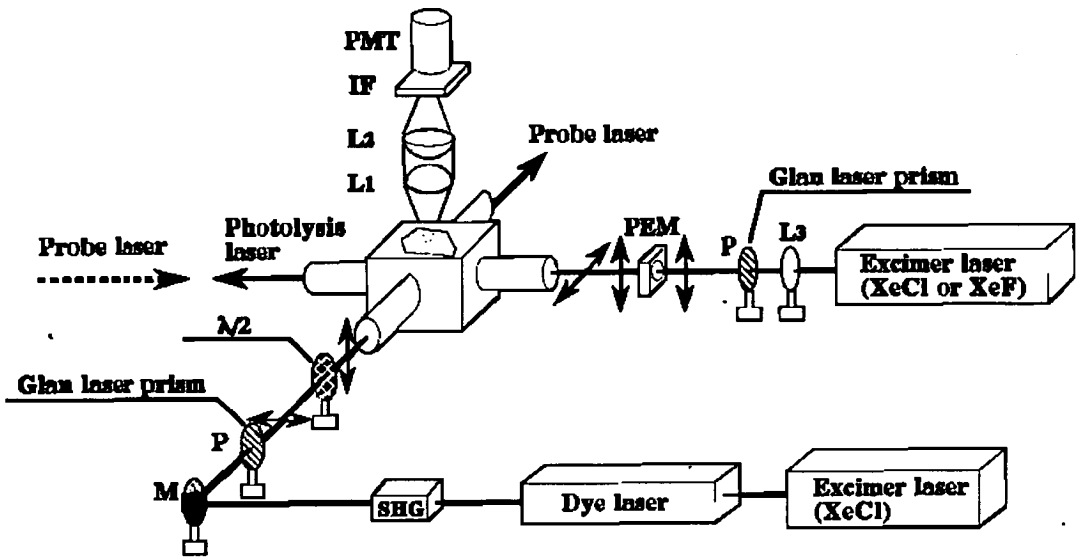

Figure 1.2: Schematic experimental configuration for polarisation sensitive, Doppler-resolved LIF measurements of nascent OH products. M=mirror, P=polariser, λ/2=half-wave plate, PEM=photoelastic modulator, L=lens, IF=interference filter, SHG=second harmonic generation. Reproduced from [18].

The $O(^3P)$ precursor, commonly NO_2, and the hydrocarbon reagent are flowed through a reaction chamber at known total pressure. The reaction is initiated by firing the photolysis laser, typically an excimer laser or the harmonic of a Nd:YAG laser, that produces a relatively high-powered laser pulse. The OH product is probed by laser-induced fluorescence (LIF) after a pre-determined delay, chosen to ensure that nascent products are detected.

The average number of collisions, Z_{OH}, suffered by a nascent OH product molecule is proportional to the product of pressure p and the time difference between production and detection, Δt,

$$Z_{OH} \propto p\Delta t \qquad \text{equation (1.1)}$$

which can be relatively easily controlled.

Typical operating conditions are pressures of the order of ~100 mTorr and delays of order ~100 ns, which would roughly correspond to 0.1 collisions on average between initiating the reaction and probing the products.

While the photolytic production of $O(^3P)$ removes the OH background source of the earlier microwave based $O(^3P)$ production methods, several authors reported a frustratingly high $OH(v'=0)$ signal levels originating from an OH containing impurity in commercially available NO_2.

Such laser-photolytic methods were pioneered in studies of $O(^3P)$ reactions with the inorganic reagents HBr [19] and silanes [20]. Whitehead's group applied the technique with germane [21] and then produced the first publication [22] specifically on reactions with hydrocarbons. McKendrick and coworkers [23] extended the

method by generating higher translational energies using photolysis of NO_2 at shorter wavelengths, energetically just below the threshold for $O(^1D)$ production.

For the first time, in addition to the usual series of representative primary, secondary and tertiary hydrocarbons, they were able to report LIF detection of OH from the parent $O(^3P)$ with CH_4 reaction. This presents the most challenging case, as discussed above, since a combination of a high barrier and unfavourable kinematics, which cause inefficient conversion of the $O(^3P)$ laboratory frame velocity to centre-of-mass collision energy, makes it difficult to get sufficient OH product yield for detection.

The most recent refinement of the pulsed photolysis-pulsed probe approach is the work of Tsurumaki *et al.* [18], which is contemporary with this study, who have taken the first step into the field of $O(^3P)$ + hydrocarbon "stereodynamics". They have exploited explicitly the anisotropy in the recoil distribution of $O(^3P)$ atoms formed by polarised laser photolysis of NO_2, in conjunction with sub-Doppler resolution of the OH product LIF lineshapes excited by a polarised probe laser.

In a variation of a photoinitiated experiment Suzuki and Hirota reported [24] a comparative study for the reactions of $O(^3P)$ and $O(^1D)$ with methane. This remains the only study so far in which information on the internal state of the organic radical coproduct has been measured directly for reactions of $O(^3P)$ with hydrocarbons. While their main focus was on the reaction of CH_4 with $O(^1D)$, they also tackled the reaction with $O(^3P)$ to provide a comparison of the dynamics. The CH_3 radical was observed by tuneable continuous wave (c.w.) infrared diode laser spectroscopy in a

multipass absorption cell. A pulsed excimer laser initiated reaction. For the $O(^3P)$ experiments, SO_2 was chosen as precursor, for $O(^1D)$ N_2O, and photolysed at 193 nm, in a mixture with CH_4 at a total pressure of 200 mTorr.

The relatively long timescale for detection limited the nascent product state information that could be extracted. The CH_3 umbrella mode distribution was obtained by extrapolation to time zero, but the nascent rotational distribution was not recovered.

For the reaction of $O(^1D)$ with methane, there is also data available on the internal CH_3 distribution based on resonance enhanced multiphoton ionisation (REMPI) experiments [25,26,27].

That completes the survey of experimental methods used to probe the dynamics of reactive $O(^3P)$ with hydrocarbon collisions. The quantities that have been measured and the conclusions that have been drawn will be described below.

In addition to these reactive studies, it is worth mentioning a quite distinct approach to the study of non-reactive $O(^3P) + CH_4$ collisions. Liuti, Pirani, Aquilanti and coworkers [28,29] have developed a molecular beam-static gas scattering apparatus. The $O(^3P)$ velocity was selected by chopping a supersonic beam expansion from a microwave discharge of O_2 in He. A Stern-Gerlach magnet arrangement was used to select a specific $O(^3P_j)$ spin-orbit state [30]. Velocity and j-dependent absolute integral cross-sections were measured by detecting glory-scattered $O(^3P)$ atoms with a quadrupole mass spectrometer.

1.3.1 Experimentally Determined Dynamical Quantities

1.3.1.1 Excitation Functions

The reaction cross-section, σ, as a function of translational collision energy, E_T is called the excitation function. The only careful measurement of the excitation function for $O(^3P)$ with hydrocarbon reactions was carried out during the original crossed-beam study by Andresen and Luntz [14]. Because of the state-resolved nature of LIF detection, the excitation function is naturally specific to the OH level being probed. However, since the product rotational state distribution was found to be relatively insensitive to E_T as explained below, the N'=1 excitation functions were taken to be representative of the total production of a given OH vibrational level. The results for reactions of $O(^3P)$ with primary, secondary and tertiary hydrocarbons are depicted in figure 1.3.

For both probed vibrational levels, OH(v'=0, v'=1), and for the different categories of hydrocarbon, the excitation function shows clearly that reaction only takes place once the collision energy exceeds a specific threshold energy, E_0. The variations in E_0 with the type of C-H bond mirror very closely those of the kinetically determined activation energies, E_a.

In addition, Andresen and Luntz noted that E_0 is the same for both the vibrational ground (v'=0) and excited state (v'=1) production of OD from the $O(^3P)$ + deuterated cyclohexane reaction. It can be concluded therefore that both of these product vibrational states lie energetically below the top of the barrier.

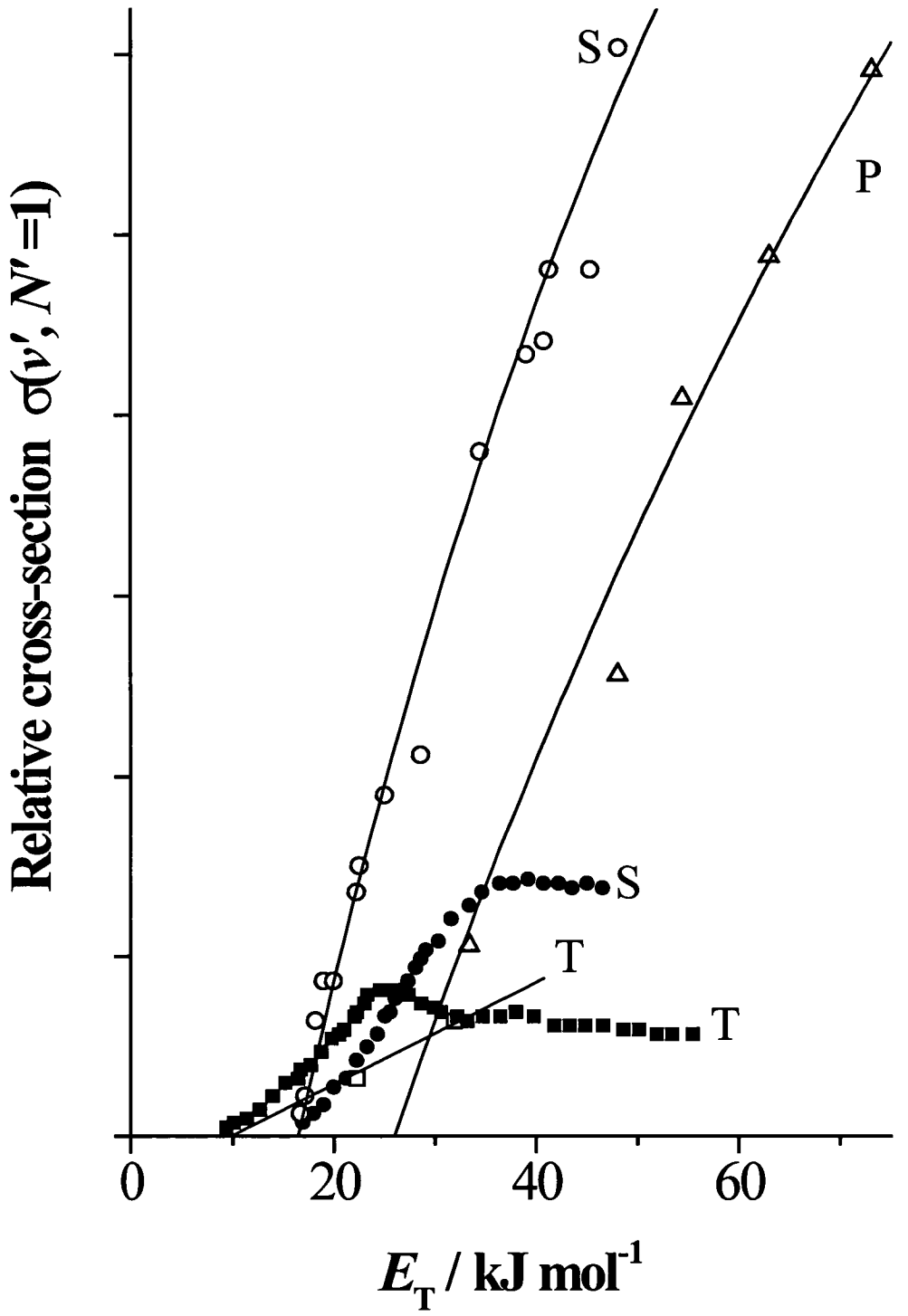

Figure 1.3: OH(v', N'=1) excitation functions for representative O(^{3}P) + HR reactions. T= tertiary ($(CH_3)_3CH$) with (■) v'=1; (□) v'=0. S=secondary (*cyclo*-C_6H_{12}) with (●) v'=1; (○) v'=0. P=primary ($(CH_3)_4C$) with (△) v'=0. Taken from [7] which was redrafted from figure 8 of reference [14].

The cross-sections typically rise more or less linearly with energy immediately above threshold energy. The slopes of these functions are related to the Arrhenius pre-exponential *A*-factors, and the relative values are again in good agreement with thermal rate constants for different types of hydrocarbon. The excitation function for OH(v'=0) continues to rise smoothly over the available energy range. In contrast, the excitation function for OH(v'=1) reaches a maximum and then abruptly stops rising for both secondary and the tertiary hydrocarbons.

Measuring the excitation function in a photolysis-probe setup is very difficult, but the translational energy can still be varied in a crude fashion through the wavelength used to photolyse the O(^{3}P) precursor. A qualitative rise of the reactivity was observed, and most notably, in the case of methane, the reaction could only be detected at sufficiently short photolysis wavelengths, indicating that only then is the collision energy sufficiently high to overcome the barrier [23]. A proper quantification of the effect in this experimental setup would be possible in principle, but beside corrections for variations in the precursor absorption cross-section and photolysis laser pulse energy with wavelength, the main hurdle to a quantitative interpretation remains the width of the collision energy distribution, which can be calculated [17] as will be done in section 4.4. An example to illustrate the effect is shown in figure 1.4.

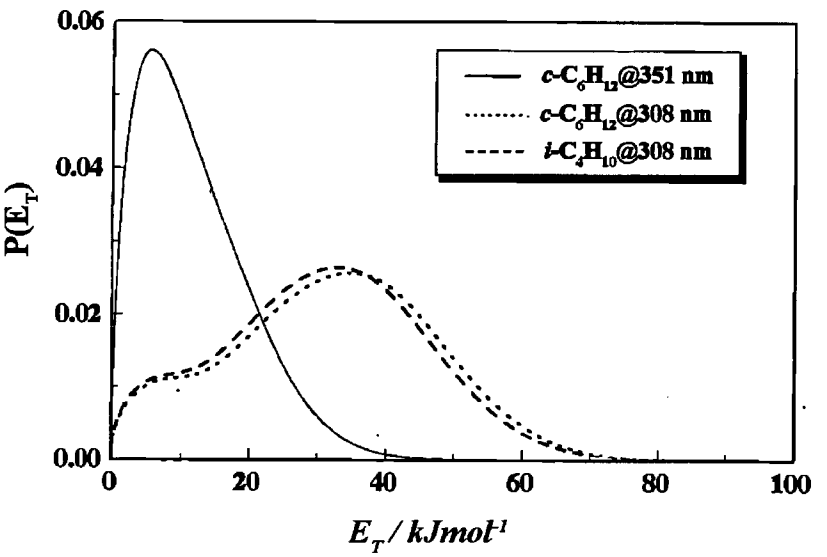

Figure 1.4: Collision energy (E_T) distributions for $O(^3P)$ + HR reactions with HR= *cyclo*-C_6H_{12} and *iso*-C_4H_{10} and different NO_2 photolysis wavelengths as indicated. Reproduced from figure 2 in [18].

1.3.1.2 Internal state distributions in the OH product

The distribution over the internal levels of the OH coproduct (vibrational, v'; rotational, N'; spin-orbit, F_1/F_2; and Λ-doublet, Π(A' or A") is obtained directly by analysis of the relative intensities of lines in the LIF excitation spectrum, similar to the method used in this study and discussed in detail in section 4.3. Aspects of the internal state distribution have been reported for a wide range of hydrocarbons and experimental conditions [7].

1.3.1.2.1 OH vibrational states

As explained above, the product vibrational state partitioning will be a function of E_T, and so different experimental conditions have to be compared carefully. Nevertheless, there is, on the whole, a reasonable agreement between results for a common hydrocarbon. There is a clear trend towards increasing relative production of OH(v'=1) along the series primary < secondary < tertiary, achieving inversion for the tertiary hydrocarbons [14]. Supporting this trend, any production of OH(v'=1) from the reaction of $O(^3P)$ with CH_4 was reportedly too weak to be detected [23].

In marked contrast, reactions of $O(^1D)$ with saturated hydrocarbons populate a whole range of vibrational levels in the OH product up to v'=4. Reactions with substituted hydrocarbons produce a nascent OH vibrational distribution which peaks strongly at the lowest level (v'=0) and populates the higher levels roughly in equally low amounts, methane shows a distinct behaviour, rising and peaking at OH(v'=2) before tailing off up to OH(v'=4) [31,32,33].

1.3.1.2.2 OH rotational states

The N' distribution for $O(^3P)$ with hydrocarbon reactions has been widely measured for both OH(v'=0) and (v'=1) [14,16,18,22,23]. All measurements report only a relatively small amount of the total energy available being channelled into OH product rotation, f_{rot}, producing a characteristically "cold" rotational distribution, for all hydrocarbons and all vibrational levels. The lack of rotational energy release in the OH product is probably the principal dynamical characteristic of this class of reactions.

The crossed beam data have to be adjusted for an assumed form of the differential cross section to compare them [14,16] with the photolysis-probe experiments. In general, the results are rather insensitive to the form of the differential cross section and are in good agreement with the photolysis-probe studies [18,22,23] where OH product densities at short times are directly related to relative cross-sections. The OH(v'=0) product usually features a slightly hotter than thermal (300 K) rotational distribution, that in OH(v'=1) is considerably colder. This is demonstrated for the case of isobutane in figure 1.5.

The nascent LIF excitation spectra look very similar for different hydrocarbons or E_T. This is shown for a variety of different hydrocarbons in figure 1.6. The same is true for the derived nascent rotational distributions. Closer inspection reveals a slight trend towards hotter distributions at higher average E_T, but not in proportion to the extra energy available (i.e. f_{rot} declines with increasing E_T). These results will be discussed in more detail in consideration of the results of this study in section 5.1.

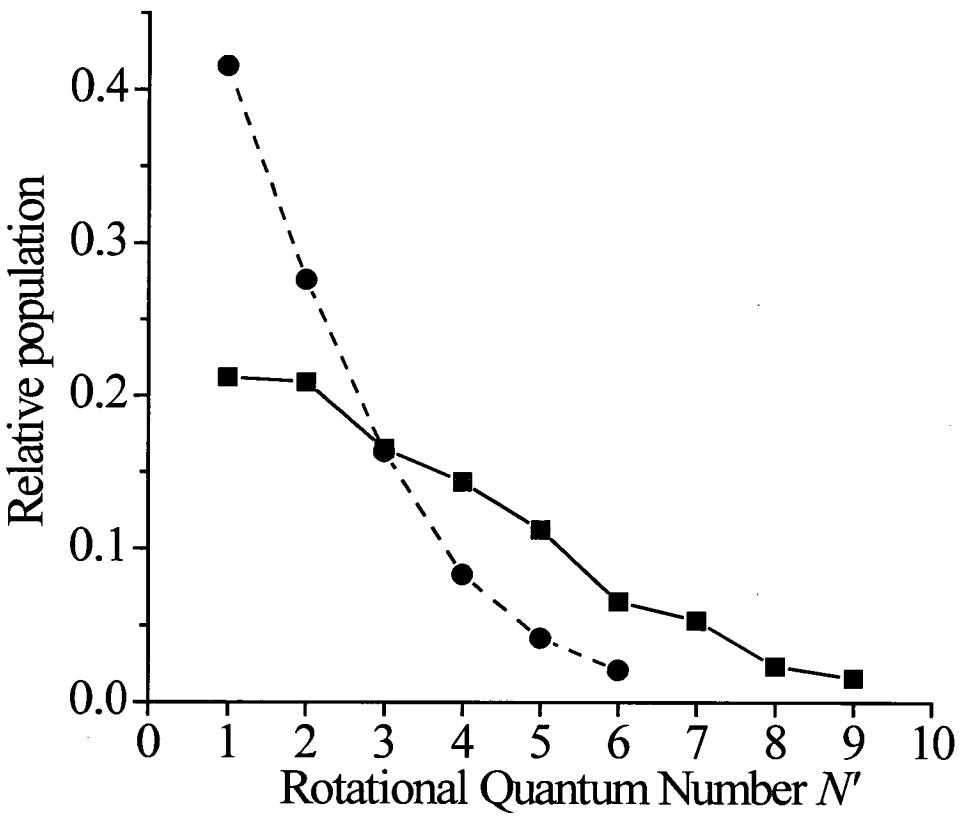

Figure 1.5: Contrasting rotational populations in OH v'=0 (■) and v'=1 (●) from the reaction $O(^3P)$ + $(CH_3)_3CH$ initiated by 308 nm photolysis of NO_2. Reproduced from [23].

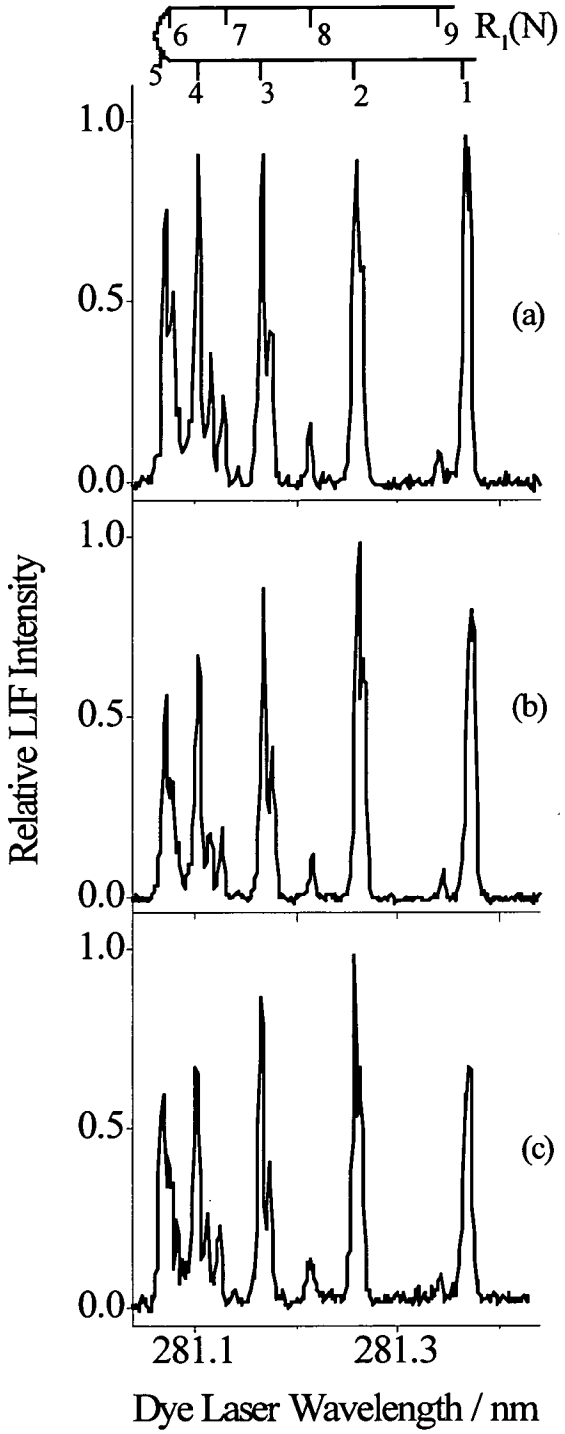

Figure 1.6: Nascent LIF spectra of the R_1 branch region of the OH A-X (1,0) band for reaction of $O(^3P)$ with $(CH_3)_3CH$ (upper panel), *cyclo*-C_6H_{12} (centre panel) and C_2H_6 (lower panel). NO_2 was photolysed at 308 nm. Reproduced from [23].

Similarly, a slight broadening of the distribution in the sequence tertiary < secondary < primary < CH_4 was observed [23], which is notably the *opposite sense* to the variation in $<E_{av}>$, and therefore implies the observed increase in f_{rot} noted above. A clear demonstration of this effect can be seen in figure 1.7 where a comparison between different hydrocarbons and different photolysis wavelengths has been depicted.

Again, there is a marked contrast of the OH rotational distributions produced by reactions with $O(^1D)$ compared to $O(^3P)$ atoms. The former produces a significantly different pattern [32]. For the nascent OH(v'=0) product, rotational distributions extending beyond N'>20 are observed for all hydrocarbons. The "hottest" distribution is observed for methane. The larger the hydrocarbon gets, the "colder" the distribution becomes. But even neopentane, which displays the coldest distribution of all hydrocarbons measured by Park and Wiesenfeld [32], peaks at a moderate value of N'=6. All cases still display significant rotational population in high N' levels even for high vibrational excitation in the OH product. Furthermore, the measured distributions in the higher levels do not look particular "Boltzmann-like" which would peak relatively early with a long tail. Instead they tend to be very shallow or as in the case of OH(v'=1, 2) produced by reaction of $O(^1D)$ with ethane displaying a long rise with increasing N' and a sharp drop after the maximum, similar to the appearance of statistical prior distributions.

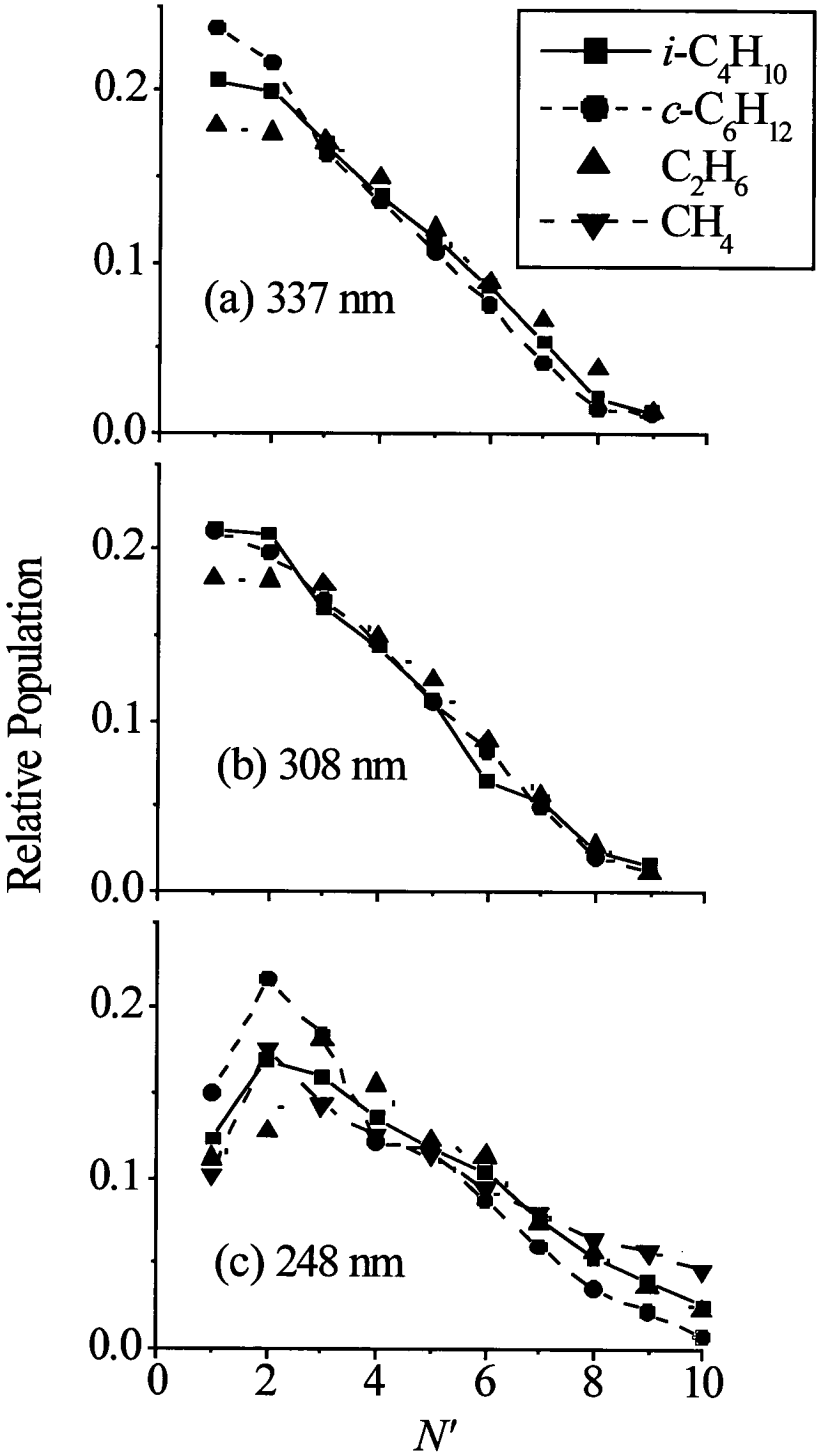

Figure 1.7 OH v'=0 F_1 rotational populations from reactions of O(^{3}P) with $(CH_3)_3CH$ (■), *cyclo*-C_6H_{12} (●), C_2H_6 (▲) and CH_4 (▼) initiated by photolysis of NO2 at 337 nm (upper panel), 308 nm (centre panel) and 248 nm (lower panel). Reproduced from [23].

The OH rotational distribution from the reaction of $O(^1D)$ with methane shows a distinct bimodal behaviour in the surprisal analysis, for the lower vibrational levels. The lower rotational levels seem to be less populated than the statistical expectation, while the higher rotational levels are more populated.

1.3.1.2.3 OH fine-structure states

OH in its electronic ground state is characterised by $^2\Pi_i$ symmetry. The spin-orbit splitting between the two states, $^2\Pi_{3/2}$ and $^2\Pi_{1/2}$, is relatively large compared to the rotational constant and at least for low values of N', Hund's case (a) coupling is a reasonable description [15]. This will be discussed in further detail in section 2.2.3.2. The rotational levels are divided into two discrete $^2\Pi_{3/2}$ and $^2\Pi_{1/2}$ spin-orbit manifolds, with the respective lowest levels separated by ~125 cm^{-1}. The splitting is inverted and the lower-lying $^2\Pi_{3/2}$ levels carry the spectroscopic label F_1, while the higher lying $^2\Pi_{1/2}$ levels are labelled F_2. Each rotational level is also further split by Λ-doubling into Π(A') and Π(A") components with a relatively negligible energy separation.

All measurements consistently reported a preference for the lower-lying OH F_1 spin-orbit state for the reaction of $O(^3P)$ with hydrocarbons. The preference was found to decrease only slightly with N' after correcting for the spatial $(2j'+1)$ degeneracy and be independent of the nature of the hydrocarbon [23], as shown in figure 1.8. A summary of the reported F_1 / F_2 ratios averaged over N' are listed in detail in the latest review [7]. A more detailed discussion of this effect, the results of this study and models proposed to rationalise it can be found in section 5.2.

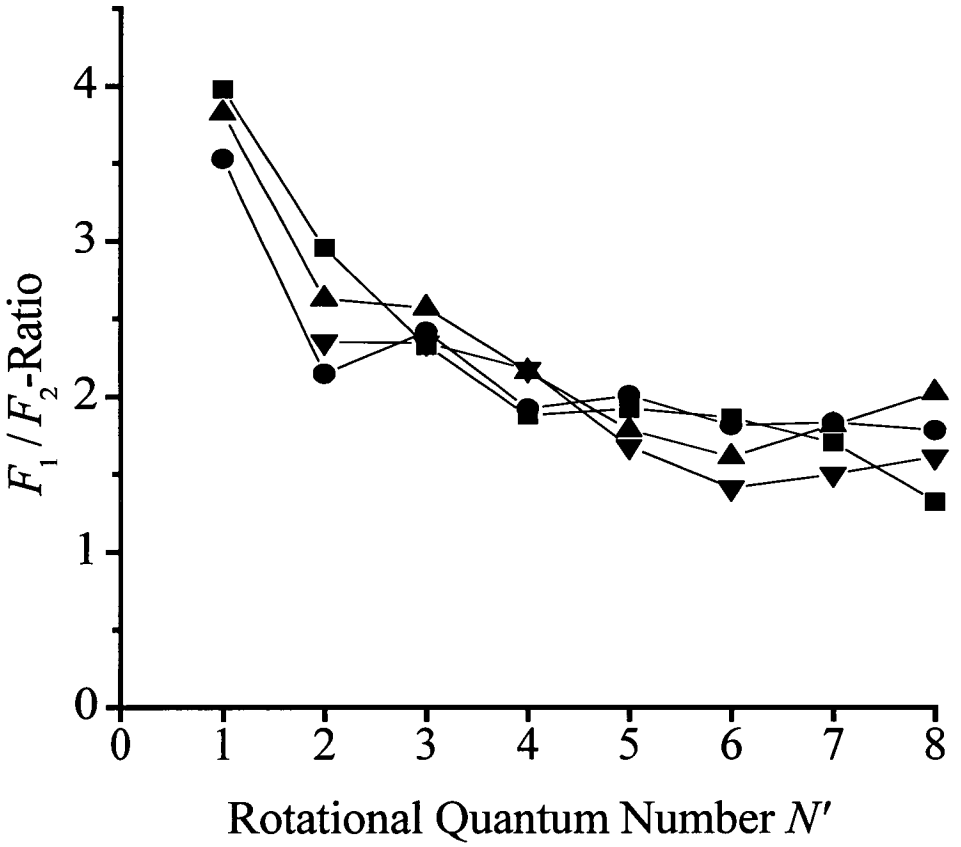

Figure 1.8: OH(v'=0) F_1/F_2 spin orbit branching ratios from reactions of O(^{3}P) with $(CH_3)_3CH$ (■), *cyclo*-C_6H_{12} (●), C_2H_6 (▲) and CH_4 (▼) initiated by photolysis of NO_2 at 248 nm. Reproduced from reference [23].

While there is a strong indication from the experimental data for a non-statistical distribution in the spin-orbit manifolds, neither of the Λ-doublets have been found to be preferentially populated. The only possible exception is an isolated report [22] for cyclooctane, which may favour the Π (A') levels with near-statistical significance. This has not been independently confirmed.

The behaviour exhibited by $O(^1D)$ reactions is, again, profoundly different. No preference for any spin-orbit states has been observed for any of the hydrocarbons under investigation [32]. Instead, a preference for the Π (A') Λ-doublet level is reported for all hydrocarbons. This effect is strongest for methane and decreases with increasing size of the hydrocarbon [32].

1.3.1.3 Internal state distributions in the organic radical coproduct

1.3.1.3.1 Direct observations

As noted above, there is only one direct experimental observation of the internal state distribution of a hydrocarbon co-product fragment, which is CH_3 from the reaction of methane with $O(^3P)$ and $O(^1D)$ [24]. This work was focussed on the reaction of CH_4 with $O(^1D)$, and only more limited information was provided on the $O(^3P)$ reaction.

In both cases, the vibrational distribution of the CH_3 ν_2 out-of-plane bending "umbrella" mode was found to be non-inverted, declining in the ratio 1:0.6:0.4:0.2 for the first four levels in the $O(^3P)$ reaction. For CH_4, the higher observed levels are only accessible for collisions in the high-energy tail of the E_T distribution. This experimental result is displayed in figure 1.9 where it is also compared to the results

of a recent quantum scattering calculation which will be discussed in section 1.4.1.4 in detail.

The CH_3 ν_2 distribution was surprisingly similar to the one produced by the $O(^1D)$ with CH_4 reaction, which displayed the same branching ratio for N_2O as photolytic precursor, and 1:0.6:0:2 for O_3 as photolytic precursor, with no significant population in the v'=3 level. If compared with statistical prior distributions, $O(^1D)$ produces a "colder" distribution than statistically expected, while $O(^3P)$ produces a "hotter" one in this specific vibrational mode.

While this is the only direct experimental information available for the internal state distribution for the hydrocarbon product from reactions with $O(^3P)$, more information is available for $O(^1D)$ reactions. In a traditional jet expansion photolysis probe set-up, Kleinermanns and coworkers [25,26,27] used REMPI to investigate the CH_3 product internal state distribution for a series of hydrocarbons.

The existence of a CH_3 product from the reaction of saturated hydrocarbons other than CH_4 with $O(^1D)$ requires the fission of a C-C bond during the progress of the reaction, a features which has not been observed for reactions of $O(^3P)$ with saturated hydrocarbons.

Kleinermanns and coworkers reported detailed vibrational distributions for the ν_1 symmetric stretch and ν_2 umbrella modes of CH_3. They found significant populations in the higher levels of these vibrations, but in no case did inversion occur. In all cases, the maximum population was found in the lowest vibrational level and it declined monotonically over the next two excited levels. They also observed

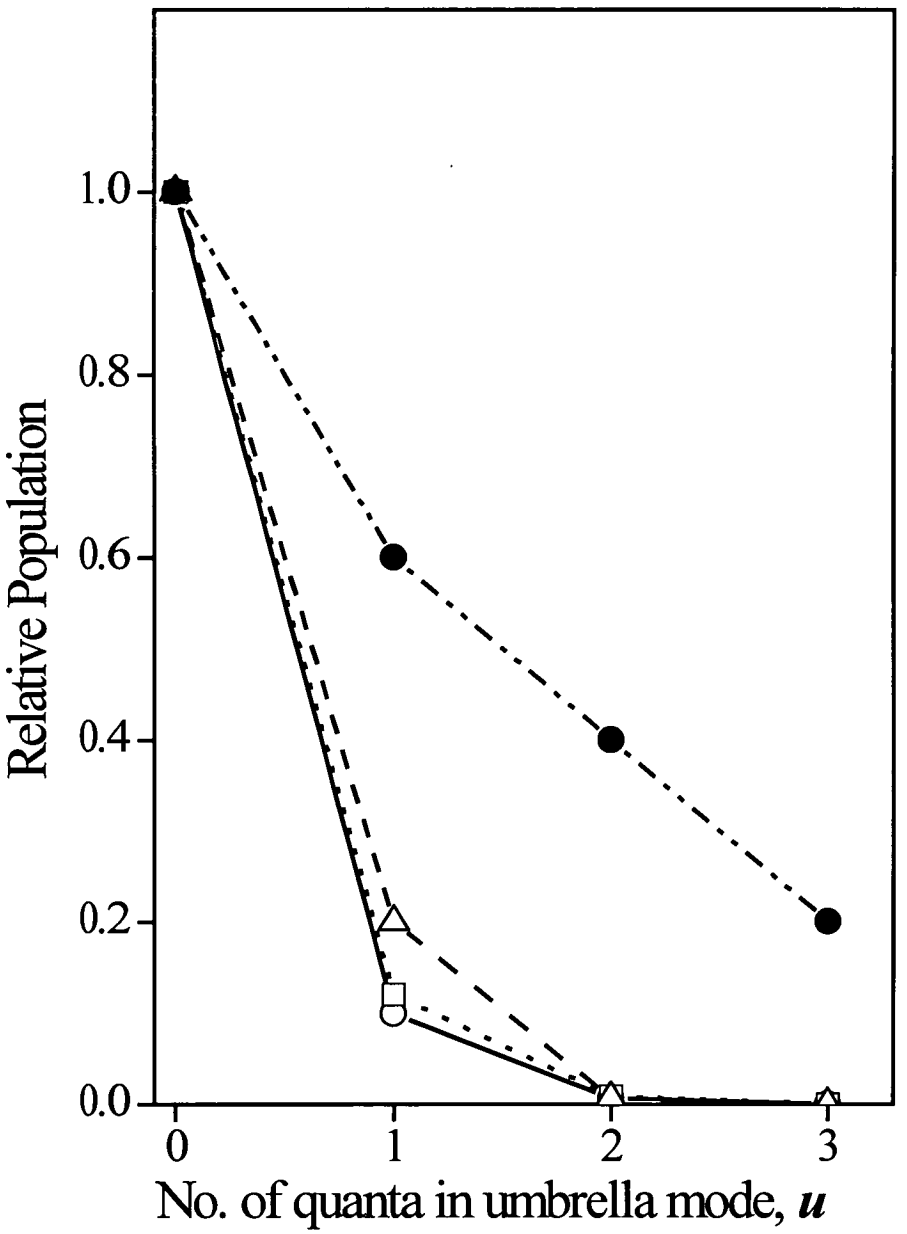

Figure 1.9: Product CH_3 umbrella mode distributions from the reaction of $O(^3P)$ + CH_4. Experimental results (●) from [24], initiated by 193 nm photolysis of SO_2 giving a broad collision energy distribution with $\langle E_T \rangle$=32 kJ mol^{-1}. Reduced-dimensional quantum scattering predictions of a 3 DF model from reference [49]: (○) E_T=32 kJ mol^{-1}, (□) E_T=43 kJ mol^{-1}, (△) E_T=53 kJ mol^{-1}. Redrafted from figure 6 in [49].

very high rotational excitation of the CH_3 fragment nearly up to the energetic limit.

These results are consistent with the idea that reactions of $O(^1D)$ with saturated hydrocarbons proceed via an insertion of the $O(^1D)$ atom into the C-H bond, forming a chemically activated alcohol intermediate, followed by decomposition of this complex.

1.3.1.3.2 Indirect evidence

While the study of Suzuki and Hirota [24] remains the only direct study of the internal state distribution of the hydrocarbon-radical co-product for $O(^3P)$ reactions, several authors tried to establish some information indirectly based on observation of the OH radical and exploiting energy conservation [16,23], or through features of the OH excitation functions [14]. The most recent indirect information comes from the Doppler-resolved OH LIF experiments of Tsurumaki *et al.* [18].

By the virtue of the experimental method, the internal state of the OH radical is known, while the translational energy is derived from composite Doppler profiles. Therefore, the remaining energy out of the total energy available has to be in the hydrocarbon fragment. While in principle the total energy balance is extracted from the experiment, photolytically produced $O(^3P)$ atoms have a significant spread in the translational energy distribution restricting the quality of this information.

Furthermore, the information is product-channel specific, which in case of Tsurumaki *et al.*'s results means only the OH(v'=1, j'=3.5) product of the $O(^3P)$ with cyclohexane reaction [18]. They reported a significant fraction of the available energy being deposited in the cyclohexyl radical as shown in figure 1.10. The amount

of energy increased in rough proportion to a change in $\langle E_{av} \rangle$ from 12 to 33 kJ mol^{-1}.

In a similar experiment, Brouard and coworkers investigated the OH ($^2\Pi_{3/2}$, v'=0, N'=5) and OH (v'=4, N') products of the reactions of O(^{1}D) with methane [34,35]. Only very low kinetic energy release was observed and nearly all of the available energy is therefore expected to be in internal excitation of the fragments, which is also consistent with an insertion-type mechanism.

In contrast, all available, admittedly more limited and less direct, information on the reactions of O(^{3}P) with saturated hydrocarbons indicate a large fraction of the available energy in the translational motion of the fragments.

1.3.1.4 Differential cross-sections

As mentioned above, there are no conventional mass-spectrometric crossed molecular beam studies for O(^{3}P) + saturated alkane reactions. Therefore Tsurumaki *et al.*'s [18] Doppler-resolved OH LIF measurements are the only direct observation of the differential cross-sections (correlation between reagent, $\boldsymbol{k}$, and product, $\boldsymbol{k'}$, relative velocity vectors).

Probing OH(v'=1, j'=3.5) on the $R_1(3.5)$ and $^RQ_{21}(3.5)$ transitions, whose transition dipole moments are perpendicular to one another, composite Doppler profiles were obtained from different experimental geometries and different relative pump-probe polarisations. These profiles contain information about the differential cross section which can be derived in terms of a chosen set of product translational energy-dependent angular basis functions.

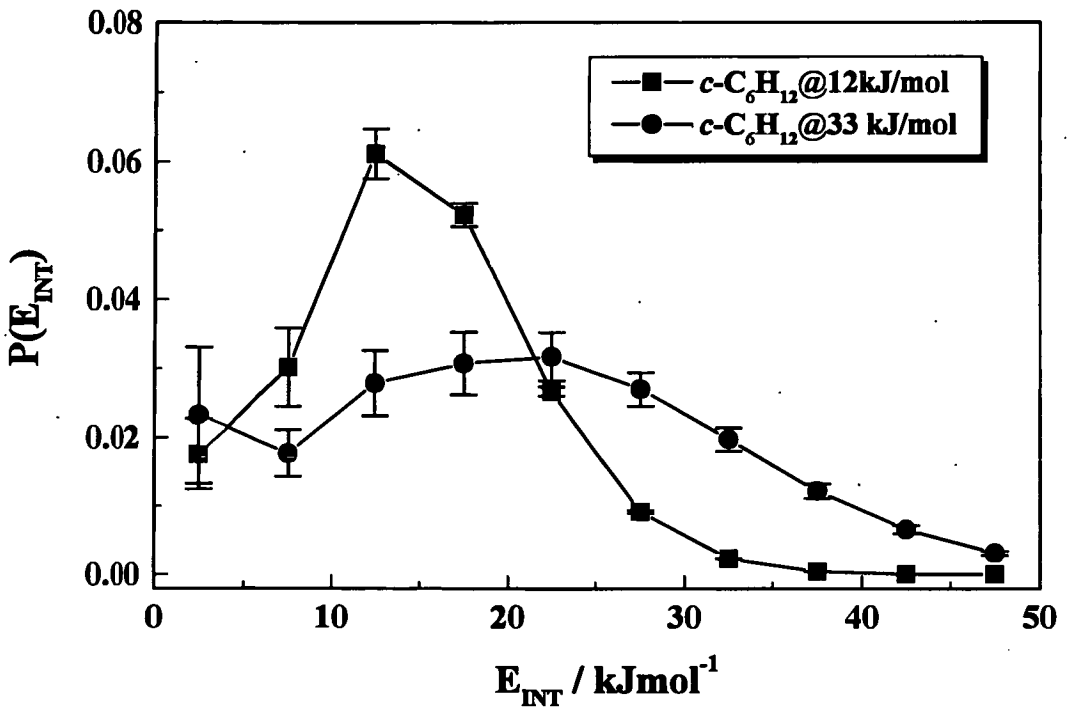

Figure 1.10: Internal energy (E_{INT}) distribution of the *cyclo*-C_6H_{11} radical coproduct of the reaction of $O(^3P)$ with *cyclo*-C_6H_{12} at $\langle E_T \rangle$=12 kJ mol^{-1} (■) and 33 kJ mol^{-1} (●). Derived indirectly from the measured translational energy distribution of the OH v'=1, j'=3.5 product. Reproduced from [18].

The differential cross-section for the reaction of $O(^3P)$ with cyclohexane was measured at two different photolysis wavelengths of the NO_2 precursor molecule at 351 and 308 nm. The collision energy distribution at the higher photolysis wavelength (351 nm) could be described by a mean collision energy, $\langle E_T \rangle$ of 12 kJ mol^{-1}. The hydroxyl-radical scattering was found to be predominantly in the backward hemisphere. For the higher energy, $\langle E_T \rangle$ = 33 kJ mol^{-1} (photolysis at 308 nm) a profound shift towards scattering into the forward hemisphere was reported, without much residual preference for backscattering as shown in figure 1.11.

The reaction of $O(^3P)$ with isobutane was only measured at one photolysis wavelength of 308 nm which corresponds to $\langle E_T \rangle$ = 31 kJ mol^{-1}, which in contrast to cyclohexane produced broad scattering with a slight preference towards sideways scattering.

Again, due to increased signal levels, the differential cross-sections for $O(^1D)$ reactions could be measured for the alkane parent compound, methane [34]. The differential ($\boldsymbol{k},\boldsymbol{k}'$) cross section was found to be indistinguishable for different Λ-doublets in the OH ($^2\Pi_{3/2}$, v'=0, N'=5) product with profound preference in both cases for forward and backward scattering which is generally regarded as an indication for the presence of a long-lived complex.

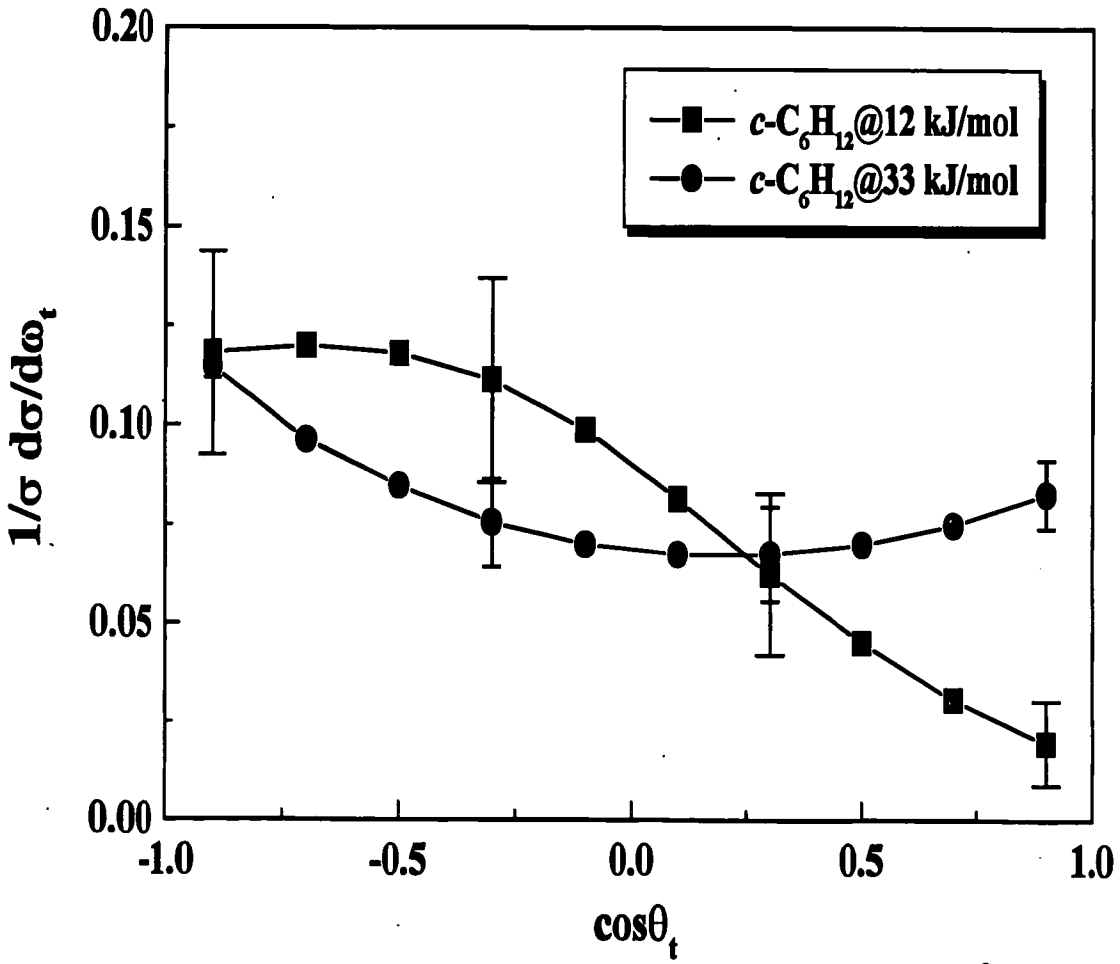

Figure 1.11: Differential cross-section of the OH v'=1, N'=3, F_1 product of the O(^{3}P) + *cyclo*-C_6H_{12} reaction averaged over all product translational energies at <ET>=12 kJmol^{-1} (■) and 33 kJ mol^{-1} (●). Reproduced from [18].

In addition, the correlation of the OH rotation $\boldsymbol{j'}$ with respect to the plane defined by the velocity vectors $\boldsymbol{k}$ and $\boldsymbol{k'}$ was measured for OH ($^2\Pi_{3/2}$, v'=0, N'=5) as well as the OH ($^2\Pi_{3/2}$, v'=4, N'=8) [35] product. The OH ($^2\Pi_{3/2}$, v'=4, N'=8) product was found to have its $\boldsymbol{j'}$ vector aligned perpendicular to the plane. This was also the case for the OH ($^2\Pi_{3/2}$, v'=0, N'=5) product in the Π (A') Λ-doublet state, while the OH ($^2\Pi_{3/2}$, v'=0, N'=5) in the Π (A") state is produced with a nearly isotropic distribution. The comparison is not perfect since the OH ($^2\Pi_{3/2}$, v'=4, N'=8) product was averaged over both Λ-doublets. Interestingly enough, the Λ-doublet which is preferentially produced [32] is the Π (A') one, which also produces a strict alignment of the $\boldsymbol{j'}$ vector.

These results can be interpreted as evidence for the presence of at least two different mechanisms. The dominant one produces the OH product with a strong alignment of the rotational $\boldsymbol{j'}$ vector and the electronic orbitals of the OH product. This is a direct process without much time to distribute the excess energy evenly into the different degrees of freedom. On the other hand, the second kind of mechanism seems to take place via a long living intermediate complex which decomposes without much steric constraint and with a rather statistical distribution of the energy over the available degrees of freedom. This interpretation is also strengthened by the bimodal behaviour of the rotational distribution in the lower vibrational levels of the OH product.

1.4 Interpretation and Theoretical Modelling

The whole range of experimental observations is now drawn together in the next subchapter to provide a specific picture for the $O(^1D)$ and $O(^3P)$ reactions with hydrocarbons. This picture will then be set against theoretical prediction at different levels of theory. This is followed by a similar analysis of electronic fine-structure effects observed in the reactions of $O(^3P)$.

1.4.1 Nuclear Motions

1.4.1.1 Qualitative conclusions based on the experimental data

For the reactions of $O(^3P)$ with hydrocarbons the OH vibrational distribution probably presents the most straightforward data to interpret. The lowest vibrational excitation is found for CH_4 and primary hydrocarbons which increases with increasing exothermicity of the reaction until even inversion is achieved for tertiary hydrocarbons. This is strongly characteristic of a direct abstraction reaction, as first pointed out by Andresen and Luntz [14]. This conclusion is supported by the efficient conversion of additional E_T to OH vibration. From this point of view, the system can satisfactorily be treated as a pseudo-triatomic O + H-R reaction. The hydrocarbon fragment R behaves as a spectator and the only influence is due to indirectly changing the strength of the H-R bond.

In this simple picture, for a fixed E_T the main factor for vibrational energy release in the OH product is the location of the barrier along the O--H--R reaction co-ordinate. The more exothermic the reaction is, the earlier the barrier lies and the more

translational energy can be channelled into OH product vibration in accordance with the well-established "Polanyi Rules" for direct reactions [36]. The kinematics of the reactions can be classified as heavy + light-heavy (H+LH), which tends to enhance OH vibration due to H-R repulsion in the exit channel [37,38]. No evidence for a long lived complex was found, which may lead to a statistical energy partitioning.

In addition, the universally observed cold OH rotational distributions have also been widely interpreted [14,16,22,23] as evidence for a direct process in which the incoming $O(^3P)$ interacts with a single H-C bond. The lack of rotational excitation is the main piece of experimental evidence for a preferred collinear geometry. A more detailed discussion will be carried out in the light of the new results of this study in section 5.1.

However, not all of the experimental observations can be accommodated in this simple triatomic picture. Suzuki and Hirota [24] estimate the CH_3 ν_2 umbrella mode excitation to be considerably hotter than the statistical prior distribution. Since the CH_3 fragment passes from a tetrahedral geometry in the reagent CH_4 to a planar equilibrium geometry in the CH_3 product, some excitation of this mode is to be expected. Suzuki and Hirota argue that even if this transformation takes place by a smooth relaxation up to the saddle point, whose geometry will be discussed in section 1.4.1.3, the final distribution is still sensitive to the form of the potential surface beyond that point, without providing further details.

McKendrick and coworkers [23] tried to rationalise the overall internal energy partitioning in the reaction of $O(^3P)$ with CH_4 in order to estimate the translational

energy release in the products. The "cold" rotational distribution can only be interpreted as characteristic of the preferred geometry at the saddle-point if significant repulsion between the fragments takes place, in a sense that this "freezes" the saddle-point geometry in the rotational motion of the OH fragment.

The main problem was posed by the establishment of the average collision energy for a reactive encounter. Most of the internal modes of the CH_3 fragment have not been measured and could therefore, in principle, hold an unknown amount of energy. In addition, McKendrick *et al.* [23] pointed out that although Suzuki and Hirota [24] did not report a truly nascent CH_3 rotational distributions, they still found relatively hot rotational temperatures at early times. This is surprising with respect to a collinear triatomic model, because very little torque should be imparted to the CH_3 group. The amount of energy channelled into OH and CH_3 product translation could not be established convincingly.

It is even more difficult for the higher hydrocarbons to draw firm conclusions from the very limited information available about co-product internal state partitioning. An earlier estimate by Dutton *et al.* [16] suggested that ~80% of $\langle E_{av} \rangle$ for the reaction with cyclohexane is unaccounted for in the internal states of the OH product.

Tsurumaki *et al.*'s experiment [18] is probably the most direct way to establish the branching between internal and translational energy for the hydrocarbon fragment. The experimental information is limited to the hydrocarbon radical fragment produced in conjunction with the OH(v'=1, N'=3.5) product. It is difficult to

estimate how representative this product channel is with respect to the total reactive flux, especially since the main product channel produces OH(v'=0).

Tsurumaki *et al.* emphasised that the proportionality between this internal energy and $<E_{av}>$ is not consistent with the cyclohexyl radical being merely a spectator. Andresen and Luntz [14] arrived at a similar conclusion based on the analysis of the excitation function. The excitation function for OH(v'=1) turns over at higher collision energies, as shown in figure 1.3, which was interpreted as internal modes in the hydrocarbon radical being now accessed by the reaction.

While the reactive flux in Tsurumaki *et al.*'s experiment [18] for the OH(v'=1) product was found to be predominantly backscattering for cyclohexane, at least for the lower $<E_T>$, which supports a rebound mechanism via a collinear geometry, there seems to be a substantial change towards isotropic scattering with increasing $<E_T>$.

While it is no surprise to observe a stronger forward scattering component in a reaction with a barrier with increasing $<E_T>$, it is difficult to establish the consistency of the magnitude of the change with the accepted dynamical picture on purely qualitatively arguments. Following Tsurumaki *et al.*'s [18] argument, the similarity of the differential cross-sections for cyclohexane and isobutane is accidental and due to two opposite effects cancelling each other.

The lower barrier for isobutane would lead to a larger range of reactive impact parameters in a simple line-of-centres model, therefore more forward scattering for isobutane is expected with respect to cyclohexane.

But at the same time the steric constraints on the approach of the oxygen atom are less favourable, closing down the cone-of-acceptance relative to cyclohexane, and widening less for increasing energy. This effect is supposed to be responsible for the relative favouring of forward scattering for cyclohexane at higher energies. Lacking the data for different energies for isobutane it is difficult to judge the validity of this argument.

In addition, Tsurumaki *et al.* [18] quoted the distinct temperature dependence of the thermal rate constants for secondary and tertiary hydrocarbons as further support for their conclusions about the stereodynamics. A similar stereochemical reason was suggested above for modest variations in the degree of OH rotational excitation for the different hydrocarbons, supporting Tsurumaki *et al.*'s arguments.

The picture evolving for $O(^1D)$ reactions is very different. For a long time discussions have focussed on the involvement of an insertion mechanism. With respect to the vibrational partitioning in the OH product, CH_4 produces the most excited distribution, peaking at $OH(v'=2)$. The amount of excitation decreased rapidly with the size of the hydrocarbon, with the exception of propane, which seems to be slightly more vibrationally excited than ethane [32].

The higher hydrocarbons tend to favour channels involving C-C bond rupture rather than the OH channel. $OH(v'=0)$ is the predominant product in the OH producing channel for all hydrocarbons except methane. The nature of the C-H bond attacked does not seem to have a significant influence, although it is difficult to judge on the basis of the available data. In contrast to the $O(^3P)$ reaction, there is no barrier

to the reactions and the relative gain of exothermicity due to a higher substituted hydrocarbon is small compared to the total energies involved.

If insertion, and therefore a "long-lived" complex is assumed, some relaxation of the available energy into the internal modes of the complex can be expected which will also be more efficient for the larger hydrocarbons due to a higher density of states. When the complex finally falls apart, less excitation can be found in the OH vibration for larger hydrocarbons than for the smaller ones. The same argument should hold for the rotational distribution in the various vibrational levels. In general, a wide spread over the rotational levels is observed for the higher vibrational levels, suggesting that complete randomisation has not taken place.

In contrast, the rotational population in the OH (v'=0) state cools down rapidly with increasing size of the hydrocarbon. Many authors have analysed the rotational population with the help of surprisal analysis. The data often can be represented as two surprisals, indicating the presence of two different mechanisms. Only a weak recoil of the OH product was observed [34,35] which also indicates that the exothermicity in the reaction is not channelled into translation of the products but into their internal modes. Interestingly enough, Suzuki and Hirota [24] still observe a cold CH_3 ν_2 vibrational distribution which is essentially the same as for $O(^3P)$ and supported by the REMPI data for the ν_2 and ν_3 modes [25,26,27].

Maybe the most interesting indication for the presence of different mechanisms is Brouard *et al.*'s data on the differential cross-sections [34,35]. The different alignment of the OH $\boldsymbol{j'}$ vector relative to the $\boldsymbol{kk'}$ plane for the two different Λ-

doublets might in fact strongly indicate the presence of two independent mechanisms. At the moment this is essentially a single isolated measurement, whose meaning should not be overinterpreted. The accepted view based on the experimental data is the presence of at least one insertion type mechanism along with a more abstraction kind mechanism. Their relative importance is still a matter of active debate.

1.4.1.2 Semi-empirical Surfaces

Together with the first experimental study [14] on the dynamics of $O(^3P)$ + HR reactions, Luntz and Andresen published a quasi-classical trajectory (QCT) study [39] which was performed on pseudo-triatomic O-H-R semi-empirical potential surfaces (PESs) for representative primary, secondary and tertiary hydrocarbons. The PES was constructed via the simple London-Eyring-Polanyi-Sato (LEPS) formalism. The hydrocarbon radical product was assumed to be a structureless particle.

The three Sato parameters, which control the degree of repulsion in each of the pairwise potentials, were optimised for the case of a secondary hydrocarbon (*cyclo*-C_6H_{12}). They were fitted essentially to three aspects of the experimental results: the OH (v'=1) / (v'=0) ratio; the rotational state distribution in OH (v'=0); and the barrier height. Although this introduces some degree of circularity in the construction of the PESs to reproduce the desired results, Luntz and Andresen [39] emphasised that the surfaces for the primary and tertiary hydrocarbons were not independently adjusted. All surfaces have a preferred collinear approach geometry by virtue of their construction.

The QCT calculations successfully reproduced the observed experimental trends in OH vibrational excitation with different hydrocarbons. The LEPS surfaces showed the expected variation in location and magnitude of the barriers resulting from the changes in C-H bond strength (an input in their construction) and hence exothermicity. The calculation was also successful in predicting the experimental rotational distribution, which will be discussed in the appropriate section 5.1.2.

Luntz and Andresen also calculated differential cross-sections on the LEPS surfaces, which they reported to be strongly backscattered [39]. In the case of a secondary hydrocarbon at E_T = 30 kJ mol^{-1}, the scattering was reported to be entirely confined to the backward hemisphere. This result is much more extreme than the experimental observations made by Tsurumaki *et al.* [18] for OH (v'=1, j'=3.5). The experimental distribution show a much larger forward scattering component even for the lower energy $\langle E_T \rangle$ of 12 kJ mol^{-1}, and especially at the more comparable value of 33 kJ mol^{-1}. The calculations also showed a slight broadening of the differential cross-sections with increasing E_T.

Clary, Connor and Southall [40] performed quantum scattering calculations based on the vibrationally adiabatic distorted wave (VADW) approximation on the same LEPS potentials. Technical difficulties were encountered in applying this method to a heavy + light-heavy system. The calculation of cross sections tended only to converge at relatively low E_T.

Beside these problems, model primary and tertiary hydrocarbons produced cold OH rotational distributions in accordance with the experimental results [14] and the

previous QCT calculation [39]. Some problems were identified in the assumption of an artificial $^1\Sigma$ symmetry for the real $^2\Pi$ OH molecule. In consequence, it was concluded that the results should best be plotted as a function of rotational energy rather than of quantum number. The calculated differential cross-sections were again all backward peaked as in the previous QCT calculations. The OH product was also found to have $\boldsymbol{j'}$ aligned preferentially perpendicular to $\boldsymbol{k}$, typical of a recoil reaction through a collinear geometry. This prediction is yet to be tested by experiment.

1.4.1.3 Ab Initio Surfaces

Nearly simultaneously with the first experimental studies of the higher hydrocarbons by Andresen and Luntz [14], Walch and Dunning [41] published the first *ab initio* treatment of the reaction of $O(^3P)$ with CH_4. They concentrated their effort mainly on the transition state geometry and the barrier height.

Elementary considerations of electronic configurations in a collinear C_{3v} geometry showed that the reactants and products are connected via a degenerate surface of ^3E symmetry which corresponds to one of the two half-filled p-orbitals of the oxygen atom pointing towards the H-C bond, while the non-reactive surface of $^3A_2$ symmetry corresponds to the filled p orbital pointing towards the H-C bond. These geometric considerations are depicted in figure 1.12.

The calculation was carried out using polarisation configuration interaction (POL-CI) wavefunctions on a strongly orthogonal generalised valence bond (SOGVB) orbitals basis set. The saddle-point was found to be preferentially of collinear O-H-C geometry, $\alpha \sim 180°$.

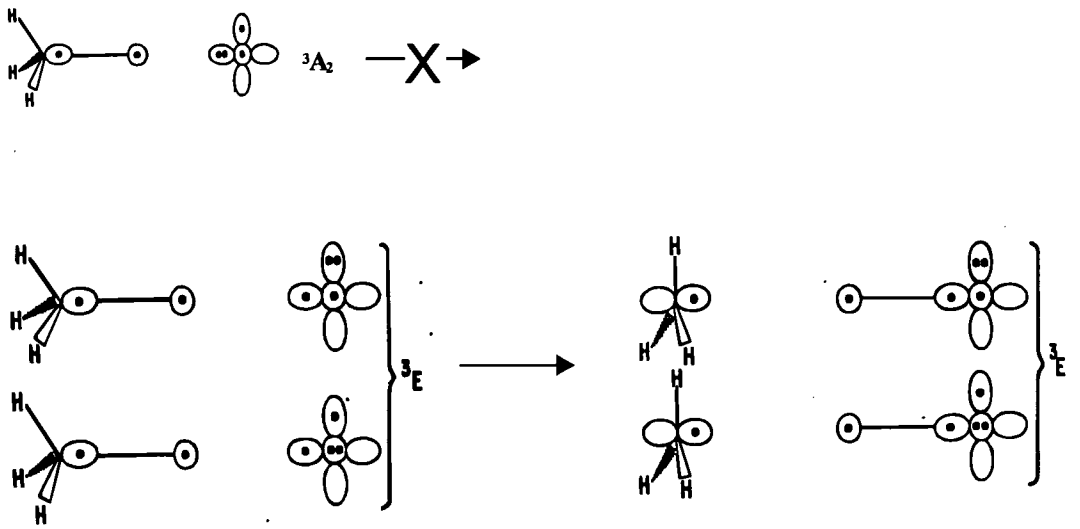

Figure 1.12: Schematic orbital correlations in the reaction $O(^3P) + CH_4$ in C_{3v} geometry. The degenerate ^3E surface correlates with $OH + CH_3$ products but the $^3A_2$ surface does not. Adapted from similar diagrams in [41].

This conclusion was derived completely independently of the experimental results of Andresen and Luntz [14] who came to the same conclusion for the higher hydrocarbons.

The geometric properties of the calculated saddle-point together with results of later calculations are summarised in reference [7]. The parameters of interest for its geometry are shown in figure 1.13. Walch and Dunning [41] found the C-H and O-H bonds moderately extended by 25% and 21%, respectively, with respect to their equilibrium distance in the free OH and CH_4 molecules. Therefore the barrier is roughly centrally located between reactants and products, as might be expected for an approximately thermoneutral reaction. The effect on the CH_3 group was small, with nearly unchanged bondlength of the non-reactive C-H bonds and only a modest change towards planarity.

For slightly non-linear O-H-C geometries, the ^3E surface splits into $^3A'$ and $^3A''$ surfaces. These correspond to the remaining unpaired orbital on the O atom lying in or perpendicular to the plane of bending, respectively. On either surface, the deviation from collinearity of the C-H-O angle α is a signed quantity, defined by whether the O atom is bent towards or between non-reactive C-H bonds on the CH_3 group. The $^3A'$ surface lies slightly higher in energy. Both surfaces have very similar bending potentials. At an angle from collinearity of $\Delta\alpha = \pm 30°$, the energy increased by ~10-11 and ~8-9 kJ mol^{-1} for $^3A'$ and $^3A''$ surface respectively, without much dependence on the sign of $\Delta\alpha$.

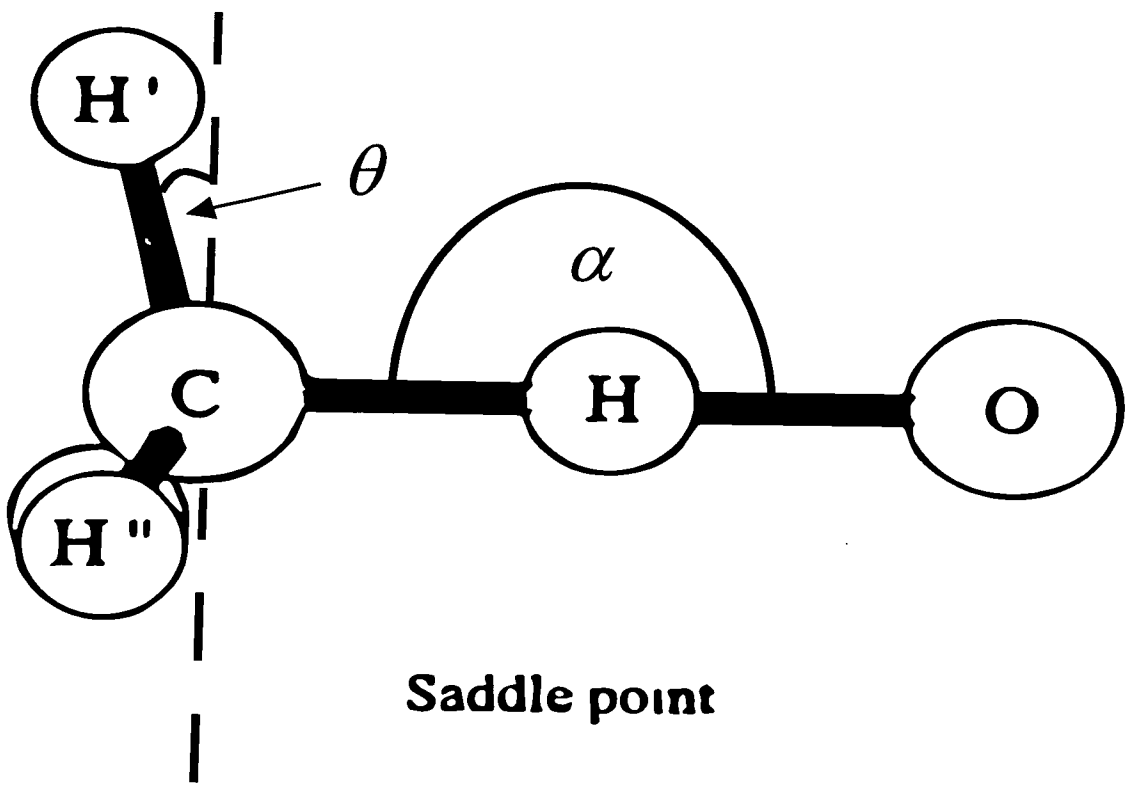

Figure 1.13: Definition of angles and distances in the O-H-C saddle-point. α is the angle of attack of the O atom relativce to the H-C bond. θ measures the departure of the CH_3 unit from planarity. The H' and H" atoms are non-reactive and not distinguished in C_{3v} symmetry. Derived from a similar diagram in [41].

No dynamical information was available to test their calculation against. Therefore, Walch and Dunning calculated the temperature dependence of the thermal rate constant via transition state theory. They corrected the calculated barrier height for an estimated error in the basis set and included tunnelling via the Wigner formalism [42]. This produced a good agreement with the experimental trend over the range 300 - 2000 K.

The next attempt to calculate the saddle-point geometry was conducted by Gonzalez, McDouall and Schlegel [43], as part of a comparative study of the reactions of CH_4 with H, OH and $O(^3P)$. The geometries and vibrational frequencies were calculated at the HF(Hartree-Fock) / 6-31G** and UMP2 (unrestricted Møller-Plesset, 2nd order perturbation) / 6-31G** level. The barrier heights and the heats of reaction were calculated by 4th order Møller-Plesset perturbation theory with spin projection (PMP4(SDTQ)) using a 6-311G** basis set.

Both the $^3A'$ and $^3A''$ surface were considered for $O(^3P) + CH_4$. While the geometry of the saddle-point was calculated to be essentially linear on both surfaces, in accordance with Walch and Dunning, the activation barrier was quite seriously over-estimated compared to both the POL-CI result [41] and to the experiment. After including tunnelling [42] and scaling of the the barrier height to the results of Walch and Dunning a good agreement was achieved for the calculated transition-state thermal rate constant with the experimental value.

Recent years have seen a new boom in attempts to tackle the $O(^3P) + CH_4$ reaction. A comparative study by Jursic [44] applied different levels of density

functional theory (DFT) to the reaction of $O(^3P)$ with methane. He compared saddle point geometries and the corresponding energies.

The first truly multidimensional calculation was carried out by Corchado *et al.* [45]. The employed dual-level approach. In the higher level they calculated geometries, energies and vibrational frequencies of the reactants, products and the saddle-point at the highest practical level of *ab initio* theory (UMP2/cc-pVTZ).

As before, the saddle-point was found to be collinear. The bending potential on the $^3A'$ and $^3A''$ surface was found by Corchado *et al.* [45] to be slightly less steep than the one in Walch and Dunning's calculation [41]. The barrier to reaction was predicted to increase by slightly lower amounts (~6-8 kJ mol^{-1}) for $\Delta\alpha = \pm 30°$.

In order get a description of the PES at points not explicitly calculated by the higher level calculation, Corchado *et al.* [45] adapted a PES previously calculated for the reaction of hydrogen with methane [46].

$$CH_4 + H \rightarrow CH_3 + H_2 \qquad \text{reaction (1.4)}$$

This PES was the first one able to describe areas outside the collinear reaction geometry analytically. The calculation of the rate constant also included for the first time multidimensional tunnelling.

After adapting the barrier height of the surface to Walch and Dunning's [41] value, they were able to calculate the thermal rate constant in the range 300-2500 K in satisfactory agreement with the experimental values. This could only be achieved by having a large tunnelling contribution at moderate temperatures.

1.4.1.4 Recent theoretical developments

This completes the survey of the theoretical progress up to the point were this experimental study was started. The subsequent significant progress made on the theoretical side, mainly in developing new tools and approximations, increased the understanding of the reaction of $O(^3P)$ with methane greatly. This work was done during the period of this study and had a profound influence on its direction. This subsequent theoretical work will now be presented.

One of the geometrical pre-conditions for a PES is the tetrahedral symmetry with respect to an exchange of the hydrogen atoms, i.e. they are all equal in the absence of the oxygen atom. This was not fulfilled for Corchado *et al.*'s [45] surface as realised by Espinosa-García and García-Bernáldez [47]. They adjusted the surface which was now called symmetric PES (labelled SPES) to replace the original asymmetric PES (APES). In most of the other important aspects, the variation between the two surfaces was very small.

This surface was then used to carry out fairly sophisticated variational transition-state theory calculations of the rate constant for both CH_4 and its deuterated analogue CD_4 [47]. The calculations were restricted to the $^3A''$ surface, and the results multiplied by the necessary stoichiometric factor. The agreement with the experiment was fairly good for CH_4, but no experimental data was available with which to compare their results for CD_4.

An analysis of the reaction path led them to conclude a strong coupling of the reactive stretch and the umbrella vibrations in the CH_4 molecule, suggesting a strong

enhancement of the reaction if these modes could be excited.

The first state-to-state quantum scattering calculation for the $O(^3P)$ + CH_4 reaction was performed by Clary [48] on the above mentioned APES surface. As before, the calculations were only carried out on the $^3A''$ surface. Only active degrees of freedom were treated explicitly in the scattering calculation in a method known as the rotating bond approximation (RBA). In this case, they included local reactive C–H and O–H stretches, an angle which corresponds to a rocking vibration in CH_4 and transforms into CH_3 rotation for the separated products, and an angle corresponding to the umbrella vibration in the CH_3 product. Other degrees of freedom were treated by a simpler energy shift approximation.

By focussing on the arbitrarily chosen co-ordinates, certain aspects of the reaction can be predicted. In particular the rovibrational state distribution of the CH_3 product can be partially predicted and the influence of selective vibrational excitation of the CH_4 can be studied. Again, the local C-H stretching and umbrella modes of CH_4 are predicted to significantly enhance the reactivity. The umbrella mode can be expected to have an important influence on the dynamics of the reaction since its vibrational frequency is reduced from 1248 to 517 cm^{-1} during the geometry change from tetrahedral CH_4 to planar CH_3. In this case, the RBA is effectively a four active degree of freedom (4DF) model if the scattering coordinate is included.

The calculated state-selected excitation functions to predict state specific thresholds for the reaction, with the lowest reaction threshold for excitation in the C-H stretching mode. They are shown in figure 1.14.

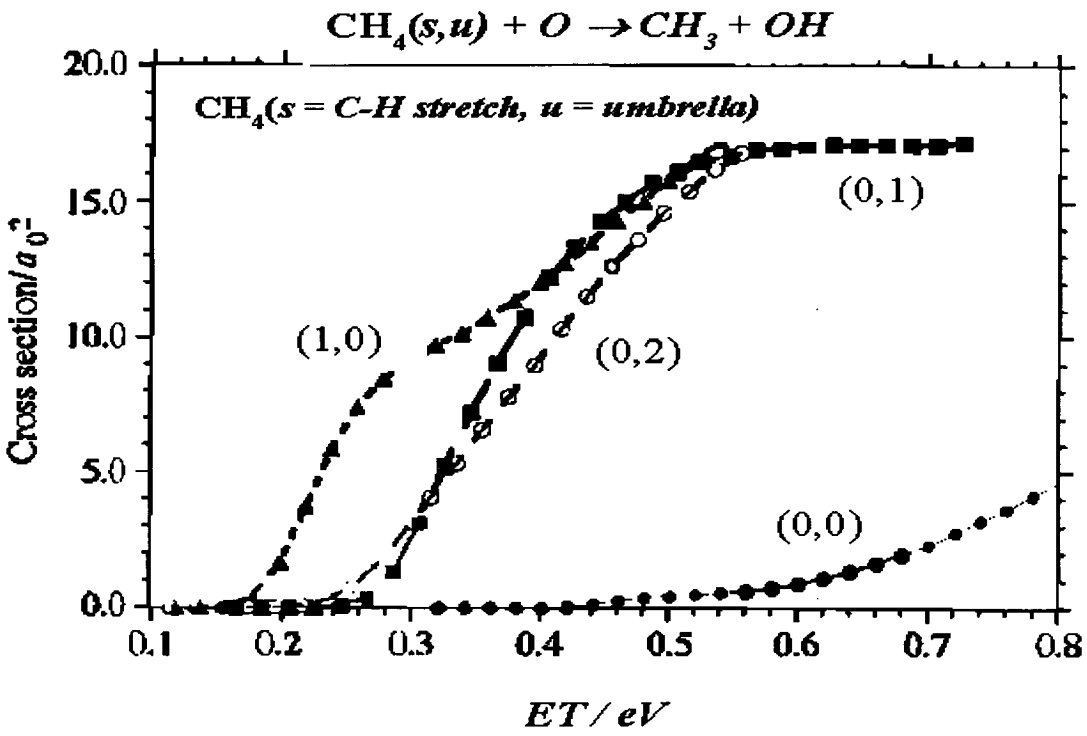

Figure 1.14: Rotating bond approximation predictions of the excitation functions for reaction of $O(^3P)$ with vibrationally state-selected CH_4 (s,u). The labels s and u indicated the respective number of quanta in a local C-H stretching vibration and the umbrella mode. Reproduced from figure 3 in [48].

The predicted enhancement of this reaction by selective vibrational excitation of the CH_4 product of the RBA and the following reduced dimensional theoretical studies were the motivation for carrying out the experiments described in section 5.

In thermal samples, the contribution of the vibrational excited states of methane is not thought to play a major role since their population is negligible until very high temperatures. An exception is the umbrella mode which is thought to be very important, even to dominate the thermal rate constant at moderate temperatures. It's effect is calculated to exceed the tunnelling contribution for the vibrational ground state, which is obviously the dominant state but suffers from a very high threshold.

The CH_3 product-state partitioning for a zero-impact-parameter collision shows an alternate population of even or odd rotational states, depending on whether the CH_4 rocking vibration contains an even or odd number of quanta, respectively. Only low rotational excitation of the CH_3 product is predicted.

The continuing theoretical challenge is to develop models of reduced dimensionality to tackle reactions which contain too many degrees of freedom to be solved exactly. Following up on the RBA work, Palma and Clary [49] constructed a more rigourous Hamiltonian for reduced-dimensional quantum scattering in systems of the generic type $X + YCZ_3$ (3DF). They derived a more general expression for the kinetic energy operator that, in turn, could be reduced by further approximations to isolate selected degrees of freedom of interest.

The implementation of this model for $O(^3P) + CH_4$ [49] included the relative velocity of the reactants and products, a C–H stretch in the reactants, an O-H stretch in the products, and the CH_3 umbrella motion for both sides. This was applied to the APES surface of Corchado *et al.* [45], and the outcome compared with the previous RBA calculations [48]. Where they were comparable, the models were in at least qualitative agreement, with some quantitative differences about the efficiency of the CH_4 stretching and umbrella vibrational modes in promoting reactivity. The differences are most likely caused by different operators used to describe the umbrella motion. One prediction of the 3DF model was a non-inverted CH_3 product umbrella mode distribution. This is in good qualitative agreement with Suzuki and Hirota [24] results, as shown in figure 1.9, although the experimental distribution is quantitatively considerably hotter than the calculated one even if the range of experimental collision energies is taken into account.

Extending their previous work, Palma and Clary [50], introduced a 4DF model by invoking a different set of approximations to reduce their general Hamiltonian [49]. The symmetric C-H stretch and a hypothetical asymmetric C-H stretch, treated explicitly for the reactants in addition to the familiar umbrella mode. On the product side, the symmetric stretch and umbrella modes of CH_3 as well as the OH stretch were treated. The calculations were again carried out on the original Corchado *et al.* APES surface [45], although it was noted that test calculations using the SPES surface [47] produced very similar results.

There was some excitation in the CH_3 umbrella motion predicted. The product umbrella mode distribution was strongly coupled to the reactant distribution in this vibrational mode. Vibrational ground state methane gave a non-inverted distribution similar to the previous prediction [49]. Excitation of the CH_4 umbrella mode leads to a hotter distribution in the CH_3 product as might be expected. More surprisingly, excitation of both the symmetric and asymmetric stretch produced an inverted CH_3 umbrella mode distribution over at least part of the collision energy range examined.

Palma and Clary subsequently [51] refined their 4DF model calculation using the improved SPES by Espinosa-Garciá *et al.* [47] and extended it to the $O(^3P) + CD_4$ reaction. Again, it was found that excitation of the symmetric and asymmetric stretch enhances the reaction, but the umbrella mode lowers the reaction threshold much more for the non-deuterated reaction than for the deuterated one.

The predictions of the these studies [48-51], especially with respect to excitation of the CH_4 stretching modes will be discussed in the light of the results of this experimental study in section 5.6.3.1.

At the same time, Yu and Nyman [52] performed a similar quantum scattering study using the alternative rotating bond umbrella model on the SPES surface [47]. It also represents a 4-dimensional model (4DF). It includes a reactive C–H stretch, H–CH_3 bending, and the umbrella mode in the reactants, as well as the O–H stretch, CH_3 rotation and CH_3 umbrella motions of the products.

The excitation of any of the reactant modes effectively reduced the translational energy threshold and promoted reactivity. As before in Clary's studies [48,50], the

CH_4 umbrella mode excitation was partially preserved in the same motion in the CH_3 product. However, in contrast, Yu and Nyman did not find a conversion of C–H stretching into the CH_3 umbrella motion. In addition, a noticeable population in the O–H stretching vibration was predicted following vibrational excitation of either the H–C stretch or H–CH_3 bend on the reactant side. These discrepancies might be due to different operators used to describe the umbrella mode in the different studies as suggested by Palma and Clary [50].

Yu and Nyman [52] also predicted the CH_3 rotational distribution to be relatively cold for reactions with ground state methane. It changes significantly and becomes hotter and unusually bimodal on excitation of either the H–C stretch or H–CH_3 bending motions. Along with many of the other detailed theoretical predictions it remains untested by experiments. It is not clear how many of these effects will survive in higher-dimensional scattering calculations.

Another approximation was deployed by Wang and coworkers [53]. They used the semi-rigid vibrating rotor target (SVRT) model to produce a description that treats the rotation of the non-reactive CH_3 group in the methane reactant explicitly. In total four of the 12 internal coordinates are treated, including the H-CH_3 bondlength, the changing angle between the reactive and non-reactive C-H bonds and the CH_3 rotation in the methane reactant. Wang *et al.* then performed wavepaket calculations on the above mentioned APES [45] and a surface developed for the H + CH_4 reaction [54], surprisingly without further adjustments. Their calculation produced a significant tunnelling effect, general higher reaction probabilities and a better

agreement with the thermal rate constant on the latter than on the former. By virtue of the method, no product state distributions could be derived and the thermal rate constant is the only parameter these results can be tested against.

González *et al.* [55] independently developed an alternative analytical potential for the $O(^3P) + CH_4$ reaction. They located the stationary points on the surface and the connection between them at full *ab initio* level (unrestricted 2nd order Møller–Plesset perturbation theory (UMP2) with a large basis set). The energies of the stationary *ab initio* points were then calculated using spin-projected unrestricted 4th order Møller–Plesset perturbation theory (PUMP4) using the same basis set. The saddle-point properties agreed well with the results of Corchado *et al.* [45]. The now familiar very nearly identical, preferred collinear geometries were obtained on the $^3A''$ and $^3A'$ surfaces. They encountered some technical problems trying to locate a saddle point on the $^3A'$ surface with a single imaginary frequency, as was also reported by Corchado *et al.* [45]. A shallow minimum in the product valley disappeared on the inclusion of basis-set superposition error and the addition of zero-point energy.

This grid of *ab initio* points, mainly distributed along the collinear minimum energy path and the saddle-point bending potential on the ground $^3A''$ surface, was then fitted by González *et al.* [55] to a pseudo-triatomic O–H–(CH_3) analytical potential. For this purpose, the CH_3 group was assumed to be structureless. The potential was expressed as a sum of two-body terms as function of the diatomic (or pseudo-diatomic) distances and a three-body term which was damped in the range of

any one atom from the other two. Using variational transition state theory (VTST) González *et al.* [55] calculated the thermal rate constant on this analytical surface, and for comparison, on the full-dimensional grid of the *ab initio* points. In both cases quite satisfactory agreement with the experimental values was achieved.

In addition, quasi-classical trajectories (QCTs) were also run on the analytical triatomic potential. Although the accuracy of the rate constants was poorer, OH internal product state distributions were derived and together with other dynamical attributes could be used for comparison with experiment. The result of this trajectory calculation as well as the latest QCT study on the same surface González *et al.* [56] will evaluated critically discussed with respect to the new results in section 5.1.2.

The latest QCT studies [55,56] provide a lot of detailed information on the OH product, but the methane reactant is still not satisfactorily treated. While the recent quantum scattering calculations [48-52] try to tackle this problem, they assume exact collinear approach, which may itself be a substantial approximation. Furthermore, as long as the calculations do not treat the real spectroscopic states in respect to their motion as well as in their degeneracy properly, it is hard to see how these calculations might be compared rigourously with experimental evidence.

1.4.1.5 Theoretical work on reactions of O(^{1}D) with methane

Theoretical work on O(^{1}D) reactions developed only more recently than the corresponding work for O(^{3}P). The first *ab initio* study to treat the OH producing channel from CH_4 was conducted by Arai and coworkers [57]. They concluded that the minimum energy path would be a collinear approach of the O(^{1}D) atom. The

$O(^1D)$ atom faces a small barrier (8.6 kJ mol^{-1}) and then deviates to the minimum ground state methanol geometry. This surface is directly correlated to the channels producing CH_3 and OH as well as CH_3O and H as products.

In a similar work to the study of the $O(^3P)$ + CH_4 reaction described above, González *et al.* calculated an *ab initio* surface on the same level of theory [58] as for the $O(^3P)$ reaction. Again, this surface was fitted to a pseudo-triatomic analytical function. This surface was then used for QCT calculations at different collision energies. The calculations [59] suggests a significant broadening of the rotational populations with increasing collision energy in all OH vibrational product levels. The effect increases with increasing vibrational level. The experimental [32,59] rotational distributions for all vibrational levels were well reproduced by the calculation. There was some less good agreement with a nearly later experimental study [60].

González and coworkers identified trajectories which come close to producing geometries near the minimum energy configuration, stable methanol. These were classified as insertion, while the reactive trajectories which did not fulfil this criterion were classified as direct abstraction. While the fraction of reactive flux via the direct abstraction increases with E_T and produces a strongly inverted vibrational OH product distribution, it plays only a minor role compared to the insertion.

The insertion component was split into two groups. The first one, involving only short lifetimes of the collision complex (direct reaction insertion mechanism), leads to an inverted OH vibrational distribution. The second group survived for several vibrational periods (non-direct reaction, insertion mechanism) and produces a

non-inverted vibrational distribution. The average lifetime was calculated to be 0.2 ps, decreasing slightly with increasing E_T.

There are several experimental measurements of the collision complex lifetime which are not in agreement with each other, ranging from 0.8 ps [61] in a stationary high pressure flash photolysis experiment to 3 ps [62] in a $O_3 \cdots CH_4$ van der Waals cluster study. A continuation of this O_3-CH_4 cluster reaction study identified three different reaction times [63], which was argued to be consistent with a mechanism consisting of abstraction and two insertion components. It is however, unclear to what extent the cluster data can be compared directly to the free gas-phase reaction. In addition a statistical adiabatic channel (SACM) calculation predicted a lifetime of 10 ps [64].

The surface used in reference [59] was found to be deficient for it displayed a barrier and did not manage to predict the thermal rate constant properly. Therefore, González and coworkers [65] developed a new surface without a barrier and used it for a QCT study. The vibrational distributions were found to be in good agreement with the experiment, which was also true for the rotational distributions in the OH ($v' \geq 2$) levels. The rotational excitation in the two lowest vibrational states was found to be overestimated with respect to the experimental values. Furthermore, the calculation predicted a $\boldsymbol{kk'}$ angular distribution for OH ($v'=4$, $N'=8$) in good agreement with the experiment [35], while the agreement was poorer for the OH ($v'=0$, $N'=5$) data. The conclusions on the microscopic mechanism were essentially the same as in the earlier calculation [59].

1.4.1.6 Electronic effects of the reaction of O(^{3}P) with saturated hydrocarbons

While the present level of theory for O(^{3}P) with hydrocarbon reactions has achieved quite a detailed study of the nuclear motion it is still far from predicting electronic fine-structure effects. All experimental reports note a distinct preference for the $^2\Pi_{3/2}$ (F_1) spin-orbit manifold of the OH rotational distributions even after correcting for the different spatial degeneracy of the two spin-orbit manifolds.

The present state of the discussion and the proposed models which manage to explain F_1 spin-orbit preference successfully as an electronic coupling phenomenon [66] will be presented in conjunction with the discussion of the relevant experimental results of this work in section 5.2.

1.5 Open questions

A wide range of work, both theoretical and experimental has been carried out to study the reactions of $O(^3P)$ with saturated hydrocarbons as has been laid out in the previous sections. Nevertheless, there still remain important questions to be addressed.

There is a obvious lack of information about the fate of the hydrocarbon fragment. Only one direct experimental study has been carried out [24] and the information provided was rather limited.

The effect of deuteration of the hydrocarbon on the dynamics has never been pursued systematically and only sporadic information has been reported. This may provide a very sensitive test on the accepted mechanistic picture of a collinear abstraction.

Several recent predictions of calculations need to be tested experimentally. These include the shape of the $\boldsymbol{kk'}$ differential cross-section, which, so far was only measured for one specific product state [18], as well as the predicted preferentially perpendicular alignment of the $\boldsymbol{j'}$ vector of the OH product [40,56].

Detailed predictions have also been made with respect to the relative reactivity of specific vibrational modes in the CH_4 / CD_4 reactant. Experimental confirmation would be critical to assess the validity of the approximations made in the calculations.

The observed preference in the F_1/F_2 spin-orbit ratio has been reproduced successfully in a model, but the agreement may have been fortuitous. If the preference is truly created by an electronic effect, deuteration of the hydrocarbon provides a sensitive test of its independence from the nuclear framework.

This study aims to answer or clarify some of these questions. Therefore the main part of the present study tries to establish the effect of deuteration on the reactions of $O(^3P)$ with saturated hydrocarbons. Four representative reactions were chosen to assess the effect of deuteration, namely

$$O(^3P) + CH_4 \rightarrow OH\ X\ ^2\Pi_i\ (v'=0/1) + CH_3 \qquad \text{reaction (1.5)}$$

$$O(^3P) + \textit{cyclo}\text{-}C_6H_{12} \rightarrow OH\ X\ ^2\Pi_i\ (v'=0/1) + \textit{cyclo}\text{-}C_6H_{11} \qquad \text{reaction (1.6)}$$

$$O(^3P) + CD_4 \rightarrow OD\ X\ ^2\Pi_i\ (v'=0/1) + CD_3 \qquad \text{reaction (1.7)}$$

$$O(^3P) + \textit{cyclo}\text{-}C_6D_{12} \rightarrow OD\ X\ ^2\Pi_i\ (v'=0/1) + \textit{cyclo}\text{-}C_6D_{11} \qquad \text{reaction (1.8)}$$

Reaction (1.7) will be studied for the first time experimentally and only one report [23] on reaction (1.5) is known and further confirmative data would be helpful.

In addition, the study aims to provide some information on the effect of selective vibrational excitation in the CH_4 precursor of reaction (1.5) by exciting the ν_3 vibration.

$$O(^3P) + CH_4\ (\nu_3, v=1) \rightarrow OH\ X\ ^2\Pi_i\ (v'=0/1) + CH_3 \qquad \text{reaction (1.9)}$$

1.6 Introduction to the reaction of $O(^3P)$ with unsaturated hydrocarbons

1.6.1 Short summary of the general picture

The introduction of a double or triple bond into the nuclear framework of a hydrocarbon has a profound effect on the chemistry. Similar to the reactions of $O(^1D)$ with alkanes, new channels become accessible. The $O(^3P)$ atom attacks preferentially the unsaturated bond to form a biradical which may or may not rearrange before decomposition along several pathways may occur. It would be impossible to provide a detailed review of the reactions of $O(^3P)$ atoms with unsaturated hydrocarbons here. Only a brief overview will be given here with no claim for completeness. More comprehensive discussions can be found elsewhere [67,68].

In the case of ethene, the reaction with $O(^3P)$ was found to proceed via two main channels producing the methyl radical or hydrogen atoms with the corresponding fragment.

$$O(^3P) + C_2H_4 \rightarrow CH_3 + CHO \qquad \text{reaction (1.10)}$$

$$O(^3P) + C_2H_4 \rightarrow H + C_2H_3O \qquad \text{reaction (1.11)}$$

where reaction (1.10) is the majority product channel. No OH product, corresponding to an abstraction channel similar to the reaction with alkanes was found. It is thought to be subject to a significant activation barrier and endothermic by about 25 kJ mol^{-1} [69].

However, OH can be detected as product from reactions with alkenes which have alkane chains attached. Its internal distribution displayed the same qualitative

features as the products from saturated alkanes, namely "cold" rotational distribution in the OH (v'=0) and a even "colder" distribution in the OH (v'=1) product [70,71]. The hydrogen was found to originate selectively from the saturated chain and predominately at the allylic position.

A similar pattern was found for alkynes where the parent compound C_2H_2 also displays no abstraction product [72] but OH was detected from the reaction with propyne with the by now familiar "cold" rotational distribution [71].

1.6.2 Introduction to $O(^3P)$ + H_3CCN

One of the main problems in experimental reaction dynamics is that the product detection is either universal, i. e. mass spectrometry and little or no information about the internal product state distribution, or too selective and usually only applicable to one of the products. In an ideal world, a experiment would provide information about all products and all their states simultaneously. But even a less ambitious wish, to know the internal states coproduct which correlate with a specific product remains usually unfulfilled.

The right choice of a reactive system might help to bring these wishes a bit closer. Larger unsaturated systems tend to show H abstraction in competition with addition-decomposition by the attacking $O(^3P)$ atom. A candidate molecule which can be primarily viewed as an unsaturated system rather than a functionalised hydrocarbon is acetonitrile, H_3CCN. The present state of knowledge about the reaction of acetonitrile with $O(^3P)$ atoms is presented in the following section.

The reactions of $O(^3P)$ with acetonitrile have so far only been studied kinetically. No positive identification of the nascent products has been achieved so far.

$$O(^3P) + H_3CCN \rightarrow \text{Products} \qquad \text{reaction (1.12)}$$

It is thought to proceed via three possible main reactive channels:

$$O(^3P) + H_3CCN \rightarrow OH + H_2CCN \qquad \text{reaction (1.13)}$$

$$O(^3P) + H_3CCN \rightarrow CH_3 + NCO \qquad \text{reaction (1.14)}$$

$$O(^3P) + H_3CCN \rightarrow HCN + H_2CO \qquad \text{reaction (1.15)}$$

Bonanno *et al.* [73] measured the absolute rate constant for reaction (1.12) in the temperature range of 383-500 K by the flash-photolysis resonance fluorescence method (FPRF) in a slow flow cell. They observed the decay of $O(^3P)$. In a fast flow setup they tried to identify the products by electron spin resonance (ESR) and mass spectrometry (MS). Both of the latter methods led to a higher rate constant than by FPRF, which is thought to be due to adsorption of the acetonitrile on the walls in the case of the FPRF measurements. No pressure dependence was observed in the region of 100-400 mTorr. The MS analysis reveals peaks corresponding to HCN, H_2CO and NO.

No hydrogen isotope effect was observed at low temperature but some at high temperature, therefore the authors concluded that H-abstraction only becomes important at high temperatures. Bonanno *et al.* proposed on that basis that reactions (1.14) and (1.15) describe the main channels of reaction (1.12).

Nearly twenty years later, Budge *et al.* [74] measured the rate constant of reaction (1.12) again over a temperature range of 320-578 K at a pressure of 1 Torr. $O(^3P)$ atoms were produced by titrating $N(^4S)$ atoms with NO and their concentration monitored by NO_2 fluorescence. The final products were analysed by gas-chromatography. The measured rate constants showed good Arrhenius behaviour. The slope of the Arrhenius plot agreed well with the results in [73], but the pre-exponential factors did not. The activation energy (E_A) for the reaction taken from a linear fit of the Arrhenius plot yielded a value of about 5 and 17 kJ mol^{-1} based on the earlier [73] and the later study [74] respectively.

It should be noted that Budge and Roscoe did not find a significant difference between the value of E_A for the reaction of $O(^3P)$ with H_3CCN and H_3CH_2CN which is given as 16 kJ mol^{-1}.The latter value is very close to what would be expected as activation barrier for a H abstraction from a tertiary hydrocarbon which is given as about 21 kJ mol^{-1} [7]. Budge and Roscoe concluded that the reaction (1.12) must be initiated by reaction (1.14).

The knowledge about reaction (1.12) is obviously limited. It was therefore considered to be a good candidate to test the presence of different channels, namely (1.13) and (1.14) and to positively identifying the nascent radical products, OH and NCO including their internal distribution. The results of direct experimental tests of this type will be presented in chapter 6.

Chapter 2: Spectroscopy of the investigated systems

2.1 Methods applied in the current study

The main spectroscopic technique deployed in this study was laser-induced fluorescence (LIF) to study the internal state distribution of products of chemical processes. All studies were carried out using LIF in a photolysis-probe setup. The studies of reactions with vibrational excited methane used the photolysis-probe setup together with an infrared (IR) pump laser system to produce vibrationally excited methane. These techniques will now by described in more detail. Unless otherwise referred to all detailed spectroscopic information was taken from Herzberg's priceless spectroscopy compilation [75,76,77].

2.1.1 Laser induced fluorescence (LIF)

The technique of laser-induced fluorescence as applied in this work is based on selective excitation of a given rovibronic level of a given molecule to a higher rovibronic level using a laser. In this excited state the molecule might undergo collisions which might lead to electronic, vibrational and / or rotational deactivation as well as radiate back into a lower vibronic state before or after collisions have taken place. If the excitation wavelength is kept constant, this radiation which is emitted by the molecule may contain several wavelengths which can be dispersed by a prism or a monochromator. This spectrum contains information about the rovibrational structure of the lower state. The intensities of these transitions are proportional to the overlap of the vibrational and rotational wavefunctions of the initial and final state

which are known as Franck-Condon and Hönl-London factors respectively. This method is called dispersed fluorescence (DF).

A second way of using LIF is to scan the excitation laser and collect the total fluorescence whenever the excitation laser wavelength coincides with an optical transition. If desired, the use of a filter allows separation of specific transitions. The resulting spectrum resembles very much an absorption spectrum of the molecule. The intensity of the fluorescence signal not only depends on the transition probability of the excitation but also on the transition probability of the fluorescence if other loss processes are present as well. This method is called fluorescence excitation (FE). In principle, the spectrum contains the same information as an absorption spectrum but the signal-to-noise ratio is generally much higher, particularly for pulsed light sources, because transitions can be excited selectively and detection which occurs in emission can also be narrowed to a specific wavelength range. In standard absorption spectroscopy, a small change in intensity is measured against a large transmitted background. Instabilities in the light source strongly affect the signal-to-noise level, therefore c. w. light sources are generally used. LIF can use pulsed light sources and measures the emitted fluorescence against, in principle, a zero background.

LIF is very sensitive and quite commonly used to obtain dynamical and kinetic information as well as in trace-gas detection and monitoring combustion [78,79]. Its major limitations are restrictions imposed by the studied species, i.e. the molecule has to have stable, optically accessible states with adequate fluorescence quantum yield and the environment must not be opaque in the wavelength region used.

2.1.2 Infrared pumping of a specific vibrational mode

While LIF is used to detect the products of chemical reactions, the infrared pumping of a rovibrational mode is used to change the nature of the reactants. Instead of using a thermal sample which has its internal modes populated in accordance with Boltzmann statistics, specific rovibrational transitions are pumped by means of an IR laser, therefore increasing the relative population in a given excited rovibrational level. This allows the study of the dynamics as function of the vibrational distribution in the reactants. It was, for example, successfully applied to reactions of CH_4 with Cl in the past [80,81,82,83,84]

2.2 Introduction to the spectroscopy of the molecules of interest

2.2.1 Hund's coupling cases

In an open shell molecule there may be up to four different sources of angular momentum resulting from the motion of the nuclei and electrons in the system. The rotation of the nuclei produces an angular momentum as does the orbital motion of the electrons. In addition to these relative motions, electrons do and nuclei may contribute a component of angular momentum due to the intrinsic spin of the particles. The question therefore arises, if and how these angular momenta may influence each other. Neglecting the nuclear spin, Hund derived descriptions for limiting cases of different coupling phenomena. Only the so-called Hund's coupling cases (a) and (b) are of relevance for this work and are now described in more detail.

2.2.1.1 Hund's coupling case (a)

Hund's case (a) describes a limiting case in which the angular momentum resulting from the orbital motion of the electrons $\boldsymbol{L}$ is directly coupled to the internuclear axis. The orbiting electrons induce a magnetic field which lies along the direction of the internuclear axis. The electronic spin $\boldsymbol{S}$ couples to this magnetic field and gets also aligned along the internuclear axis. This coupling is much stronger than the one of the electronic spin to the magnetic field induced by the nuclear motion.

The projections of the electronic angular momentum ($\boldsymbol{L}$) and electronic spin ($\boldsymbol{S}$) onto the internuclear axis are given by Λ and Σ respectively defined by the quantum numbers Λ and Σ which are "good" quantum numbers. That is they remain well defined in an accurate quantum mechanical description of the system. The vectorial addition of the projections leads to a new quantity Ω described by the quantum number Ω, which also remains a good quantum number as long as the conditions of Hund's case (a) are fulfilled.

$$\Omega=\Lambda+\Sigma \qquad \text{equation (2.1)}$$

The coupling between the angular momentum resulting from the nuclear motion ($\boldsymbol{R}$) and the combined projection of the electronic motions produce the resulting total angular momentum, $\boldsymbol{J}$, which is a conserved quantity.

$$\boldsymbol{J}=\boldsymbol{R}+\Omega \qquad \text{equation (2.2)}$$

$\boldsymbol{J}$ is constant in both magnitude and direction, therefore the vectors $\boldsymbol{R}$ and Ω perform a nutation around it, while $\boldsymbol{L}$ and $\boldsymbol{S}$ precess around the internuclear axis. This is shown in the upper panel of figure 2.1.

2.2.1.2 Hund's coupling case (b)

The motion of the nuclei also induces a magnetic field. If this field is stronger than the magnetic field induced by the orbital motion of the electrons, the electronic spin decouples from the latter and couples to the magnetic field of the rotating nuclei. The electronic orbital angular momentum $\boldsymbol{L}$ remains coupled to the internuclear axis. Therefore, a new quantum number $\boldsymbol{N}$ is introduced which describes the resulting angular momentum from the vectorial addition of the angular momentum of the rotating nuclei ($\boldsymbol{R}$) and the projection of the electronic orbital motion (Λ) onto the nuclear axis. The electronic spin $\boldsymbol{S}$ then couples with $\boldsymbol{N}$, described by the quantum number N, which remains a "good" quantum number in Hund's case (b), producing the total angular momentum $\boldsymbol{J}$. This is shown in the centre panel of figure 2.1.

The internuclear axis performs a nutation around $\boldsymbol{N}$, which is much faster than the precession of $\boldsymbol{N}$ and $\boldsymbol{S}$ around $\boldsymbol{J}$. In the case of no contribution from the orbital motion of the electrons, that is Λ=0, $\boldsymbol{N}$ stands perpendicular to the internuclear axis as shown in figure 2.1. While Hund's case (a) describes well, for example, a slowly rotating OH X $^2\Pi_i$ molecule, Hund's case (b) is a better description for the fast rotating molecule.

Hund's Case (a) Vector Diagram

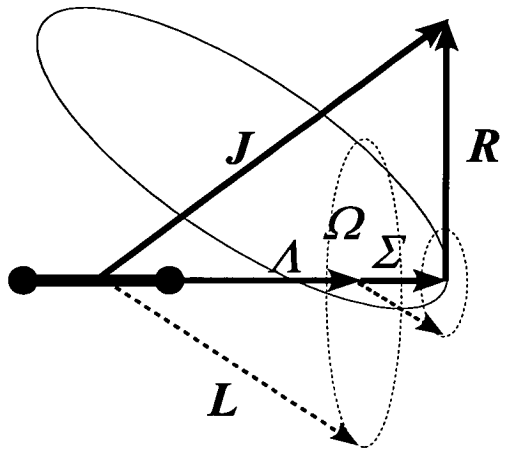

Hund's Case (b) Vector Diagram

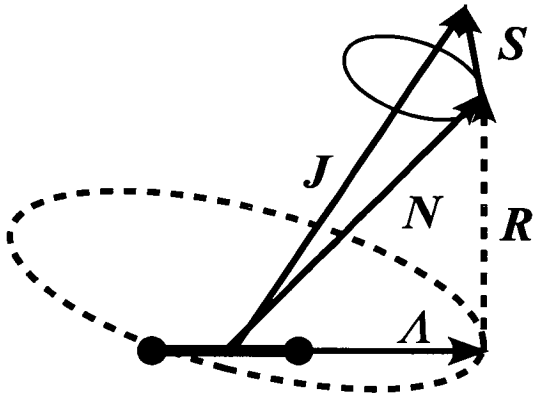

Hund's Case (b) Vector Diagram for molecule with Λ =0

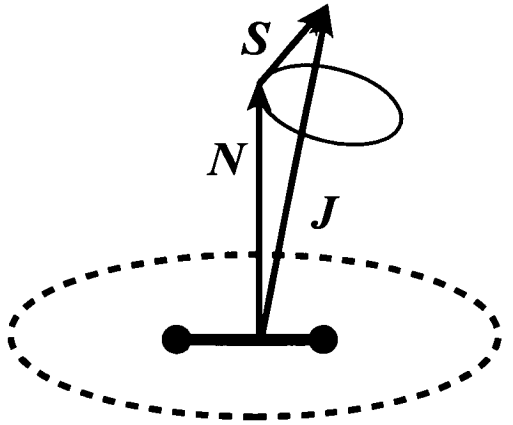

Figure 2.1: Vector diagrams for the Hund's coupling cases of relevance in this study: Hund's case (a), upper panel; Hund's case (b) for a molecule with Λ>0, centre panel; Hund's case (b) for a molecule with Λ=0, lower panel. Vectors as described in the main text.

2.2.3 The OH / OD radical

2.2.3.1 General Introduction

Most of the dynamical information obtained in this study is derived from spectra of OH / OD radicals after the reaction. It is therefore worth to discuss the spectroscopy of these radicals in some detail.

The OH-radical is one of the most exhaustively studied reactive species in the gas-phase because of its importance in atmospheric and combustion chemistry as well as its occurrence in interstellar space [85,86,87,88]. Its spectroscopy is well understood [75,15] and quite regularly used for dynamical studies [89,90,91,32,92].

The OD radical is less commonly used in studies, mainly because of the lower abundance of deuterium. The spectroscopy of both radicals is very similar [15,93] and therefore they are treated together in this chapter. The main differences are the difference in mass, changing the rotational constant, the zero-point energy, the energy gap of the vibrational levels and the fact that the magnitude of the nuclear spin is ½ for hydrogen and 1 for deuterium.

The following subchapters discuss the OH radical in some detail. Unless explicitly mentioned the same arguments hold in the case of OD and are therefore not outlined again. For this study two electronic states of the OH / OD radical are of relevance.

2.2.3.2 The X $^2\Pi_i$ state of the OH-radical

The electronic ground state of the OH radical has the dominant configuration $(1\sigma)^2(2\sigma)^2(3\sigma)^2(1\pi)^3$ and is labelled X $^2\Pi_i$. A Π-state corresponds to an orbital angular momentum Λ equal to ±1. The value of Ω is given as

$$\Omega = \Lambda \pm \Sigma \qquad \text{equation (2.3)}$$

producing two possible values, Ω=1/2 and 3/2 giving rise to two different manifolds, separated in energy by the so-called spin-orbit splitting. The subscript i stands for "*irregular*" and indicates that the $^2\Pi_{3/2}$ component is lower in energy than the $^2\Pi_{1/2}$ manifold. The different Hund's coupling cases have to be taken in account in order to develop a proper spectroscopic description of the system. In the case of low rotation, the OH ground state can be described with Hund's case (a). There are two distinct spin-orbit manifolds of rotational levels, corresponding to the two different values of Ω.

The fast rotating OH X $^2\Pi_i$ molecule is better described by Hund's case (b). The levels with the same quantum number N are split due to spin-rotation splitting. Each level of N gives rise to two levels with different values of J.

$$J = N \pm 1/2 \qquad \text{equation (2.4)}$$

Additionally, any states with $L \neq 0$ are orbitally degenerate. Taking alternative linear combinations of wavefunctions with oppositely signed Λ values produces two states, one of which is symmetric and the other antisymmetric with respect to the plane of rotation of the molecule, giving rise to A' and A" levels respectively.

The value of N, which is only well-defined in Hund's case (b), can be nominally assigned in case of low rotation (Hund's case (a)) by extrapolation. Any given (v, N)-level in the electronic ground state of the OH-radical has therefore four fine structure levels ($J=N\pm1/2$ and A', A'').

2.2.3.3 The A $^2\Sigma^+$-state of the OH-radical

The first excited state has a dominant electronic configuration of $(1\sigma)^2(2\sigma)^2(3\sigma)^1(1\pi)^4$ and is labelled $^2\Sigma^+$. The appropriate description is Hund's case (b). The levels are split due to the coupling of the angular momentum of the motion of the nuclei and the electronic spin, the spin-rotation splitting, which is in general very small.

Both, OH and OD are subject to predissociation. For the A $^2\Sigma^+$ (v=1) state of OH predissociation starts about N=14 and is therefore not a problem in this study, since the reactive populations barely reach out to such a high rotational quantum number. In contrast the of A $^2\Sigma^+$ (v=2) state of OH is subject to predissociation for all, including the lowest, rotational levels. The OD A $^2\Sigma^+$ (v=1,2) states are not subject to predissociation in the rotational levels accessed in this investigation.

The main effects of predissociation is a reduction of the fluorescence quantum yield from the upper level and, in principle, a broadening of the spectral lines. The low fluorescence quantum yield of any significantly broadened line would make it impossible to observe these transitions in this study. Both effects are accounted for in the relative method of analysis chosen as explained below.

2.2.3.4 The OH A $^2\Sigma^+ \leftarrow$ X $^2\Pi_i$ Transition

The optically allowed transitions between the states are shown in figure 2.2. For each vibronic level there are two subbands corresponding to transitions from the different spin-orbit manifolds of the X $^2\Pi_i$-state.

The one-photon transitions selection rules are for the change of total angular momentum

$$\Delta J = 0, \pm 1 \qquad \text{equation (2.5)}$$

as well as a change of the overall parity of the wavefunction

$$(+ \leftrightarrow -) \text{ and } (- \leftrightarrow +) \qquad \text{equation (2.6)}$$

In the case of pure Hund's case (b) there is also the selection rule for the change of N

$$\Delta N = 0, \pm 1 \qquad \text{equation (2.7)}$$

Transitions which fulfil all selection rules are strong. Therefore, there are twelve branches which divide themselves up into two sets of six branches for the two different manifolds.

For a thermal sample, the LIF spectra of the OH and OD A $^2\Sigma^+ \leftarrow$ X $^2\Pi_i$ (1-0) and (2-1) transitions were simulated using the LIFbase [94] simulation program. These spectra are shown in figure 2.3 for OH and figure for 2.4 OD respectively. Only the main branches were labelled. In figure 2.2 the parity is labelled with respect to the inversion symmetry of the wavefunction. The convertion to the symmetry with respect to the plane of rotation is given by Π (A') $\leftrightarrow (-1)^N$ and Π (A") $\leftrightarrow (-1)^{N+1}$.

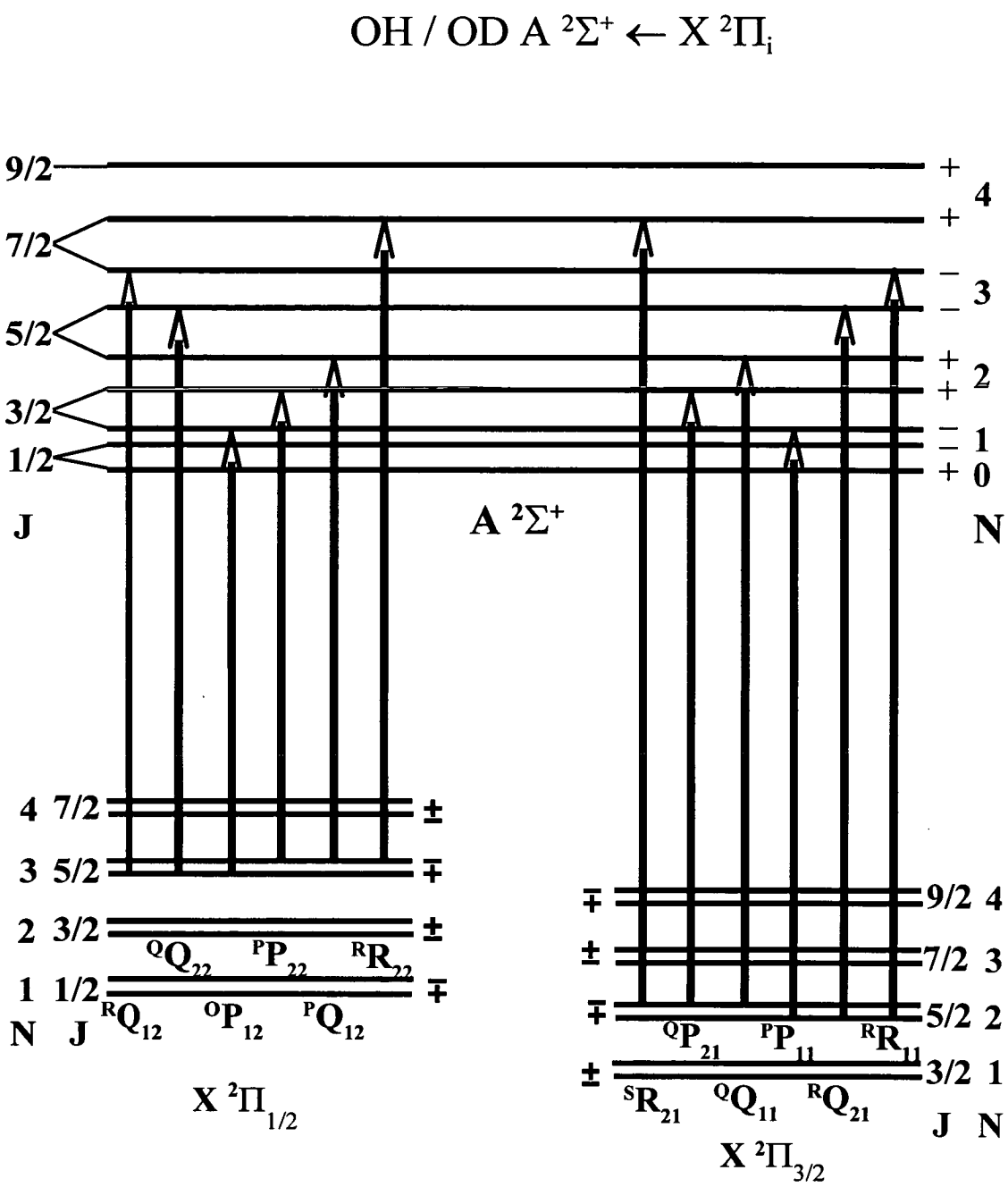

Figure 2.2: Schematic representation of the optical transitions in the OH / OD A $^2\Sigma^+ \leftarrow$ X $^2\Pi_i$ band. The transitions are labeled with the main label being the change in the total angular momentum J, ΔJ, the superscript indicating the change in the rotational quantum number N, ΔN, and the subscripts describe the level of the upper and lower state belonging either F_1 (J=N+1/2) or F_2 (J=N-1/2). Each spin-orbit manifold gives rise to 3 main and 3 subbranches, 12 in total. The main branches are also refered to as P_1, Q_1, R_1 in the F_1 spin-orbit manifold instead of the cumbersome $^PP_{11}$, $^QQ_{11}$, $^RR_{11}$ respectively and accordingly P_2, Q_2, R_2 instead of $^PP_{22}$, $^QQ_{22}$, $^RR_{22}$ in the F_2 spin-orbit manifold. For this diagram Hund's case (a) was assumed for the lower state.

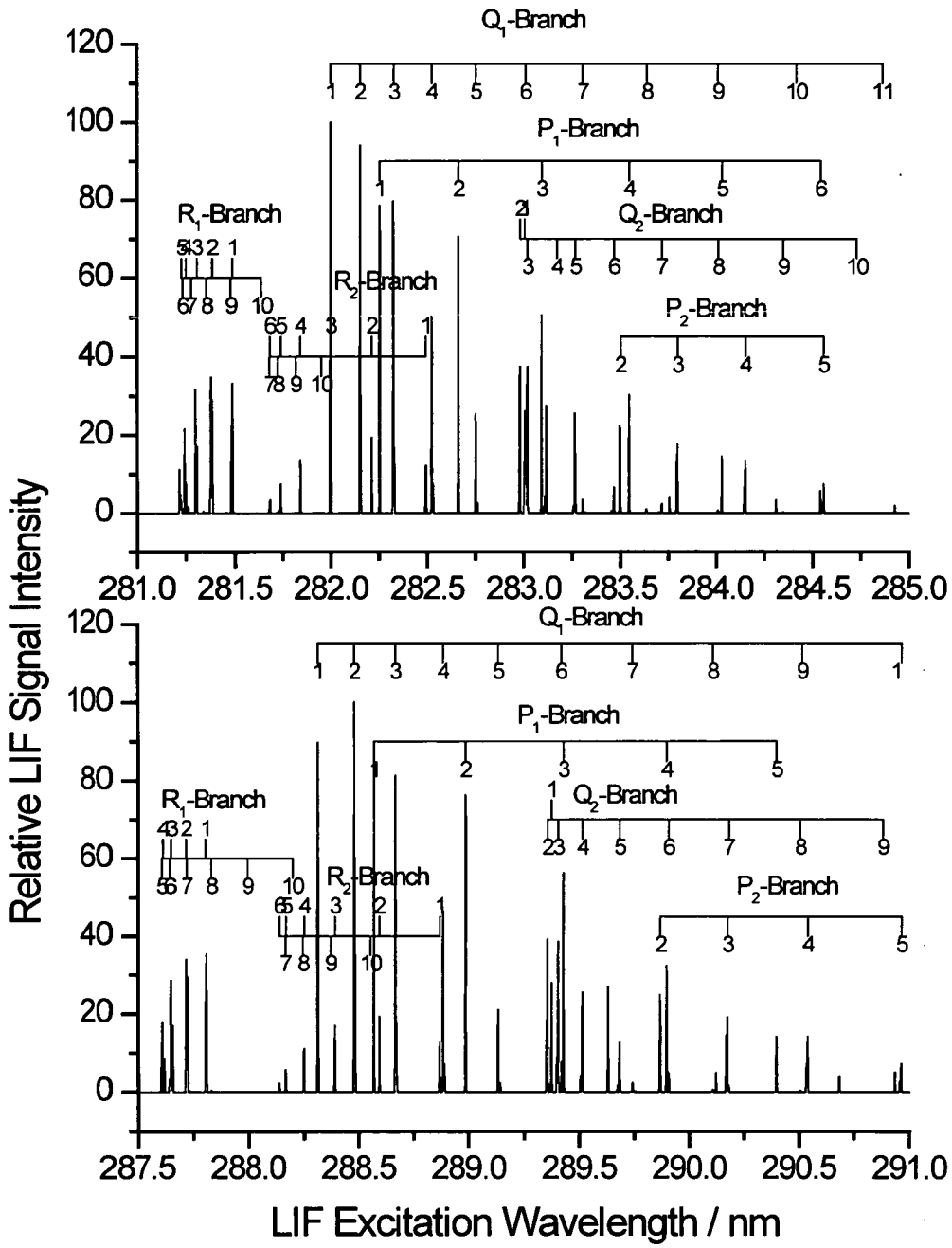

Figure 2.3: Simulated thermal (298 K) LIF spectra of the OH (v=0) (upper panel) and OH (v=1) (lower panel) A-X (1-0) and (2-1) band respectively. Only the main branches are labeled. Spectra were simulated with the LIFbase program [94].

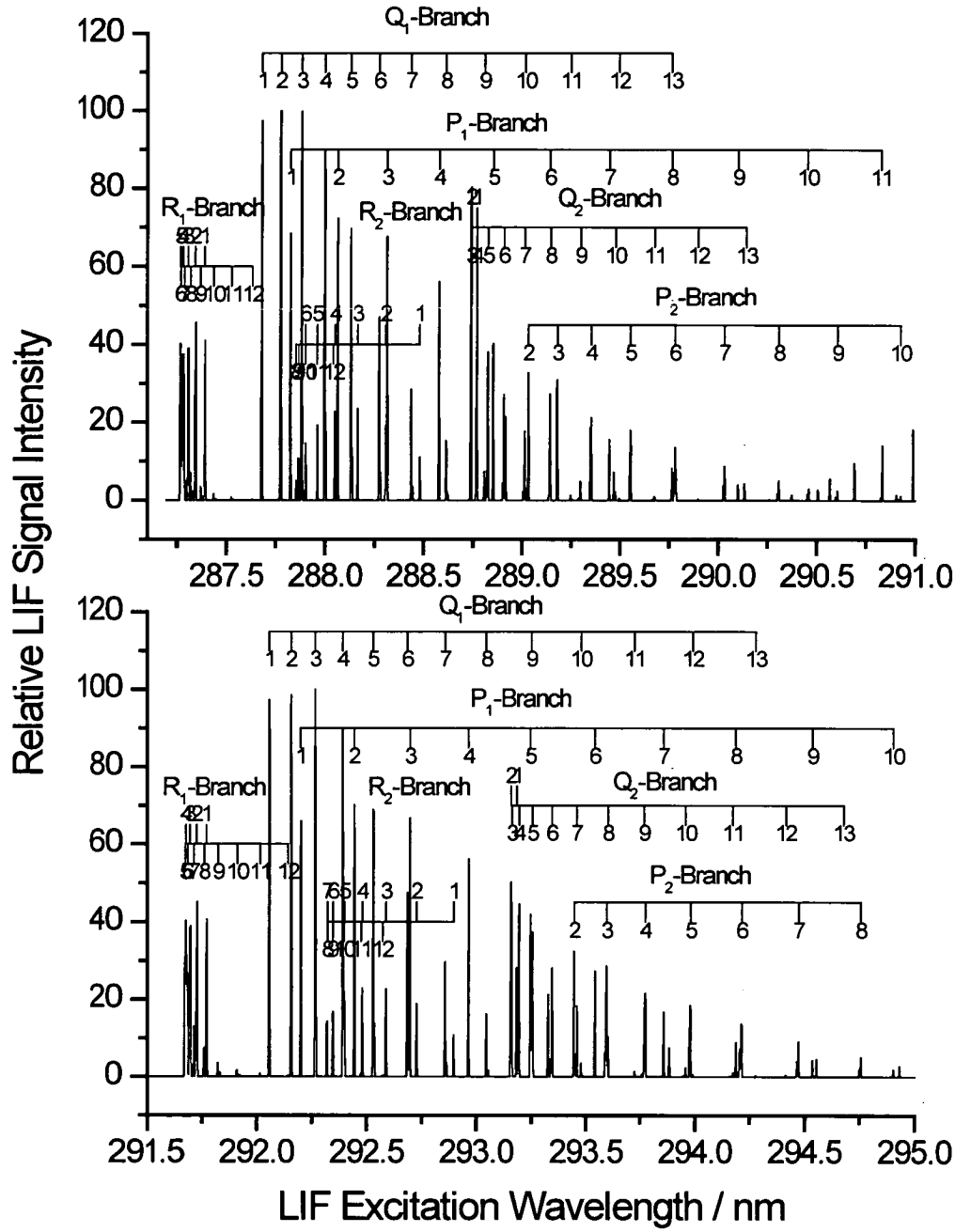

Figure 2.4: Simulated thermal (298 K) spectra of the OD (v=0) (upper panel) and OD (v=1) (lower panel) A-X (1,0) and (2,1) band respectively. Only the main branches are labeled. Spectra were simulated with the LIFbase program [94].

2.2.4 Photolysis of NO_2 at 266 nm

2.2.4.1 Accessible Product Channels

Irradiation of NO_2 with ultraviolet light at a wavelength below 397.8 nm produces O atoms and NO molecules in various electronic states according to their energetic thresholds. In the region between 397.8 and 243.9 nm only the production of $O(^3P)$ atoms is energetically possible. Below that wavelength, the production of $O(^1D)$ atoms becomes possible and below 169.7 nm the channel to produce of $O(^1S)$ becomes accessible. It should be noted that a channel producing N atoms and O_2 molecules has a threshold of 275.1 nm [95], but does not play any role in this study. Therefore a photolysis at 266 nm is expected to yield NO and $O(^3P)$. This channel has significant excess energy if produced by photolysis at 266 nm, which is at least partly expected to appear in translational motion of the oxygen atom.

2.2.4.2 Internal Energy Distribution of the NO fragment

The energy distribution has not been measured at the photolysis wavelength of 266 nm used in this work. In order to make a good estimate of the velocity of the recoiling O atoms comparisons to measured distributions at other wavelengths were made. The closest information available are measurements at 248.5 nm obtained from two different groups [96] and [97]. They show a distinct bimodal behaviour of the vibrational distribution in the NO fragment in conjunction with a high rotational "temperature" for the higher vibrational states. Linear momentum conservation requires the recoiling O atom to be roughly twice as fast as the NO fragment. A detailed discussion of this aspect can be found in section 4.4.

2.2.5 The NO radical

2.2.5.1 General Introduction

As mentioned above, the NO radical is a product of the photolysis of NO_2 at 266 nm. Together with NO_2 it plays major part in the O_3 controlling cycles in the stratosphere as well as in tropospheric processes like O_3 production and acid rain [98]. Even though it is not a product of direct interest or a necessary reactant in any of the reactions of this study, its interfering presence influenced the quality of the information obtained and required a knowledge of its spectroscopy. Three electronic states of NO are important in this study.

2.2.5.2 The X $^2\Pi_r$ state of the NO radical

The electronic ground state of the NO radical has the dominant electronic configuration $(\sigma 1s)^2(\sigma^* 1s)^2(\sigma 2s)^2(\sigma^* 2s)^2(\pi 2p)^4(\sigma 2p)^2(\pi^* 2p)^1$ which is labelled X $^2\Pi$. The $^2\Pi_{1/2}$ manifold lies 121.1 cm^{-1} below the $^2\Pi_{3/2}$ manifold, making it *"regular"* indicated by the subscript r Π_r-state. Since a $^2\Pi$ state has an orbital angular momentum and a spin component different coupling cases apply as function of the rotational state. A transition from Hund's case (a) to Hund's case (b) takes place with increasing rotation.

2.2.5.3 The A $^2\Sigma^+$ state of the NO radical

The first excited electronic state of the NO radical has the electronic configuration $(\sigma 1s)^2(\sigma^* 1s)^2(\sigma 2s)^2(\sigma^* 2s)^2(\pi 2p)^4(\sigma 2p)^2(\sigma 3s)^1$ and is therefore a $^2\Sigma^+$ state. It has an electron in a higher principal quantum number orbital, $(\sigma 3s)^1$, than the ground state and could therefore formally be classified as a Rydberg-state. It is properly described by Hund's case (b).

2.2.5.4 The B $^2\Pi_r$ state of the NO radical

The second excited electronic state of the NO radical has the electronic configuration $(\sigma 1s)^2(\sigma^* 1s)^2(\sigma 2s)^2(\sigma^* 2s)^2(\pi 2p)^3(\sigma 2p)^2(\pi^* 2p)^2$ and is a $^2\Pi$ state. The $^2\Pi_{1/2}$ manifold lies energetically below the $^2\Pi_{3/2}$ manifold making it as the ground state *"regular"*. Again, it is a $^2\Pi_r$ state to which different coupling cases apply as function of the rotational state and a transition between Hund's case (a) to Hund's case (b) takes place with increasing rotation.

2.2.5.5 The NO A $^2\Sigma^+ \leftarrow$ X $^2\Pi_r$ Transition

This system corresponds to the same system as the A $^2\Sigma^+ \leftarrow$ X $^2\Pi_i$ transitions of OH / OD which were discussed above in detail. The features are very similar. The higher moment of inertia produces a smaller B value for NO and the rotational lines tend to be much closer spaced than in OH. It should also be mentioned that the NO A $^2\Sigma^+ \leftarrow$ X $^2\Pi_r$ system shows a very non-diagonal behaviour, displaying a whole range of vibronic transitions with significant intensity. The spectrum therefore looks quite congested. These transitions are also labelled the γ-bands of NO in some literature.

2.2.5.6 The NO B $^2\Pi_r \leftarrow$ X $^2\Pi_r$ Transition

For a $^2\Pi$ – $^2\Pi$ transition the Hund's coupling schemes are of importance. If Hund's case (a) holds (i.e. low rotation) the selection rule

$$\Delta\Sigma=0 \qquad \text{equation (2.8)}$$

holds. Both $^2\Pi$ states split into their two spin-orbit manifolds F_1 and F_2. Two sub-bands connect the F_1 manifolds and the F_2 manifold of the ground upper state respectively. Each sub-band consists of P, R and Q-branches which have two transitions, one for each Λ-doublet, for each rotational level N, apart from the lowest. This results in 12 branches in total with the Q-branches tending to be relatively weak.

If both states can be attributed to Hund's case (b) the selection rule for the change in the angular momentum quantum number N is

$$\Delta N=0,\pm1 \qquad \text{equation (2.9)}$$

In addition transitions with the property of an unequal change of the quantum numbers N and J

$$\Delta N\neq\Delta J \qquad \text{equation (2.10)}$$

tend to be very weak. Again 12 bands occur which are not split into two sub-bands. The B-X or β-bands of NO are of this type. In this case, for increasing rotation a transition between Hund's case (a) and (b) takes place. Since NO is only a by-product of the photolysis and not of primary interest for this study a detailed discussion of the B-X band is not necessary and the reader should refer to Herzberg's work [75] for a more detailed discussion.

2.2.6 The CN radical

2.2.6.1 General Introduction

The CN radical is of crucial importance in combustion. It occurs, for example, as an intermediate in the oxidation of HCN by OH, an important step in forming NO_x, especially in hydrogen-rich and N_2 fuelled flames [99]. Due to its presence in interstellar clouds, a large effort has gone into understanding its spectroscopy [75].

2.2.6.2 The X $^2\Sigma^+$ state of the CN-radical

The electronic ground state of the CN radical has the electronic configuration $(\sigma 1s)^2(\sigma^* 1s)^2(\sigma 2s)^2(\sigma^* 2s)^2(\pi 2p)^4(\sigma 2p)^1$ which is therefore labelled X $^2\Sigma^+$. Being a Σ state, there is no component of the orbital angular momentum projected onto the internuclear axis. The proper description for the coupling of nuclear and electronic motion is therefore given by Hund's case (b).

2.2.6.3 The B $^2\Sigma^+$ state of the CN-radical

The second electronically excited state can be formally produced by promoting an electron out of the antibonding σ^*2s orbital to the bonding $\sigma 2p$ orbital, giving the electronic configuration $(\sigma 1s)^2(\sigma^* 1s)^2(\sigma 2s)^2(\sigma^* 2s)^1(\pi 2p)^4(\sigma 2p)^2$ which has the same symmetry as ground state, i.e. B $^2\Sigma^+$. It is also properly described as Hund's case (b).

2.2.6.4 The CN B $^2\Sigma^+ \leftarrow$ X $^2\Sigma^+$ Transition

The transition observed in the present work is the CN B-X (0-0) transition. Both electronic states are $^2\Sigma^+$ symmetry and since there is no component of angular

momentum associated with the orbital motion of the electrons the only coupling occurs between the spin and the angular momentum resulting from the rotation of the molecule. The system can therefore always be described as Hund's case (b). This is demonstrated in the lower panel of figure 2.1.

Each rotational level of N in a $^2\Sigma^+$ state is split by spin-rotation splitting into two components, corresponding to a total angular momentum quantum number J of

$$J = N \pm 1/2 \qquad \text{equation (2.11)}$$

To a good approximation, the total wavefunction Ψ_{tot}, describing the rovibronic state of a molecule can be written as the product of the electronic, Ψ_{elec}, vibrational, Ψ_{vib}, and rotational wavefunction, Ψ_{rot}, each describing its specific motion or state.

$$\Psi_{tot} = \Psi_{elec}\Psi_{vib}\Psi_{rot} \qquad \text{equation (2.12)}$$

The total wavefunction can behave in two different ways to the symmetry operation of an inversion of coordinates, either being symmetric

$$\Psi_{tot}(x,y,z) = \Psi_{tot}(-x,-y,-z) \qquad \text{equation (2.13)}$$

or antisymmetric

$$\Psi_{tot}(x,y,z) = -\Psi_{tot}(-x,-y,-z) \qquad \text{equation (2.14)}$$

Since in a given vibronic state the character of the product of the electronic and vibrational wavefunction remains constant, this symmetry property, called parity, depends only on the symmetry of the rotational wavefunction and is assigned + or – depending on equation (2.13) or (2.14) being valid. In Σ^+ states, the lowest level is of + parity. The two J levels corresponding to the same N have the same parity, which alternates with N.

The selection rule for optically allowed transitions for a $^2\Sigma^+$-$^2\Sigma^+$ system are

$$\Delta N = \pm 1 \qquad \text{equation (2.15)}$$

therefore, two branches are expected which are R and P type. Since $\Delta N=0$ is not allowed no Q branch is present. However, there is the general selection rule for the total angular momentum, namely

$$\Delta J = 0, \pm 1 \qquad \text{equation (2.16)}$$

Which gives rise to 3 components, of which the ones following $\Delta J \neq \Delta N$ tends to be much weaker. Additionally, the symmetry restriction with respect to the parity of the levels involved have to be observed, namely the levels must have different parity.

$$(+ \leftrightarrow -) \text{ and } (- \leftrightarrow +) \qquad \text{equation (2.17)}$$

The spectrum consists essentially of an R- and P-branch. Each of them would be, in the highest resolution, made up of 3 sets of lines belonging to $\Delta J=0,\pm 1$. The allowed transitions are shown in figure 2.5. The relative intensities are qualitatively shown. The branches starting from J=N+1/2, labelled R_1 and P_1 are slightly more intense than those starting from J=N-1/2, labelled R_2 and P_2. The subbranches with $\Delta J=0$, labelled $^RQ_{21}$ and $^PQ_{12}$ are much weaker than the other 2 subbranches. In the lowest level only two transitions, R_1 and ^RQ are possible. In the CN B-X (0-0) transition, the P-branches form heads towards higher wavelength since the upper state has a smaller equilibrium distance between C and N compared to the lower state and therefore the energy gaps of the transitions get subsequently smaller.

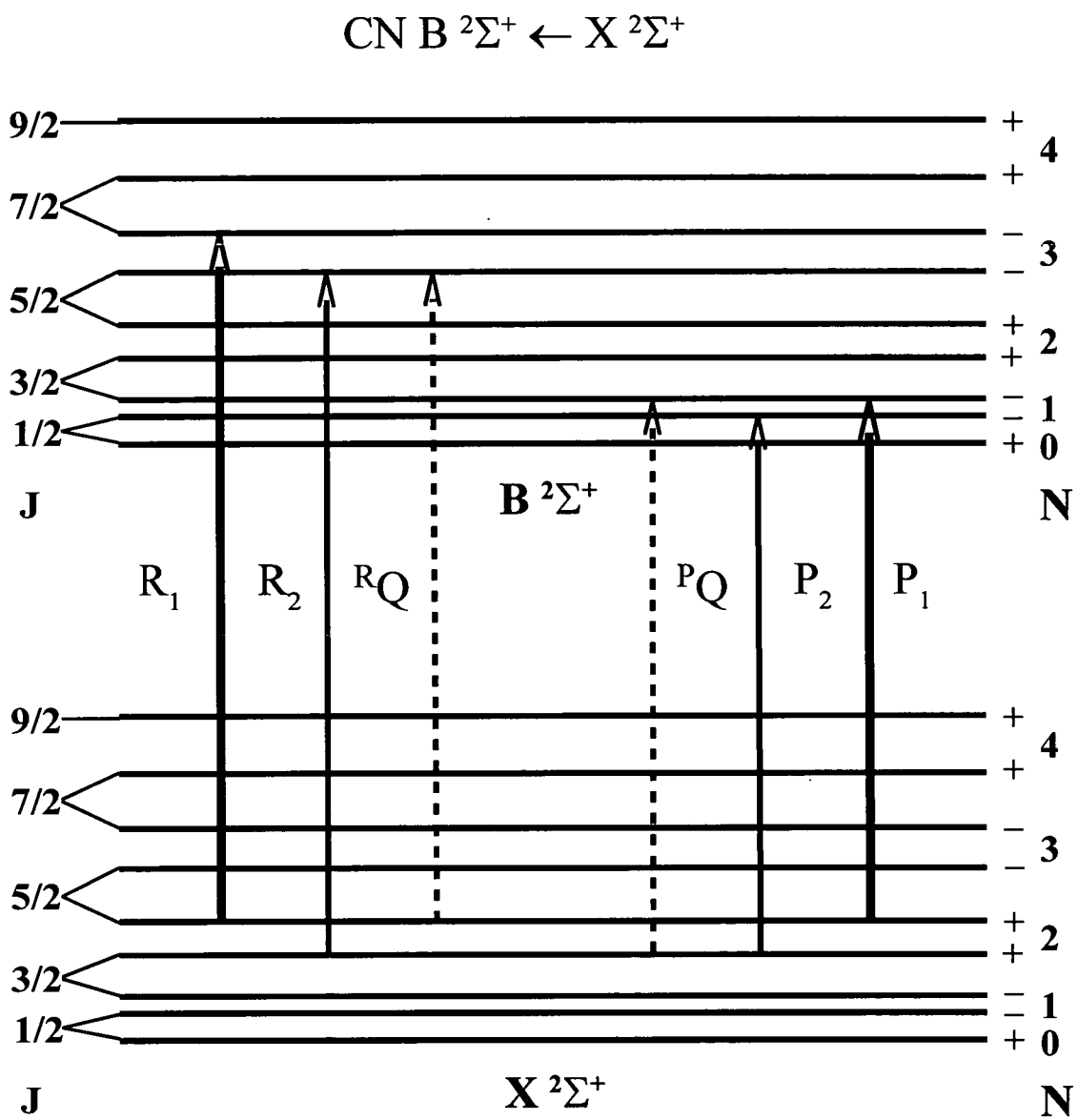

Figure 2.5: Schematic representation of the optical transitions of the CN radical CN B $^2\Sigma^+$-X $^2\Sigma^+$ (0-0) band. The dotted lines, with $\Delta J \neq \Delta N$ tend to be much weaker than the solid ones with $\Delta J = \Delta N$.

2.2.7 The NCO radical

2.2.7.1 General Introduction

The NCO radical was first studied spectroscopically by Dixon [100] in a flash photolysis experiment. Fundamental interest arises due to the Renner-Teller interaction in the ground state [101]. Most of the spectroscopic studies focussed on the $\tilde{A}-\tilde{X}$ transition but there are also studies on the $\tilde{B}-\tilde{X}$ transition. A detailed introduction is given by Wright and Dagdigian [102], where also an overview of the practical importance of the NCO radical in combustion is given. For the purpose of this study only the $\tilde{B}-\tilde{X}$ transition is of importance.

2.2.7.2 The $\tilde{X}\,^2\Pi$ state of the NCO-radical

The electronic ground state has a nearly linear equilibrium geometry and has $^2\Pi$ symmetry.

2.2.7.3 The $\tilde{B}\,^2\Pi$ state of the NCO-radical

The second excited electronic state of NCO has also a near linear equilibrium geometry and $^2\Pi$ symmetry.

2.2.7.4 The NCO $\tilde{B}$ (0,0,0) $^2\Pi \leftarrow \tilde{X}$ (0,0,0) $^2\Pi$ Transition

The situation, compared to the diatomic cases above, is further complicated by the possibility of vibronic coupling with the doubly degenerate bending vibration, ν_2. The two degenerate bending vibrations take place in perpendicular planes and if excited at 90° out of phase with respect to each other they can be described as the C

atom rotating around the internuclear axis and therefore inducing one unit of angular momentum along the direction of internuclear axis. The vibrational angular momentum $\boldsymbol{l}$, may couple with the orbital angular momentum Λ of the electrons to produce the vibronic angular momentum $\boldsymbol{K}$ and its corresponding quantum number K

$$K=|\pm\Lambda\pm l| \qquad \text{equation (2.18)}$$

The vibronic symmetries of a given vibrational level in the bending vibration depends on the possible values of K which are given as

$$K=|\Lambda+l|,|\Lambda+l|-2,\ldots 1 \text{ or } 0 \qquad \text{equation (2.19)}$$

As long as the bending vibration is not excited l=0 and K=Λ=1 for a Π system.

If excitation of the bending vibration is present the PES splits along the bending coordinate allowing additional minima away from the linear equilibrium geometry. This splitting is known as Renner-Teller splitting [103,104].

All transitions observed in this study only involved the vibrational ground state in the bending vibration. It is therefore not necessary, for the present case, to go into a detailed discussion of the Renner-Teller splitting. As with the OH $^2\Pi_i$ ground state the $^2\Pi$ states of NCO undergo spin-orbit splitting to produce a F'_1 ($^2\Pi_{3/2}$) and a F'_2 ($^2\Pi_{1/2}$) manifold. The $\tilde{B}-\tilde{X}$ transition would therefore be expected to form two subsets of transitions each with an R, P, and Q branch and its satellite, in total 12 branches. The Q branches tend to be very weak. The possible transitions are shown in figure 2.6. As shown by Dixon *et al.* [105] and confirmed by Dagdigian *et al.* [102] the $\tilde{\mathbf{B}}$ (0,0,0) $^2\Pi \leftarrow \tilde{\mathbf{X}}$ (0,0,0) $^2\Pi$ transitions are strongly perturbed by nearly isoenergetic $\tilde{\mathbf{A}}$ levels and significant mixing with the $\tilde{\mathbf{A}}$ state takes place.

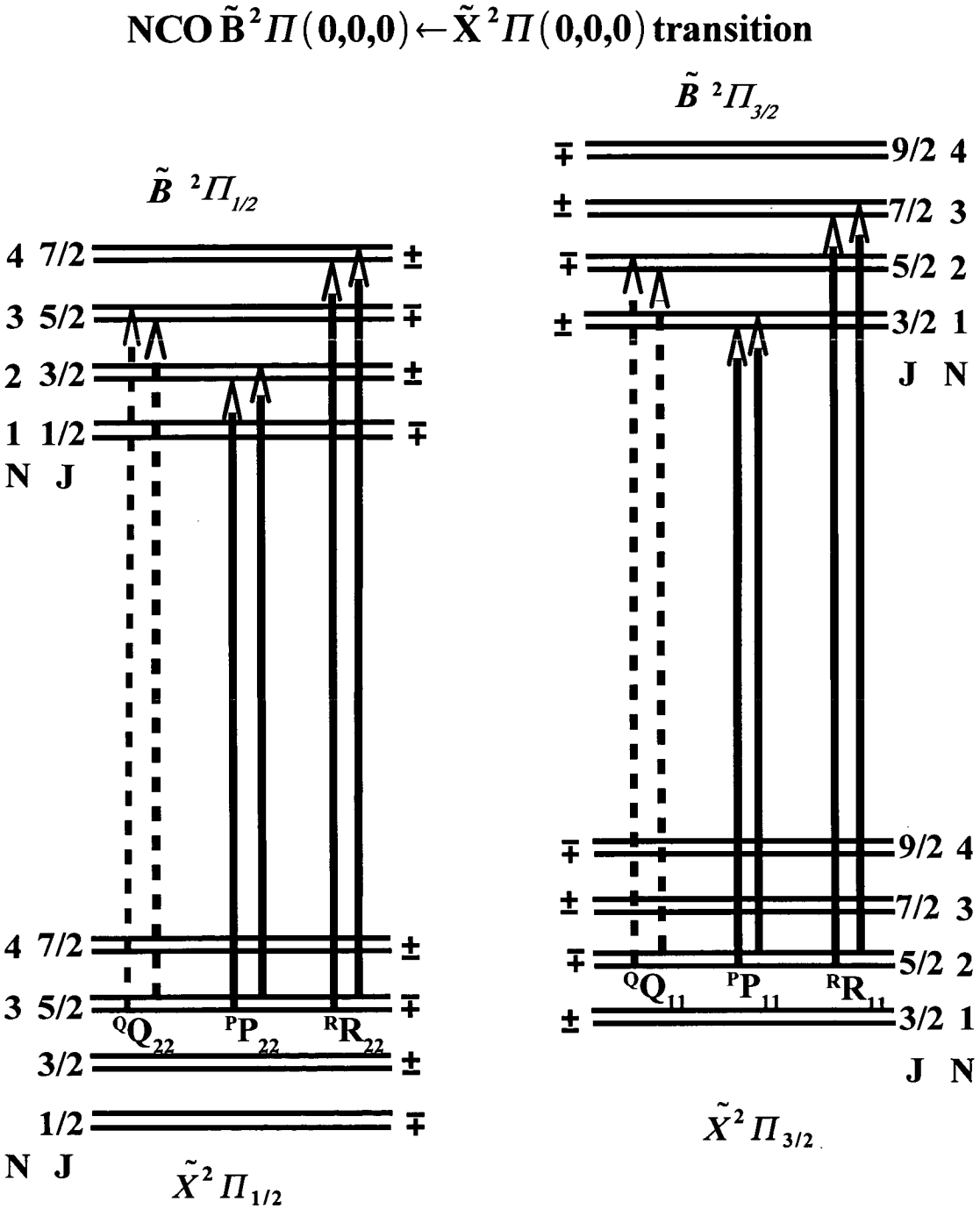

Figure 2.6: Schematic representation of the optical transitions of the NCO $\tilde{B}\ ^2\Pi$ (0,0,0) ← $\tilde{X}\ ^2\Pi$ (0,0,0) band. The different vibrational levels are not indicated. The dotted transitions are much weaker than the solid ones. Labeling as in figure 2.2. Since it is unambigious, the branches can also be labeled Q_2, P_2, R_2 for $^QQ_{22}$, $^PP_{22}$, $^RR_{22}$ and Q_1, P_1, R_1 for $^QQ_{11}$, $^PP_{11}$, $^RR_{11}$ respectively.

2.2.8 Infrared spectroscopy of the CH_4 molecule

2.2.8.1 General Introduction

The CH_4 molecule is very abundant in many different environments as diverse as interstellar space, upper and lower atmosphere of the earth, Jupiter, combustion, swamps or even sheep's and cattle's digestive systems.

2.2.8.2 Fundamental vibrations of the CH_4 molecule

The molecule is of tetrahedral symmetry (T_d) with a bondlength of about 1.09 Å. The molecule has 4 different kinds of vibrations. A non-degenerate symmetric stretch (A_1) which is labelled ν_1. In addition, there are a two-fold degenerate rocking motion (E) ν_2, as well as two sets of triply-degenerate vibrations (T_2 or F_2) ν_3 and ν_4. While all vibrations are Raman active, only the last two triply degenerate vibrations are IR active. For the purpose of this study only the ν_3 vibration is important. One possible set of linear combinations to describe the ν_3 motion geometrically is shown in figure 2.7.

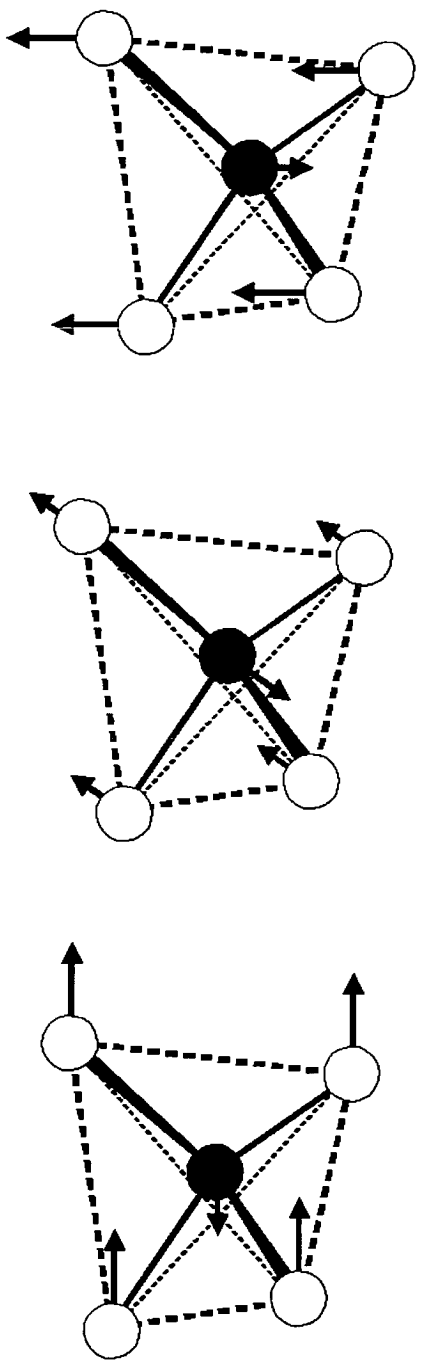

Figure 2.7: Schematic representation of the atomic displacement in the triply degenerate ν_3 mode of CH_4

2.2.8.3 Rotational Structure of the A_1 vibrational ground state

All 3 moments of inertia about the 3 principal axes have the same size, so CH_4 is a spherical top. Its rotational structure introduces an additional spatial degeneracy of $(2J+1)$ for each rotational level corresponding to the allowed orientations of the axis of rotation in space relative to an arbitrary quantisation axis. Rotational levels fall into one of three species: A, E and F. Since the four hydrogen atoms in methane have a nuclear spin of $I= 1/2$ the resultant total spin can be 2 (A), 0 (E) or 1 (F) and are called quintet, singlet or triplet according to the $2I+1$ rule.

This behaviour is analogous to the existence of ortho- and para-hydrogen in a diatomic case. Due to the spin-statistics the degeneracy of a rotational level is not simply given as $(2J+1)^2$ but follows a more complicated pattern and only approaches the $(2J+1)^2$ value at high J. The different species of rotational levels form 3 different manifolds of levels which are separated by symmetry and do not interact.

2.2.8.4 Transitions in the F_2-A_1 band of CH_4

The vibrational ground state of methane has A_1 symmetry and an excitation of the ν_3 mode is an F_2-A_1 transition. As F_2 is a triply-degenerate vibrational state the rotation around a given axis has different effects on the three degenerate vibrations which compose F_2. This is called a Coriolis interaction, and only the one vibration which is unaltered by the rotation remains unchanged (F^0), while the other two give rise to two vibrations which are the linear combinations of the initial vibrations (F^+, F^-). The Coriolis interaction effectively changes the previously equal moments of inertia, thereby removing the threefold degeneracy of an F_2 symmetry species.

For the vibration-rotation infrared transitions the following selection rules hold for a tetrahedral molecule:

The symmetry species of the dipole moment must be the same as the vibration, i.e. only vibrations of symmetry type F_2 may interact to produce an optically active fundamental transition. Furthermore, since the system is an anharmonic oscillator

$$\Delta v = \pm 1, \pm 2 \ldots \qquad \text{equation (2.20)}$$

The general selection rule for the total angular momentum quantum number J remains:

$$\Delta J = 0, \pm 1 \qquad \text{equation (2.21)}$$

The symmetry species of a given rotational level is controlled by the nuclear spin species which is not allowed to change, therefore only rotational levels with the same symmetry combine.

$$\begin{aligned} A &\Leftrightarrow A \\ E &\Leftrightarrow E \\ F &\Leftrightarrow F \end{aligned} \qquad \text{Equation (2.22)}$$

These selection rules lead to 3 different branches, an R-branch ($\Delta J = +1$) which by symmetry only accesses F^- levels in the upper state; a P-branch ($\Delta J = -1$) which only accesses F^+ levels; and a Q-branch which only accesses F^0 levels. While the R- and P-branches are expected to spread out with roughly 2B distance between the lines the Q-branch is expected to more or less fall upon itself. The allowed transitions are shown in figure 2.8. The CH_4 vibrational spectrum was simulated using the Hitran database [106] in the range of 2850 cm^{-1} and 3150 cm^{-1} where the fundamental transition of the ν_3 vibration can be observed. The simulation is shown in figure 2.9.

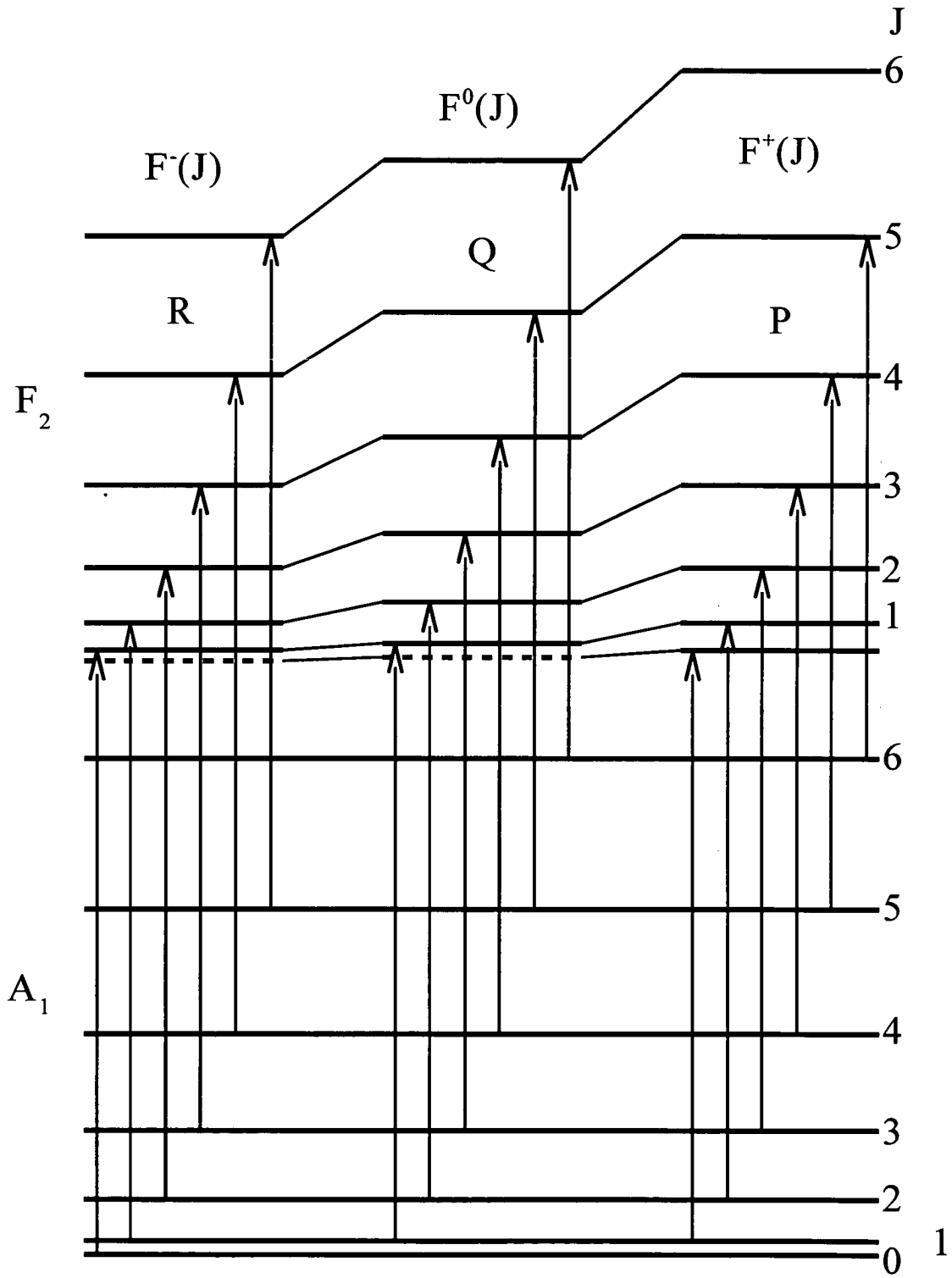

Figure 2.8: Schematic representation of the optically allowed transitions in CH_4 (ν_3, v=1) ← CH_4 (ν_3, v=0) transition. Each branch only accesses one particular manifold in the upper vibrational state.

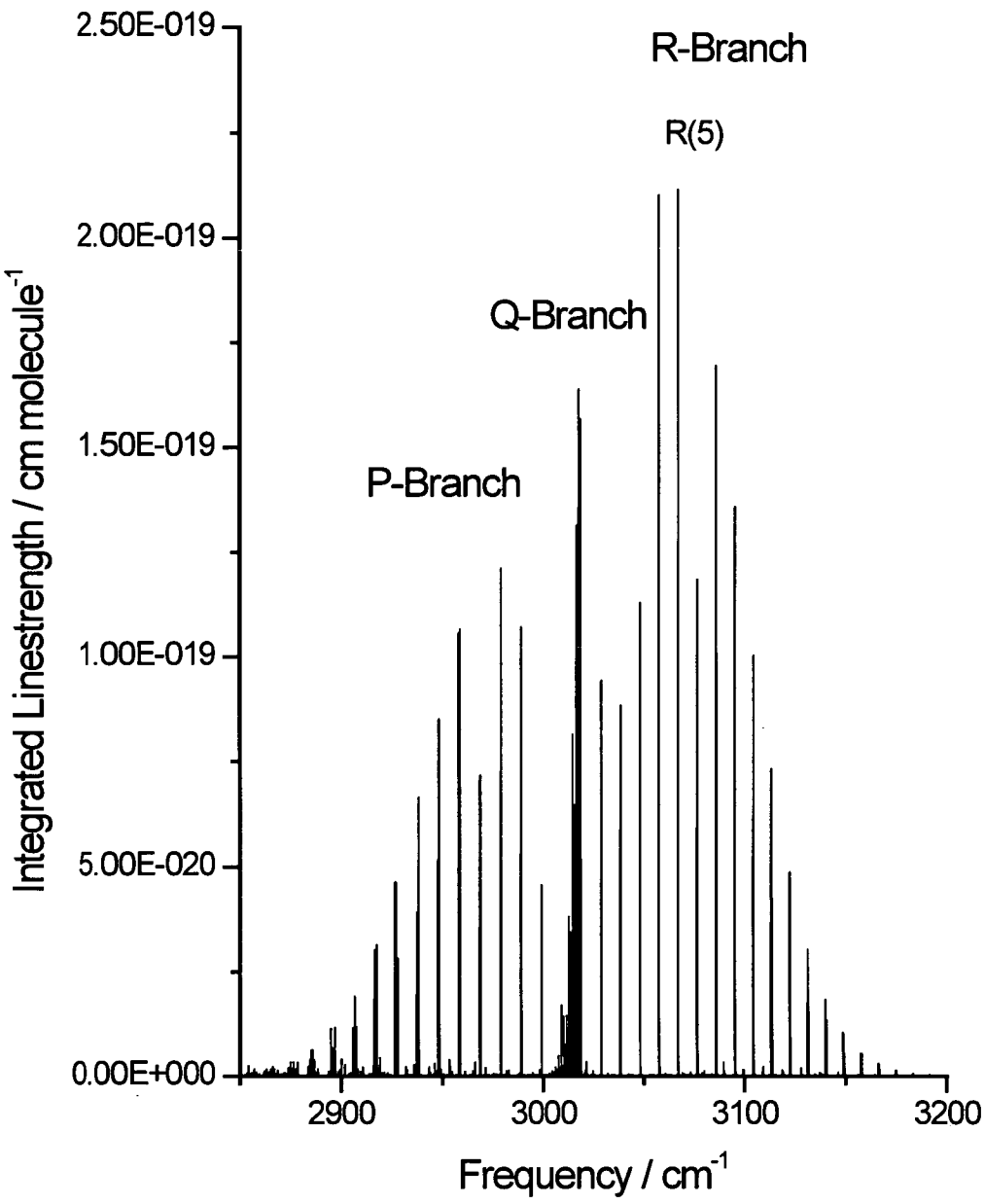

Figure 2.9: Hitran [106] simulation of the vibrational spectrum of CH_4 (ν_3, v=1).

Chapter 3: Experimental Section

3.1 General Features

The basis of the experiments presented here is a photolysis-probe setup. A Nd:YAG laser is fired at 266 nm to produce the $O(^3P)$ atoms by photolysis of NO_2 and thereby initiates the reaction. The timing between the photolysis pulse and the subsequent probe pulse is crucial. It determines, together with the pressure in the chamber, how many collisions the product molecule has undergone before detection. The aim is to detect the reaction products before any secondary collisions have occurred, thereby observing the nascent product distribution. The precursor and the reactant gas are flowed into the chamber and get pumped away in order to constantly refresh the gas mixture. The experiments have been carried out in a stainless steel reaction chamber which was used in previous work [107].

3.1.1 Vacuum cell and gas handling

A stainless steel reaction chamber, built from VG components, was used. The centre of the chamber was a six-way cross. The gases were flowed in through Swagelok connections on the top flange and were pumped away by a diffusion pump (Diffstak 100) supported by a liquid N_2 trap and backed by an Edwards (E2M8) rotary pump.

The gases were stored in small cylinders in a custom built stainless-steel manifold. The manifold could be separated into parts allowing the photolytic precursor and the reactant gas to be kept separate and only mix in the chamber. This

reduced unwanted reactions, especially H-exchange between NO_2 and hydrocarbon.

The gas flow could be adjusted by cut-off and needle valves (Swagelok SS22R54) to produce the desired mixture in the cell. In the case of hydrocarbons that are liquids at room temperature, the hydrocarbon was subjected to repeated freeze-thaw cycle to remove any volatile impurities. The vapour pressure of the liquid hydrocarbons used was sufficient to establish a proper flow rate in the pressure regime of interest. Gases were used without further purification out of the cylinders with purities stated by the manufactures as shown in table 3.1

Substance	***Purity***	***Source***
CH_4	99.995 %	BOC
CD_4	99.99 %	Eurisotop
cyclo-C_6H_{12}	99 %	BDH
cyclo-C_6D_{12}	99.5 %	Goss
NO_2	98.3 %	BOC
ICN	99 %	Aldrich
H_3CCN	99.9%	Aldrich
O_2	99.9995 %	BOC

Table 3.1: Purities and sources of the chemicals used in this study

For an experiment, gases were flowed into the cell to produce a pressure rise 0.2-0.5 mTorr per second. Once the relative flow rates for both gases were set, the total flow was balanced out by partially opening the butterfly valve above the diffusion pump until the desired total pressure was reached and stabilised. The gas flow and the total pressure in the cell had to be kept constant over the period of the measurement.

In total 3 capacitance manometers (MKS Baratron, 0-10 Torr, 627A11TAC; 0-1 Torr 127AA-00001A; 0-1000 Torr 626A13TAD) were attached to the cell and gas manifold to measure the gas pressure at various places simultaneously. In addition an ion-gauge (VIG8, thorimated iridium; controller IGC17F) allowed measurements of pressures as low as 10^{-3} to 10^{-9} mbar inside the cell and the gas manifold. The chamber and the lines of the gas manifold would be pumped down to about $1x10^{-6}$ mbar before any gases were flowed in.

Two arms about 25 cm length were attached to the chamber and Brewster angle quartz windows (Ø 50 mm, thickness 5 mm) or in the case of the optical pumping experiments CaF_2 windows of the same dimensions, were attached to the them. Both arms were equipped with home-made baffles to reduce the amount of scattered light. The flange leading to the light detection system had an adjustable lens holder and baffles inside the chamber attached to it and a quartz window to allow the fluorescence to pass out of the chamber. All metal parts of the chamber were painted black on the inside to reduce scattered light.

3.1.2 Opto-acoustic Cell

The opto-acoustic cell used in these experiments was a custom built hollow stainless steel cube (length: 10 cm) with 6 openings which fitted 10 cm flanges sealed with viton O-rings. Two opposite flanges were fitted with CaF_2 windows (Ø 50 mm, thickness 5 mm). Another flange connected to a small gas manifold equipped with a capacitance manometer (MKS Baratron 0-1000 Torr, 22BA-010000DB) to

measure the pressure in the cell and a connection to an Edwards (E2M8) rotary pump. The top flange could be connected to the main gas manifold of the reaction chamber to supply gases and pump it out using the diffusion pump. The gas flow could be regulated via a cut-off valve (Swagelok SS-4P-4T-RD) and a needle valve (Swagelok 162450-SS-SS4). In addition, the top flange mounted the microphone holder. The microphone (Brüel & Kjær, condenser microphone, Serial Number 1065701) was connected to a home built amplifier to amplify the signal between 30 and 3000 times. The opto-acoustic cell and accessories were originally built for the research group of Gus Hancock in Oxford and kindly lent out for these experiments, which is gratefully acknowledged.

3.1.3 Laser systems

In total, 4 different laser systems were deployed in the different experiments. To photolyse the precursor, the fourth harmonic (266 nm) of a Nd:YAG laser was used. It came either from a Spectron (SL805G-10) laser which produced about 30 mJ in a circular beam with about 1 cm diameter or in the later stages from a Continuum (SL II-10) system which produced about 70 mJ of the desired wavelength in a 1.5 cm diameter circular beam.

The probe laser for all experiments was a Nd:YAG (Spectron SL803G) pumped dye laser (Spectron SL4000G) system. The dye laser was pumped with the second harmonic at 532 nm from the Nd:YAG system to pump dye mixtures of Rhodamine 590 and Rhodamine 610 in methanol to produce about 70 mJ of energy

between 560-590 nm. The probe beam was passed through a KDP (KH_2PO_4, D176) crystal cut at an angle of 68° to double its frequency. The energy of the doubled probe beam between 280 nm and 295 nm was typically between 1.5 mJ and 3 mJ in a circle of ~0.5 cm diameter.

The laser system used for the IR-pumping experiment consisted of a Nd:YAG system (Continuum, PREC II 8000) equipped with a beamsplitter to produce one beam at 532 nm with about 450 mJ of energy per pulse and one at 1064 nm with about 250 mJ of energy per pulse. The former beam was used to pump a dye laser (Sirah PRSC-LG-18) filled with Styril 9 to give about 60 mJ of tuneable light around 805 nm. The dye beam was then difference-frequency mixed with the 1064 nm beam using a $LiNbO_3$ crystal cut at 48.7° angle. The mixed beam of tuneable IR between 2850 cm^{-1} and 3150 cm^{-1} with a gaussian spectral profile and a bandwidth of lower than 0.1 cm^{-1} [108], had an energy of about 0.6 mJ per pulse. All lasers were fired at a frequency of 10 Hz. The photolysis and probe laser counter-propagated through the chamber with the tuneable IR pump beam being parallel to the photolysis beam.

3.1.4 Light detection

The fluorescence was detected at right angles with respect to the laser beams. A collection lens inside the chamber produced collimated light which passed through a quartz window. The light was detected by two different methods. In the first method, the light was focused outside the chamber by a quartz focussing lens (50 cm focal length) into a monochromator (Hilger and Watts, Monospek 1000, 1 m focal length,

bandwidth 2 nm with slits fully open) and then detected by a photomultiplier (Thorn, B289). In the second method, the light passed through a custom made interference filter (Laser Components, peak wavelength: 317 nm, bandwidth 8 nm, 60 % peak transmission) through a quartz focussing lens onto the photocathode of a photomultiplier (Thorn B2. series). The first method produced a very good discrimination against unwanted signals, especially the strong signal from the photolysis laser as well the probe laser wavelength. These spectra have in general a very good signal-to-noise ratio. A major drawback of this method was that the narrow bandwidth of the monochromator discriminated against emission of fluorescence where it was not optimised. In the case of the monochromator being optimised for a low N' line the discrimination against high N' lines was significant and produced an artificially "colder" rotational distribution than the actual distribution. This problem was overcome using the interference filter.

In case of NCO detected on the $\tilde{B}-\tilde{X}$ transition only a UV3 filter was used in front of the PMT. The CN B-X transitions were in general observed using an interference filter (Elliot Scientific, peak wavelength 390 nm, bandwidth 10 nm, 25% peak transmission).

In the case of absorption measurements a pyroelectric joulemeter (molectron J3-09DW) was used to observe the variation of energy in the beam after passing through the chamber.

3.1.5 Data collection and experimental control

All experiments beside the optical pumping, absorption and opto-acoustic measurements were carried out under fully synchronised control using the IO software package developed earlier in the laboratory [109] on a personal computer. The software controlled the wavelength of the probe laser and if needed, of the monochromator. The program communicated with a pulse delay generator (LeCroy 4222 PDG) via CAMAC-crate communication lines (CAMAC, IEE583) to produce four delays which triggered the flashlamps and Q-switches of the lasers as well as the supersonic nozzle, if used, via a home built line driver. In addition, a digital delay generator (Princeton Model 9650) was used to trigger the pump laser system as well as an additional digital delay generator (Stanford Research System DG 535) for the photolysis laser in the IR-pumping experiments.

Signals from the photomultiplier tubes, the pyroelectric joulemeter or the microphone were, if necessary, amplified 5 times by a fast preamplifier (SRS SR240). The amplified signals passed into a transient digitiser (100 MHz dsp 2001 A) which was triggered by the probe laser Q-switch and, displayed on the computer screen. The software allowed for several datasets to be taken depending on the number of delays and gates involved. If more than one delay was used, the software collected data by cycling through all delay sets at a given point until the number of data points were taken. The data were saved on the PC. A schematic of the experimental setup is given in figure 3.1.

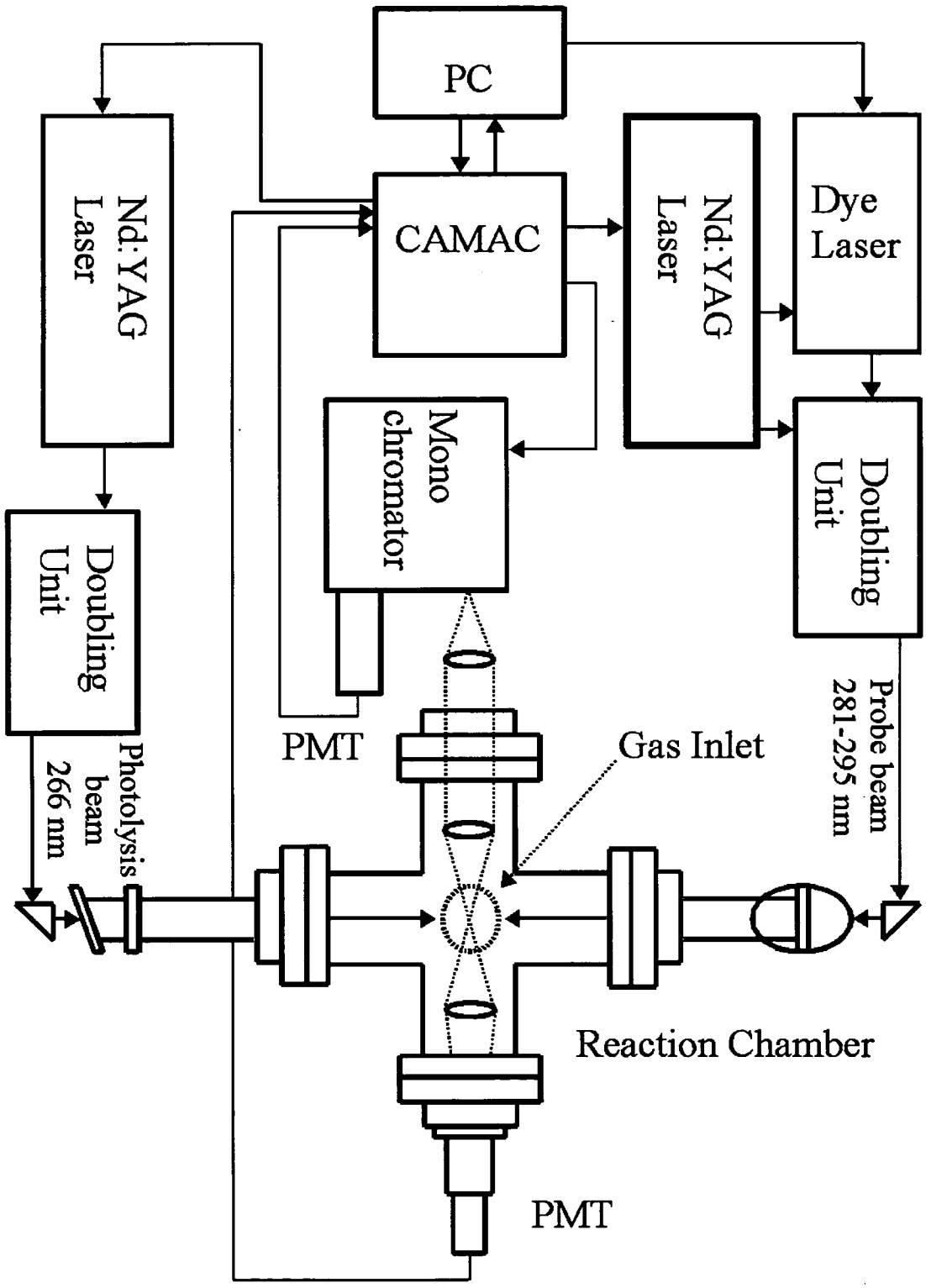

Figure 3.1: Schematic experimental setup for LIF bulk experiments. The gases flow in from above the plane of the paper.

3.2 Special Features

3.2.1 LIF experiments in the bulk gas-phase

For a standard LIF experiment, a stable gas flow of the photolytic precursor and the other reactant in the ratio of interest and to a chosen total pressure was established. Experiments carried out under these flowing conditions in the reaction chamber will be referred to as "bulk" phase experiments from now on.

Usually three different delays between photolysis and probing were used. A very short delay and a slightly longer delay observed the reactive product while a long delay was used to establish a thermal reference spectrum to be able to account for the detection sensitivity in the system. Details on the use of the thermal reference spectrum are discussed in the next chapter.

For excitation scans, the wavelength of the probe laser was scanned, while for dispersed fluorescence scans the probe laser wavelength remained constant and the monochromator was scanned.

Usually the working pressures were set at 100-500 mTorr with relative delay times between 100-250 ns with 20000 ns for the thermal spectrum. The conditions usually corresponded to an average of 0.1 to 0.5 collisions for the reactive products before probing for the first relative delay. A detailed list of the conditions will be given in the next chapter.

3.2.2 LIF experiments using a supersonic nozzle

For these experiments the gas was not flowed directly into the chamber, but a supersonic pulsed nozzle (General Valve 1250 PSA, Serial Number 9-181-900, 1 mm orifice) was used to inject small amounts of the reaction mixture into the reaction chamber. The diffusion pump was not throttled and the background pressure was as low as $1x10^{-6}$ mbar and rose to about $1x10^{-5}$ mbar while the nozzle was firing.

The nozzle fires a small pulse of gas. Its shape depends on several parameters like the size of the orifice, gas mixture, backing pressure, opening time, spatial and temporal development and so on. Several experiments were conducted to characterise the pulse coming out of the valve. Altering the delay between the nozzle firing and the photolysis laser, with a fixed photolysis-probe delay, extracts different parts of the gas pulse in the reaction zone. A typical result is shown in figure 3.2. The actual gas pulse can be followed by observing the photolytic OH signal. The information of interest though, is the development of the reactive signal which is also displayed in figure 3.2. The time difference between the opening of the nozzle and the firing of the lasers includes the actual time delay between the electronic pulse and the opening of the nozzle as well as the process of opening and flowing of the gas and the time needed to travel into the observation zone.

The nozzle was controlled via a pulsed nozzle driver (General Valve, IOTA ONE) which allowed separate adjustment of the opening time of the nozzle and to fire it internally or externally controlled. The backing pressure behind the valve was usually about 600 Torr of an equal mixture of NO_2 and hydrocarbon. The delay

between firing the nozzle and the photolysis and probe laser was adjusted according to the response function under these conditions to carry out the experiments at the rising edge of the peak.

3.2.3 Absorption measurements

The absorption measurements with CH_4 and NO_2 / CH_4 were conducted by shooting the tuneable IR-beam through the chamber and measuring the energy of the pulses as function of the IR wavelength with the pyroelectric joulemeter. They were not normalised for IR beam pulse energy variations. In general, the fast preamplifier was not used and the data of the pyroelectric joulemeter were put straight into the transient digitiser. The CH_4 pressure in the chamber ranged from 1 to 100 Torr with a pathlength of about 1 m.

3.2.4 Opto-acoustic measurements

For the opto-acoustic measurements of CH_4 the tuneable IR beam went through the opto-acoustic cell and signal was detected by a microphone. Again, there was no correction for the power dependence and the preamplifier was not used. The signal was amplified by the microphone amplifier which usually produced a large signal at its smallest possible amplification (x3). The CH_4 pressure in the opto-acoustic cell was usually between 5 and 20 Torr.

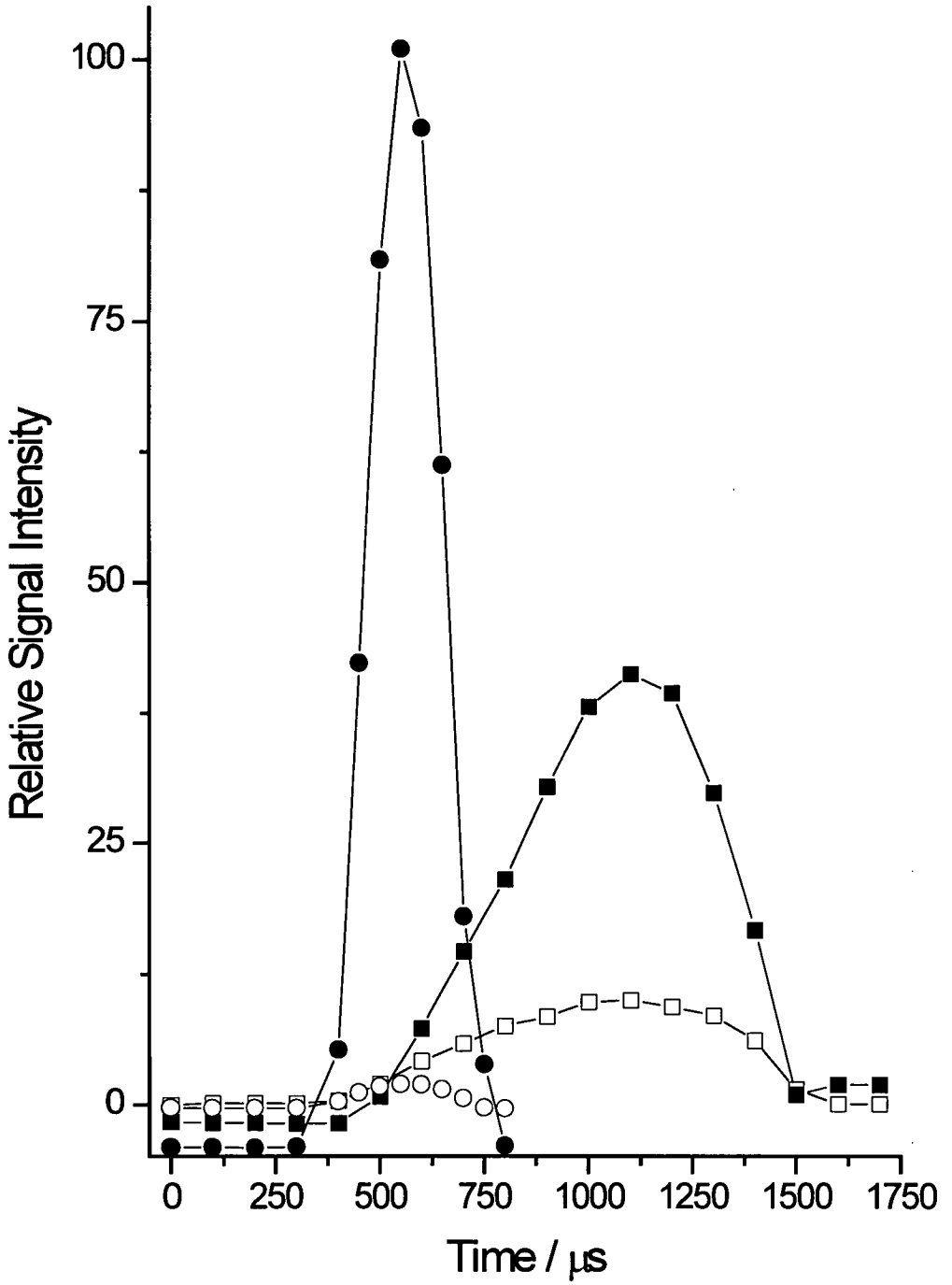

Figure 3.2: Response function of the supersonic nozzle. OH LIF signal as function of delay between the firing of the supersonic nozzle and the probe laser. Δt (Photolysis-Probe)=1μs. The open squares correspond to the photolytic OH contribution with a backing pressure of 160 Torr of NO_2 behind the nozzle and an opening time of 800 μs, while the open circles represent 640 Torr of NO_2 and an opening time of 300 μs. The solid symbols display the corresponding conditions with the same total pressure made up of a equal mixture of CH_4 and NO_2 and therefore display the bimolecular OH signal produced by reaction with CH_4.

3.2.5 IR-pumping experiments

The experimental setup for the IR-pumping experiments is essentially a combination of a normal bulk phase LIF experiment and an opto-acoustic measurement. The IR laser beam enters the main reaction chamber collinearly with the photolysis beam, counter-propagating the probe laser beam. For alignment purposes and to protect the gold mirrors the beam was restricted by a set of irises before and after the reaction cell. After passing through the second iris the beam was steered into the opto-acoustic cell to allow monitoring of the IR wavelength and the optical alignment through the whole system. Otherwise the conditions used were similar to the normal LIF bulk experiments. The choice of delays will be discussed below in more detail. A schematic representation of the setup is shown in figure 3.3. The total pressure in the reaction chamber was between 500 and 1000 mTorr, made up by equal amounts of CH_4 and NO_2. To establish if any enhancement took place, spectra were recorded at 100, 500 and 20000 ns delay between photolysis and probe laser. Each delay was recorded twice, one time with the IR pump laser firing in coincidence with the photolysis laser and one time delayed by 10000 ns after the probe laser.

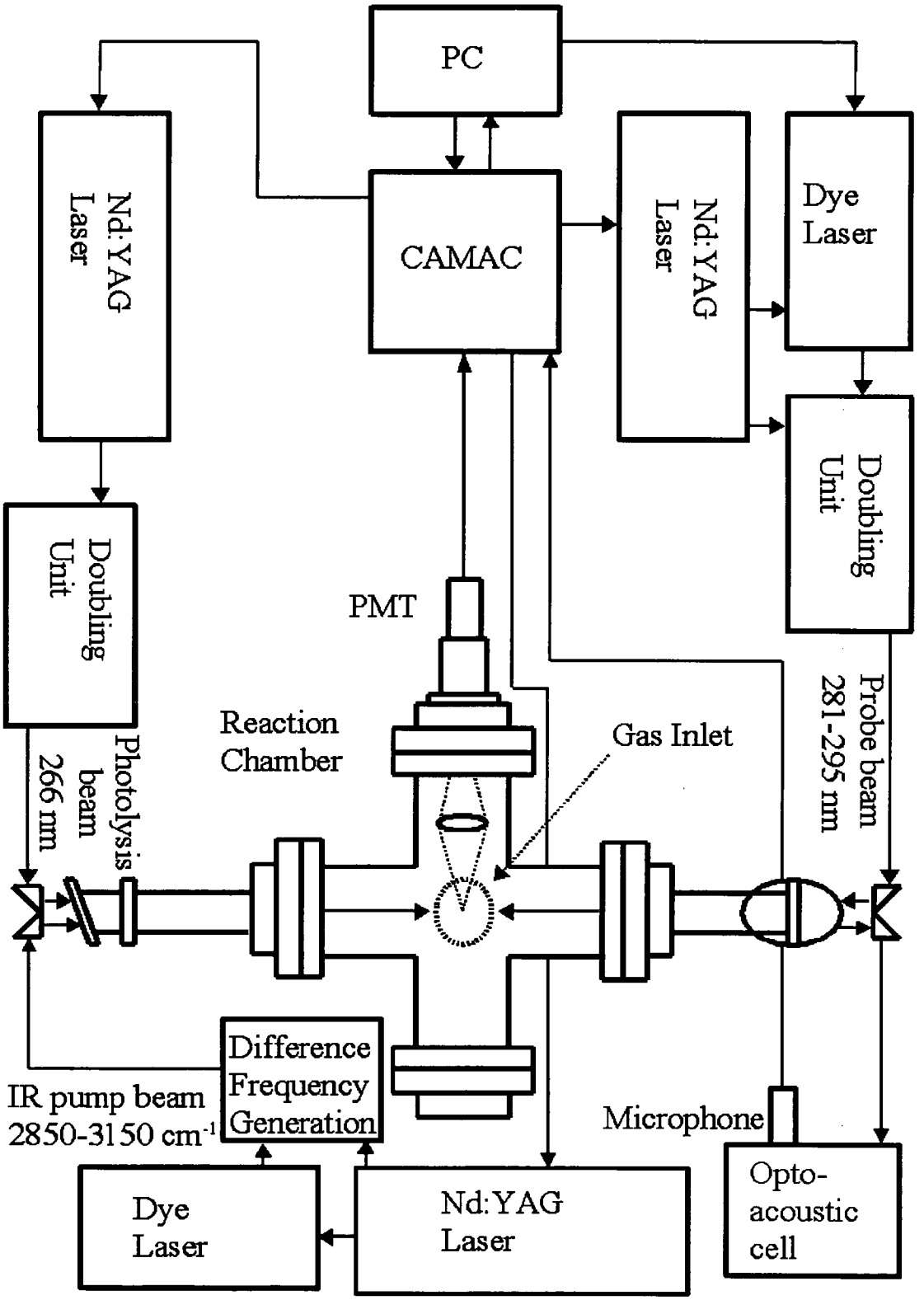

Figure 3.3: Schematic experimental setup for IR-pumping experiments. The gases flow in from above the plane of the paper.

Chapter 4: Results: Reactions of ground state oxygen atoms with saturated hydrocarbons

4.1 General remarks

This chapter will present the main results of this study. Experimental features and appearance of the raw data will be discussed first, followed by a presentation of the tools and methods used to analyse it. The second part of this chapter will present the actual results while the detailed discussion is left for the discussion chapter.

4.2 Experimental features and raw data

4.2.1 Preliminary observations

While LIF is a selective method, the sources of fluorescence are not necessarily the ones of interest. The photolysis of the commercial grade NO_2 produced a significant amount of OH in the ground state. This is presumably due to an H containing impurity which can be photolysed at 266 nm. This problem was reported by other experimentalists as well [23]. The resulting OH signal is largest at short time delays and disappears with time. This problem was not present in studies of OD.

The desired OH/OD laser-induced fluorescence excited from OH/OD produced by bimolecular reaction was only present if the photolysis laser fired before the probe laser in time and both reactants, the photolytic precursor and the hydrocarbon were present in the observation volume in the chamber. The integrated intensity of the LIF signal grew in with time up to a few microseconds before decreasing in intensity due

to fly out effects, reduced production rate and secondary reactions. This time dependent behaviour forms the basis of the method of analysis as presented below.

Spontaneous as well as laser-induced NO fluorescence was also present and interfered with the OH / OD LIF signal detection. While, again, the intensity decreased with time it could be significant at early time delays.

4.2.2 Experimental conditions

The experimental challenge consisted of finding conditions which collected as much LIF signal excited from the products of the bimolecular reaction, at a combination of low pressure and short delay times to keep it representative of the nascent products while at the same time discriminating against unwanted fluorescence. A set of typical experimental conditions used in this study are displayed in table 4.1.

4.2.3 Detection of OH and OD LIF excitation spectra

OH and OD LIF excitation spectra were recorded and analysed as will be explained in detail below. For the purpose of pointing out some elementary features of the results, typical sets of collected data for OD and OH are shown in figures 4.1 and 4.2 respectively. It can be seen clearly, that the signal-to-noise ratio is much better for the secondary hydrocarbon than for the methane compound.

Reaction	*p(NO_2) / mTorr*	*p(hydro-carbon) / mTorr*	*Δt / ns (photolysis -probe)*	*Filter / Mono-chromator / nm*	*Probe Laser Wavelength range / nm*	*Product*
$O(^3P)$ + cyclo-C_6H_{12}	NO_2 / 50	50	50, 150, 20000	if: 317 mono: 318.9 (1-1) 312.8 (2-2)	 281.0-285.0 287.5-291.0	OH $A^2\Sigma^+$- $X\ ^2\Pi_i$ (1-0) (2-1)
$O(^3P)$ + cyclo-C_6D_{12}	NO_2 / 50	50	100, 20000	if: 317 mono: 312.8 (1-1) 317.0 (2-2)	 287.0-291.0 291.5-295.0	OD $A^2\Sigma^+$- $X\ ^2\Pi_i$ (1-0) (2-1)
$O(^3P)$ + CH_4	NO_2 / 100	100	50, 300, 20000	if: 317 mono: 318.9 (1-1) 312.8 (2-2)	 281.0-285.0 287.5-291.0	OH $A^2\Sigma^+$- $X\ ^2\Pi_i$ (1-0) (2-1)
$O(^3P)$ + CD_4	NO_2 / 100	100	250, 20000	if: 317 mono: 312.8 (1-1) 317.0 (2-2)	 287.0-291.0 291.5-295.0	OD $A^2\Sigma^+$- $X\ ^2\Pi_i$ (1-0) (2-1)
$O(^3P)$ + cyclo-C_6H_{12}	NO_2 / 40	40	100, 300, 20000	mono: 280-360	$Q_1(1)$	(DF)[a] OH A – X (1-v'')

Table 4.1: Typical experimental conditions for bulk LIF experiments. OH and OD were detected on the $A^2\Sigma^+$- $X\ ^2\Pi_i$ band. [a] Dispersed fluorescence.

For the deuterated samples no initial background was detected and all the recorded signal originates from OD produced by the bimolecular reactions (1.7) and (1.8). For the first few 100 ns the growth will be approximately linear with time, before fly out and secondary reactions for OD as well as the slowed production due to deceleration of the $O(^3P)$ atoms become important.

For OH, there is the above mentioned significant background due to a rogue compound in the NO_2. This photolytic contribution to the total signal is significant in size, making up about 2/3 of the signal for reaction (1.6) and most of the recorded signal for reaction (1.5) for the OH (v'=0) product at the shortest time delay between photolysis and probe, usually 50 ns.

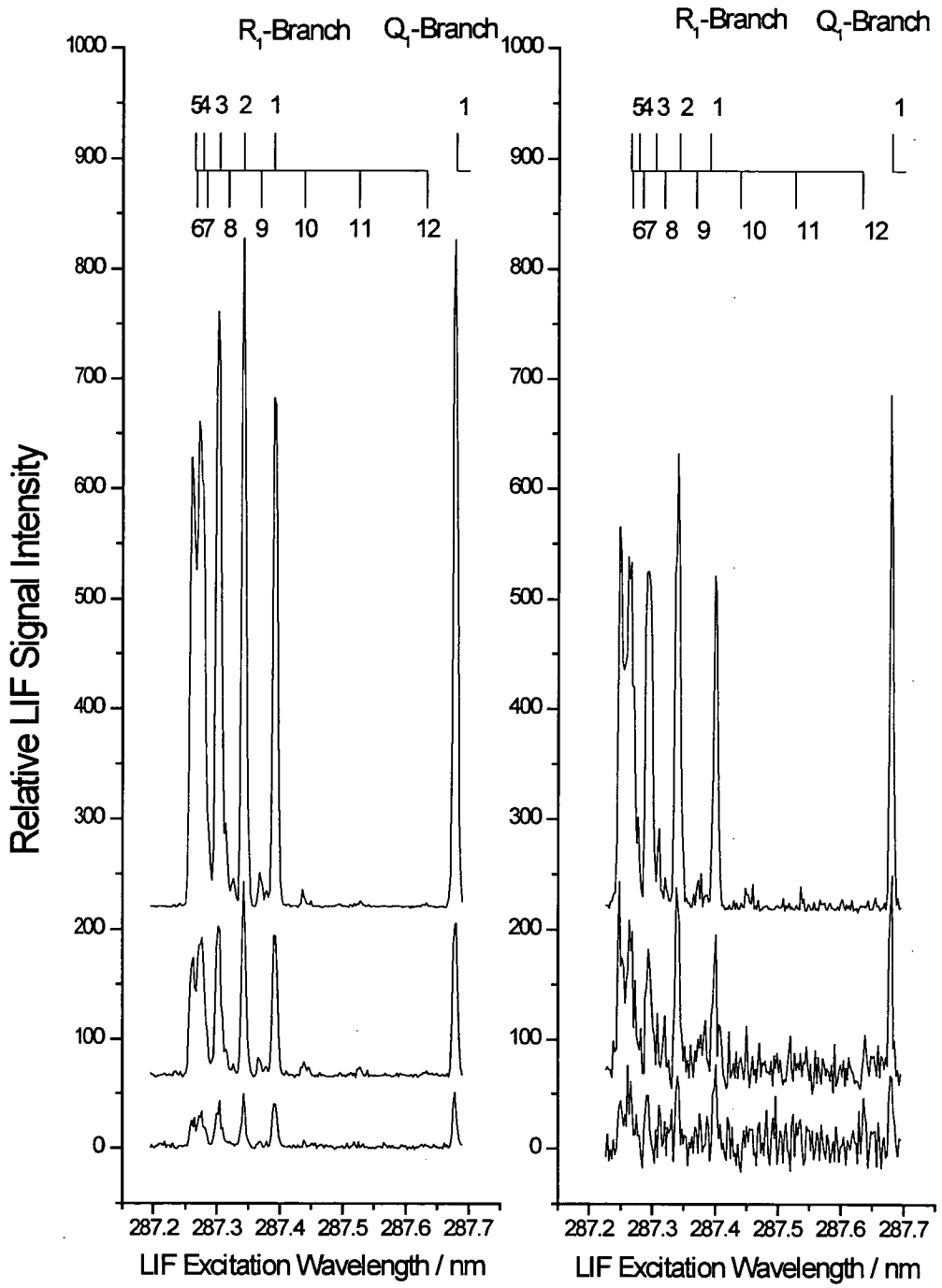

Figure 4.1: OD $A^2\Sigma^+$-$X^2\Pi_i$ (1-0) excitation spectra of the R_1-branch region. The left hand side shows OD produced by $O(^3P)$+ *cyclo*-C_6D_{12}, the right hand side $O(^3P)$ + CD_4. The pressures are 50 mTorr NO_2 and 50 mTorr *cyclo*-C_6D_{12}, and 250 mTorr NO_2 and 250 mTorr CD_4 respectively. The delays shown are 50, 200 and 20000 ns.

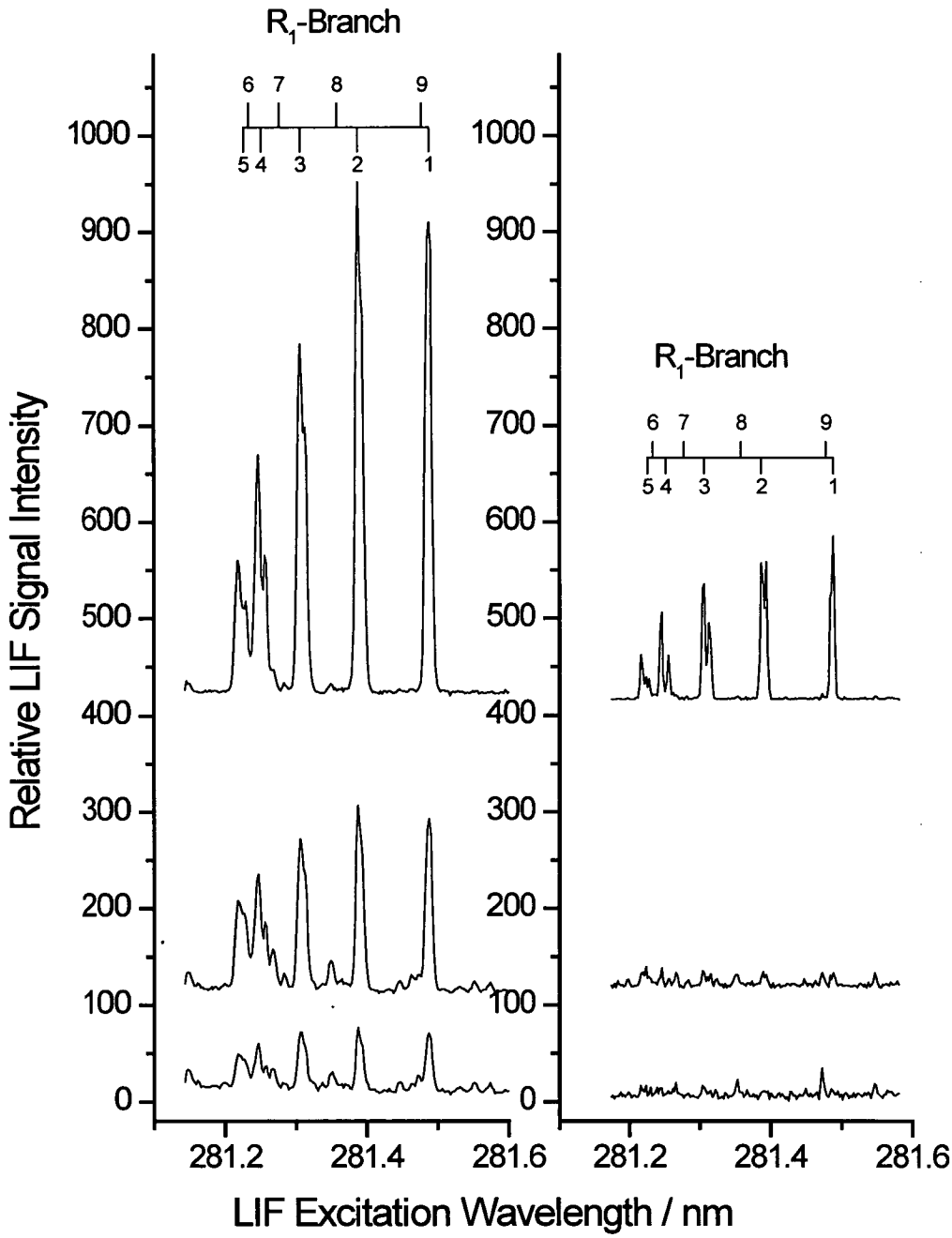

Figure 4.2: OH $A^2\Sigma^+$-$X^2\Pi_i$ (1-0) excitation spectra of the R_1-branch region. The left hand side shows OH produced by $O(^3P)$+ *cyclo*-C_6H_{12}, the right hand side $O(^3P)$ + CH_4. The pressures are 50 mTorr NO_2 and 50 mTorr *cyclo*-C_6H_{12}, and 250 mTorr NO_2 and 250 mTorr CH_4 respectively. The delays shown are 50, 200 and 20000 ns.

The photolytic OH is only produced in the vibrational ground state and is rotationally "hotter" than any of the reactive OH (v'=0) observed in this study. The bimolecular OH LIF signal grows in as the reaction proceeds.

There is also a significant signal originating from spontaneous NO fluorescence. This fluorescence is independent of the probe laser wavelength and produces a higher baseline in the recorded spectra. It is probably due to an accidental double-resonance process, where NO produced by the photolysis of NO_2 absorbs a second photon at 266 nm on the NO A-X (1,5) band. This is followed by strong emission on the NO (1,v'') bands.

It makes the largest contribution for the shortest delay times between photolysis and probe laser. The most inconvenient bands are the NO A-X (1,8) and (1,9) band whose emission fall in the same wavelength region as the OH/OD diagonal bands used to detect the emission of the reaction product. Since it is caused by the photolysis, it decreases with increasing delay time.

The photolysis of NO_2 at 266 nm produces the electronic ground state of NO in a wide array of vibrational levels, including NO (v=6). More details of this aspect are discussed in section 4.4. A serious problem is caused by excitation of the NO B-X (0,6) transitions with the probe laser which lie in the same region as the OH A-X(2,1) band which was used to probe for OH(v'=1). The excited NO fluoresces back on the B-X(0,7) and (0,8) bands which fall into the wavelength region observed by the filter or monochromator used. These unwanted NO contributions are shown in figure 4.3.

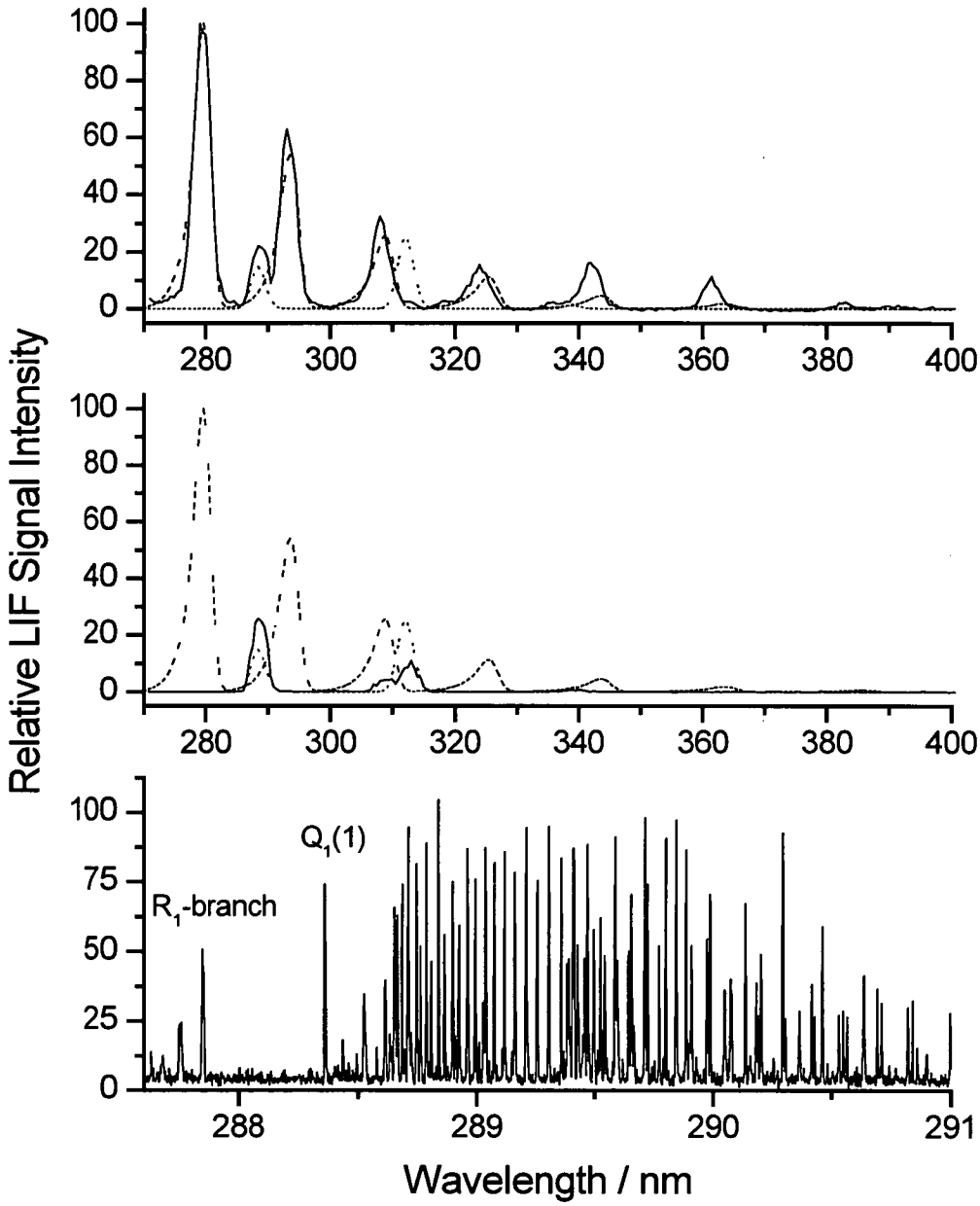

Figure 4.3: Unwanted NO contributions to the fluorescence signal. The solid line upper panel displays a dispersed fluorescence scan at a photolysis-probe delay of 50 ns. The total gas pressure was 100 mTorr, consisting to equal amounts of NO_2 and *cyclo*-C_6D_{12}.The probe laser excited the $Q_1(1)$ transition of the OD A-X (1,0) band. The dashed line is a simulation [94] of the NO (1,v'') progression, the dotted line is a simulation of the OD emission. The centre panel shows the analogue situation for a photolysis-probe delay of 20000 ns. The lower panel shows the NO B-X (0,6) fluorescence excitation spectrum in the range of the OH A-X (2,1) excitation spectrum. The R_1-branch of OH A-X (2,1) is clearly visible on the left hand side. The total gas pressure was 100 mTorr, consisting to equal amounts of NO_2 and *cyclo*-C_6H_{12}.

4.3 Methods of analysis of the observed LIF spectra

4.3.1 Methods of analysis of the bulk phase LIF experiments

4.3.1.1 General comments

The recorded data are LIF excitation spectra of OH and OD of the $A^2\Sigma^+$-$X^2\Pi_i$ (1-0) and (2-1) off-diagonal band to probe the population in the vibrational ground and first excited state, respectively. Fluorescence was detected on the $A^2\Sigma^+$-$X^2\Pi_i$ (1-1) and (2-2) diagonal bands.

The exact appearance of a given spectrum depends on several experimental parameters. Some of them are known or can be well approximated. These include the relative pressure of the gases in the reaction chamber, the transmission curve of the monochromator or interference filter used, or the amount of predissociation for a given rovibronic product level. Other parameters, also very important but usually known to a lesser degree, are the pulse-to-pulse variations of the laser systems or the absolute efficiency of the light collection and detection, as well as the degree of saturation if experimental conditions are outside the linear absorption regime. All these factors make it very difficult to obtain any absolute numbers out of the LIF excitation spectra.

Luckily, all the information of interest can be derived as relative information. The data were collected by cycling through the delay sets on a shot-to-shot basis ensuring that all long time variations, like changes in the gas mixture or drop of the photolysis laser pulse energy, affected all delay sets evenly and were kept statistical

in nature. A further discussion of the methods of analysis used for obtaining specific types of information are presented in the following subchapters in detail.

4.3.1.2 Analysis of the reactive rotational distributions

The analysis of the LIF data followed the principles outlined in previous work [107]. In case of OH measurements, three sets of data were necessary. The shortest time delay, usually 50 ns between the photolysis and probe pulse was chosen to record the contribution of OH produced by photolysis. This instantaneous contribution was produced by an H containing rogue compound, probably HNO_2 or HNO_3, in commercial-grade NO_2. In addition, it also contained OH which was produced by the bimolecular reaction of interest by this delay time.

A second, longer delay time delay, usually 150 ns in the case of *cyclo*-C_6H_{12} or 300 ns for CH_4, recorded the OH produced by both photolysis and reaction during this longer period of time.

A subtraction of the shorter time delay data from the later removes the photolysis component, provided the time difference is small enough to ensure that fly out and relaxation effects in the observation zone are negligible. The subtracted data contains only the OH signals produced from OH molecules created by the bimolecular reaction of interest during the time difference.

For the OD product no photolytic background was observed. Only one short time delay, 100 ns for *cyclo*-C_6D_{12} and 250 ns for CD_4, and one long time delay was sufficient to collect the necessary data.

The last time delay was always recorded at long time delay, usually 20 μs between photolysis and probe laser, to produce a thermalised reference spectrum. It was assumed that this OH/OD spectrum is excited from OH/OD molecules which are completely rotationally relaxed.

This assumption rests on the fact that on average 20 to 40 collisions, depending on the pressure used, have taken place for a given OH/OD molecule before it gets detected. Due to the high barrier of the reaction of $O(^3P)$ with saturated hydrocarbons, as shown in figure 1.1, the excitation functions have a late onset and only become large at high collision energies as demonstrated in figure 1.3. As discussed in section 1.3.1.1, only high velocity $O(^3P)$ atoms were able to react with methane. The reactivity is therefore expected to fall dramatically if the $O(^3P)$ atom's velocity distribution becomes significantly translationally relaxed by collisions. The amount of OH/OD produced late enough for the $O(^3P)$ atoms not to have undergone a significant number of collisions is therefore very small. Furthermore, the nascent product populations are not substantially rotationally excited and the rotational relaxation of OH/OD due to collision with polyatomic partners as methane or cyclohexane is thought to be very efficient. Therefore, it is justified to regard the long time delay spectrum as essentially rotationally thermalised.

The long time delay spectrum therefore could be compared with a simulation using a rotational temperature of 298 K. The variation of the observed and calculated thermal spectrum contains information about the detection sensitivity at any given

point in the spectrum. This includes changes in pressure, laser intensity, linestrength, transmission of filter or monochromator, degree of saturation *et cetera*. All of these factors are independent of delay between the photolysis and probe pulse and affect all delays in the same fashion.

All these unknown quantities lead to deviations of the experimental long delay time spectrum at each OH/OD line from the calculated thermal spectrum. At each point in the spectrum the detection sensitivity, DS can be defined by the ratio of the experimental thermal spectrum over the calculated one.

$$DS = \frac{relative\ Signal\ Intensity\,(experimental\ thermal\ spectrum)}{relative\ Signal\ Intensity\,(calculated\ thermal\ spectrum)} \qquad \text{equation (4.1)}$$

The thermal spectra were simulated using the LIFbase [94] program. The simulation produced relative populations in given levels. Therefore equation (4.1) can be rewritten as

$$DS = \frac{relative\ Population\,(experimental\ thermal\ spectrum)}{relative\ Population\,(calculated\ thermal\ spectrum)} \qquad \text{equation (4.2)}$$

The reactive spectra, either the direct measurement in case of OD or those with the photolytic contribution subtracted in case of OH, were also simulated. The resulting population needed to be corrected for the detection sensitivity:

$$reactive\ Population = simulated\ reactive\ Population / DS \qquad \text{equation (4.3)}$$

This method provides proper correction for experimental factors as long as the thermal population in a given level is of detectable size, so that it leads to easily identifiable lines in the spectrum to simulate. For very small population in the thermal population at a given rovibronic quantum state the value for DS can not any

longer be reliably deduced. This occurs for higher values of N', which is a problem especially for reactions with CH_4 and CD_4 which tend to populate higher rotational quantum numbers than the cyclohexane equivalents. In those cases, where a thermal simulation did not produce any significant populations, the detection sensitivity was extrapolated linearly from the last few observable thermal lines.

In addition the signal-to-noise ratio in the experiments involving CH_4 and CD_4 was usually relatively poor. The data sets were recorded at a stepwidth of 0.0025 nm. The effective bandwidth, controlled by saturation broadening, was about 0.005 nm (FWHM) as estimated on the $Q_1(1)$ line of the thermal spectrum. These spectra were convoluted with a gaussian of 0.003 nm width to reduce the noise level and to smooth the data out before simulation. This process is justified since the laser stepwidth was much smaller than the effective experimental bandwidth. The observed large signal variations between two adjacent stepping positions were random in nature and did not correspond to a real physical effect. This also provided a suitable way of correcting for slightly non-linear wavelength stepping of the probe laser because the centre wavelengths of a given gaussian could be chosen to a new basis grid. All time delays, including the long delay time one, were subject to the same procedure before being compared with the simulations as explained above.

An additional problem was caused by the narrow bandwidth of the monochromator which was generally optimised for the emission on the $Q_1(1)$ line. Due to its narrow bandwidth it discriminated against emission from high N' lines to

an extent that, for example, no population for OD(v'=1, N'>7) from O(^{3}P) + *cyclo*-C_6D_{12} could be extracted using data collected via the monochromator. In contrast populations up to N'=9 were easily identified using an interference filter. The populations recorded with the monochromator were renormalised to the fraction of the total population they represent, as defined by the interference filter data, and used for the low N' levels.

A further potential obstacle might be thought to be the amount of predissociation in OH and OD in the upper electronic state. OH A $^2\Sigma^+$ (v'=2) especially shows strong predissociation on all rotational levels. This affects the amount of fluorescence which can be collected from a given sample of OH molecules, and therefore reducing the total signal size. However, the normalisation with respect to the thermal spectrum ensures that predissociation is also accounted for automatically, so it is not a problem in practice.

The procedure can be visualised with the help of figures (4.4) and (4.5). The upper and centre panel in figure (4.4) shows the data as recorded. In order to remove any photolytic OH contribution or any NO lines, the shorter time spectrum (upper panel) is subtracted from the longer delay time one (centre panel). The resulting experimental reactive spectrum is shown in the lower panel of figure (4.4). The simultaneously recorded long time delay spectrum, the experimental thermal spectrum, is then compared to the simulated thermal spectrum as shown in figure (4.5) and the detection sensitivity for each individual spectral transition derived.

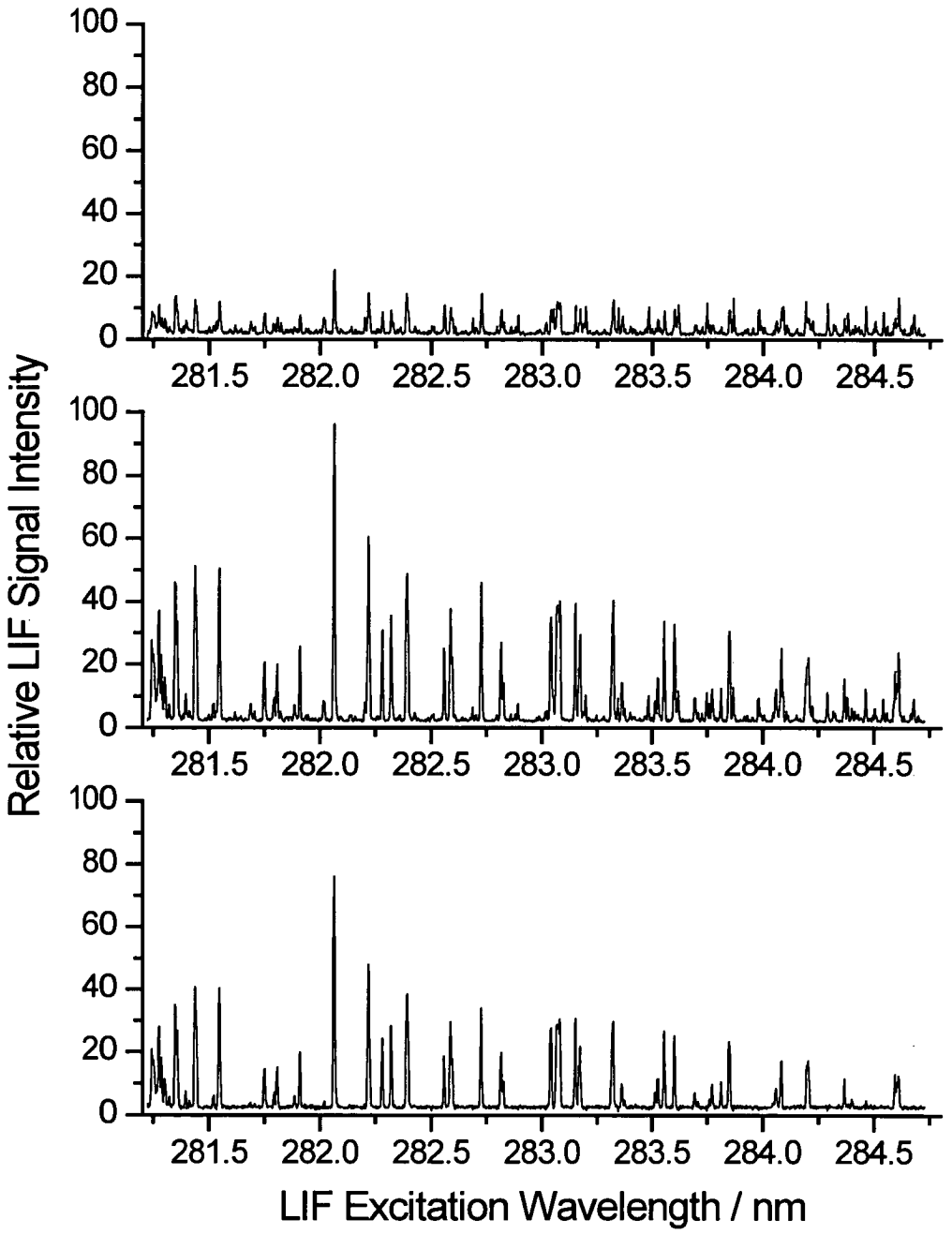

Figure 4.4: Demonstrating the subtraction method to avoid unwanted photolytic or rogue contributions to the reactive spectra OH (v'=0) *cyclo*-C_6H_{12}, delays (photolysis-probe) 50 ns (upper panel), 150 ns (centre panel) and subtraction 150 ns – 50 ns (lower panel). Total pressure: 100 mTorr with 50 mTorr of NO_2 and 50 mTorr *cyclo*-C_6H_{12}.

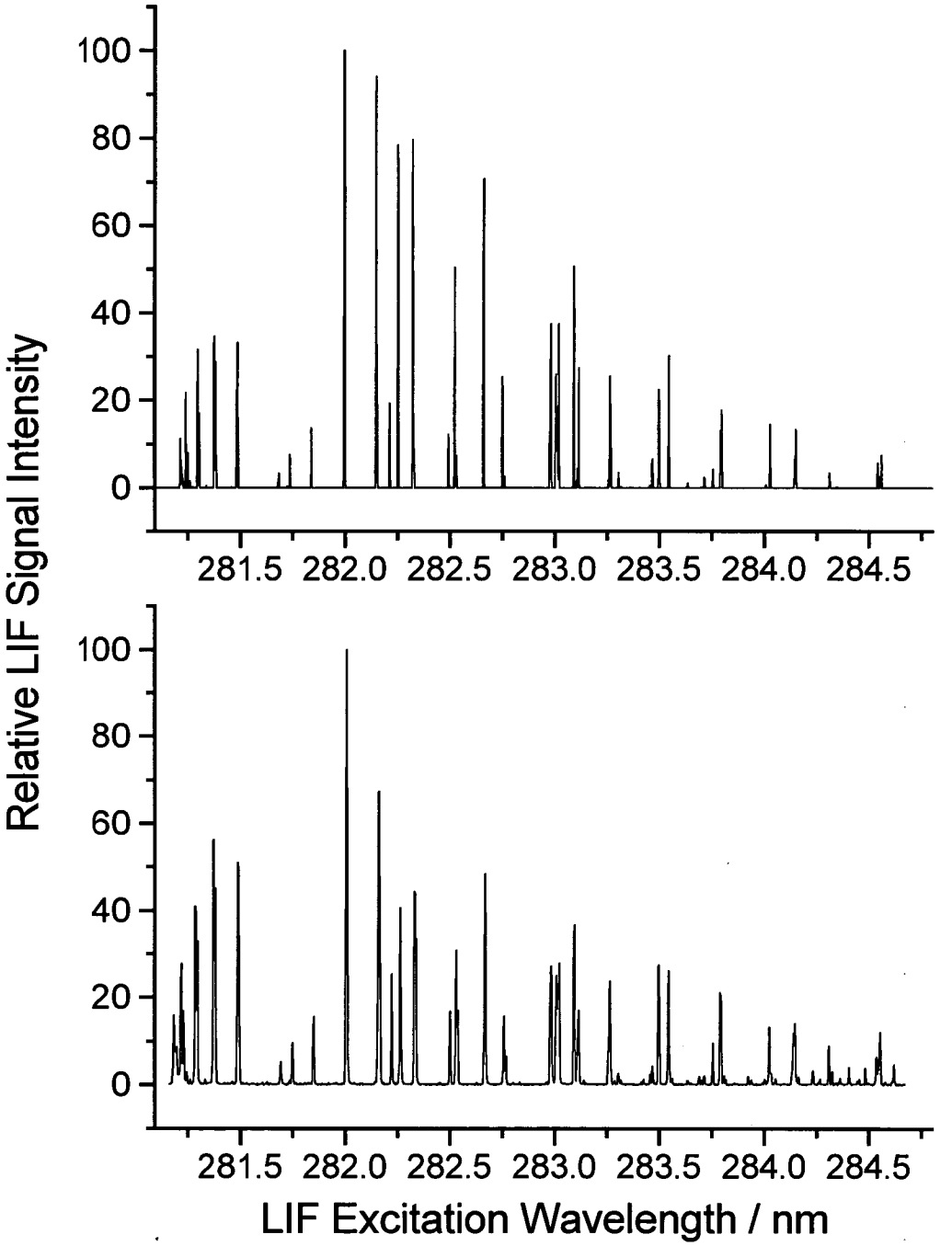

Figure 4.5: Comparison of simulated [94] (upper panel) and measured thermal spectrum (lower panel) of OD (v'=1), conditions as in figure (4.4), delay: 20 μs.

It can easily be seen in figure (4.5), lower panel, that the measured spectrum is heavily saturated while the simulation is not. This fact is also taken into account by the comparison with the thermal spectrum. For the rotational analysis, each branch in a given spin-orbit manifold was simulated separately and the nascent population derived. The data from these branches were combined and adjusted for blended or missing lines. The simulated long time OD and OH spectra which were used for comparison are shown and labelled in figure 2.3 and 2.4 respectively.

4.3.1.3 F_1 / F_2 and Λ-doublet populations

In the LIF excitation spectrum each spin-orbit manifold produces a set of branches, i.e. R, P, Q, which relative intensities contain information about the respective relative spin-orbit populations. In addition, a given Q branch always probes Π (A'') the other Λ-doublet to the respective R and P branches which probe the Π (A') in the same spin-orbit manifold.

In order to gain information about the relative population in the F_1 and F_2 spin-orbit manifolds and the Λ-doublets for a given N' the relative intensity of different branches needed to be compared. The long time spectrum was normalised to the thermal (298 K) simulation. To match the relative intensity of a specific transition in an experimental spectrum, be it the reactive or the thermal one, to the simulation, it had to be multiplied by a factor.

This factor, g, which represents the deviation from the thermal equilibrium, is proportional to the inverse of the population in the experimental spectrum. That is, it

is large if a small population is present in the experimental spectrum and small if a large population is present.

The experimentally observed reactive population in a given spin-orbit manifold for a given rotational level N', can be expressed as the ratio of the population in the experimental reactive spectrum divided by the population in the experimental thermal spectrum and multiplied by the corresponding population in the thermal simulation at 298 K. Therefore the experimental spin-orbit ratio F_1/F_2 (N') can be expressed as

$$\frac{F_1}{F_2}(N') = \frac{F_1(N')(reactive) \times F_2(N')(thermal)}{F_1(N')(thermal) \times F_2(N')(reactive)} \times \frac{F_1}{F_2}(N')(Boltzmann, 298\,K)$$

equation (4.4)

Since the factor, g, derived from the analysis of the experimental spectra is inversely proportional to the population in the experimental spectra equation (4.4) transforms into

$$\frac{F_1}{F_2}(N') = \frac{g_{F_1(N')(thermal)} \times g_{F_2(N')(reactive)}}{g_{F_1(N')(reactive)} \times g_{F_2(N')(thermal)}} \times \frac{F_1}{F_2}(N')(Boltzmann, 298\,K)$$ equation (4.5)

The same line of argument holds for analysis of the spectra with respect to the relative population in the Λ-doublets of the nascent OH/OD product. As discussed in section 2.2.3.2 above, the Λ-doublets are an interaction between the orbital motion of the lone electron and the rotational motion of the nuclei. In the limit of high rotation they correspond to the half filled π-orbital being in the plane of rotation (A') or perpendicular to it (A''). The relative population in the two levels produced by the reaction, where A'(N') and A''(N') are the populations in each level in a given

rotational state, can be expressed as

$$\frac{A'}{A''}(N')=\frac{A'(N')(reactive)\times A''(N')(thermal)}{A'(N')(thermal)\times A''(N')(reactive)} \qquad \text{equation (4.6)}$$

The equivalent Boltzmann factor from equation (4.4) can be omitted from equation (4.6) because the relative ratio in a thermal sample is equal to unity to a very good approximation.

Since again the analysis of the spectra yielded only a factor, g, which is inversely proportional to the relative populations, equation (4.6) gets transformed in the same way as equation (4.4) above into

$$\frac{A'}{A''}(N')=\frac{g_{A'(N')(thermal)}\times g_{A''(N')(reactive)}}{g_{A'(N')(reactive)}\times g_{A''(N')(thermal)}} \qquad \text{equation (4.7)}$$

The data for the F_1/F_2 ratio for a given N' can be derived from the pairs Q_1/Q_2, R_1/R_2 and P_1/P_2, while the relative Λ-doublet ratio can be derived from the pairs R_1/Q_1, P_1/Q_1 in the F_1 spin-orbit manifold as well as R_2/Q_2 and P_2/Q_2 in the F_2 spin-orbit manifold. The quality of the Λ-doublet data depends crucially on the quality for the Q_1 and Q_2 values respectively. In the case of the Q_2 branch, the lines often blend on top of each other or other lines in the spectrum and the data are in general of much poorer quality. While optical saturation of the transitions has a strong effect on the relative intensity of branches which are compared for establishing the F_1/F_2 and Λ-doublet ratios, it is accounted for in the term containing the measured long time thermal ratio as in equations (4.5) and (4.7).

4.3.1.4 Estimation of vibrational branching

Establishing the vibrational branching ratio in the OH/OD product of the reaction of $O(^3P)$ with methane was not the main aim of this study. The experimental technique is not well suited for this task. However, since no experimental information on the vibrational branching ratio for the reactions of $O(^3P)$ with CH_4 and CD_4, (1.5) and (1.7) respectively, is known an attempt will be made to make an approximate estimate. Andresen and Luntz [14] established the branching ratios for the OH / OD products from the reactions of $O(^3P)$ with *cyclo*-C_6H_{12} and *cyclo*-C_6D_{12}, reactions (1.6) and (1.8), respectively.

Based on the relative signal-to-noise of the OH/OD A-X (2,1) and (1,0) LIF spectra an estimate of the vibrational branching can be carried out. In order to judge the vibrational branching in the OH/OD product of reactions (1.5-1.8) a specific signal-to-noise level for each reaction was established. Short LIF excitation scans over the R_1-branch of the OH/OD A-X (2,1) and (1,0) spectra were carried out.

For convenience the $R_1(1)$ line was chosen to be measured against the noise level. The area underneath the line was measured and divided by the width of the line that contributed significantly to the area. This number corresponds to an average signal intensity over the $R_1(1)$-line. It was compared with the scatter in the baseline around zero, in a region of the spectrum containing no lines, as measured by the standard deviation.

These numbers, specific signal-to-noise measurements for the $R_1(1)$ line only become useful information if compared to an independent measurement of the relative branching ratio for the pairs of reactions

$$O(^3P) + cyclo\text{-}C_6H_{12} \rightarrow OH\ X\ ^2\Pi_i\ (v'=0) + cyclo\text{-}C_6H_{11} \qquad \text{reaction (4.1)}$$

$$O(^3P) + cyclo\text{-}C_6H_{12} \rightarrow OH\ X\ ^2\Pi_i\ (v'=1) + cyclo\text{-}C_6H_{11} \qquad \text{reaction (4.2)}$$

and

$$O(^3P) + cyclo\text{-}C_6D_{12} \rightarrow OD\ X\ ^2\Pi_i\ (v'=0) + cyclo\text{-}C_6D_{11} \qquad \text{reaction (4.3)}$$

$$O(^3P) + cyclo\text{-}C_6D_{12} \rightarrow OD\ X\ ^2\Pi_i\ (v'=1) + cyclo\text{-}C_6D_{11} \qquad \text{reaction (4.4)}$$

Andresen and Luntz [14] proposed a ratio of 0.24 as value for the $OH(v'=1)/OH(v'=0)$ ratio from reactions (4.2) and (4.1) and for the reactions with deuterated cyclohexane, (4.4) and (4.3), the ratio $OD(v'=1)/OD\ (v'=0)$ was found to be 0.7.

Andresen and Luntz themselves were not too confident of these values. They caution against taking them too literally. The ratios of the specific signal-to-noise $OH(v'=1)_{SN}/OH(v'=0)_{SN}$ and $OD(v'=1)_{SN}/OD(v'=0)_{SN}$ measurements for *cyclo*-C_6H_{12} and *cyclo*-C_6D_{12} in this study differ from the values reported by Andresen and Luntz by a constant factor, f_{OH} and f_{OD} respectively. This factor takes into account all systematic differences but is independent of the nature of the hydrocarbon, i.e. if methane or cyclohexane is used. This can be expressed for cyclohexane as

$$\left[\frac{OH(v'=1)}{OH(v'=0)}\right]_{AL,C_6H_{12}} = f_{OH} \times \frac{OH(v'=1)_{SN,C_6H_{12}}}{OH(v'=0)_{SN,C_6H_{12}}} \qquad \text{equation (4.8)}$$

and accordingly for deuterated cyclohexane

$$\left[\frac{OD(v'=1)}{OD(v'=0)}\right]_{AL,C_6D_{12}} = f_{OD} \times \frac{OD(v'=1)_{SN,C_6D_{12}}}{OD(v'=0)_{SN,C_6D_{12}}} \qquad \text{equation (4.9)}$$

With the knowledge of the factors f_{OH} and f_{OD}, the observed signal-to-noise ratios for the reactions with methane can now be used to give an estimate of the vibrational branching OH(v'=1)/OH(v'=0) and OD(v'=1)/OD(v'=0) for these reactions:

$O(^3P) + CH_4 \rightarrow OH\ X\ ^2\Pi_i\ (v'=0) + CH_3$ reaction (4.5)

$O(^3P) + CH_4 \rightarrow OH\ X\ ^2\Pi_i\ (v'=1) + CH_3$ reaction (4.6)

$O(^3P) + CD_4 \rightarrow OD\ X\ ^2\Pi_i\ (v'=0) + CD_3$ reaction (4.7)

$O(^3P) + CD_4 \rightarrow OD\ X\ ^2\Pi_i\ (v'=1) + CD_3$ reaction (4.8)

Therefore, a vibrational branching for CH_4, reactions (4.6) over (4.5) can be calculated by

$$\left[\frac{OH(v'=1)}{OH(v'=0)}\right]_{CH_4} = f_{OH} \times \frac{OH(v'=1)_{SN,CH_4}}{OH(v'=0)_{SN,CH_4}} \qquad \text{equation (4.10)}$$

and accordingly for the CD_4 reactions (4.8) and (4.7) with

$$\left[\frac{OD(v'=1)}{OD(v'=0)}\right]_{CD_4} = f_{OD} \times \frac{OD(v'=1)_{SN,CD_4}}{OD(v'=0)_{SN,CD_4}} \qquad \text{equation (4.11)}$$

with the factors f_{OH} and f_{OD} given by equations (4.8) and (4.9), the normalisation of the signal-to-noise data for cyclohexane to the values of Andresen and Luntz [14].

4.3.2 Analysis of the IR pumping experiments

4.3.2.1 Estimation of vibrational enhancement

In case of the IR-pumping experiments two different kinds of information are of interest. The first one is how much reaction (1.5) gets enhanced by the vibrational excitation of the methane. It is very difficult to use LIF to obtain any absolute numbers, but it is possible to make a statement about an upper limit of relative enhancement for reaction (1.5) by vibrational excitation of methane.

It should be noted that only a small fraction of the CH_4 molecules present in the reaction chamber can be optically excited. This will be discussed in detail below.

The experimental observation will be the reaction of a sample of CH_4 molecules with a small fraction of vibrationally excited ones compared to a sample of CH_4 molecules with no significant vibrational excitation.

In the limit of short time after the initiation of the reaction the increase of the OH concentration can be described as a linear dependence on time. Therefore, both the reaction with vibrationally excited methane and the reaction with normal methane produce OH linearly, with a slightly steeper slope for the vibrationally enhanced reaction. The intercept of both lines at $\Delta t=0$ should coincide and would be zero if no photolytic background was present.

Since OH is formed by photolysis of the rogue H-containing impurity the intercept corresponds to the OH produced by photolysis. Under the assumption that this contribution remains constant over the period of time under investigation it can

be subtracted from the experimental values.

At any given time the OH production from the vibrationally enhanced reaction can then be compared to that of the normal reaction and a relative increase in reactivity obtained. This number is the basis of the estimate of the upper limit on the enhanced reactivity due to reaction (1.9). This is shown schematically in figure 4.6. Since the experimental conditions were not completely collision free the measurements were conducted by measuring the total integrated area under all transitions of the R_1-branch, mainly because it only covers a limited wavelength range. This method assumes that the detection sensitivity does not change dramatically with N' in a branch. This can be verified directly by comparing the long delay time spectrum with a thermal simulation.

4.3.2.2 Reactive rotational population

The second information of interest would be the nascent internal state distribution of OH as produced by the reaction of $O(^3P)$ with vibrationally excited CH_4 (ν_3, v=1), reaction (1.9). This requires essentially the same data analysis methods as discussed above. Again, only 3 sets of time delays were necessary.

The two short-delay times do not differ in the photolysis-probe delay, but in the firing of the IR pump laser which fires simultaneously with the photolysis laser at one delay, while being delayed behind the probe laser in the second delay. Since no sufficiently low product of pressure and time delay was achieved to observe nascent populations, no further discussion of the prospective data analysis is necessary.

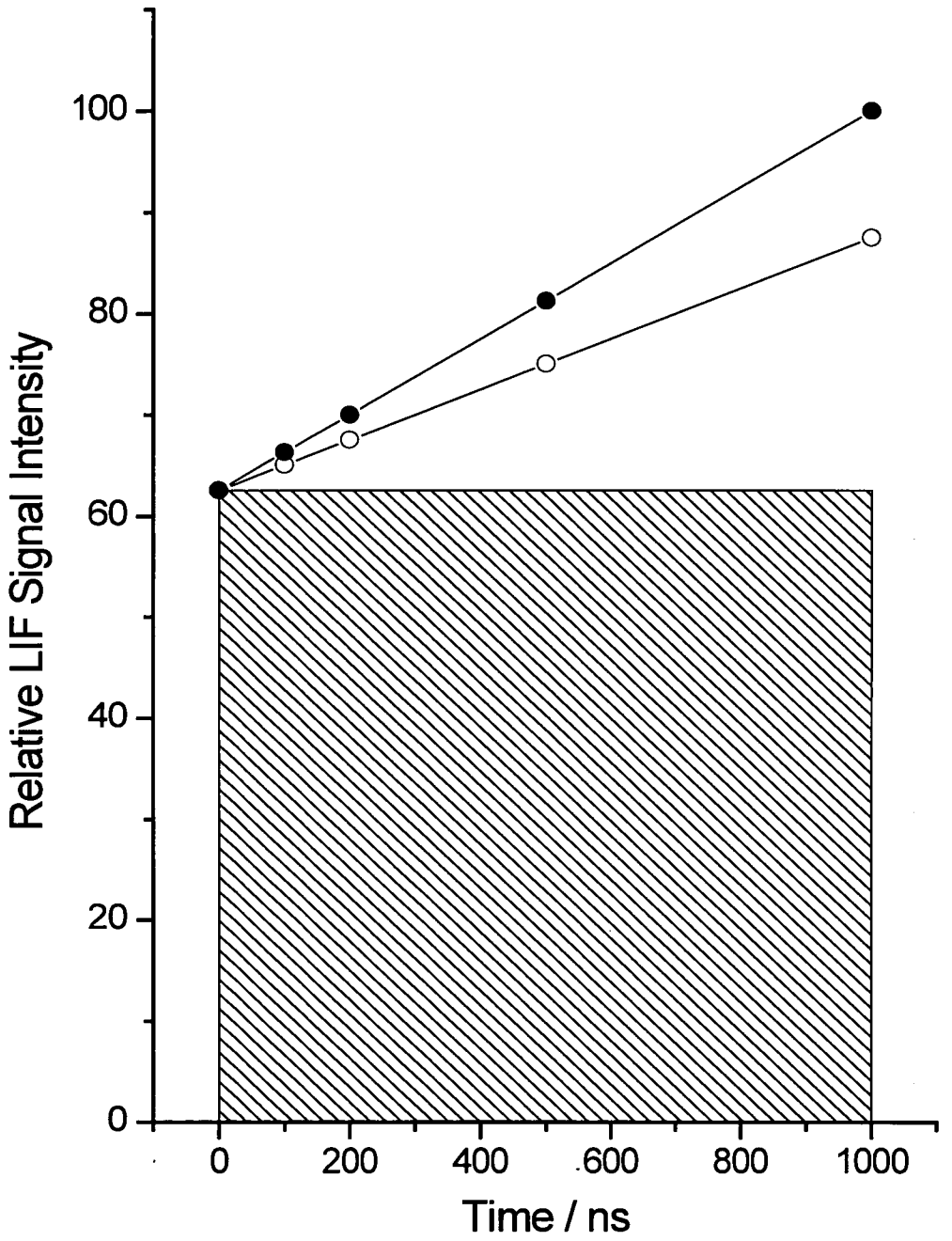

Figure 4.6: Schematic display of the vibrational enhancement of reaction (1.9). It is assumed that the reaction is observed in the linear regime and loss processes are not relevant on this timescale. The striped square represents the photolytic OH contribution by the rogue compound in NO_2. The open symbols represent OH produced by the non-pumped reaction while the solid symbols represent OH produced by the non-pumped reaction and the pumped reaction. The difference between these two lines represents the enhancement due to vibrational pumping of CH_4.

4.3.2.3 Establishing upper limits for detection

The existence of the product in question could not be established in all cases. Therefore, upper limits for production of the species are derived by comparing the signal, i.e. the area under the range of the line divided by the number of points to the level of noise on the baseline, measured by its standard deviation, as explained in the previous section. This establishes the minimum amount of product produced to be statistically significant above the noise and therefore to be observed by this experimental setup.

4.4 Calculation of the collision energy distribution

As mentioned in section 1.2, the reaction of $O(^3P)$ with saturated hydrocarbons is slow at room temperature which is mostly due to the significant barrier which has to be overcome in order to reach the product side.

McKendrick *et al.* [23] were able to observe the OH product of reaction (1.5) only by using a photolysis wavelength of 248 nm and 308 nm to photodissociate NO_2. They could not observe any reaction with photolysis of NO_2 at 337 nm, which indicates that the translational energy of the $O(^3P)$ atoms produced is not large enough to overcome the barrier at this photolysis wavelength. Therefore, photolysis of NO_2 at 266 nm was thought to produce sufficiently fast $O(^3P)$ atoms to react with CH_4.

So far, no measurements have been carried out to describe the translational product state distribution of the photolysis process of NO_2 at 266 nm. There have been studies at 248 nm [96,97], which were mostly concerned with the internal state distribution of the NO fragment. Once the energy disappearing into the vibration and rotation of the NO fragment is known, the total energy channelled into the translation of the products can be calculated. A mathematical formalism to treat the superthermal width of the energy spread was established some years ago for ion-molecule reactions [110] and adopted for hot atom-molecule reactions [17]. The spread in the collision energies is due to the relative thermal motion of the precursor and the molecular reactant.

This formalism treats the photoinitiated production and subsequent reaction of a reactant with another compound. The general scheme can be written as:

$AB + h\nu \rightarrow A + B$ reaction (4.9)

$A + C \rightarrow$ Products reaction (4.10)

or as used in this study

$NO_2 + h\nu \rightarrow O(^3P) + NO$ reaction (4.11)

$O(^3P) + RH \rightarrow R + OH$ reaction (1.3)

The distribution of collision energies, expressed as probability per unit energy, is given analytically by the equation

$$P(E_{coll})\,dE_{coll} = \left(\frac{m_{AB}^2 m_{AC}^2}{4\pi\, kT m_A m_B m_C m_{ABC} E_{exc}}\right)^{1/2} \times \left\{\exp\left[-\frac{m_{AB} m_{AC}}{m_A m_{ABC} kT} \times \left(\left(\frac{m_B m_C}{m_{AB} m_{AC}} \times E_{Exc}\right)^{1/2} - E_{coll}^{1/2}\right)^2\right] - \exp\left[-\frac{m_{AB} m_{AC}}{m_A m_{ABC} kT} \times \left(\left(\frac{m_B m_C}{m_{AB} m_{AC}} \times E_{Exc}\right)^{1/2} + E_{coll}^{1/2}\right)^2\right]\right\} dE_{coll} \quad \text{equation (4.12)}$$

where m_i is the mass of the atom / molecule i, E_{coll} is the collision energy, E_{exc} is the excess energy of the photolysis step, k is the Boltzmann constant and T is the temperature. The calculation is conveniently carried out in units of kT.

The last exponential term is small if the velocity of A is much larger than the usual thermal velocities of C. In order to estimate the excess energy the rovibronic states populated in the photolytic coproduct B have to be known or at least estimated.

For the purpose of this work, the closest measurement of the photolysis of NO_2 carried out so far was done by Dixon-Warren and coworkers [97]. This work is the basis of the following calculation. Due to the longer photolysis wavelength in this study, 266 nm instead of 248 nm, not all of the NO vibrational states are accessible observed by Dixon *et al.* [97]. The energy in the highest observed vibrational state (v'=8) is not available at 266 nm photolysis, provided only one photon is absorbed.

Therefore the NO vibrational distribution of reference [97] was cut off at the last possible energy and renormalised. For each vibrational level of NO the excess energy, E_{exc}, the difference between the photon energy at 266 nm and the energy of the vibrational level with an added average rotational energy was calculated. This excess energy was used to calculate the superthermal spread in the velocity distribution of equation (4.12).

It should be noted that the fastest $O(^3P)$ atoms are produced in conjunction with the lowest NO(v'=0) level. Since the distribution in reference [97] shows a strong peak at the lowest vibrational level a large fraction of fast $O(^3P)$ atoms can be expected. For the case that the strong peak at NO(v'=0) in reference [97] was an artefact of the measurement or simply not present at 266 nm a second distribution was calculated, assuming a smooth extrapolation of the higher v' values, to estimate the relative NO(v'=0) population. The calculated distributions are plotted in figure 4.7. The differences between the deuterated and non-deuterated hydrocarbons are small and most noticeable for methane, while negligible for cyclohexane.

The distributions, together with the thermodynamic attributes of the reactions (1.5)-(1.8) and the product state levels of interest are presented in figure 4.8. The alternative collision energy distribution is lacking the "bump" of the first one at high collision energies above the barrier and has only a "tail" instead.

Neither distribution has been experimentally confirmed, but the problems encountered by the work on reactions with methane, (1.5) and (1.7), especially the low OH/OD yields, may be an indication that a less excited, and therefore less useful distribution, in the context of this study, distribution than the one based on [97] is present.

It should be noted that the barrier heights displayed in figure 4.8 do not distinguish between the isotopes. The detailed barrier heights and energetics of the system are still a matter of debate and different values are quoted in the literature [7]. The possible maximum difference at the top of the barrier would mirror the difference in zero-point energy of C-H and C-D (which is less than 0.5 kJ mol^{-1} [75]).

A possible tunnelling contribution may also help to overcome the barrier, but is still matter of debate [46,48]. Whatever the outcome of this debate is going to be, it is obvious that only the fastest oxygen atom are actually able to react with methane. Beside its pictorial value, the collision energy distribution will be crucial to estimate the enhancement of reaction (1.9) with respect to (1.5) on the basis of theoretical predicted excitation functions, as described further below in section 5.6.3.1.

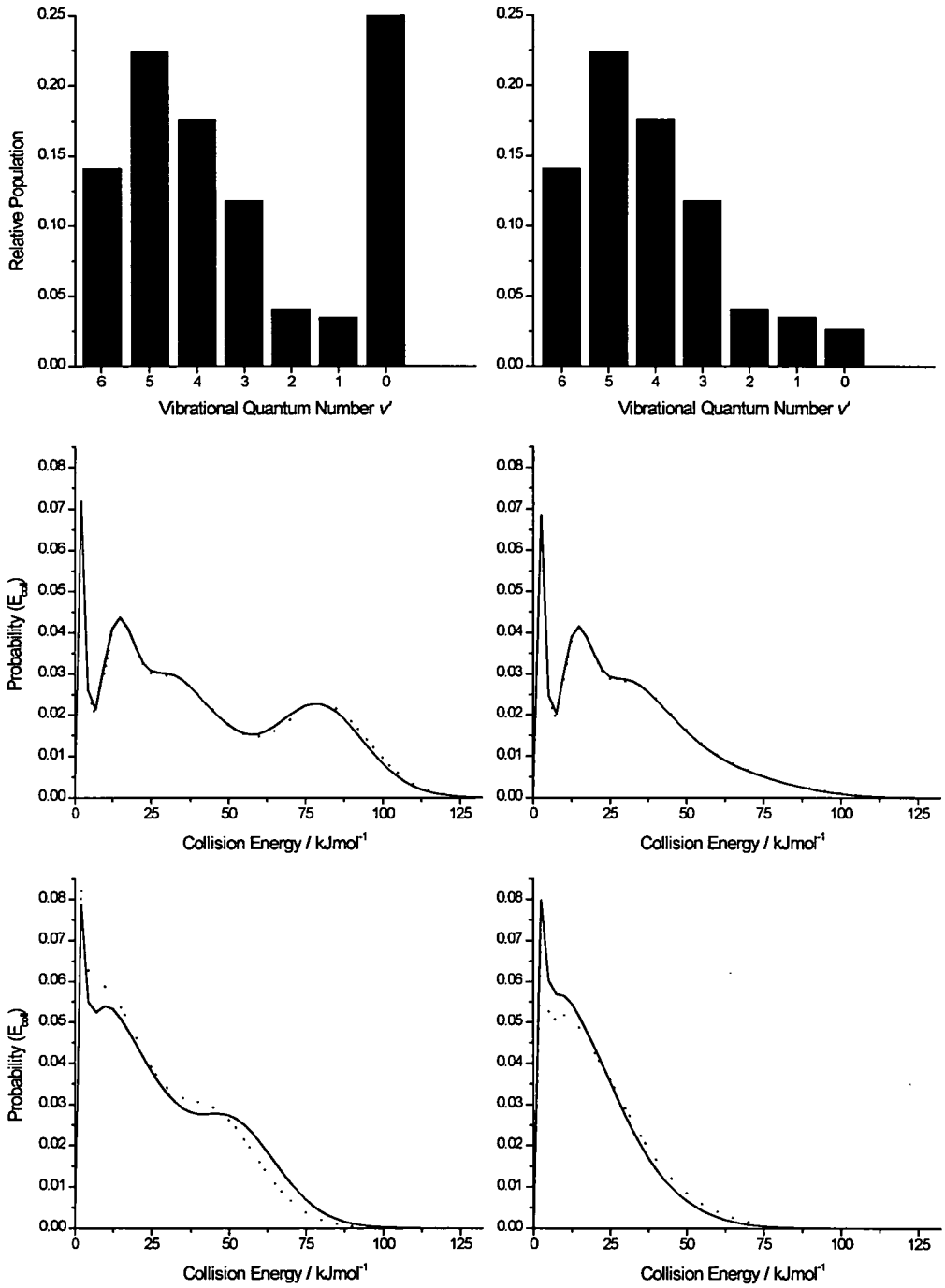

Figure 4.7: Distribution of collision energies as derived from NO internal state distribution from reference [97] (left upper panel) and adjusted as described in the main text (right upper panel). Note that the graphs are plotted with decreasing v' to emphasise its role in E_{coll}. The centre panels shows E_{coll} for *cyclo*-C_6H_{12} (dashed line) and *cyclo*-C_6D_{12} (solid line). The lower panel shows E_{coll} for CH_4 and CD_4 accordingly.

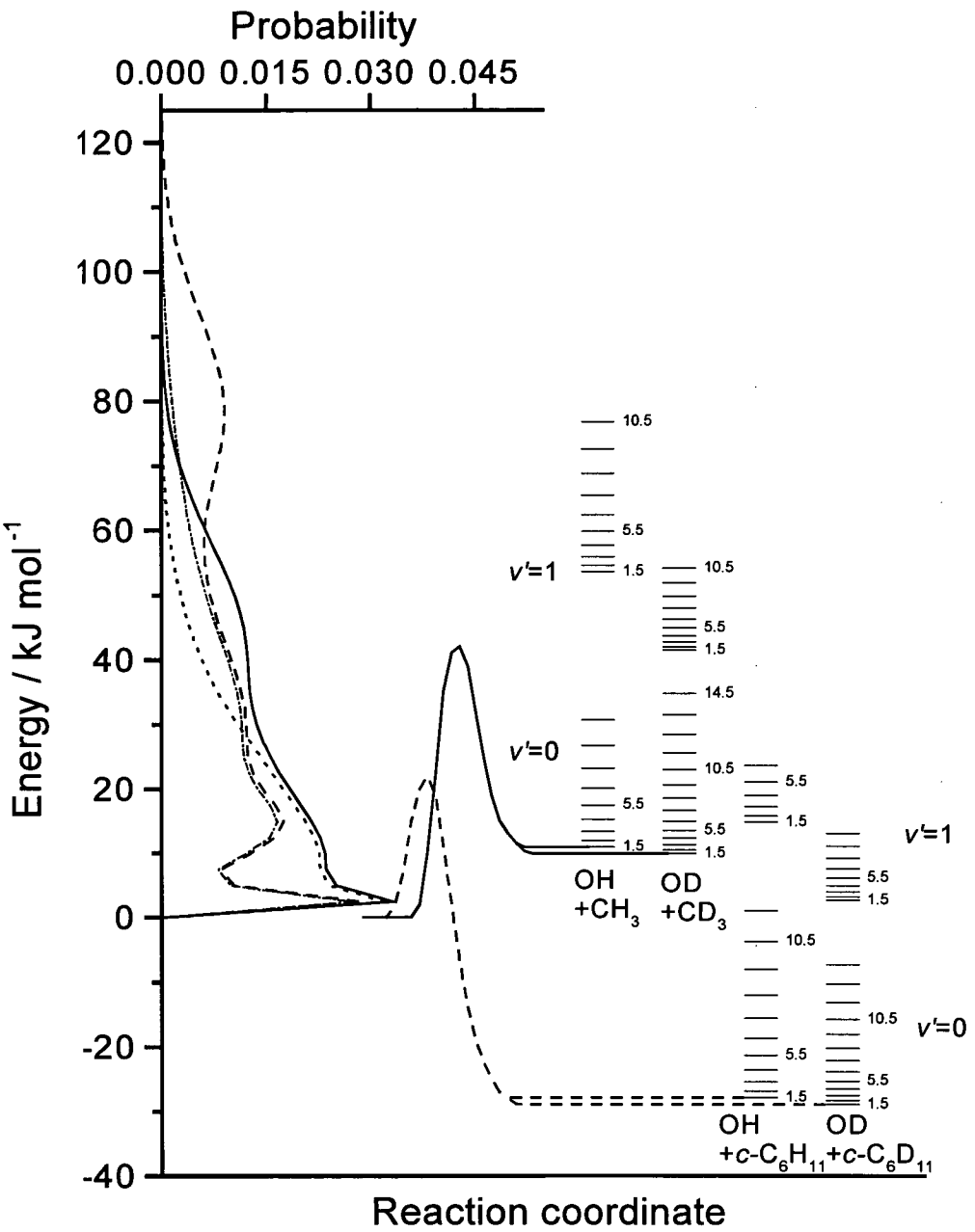

Figure 4.8: Reaction energetics of the reactions $O(^3P)$+RH/RD. The dashed lines belong to cyclohexane, the solid lines to methane with respect to the reaction coordinate along the minimum energy path. Indicated are only the energies of the $F_1(N')$ levels of the OH/OD product. Λ-doublet splittings are omitted. The distributions of collision energies are associated with the top axis assuming distribution derived from reference [97] for CH_4 (solid line) and *cyclo*-C_6H_{12} (dashed line) Distribution assuming a smooth progression to the NO(v'=0) level in the photolysis of NO_2, as explained in the main text are given for methane (dotted line), cyclohexane (dash-dotted line).

4.5 Observed internal state distribution in OH and OD reaction products in the bulk LIF experiments

4.5.1 Rotational distributions

4.5.1.1 General remarks

The rotational product state distributions of the OH and OD(v'=0) and (v'=1) products were measured for the reactions of methane and cyclohexane below.

$O(^3P) + cyclo\text{-}C_6H_{12} \rightarrow OH\ X\ ^2\Pi_i\ (v'=0) + cyclo\text{-}C_6H_{11}$ reaction (4.1)

$O(^3P) + cyclo\text{-}C_6H_{12} \rightarrow OH\ X\ ^2\Pi_i\ (v'=1) + cyclo\text{-}C_6H_{11}$ reaction (4.2)

$O(^3P) + cyclo\text{-}C_6D_{12} \rightarrow OD\ X\ ^2\Pi_i\ (v'=0) + cyclo\text{-}C_6D_{11}$ reaction (4.3)

$O(^3P) + cyclo\text{-}C_6D_{12} \rightarrow OD\ X\ ^2\Pi_i\ (v'=1) + cyclo\text{-}C_6D_{11}$ reaction (4.4)

$O(^3P) + CH_4 \rightarrow OH\ X\ ^2\Pi_i\ (v'=0) + CH_3$ reaction (4.5)

$O(^3P) + CD_4 \rightarrow OD\ X\ ^2\Pi_i\ (v'=0) + CD_3$ reaction (4.7)

No rotational OH/OD(v'=1) product state distributions for the reactions with methane

$O(^3P) + CH_4 \rightarrow OH\ X\ ^2\Pi_i\ (v'=1) + CH_3$ reaction (4.6)

$O(^3P) + CD_4 \rightarrow OD\ X\ ^2\Pi_i\ (v'=1) + CD_3$ reaction (4.8)

could be determined

4.5.1.2 Rotational distribution of the OH product

The rotational distribution in the OH fragment has been derived for OH(v'=0) for $O(^3P) + CH_4/cyclo\text{-}C_6H_{12}$ and OH(v'=1) for $O(^3P) + cyclo\text{-}C_6H_{12}$, following the procedures in section 4.3.1.2. The results are shown below in figure 4.9 for the F_1 (upper panel) and for the F_2 (lower panel) spin-orbit manifold. It can clearly be seen that the data in the F_1 spin-orbit manifold shows less scatter. In general at least two

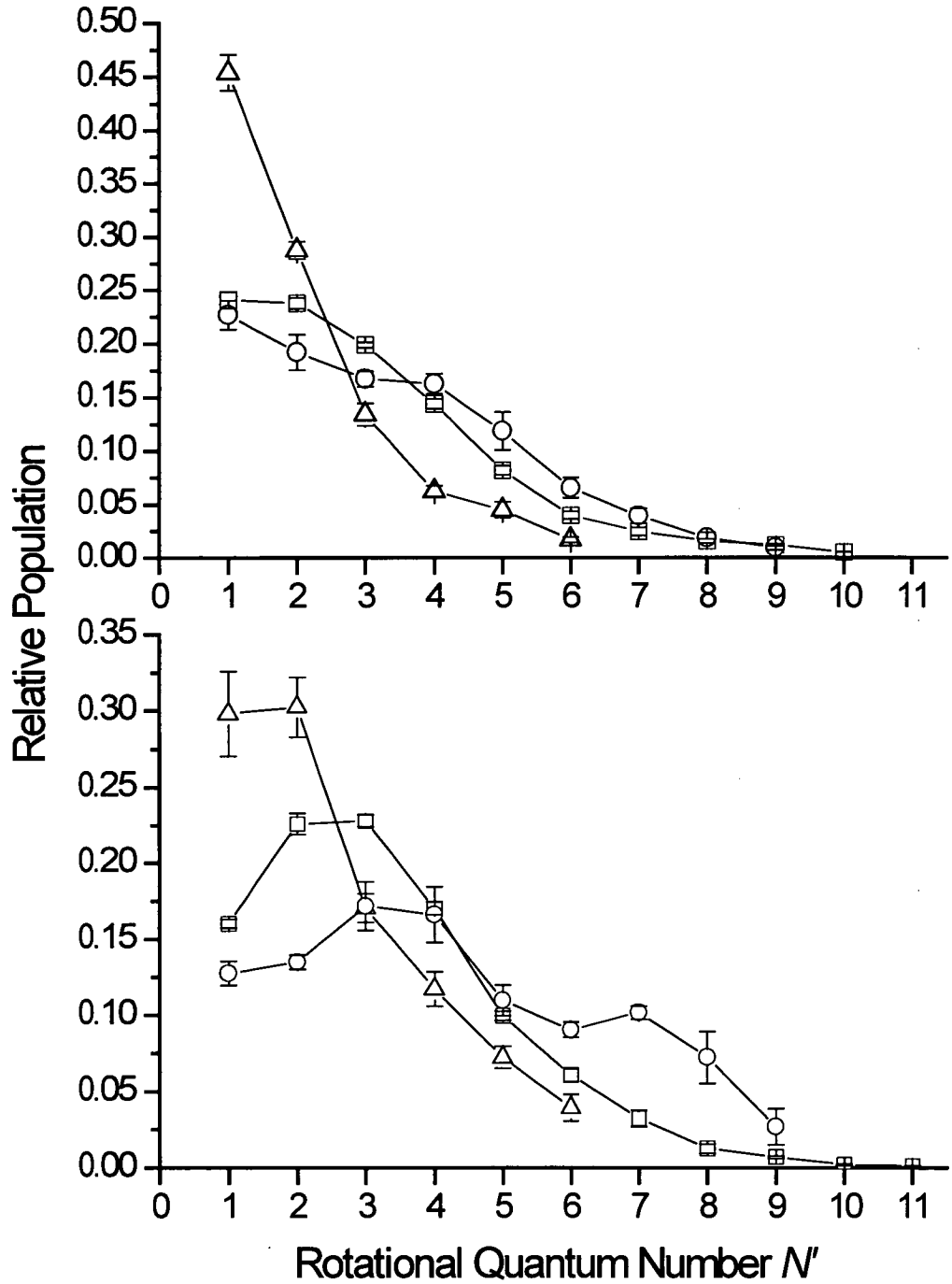

Figure 4.9: Rotational population distribution of the OH product in the F_1 (upper panel) and F_2 (lower panel) spin-orbit manifold. The open circles represent the OH(v'=0) product state distribution for the reactions with CH_4. The squares and the triangles are the OH(v'=0) and OH(v'=1) product state distributions for the reaction with *cyclo*-C_6H_{12}, respectively. The error bars represent one standard error of the mean.

separate branches could be used for a given N' to determine its population, while the branches in the F_2 manifold have a lot of blended lines and the data are therefore less reliable. The "coldest" distribution is observed for OH (v'=1) from O(^{3}P) + *cyclo*-C_6H_{12} while the OH(v'=0) product from the same reaction is "hotter" with CH_4 producing the "hottest" distribution.

4.5.1.3 Rotational distribution of the OD product

The rotational distributions for the OD products have been measured for the first time for reactions (4.3) and (4.4) as well as (4.7). They show the same trends as the respective OH products. It should be noted that the rotational constant of OD is roughly half the value of OH. The observed results are presented in figure 4.10 for the F_1 (upper panel) and F_2 (lower panel) spin-orbit manifold respectively. As before the data in the F_2 spin-orbit manifold is much less reliable for the same reasons as above.

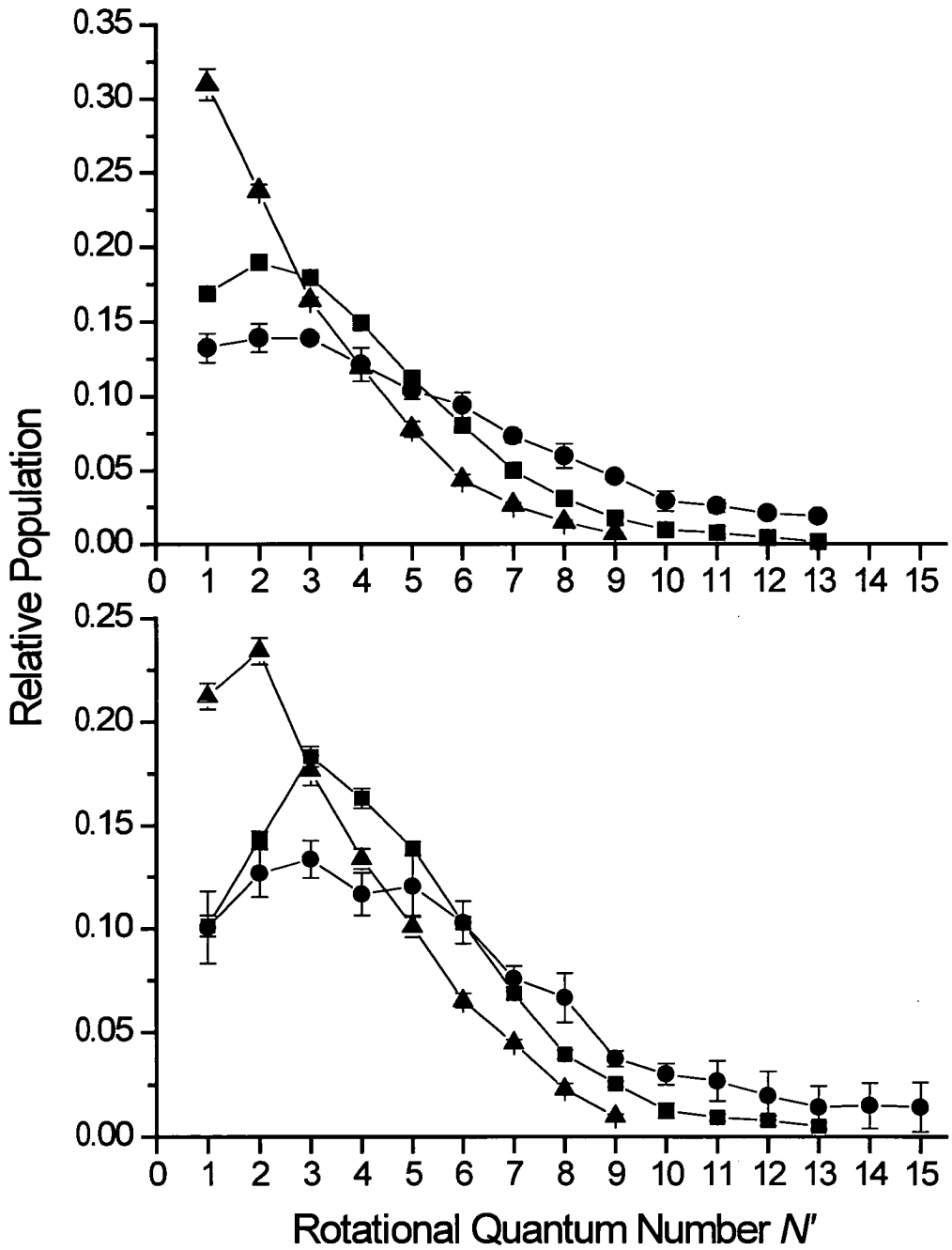

Figure 4.10: Rotational population distribution of the OD product in the F_1 (upper panel) and F_2 (lower panel) spin-orbit manifold. The solid circles represent the OD(v'=0) product state distribution for the reactions with CD_4. The squares and the triangles are the OD(v'=0) and OD(v'=1) product state distributions for the reaction with *cyclo*-C_6D_{12}, respectively. The error bars represent one standard error of the mean.

4.5.1.4 Calculation of rotational temperatures for the OH / OD products

A "temperature" can be assigned to the observed rotational distributions. The concept of temperature is not strictly valid for a reactive product since reactions tend to be a microcanonical ensemble rather than a canonical ensemble. That is reactions are controlled by having a fixed amount of energy available rather than an average energy. While a canonical ensemble can be described in terms of temperature a corresponding term does not exist for a microcanonical ensemble. A microcanonical ensemble can be statistical and described by surprisal analysis which will be explained in more detail below.

Nevertheless it can be of interest to assign a "temperature" in order to have a single, overall number to describe the amount of energy in the degree of freedom of interest. A temperature in a canonical ensemble is able to describe the various properties completely, especially it is able to describe the rotational distributions as well as the F_1/F_2 ratios for each possible rotational quantum state.

It should be noted that equal population of all degenerate m_J' states, which is implicit in the concept of a temperature, is not necessarily valid for reactive products. For example, an abstraction-type reaction may create a specific alignment of the product which may favour some m_J' states over others.

Rotational temperatures are usually derived in two different fashions. It is possible to make a Boltzmann plot, i.e. to plot the logarithm of the population

divided by degeneracy against the energy of the levels involved. In case of a proper temperature this method produces a straight line with a slope of $-1/kT$. If applied to a non-canonical ensemble this graph does not necessarily resemble a straight line. Nevertheless a linear fit could be carried out and the temperature is given by the negative of the slope of the line divided by the Boltzmann constant k. A typical result for some of the measured data is shown in figure 4.11.

The average energy, if equipartition of energy is observed, in rotation for linear rotor is given by kT, corresponding to the two degrees of freedom in rotation. Therefore, another possibility is to determine the "temperature" in the rotational motion is to equate kT to the sum of the populated energy levels multiplied by their relative populations.

$$kT = \sum_{N'=1}^{\infty} e_{N'} pop(N') \qquad \text{equation (4.13)}$$

The advantage of this method is that it produces a meaningful result even if the Boltzmann plot would show a strong curvature. The results of this calculation are shown in table 4.2. It can be seen that the amount of energy channelled into rotation of the OH / OD product as well as the derived temperatures are very similar for the deuterated and non-deuterated versions of both reactions.

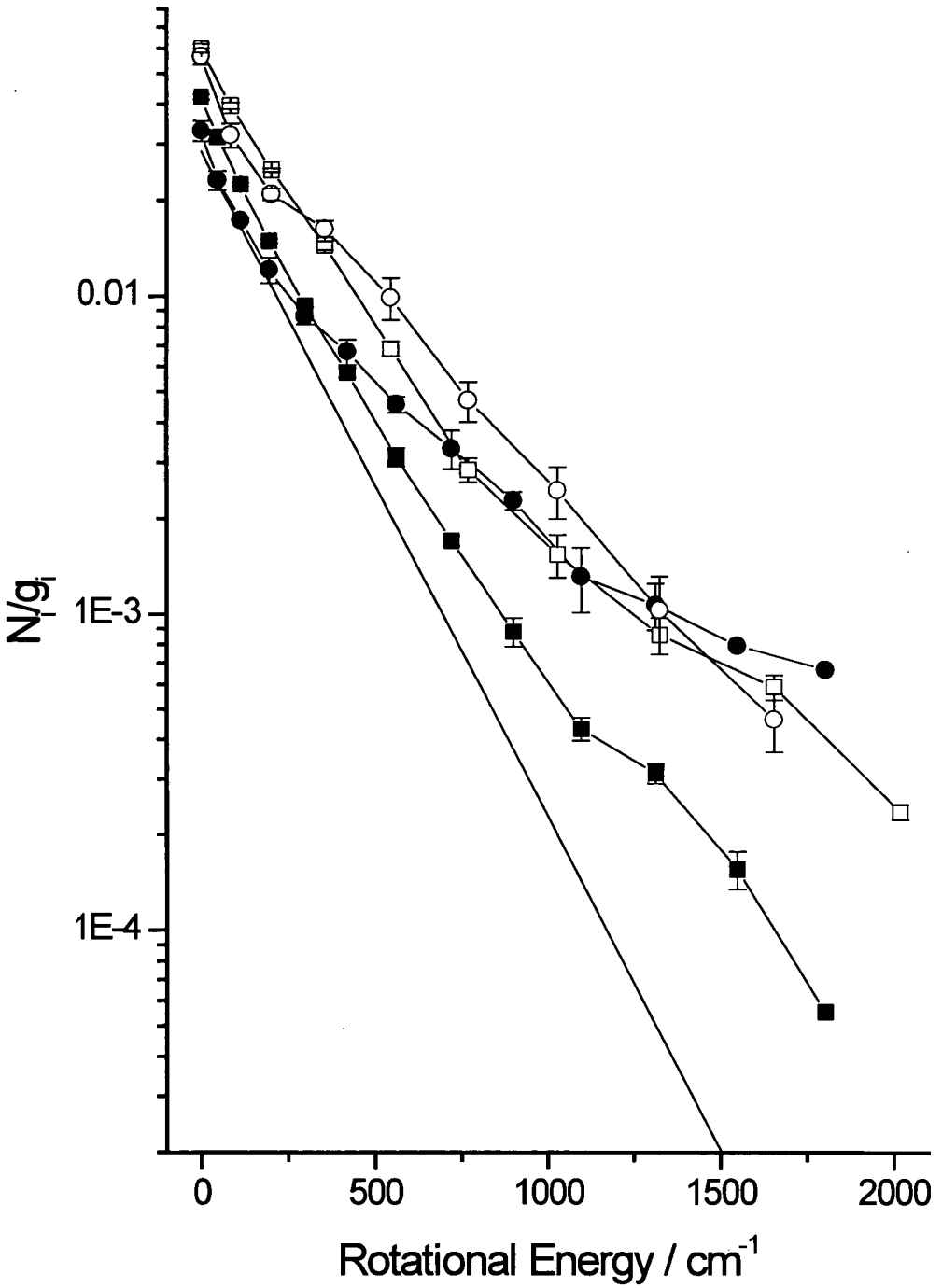

Figure 4.11: Boltzmann plot of the F_1 manifold OH/OD (v'=0) produced by reaction of $O(^3P)$ with *cyclo*-C_6H_{12} (open squares), *cyclo*-C_6D_{12} (solid squares), CH_4, and CD_4 (open and solid circles respectively). The black line denotes where a sample at room temperature (298 K) would lie.

Reaction	*average energy in rotation / cm^{-1}*	*"Temperature" of the OH / OD-product / K*
$O(^3P) + CH_4 \rightarrow OH(v'=0) + CH_3$	>323±32	>464±47
$O(^3P) + CD_4 \rightarrow OD(v'=0) + CD_3$	>391±46	>563±67
$O(^3P) + cyclo\text{-}C_6H_{12} \rightarrow OH(v'=0) + cyclo\text{-}C_6H_{11}$	261±12	376±17
$O(^3P) + cyclo\text{-}C_6H_{12} \rightarrow OH(v'=1) + cyclo\text{-}C_6H_{11}$	137±12	197±18
$O(^3P) + cyclo\text{-}C_6D_{12} \rightarrow OD(v'=0) + cyclo\text{-}C_6D_{11}$	241±8	347±12
$O(^3P) + cyclo\text{-}C_6D_{12} \rightarrow OD(v'=1) + cyclo\text{-}C_6D_{11}$	139±5	199±7

Table 4.2: Measured average energy in rotation and derived "temperatures" for the reactions of $O(^3P)$ + RH. The error represents two standard errors of the mean. The "larger than" sign takes account of the fact that for the methane reactions very high N' lines might be populated but were not treated in the analysis. This error will be larger for CH_4 because the lines tend to be spaced further apart and the high lines in the R_1-branch blend with the low lines in the Q_1-branch.

4.5.1.5 Prior distributions for the OH / OD product rotational distribution

Applying the concept of temperature to a microcanonical ensemble is, not surprisingly, unsatisfactory. Another tool for analysing a state distribution is given by surprisal analysis. The main idea is to calculate a statistical prior distribution for a fixed total energy, which populates the internal quantum states in accordance with their degeneracy and takes the translational density of states into account which absorbs the rest of the energy.

These rotational distributions tend to rise quickly at low rotational energy and fall very sharply close to the total available energy. The prior distributions correspond to the maximum entropy of the system under consideration, which in turn means a statistical distribution in phase space.

The rotational prior distribution P^0 in a given vibronic state of a product formed in conjunction with a structureless partner is given by the following expression

$$P^0 \propto (2j'+1)(E_{avail}-E_{j'})^{1/2} \qquad \text{Equation (4.14)}$$

with j' being the rotational quantum number, $E_{j'}$ the energy of the rotational quantum state in question, and E_{avail} the total available energy. This distribution is usually calculated as a function of the reduced rotational energy, g_{rot}, defined by the ratio of the energy of the rotational quantum state and the total available energy.

$$g_{rot}=\frac{E_{j'}}{E_{avail}} \qquad \text{Equation (4.15)}$$

The resulting distribution is than compared with the measured distribution and the so-called suprisal I can be calculated as the negative natural logarithm of the ratio of the experimental distribution over the calculated prior distribution

$$I(g_{rot})=-\ln\left(\frac{P^{exp}}{P^0}\right) \qquad \text{Equation (4.16)}$$

If the surprisal $I(g_{rot})$ is plotted against the reduced rotational energy it is often found to produce a straight line which would have a slope of 0 if the experimental distribution would be purely statistical.

The slope of the line is proportional to its deviation from the statistical limit. A positive slope indicates a "colder" distribution than the calculated prior, while a negative slope indicates "hotter", e.g. an inverted distribution. The larger the deviation of the slope from the value 0, the more "surprising" the result is in a purely statistical sense.

The main problem in this calculation is the choice of E_{avail}. Each value of E_{avail} could also be derived by different possible combinations in the energy distribution of the other fragment, translational and internal, which in turn would have to be weighted by their own degeneracy. In principle it would require detailed knowledge of the internal energetic structure and translation of the other fragment. At this point no knowledge with the necessary precision is available. Therefore, no attempt was made to include the internal energies of the co-fragment and it was treated as a structureless particle.

In addition, there is no well defined total energy in this experimental approach. As explained above in section 4.4, the distribution of collision energies is rather ill-defined.

The reactions under investigation are not expected to form any sort of long-lived complex which would give some indication of the possibility of unrestricted expansion into the available phase-space.

The surprisal analysis has been carried out for the reactions in this study and a typical result can be seen in figure 4.12. Mathematically, the result means that the observed rotational distributions are much "colder" than a statistical distribution would predict. The slope for the rotational distribution of the OD(v'=0) product from reaction (4.3) has a value of 17.3±0.6. This is physically and chemically rather unsurprising as will be discussed in the next chapter.

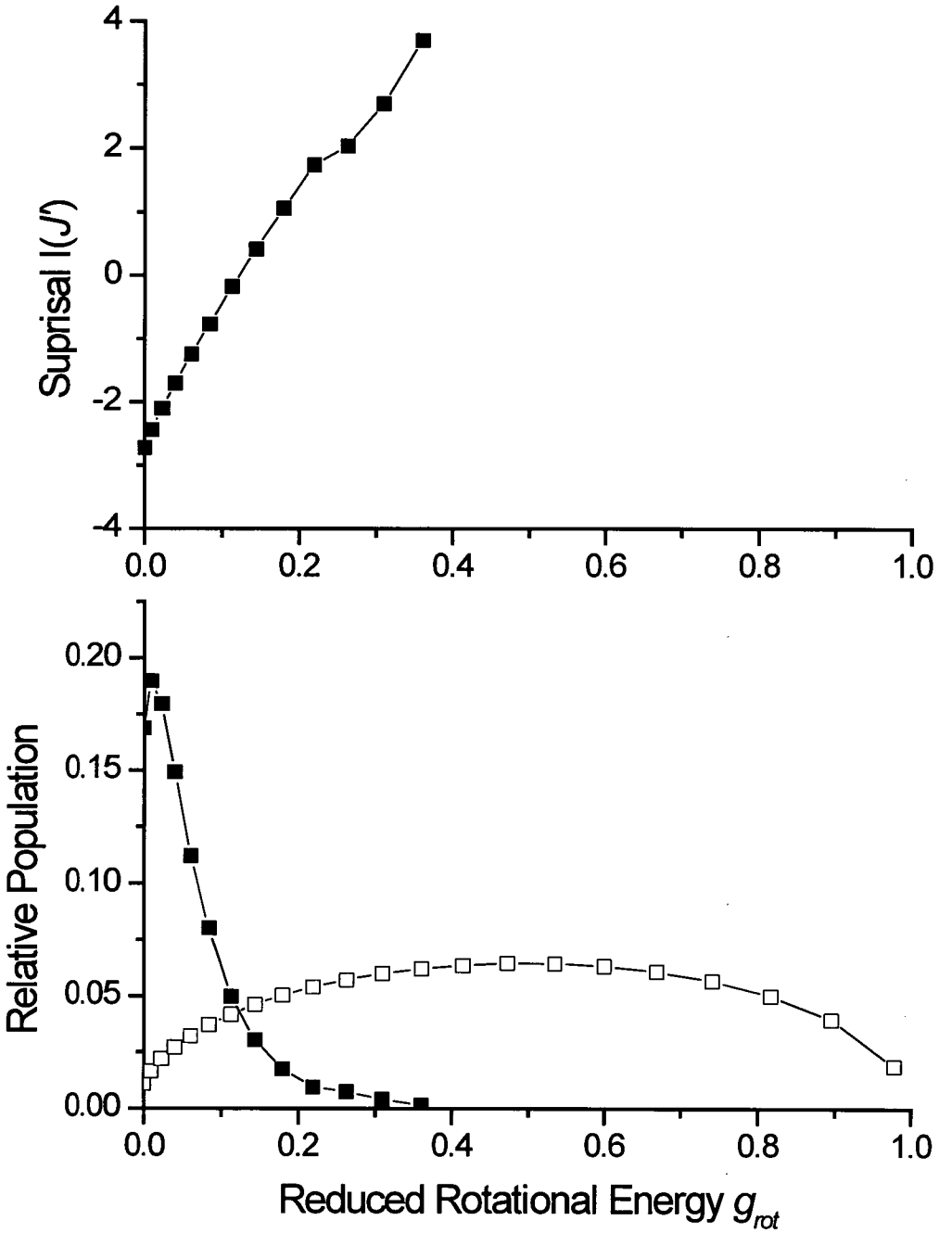

Figure 4.12: Surprisal plot (upper panel) and predicted prior distribution (open squares), assuming a structureless co-fragment and E_{avail}= 60 kJ mol^{-1} and observed distribution (solid squares) of rotational population of OD(v'=0) in the F_1 spin-orbit manifold from reaction (4.3) (lower panel). The slope of the surprisal is 17.3±0.6.

The suprisal analysis produces a boolean answer, i.e. the system behaves statistically or not. It is only a mathematical formalism and in case of a negative answer does not provide any more insight into the mechanism of the reaction. It is therefore of very limited use for the systems in the present investigation, especially since the lack of information about the behaviour of the organic coproduct would make it irresponsible to conclude too much from it.

4.5.1.6 Rotational distributions as function of rotational energy

While the representation of the rotational distribution as a function of the rotational quantum number, N', is the most common and used in figures 4.9 and 4.10, for a comparison between OH and OD this method is only of limited use.

Since the moments of inertia are different, the rotational distribution for a given average energy produces different envelopes. At a given specific energy the degeneracies of the OH and OD are different, quite apart from the fact that rotational states do not lie at the same energy.

The data from figures 4.9 and 4.10 can be replotted as a function of rotational energy. This is shown in figures 4.13 and 4.14. It can be seen that the data for a set of deuterated and non-deuterated hydrocarbons fall very well on top of each other.

This strongly indicates, that, together with the very similar calculated "temperatures" from the previous section, the amount of energy channelled into rotation of the hydroxyl product is independent of the isotope involved. This result is reported here for the first time. Its implications are a significant support for the abstraction mechanism as will be discussed below.

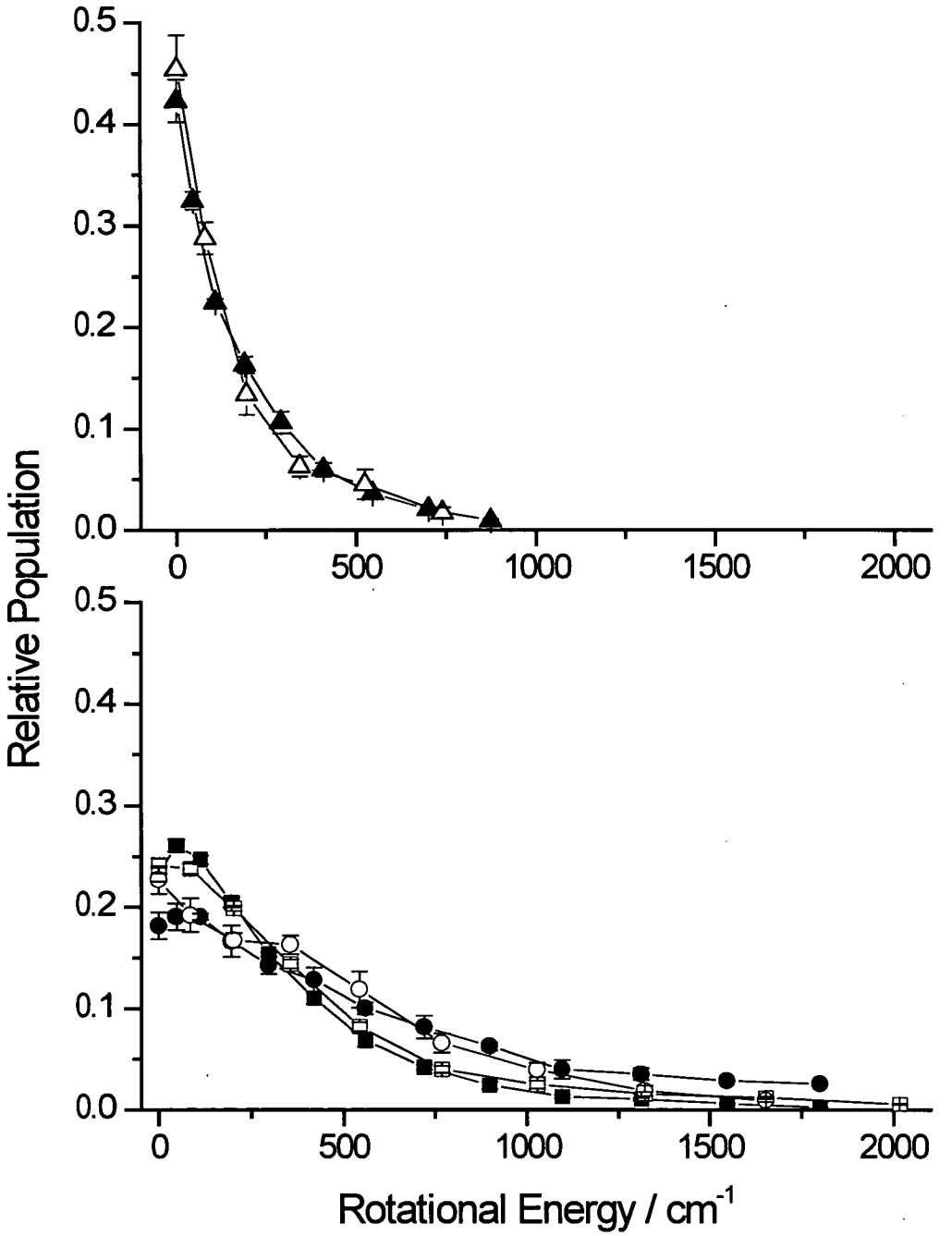

Figure 4.13: Observed rotational distributions of the F_1 manifold plotted as function of rotational energy. Symbols are the same as in figures 4.9 and 4.10. Solid symbols represent the deuterated hydrocarbon, open symbols the non-deuterated ones. Error bars are one standard errors of the mean. Normalised to the same total sum of energy.

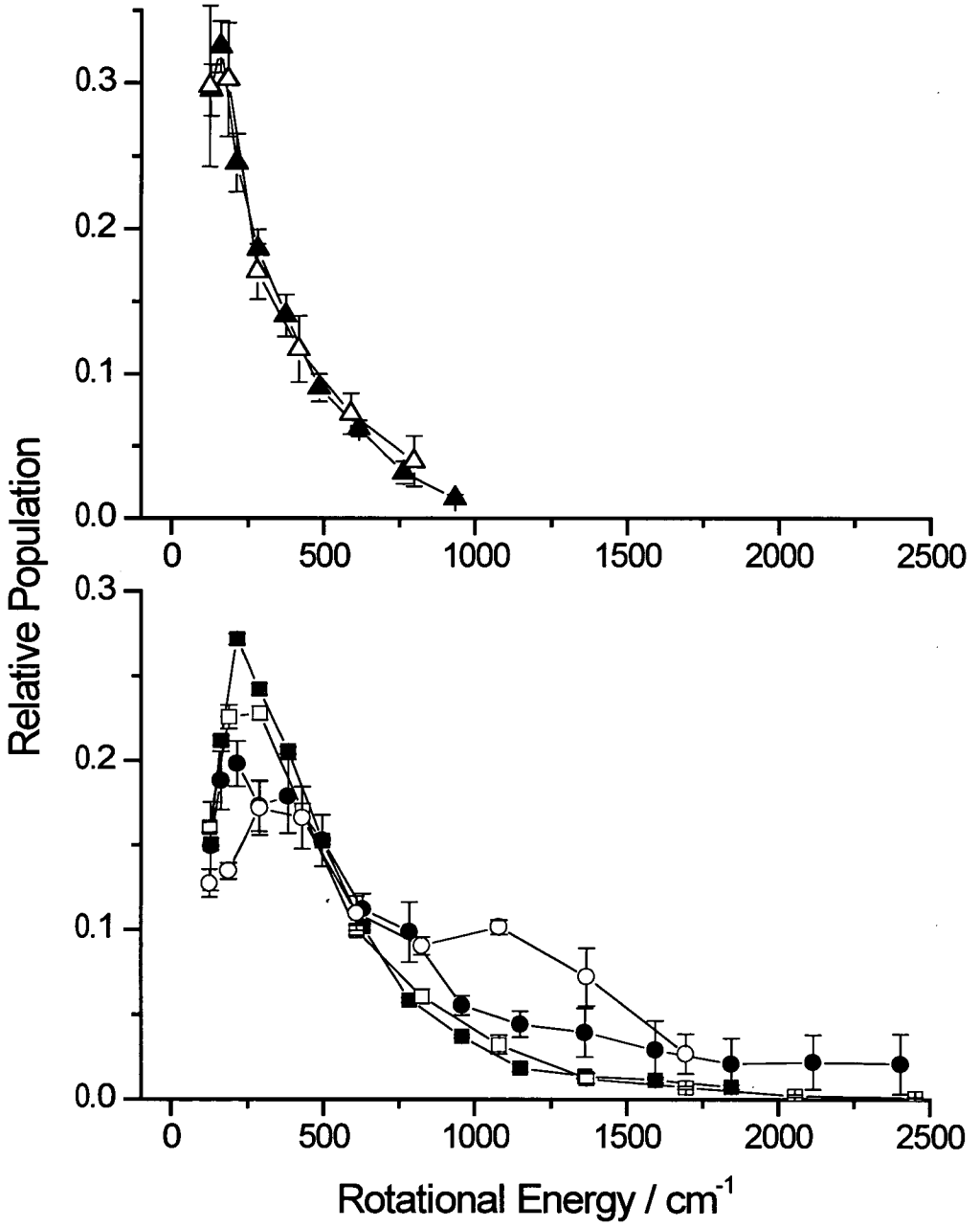

Figure 4.14: Observed rotational distributions of the F_2 manifold plotted as function of rotational energy. Symbols are the same as in figures 4.9 and 4.3. Solid symbols represent the deuterated hydrocarbon, open symbols the non-deuterated ones. Error bars are one standard error of the mean. Normalised to the same total sum of energy.

4.5.2 F_1/F_2 Spin-orbit manifold distribution

The spin-orbit fine structure distribution for the OH/OD products was measured for the same set of reactions for which rotational distribution were derived, reactions (4.1)-(4.5) and (4.7). The data derived for OH/OD(v'=0) from CH_4 and CD_4 products tend to be much noisier. The collected unprocessed results are shown in figure 4.15.

The degeneracy, g, of a given rotational level N' is depends on the spin-orbit manifold and is given as

$$g_{F_1}(N')=(2J'+1)=2N'+2 \qquad \text{(Equation 4.17)}$$

$$g_{F_2}(N')=(2J'+1)=2N' \qquad \text{(Equation 4.18)}$$

for the F_1 and F_2 spin-orbit manifold, respectively. To compare data with the same value of N' the different degeneracies have to be taken into account. This is done on the assumption that the rotational levels are populated according to their spatial degeneracy, i.e. all m_J' levels for a given J' level are equally populated. To account for the different degeneracy in the spin-orbit manifolds the F_1/F_2 ratio has to be adjusted by a correction factor, F_{corr}, to discover any underlying preference. F_{corr} is simply defined by

$$F_{corr}=\frac{N'}{N'+1} \qquad \text{(Equation 4.19)}$$

where N' is the quantum number of the specific rotational quantum state in question.

The same F_1/F_2 data are therefore presented again in figure 4.16 (upper panel), except having been multiplied by F_{corr}. The lower panel shows the same data with the widely scattered methane data removed.

The resulting limiting values for the lowest rotational state N'=1 are given in table 4.3 for the various reactions under investigation.

RH / Product	*CH_4*	*cyclo-C_6H_{12}*	*CD_4*	*cyclo-C_6D_{12}*
OH(v'=0)	2.14±0.32	1.50±0.10		
OH(v'=1)		1.48±0.35		
OD(v'=0)			1.33±0.31	1.36±0.09
OD(v'=1)				1.66±0.12

Table 4.3: Derived values for the F_1/F_2 ratio for N'=1. The error is one standard error of the mean.

The weighted mean of these measurements is given as 1.53±0.17. A more detailed discussion of this result will follow in conjunction with a detailed discussion of various models for spin-orbit branching in the next section 5.2.

4.5.2.1 Λ-doublet distribution

The measured results for the ratio of populations in the A' and A'' states for the OH/OD products from reactions (4.1)-(4.5) and (4.7) are shown in figure 4.17. Only the results in the F_1 manifold are displayed. The results in the F_2 manifold show the same behaviour, but are generally of poorer quality due to blending of lines in the region of the Q_2-branch. The results for all reactions scatter around unity and no significant preference can be observed.

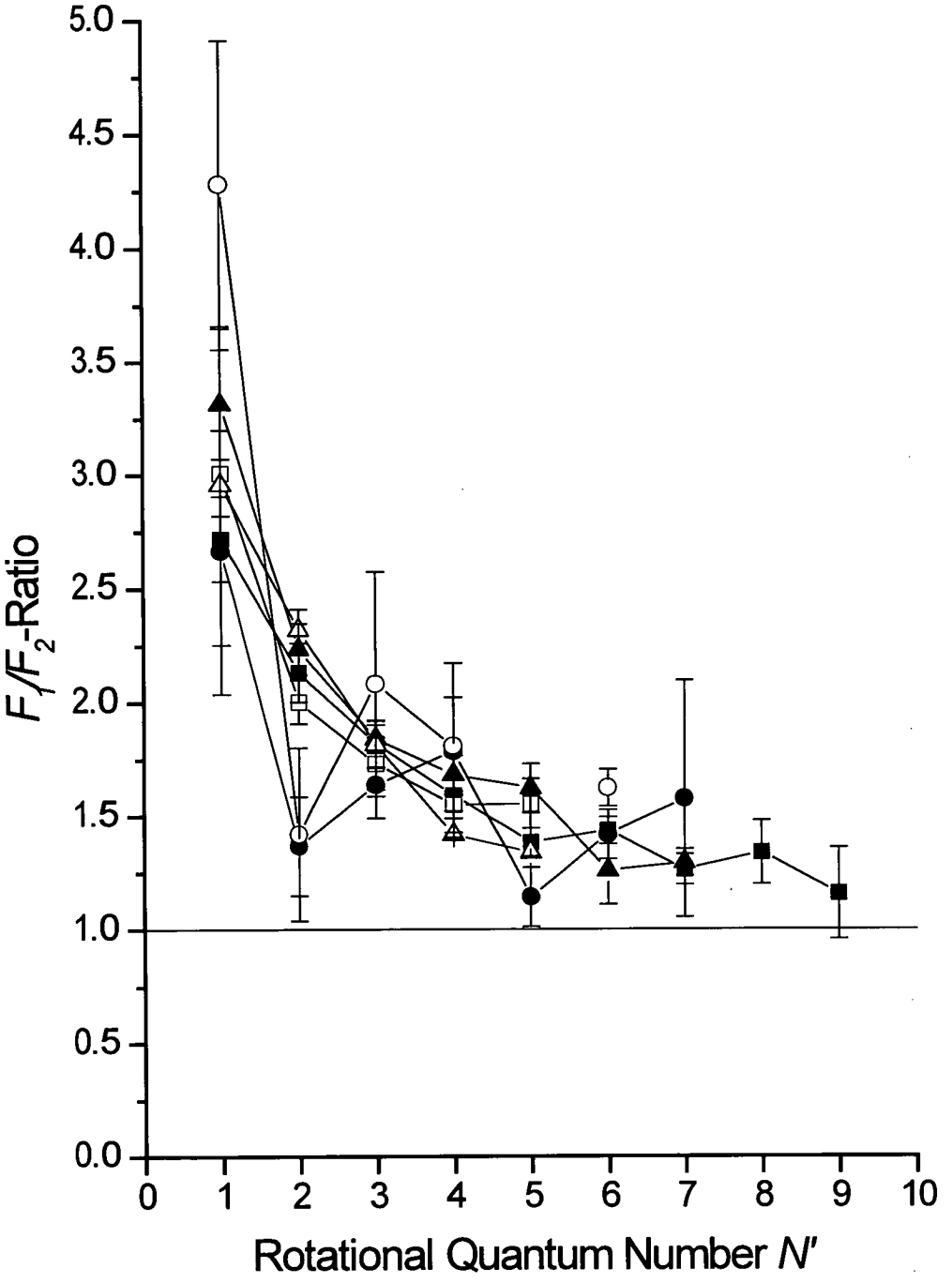

Figure 4.15: Measured F_1/F_2 ratios as a function of N'. Solid symbols represent OD data, open symbols OH data. Methane and cyclohexane, producing OH/OD(v'=0) are represented by circles and squares, respectively. The vibrationally excited OH/OD(v'=1) from the reaction with cyclohexane is shown by the triangular symbols. Error bars represent one error of the mean.

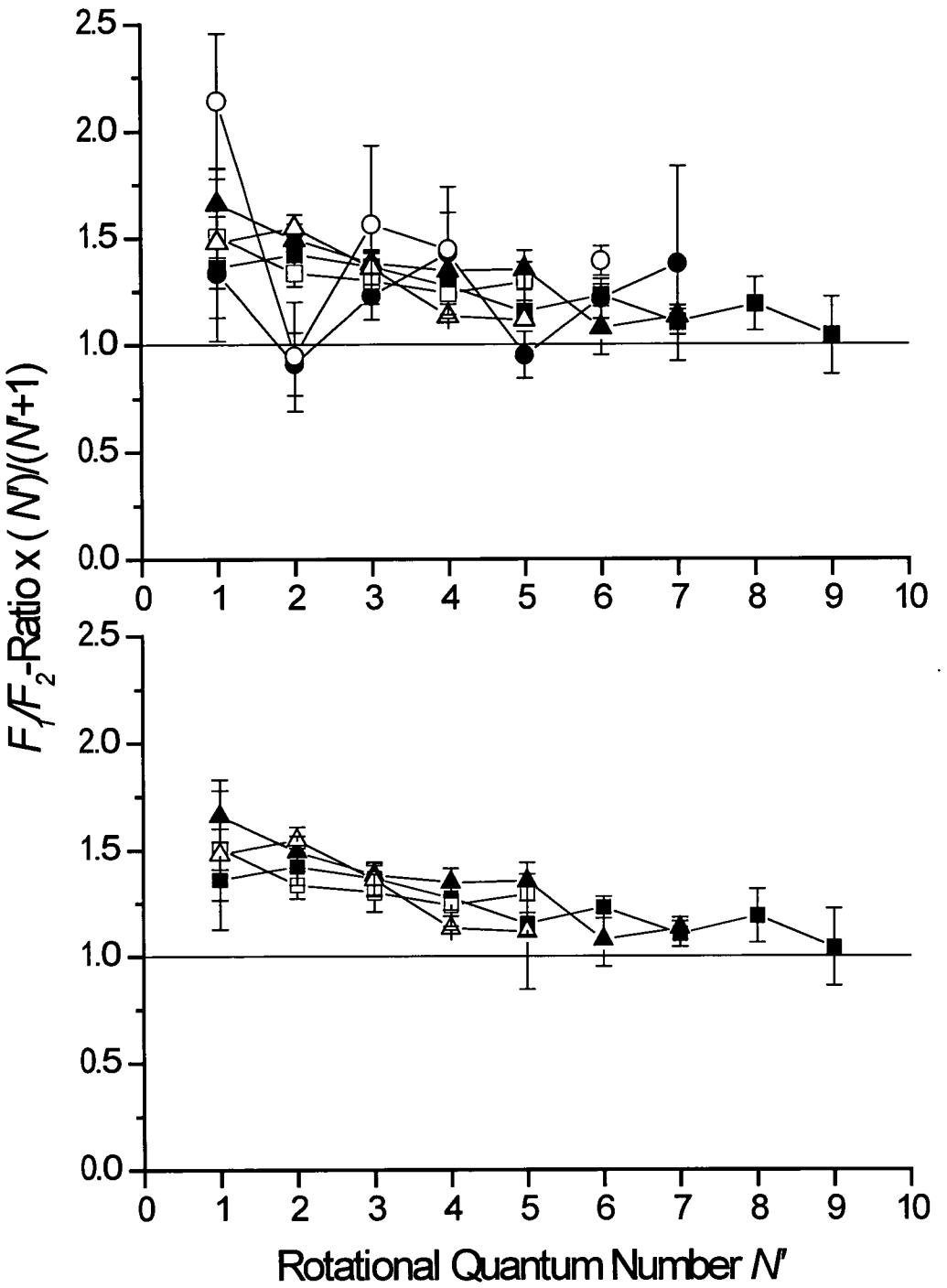

Figure 4.16: Measured F_1/F_2 ratios adjusted for degeneracy. Symbols are the same as in figure 4.15. The upper panel presents all reactions, the lower panel shows only the cyclohexane data.

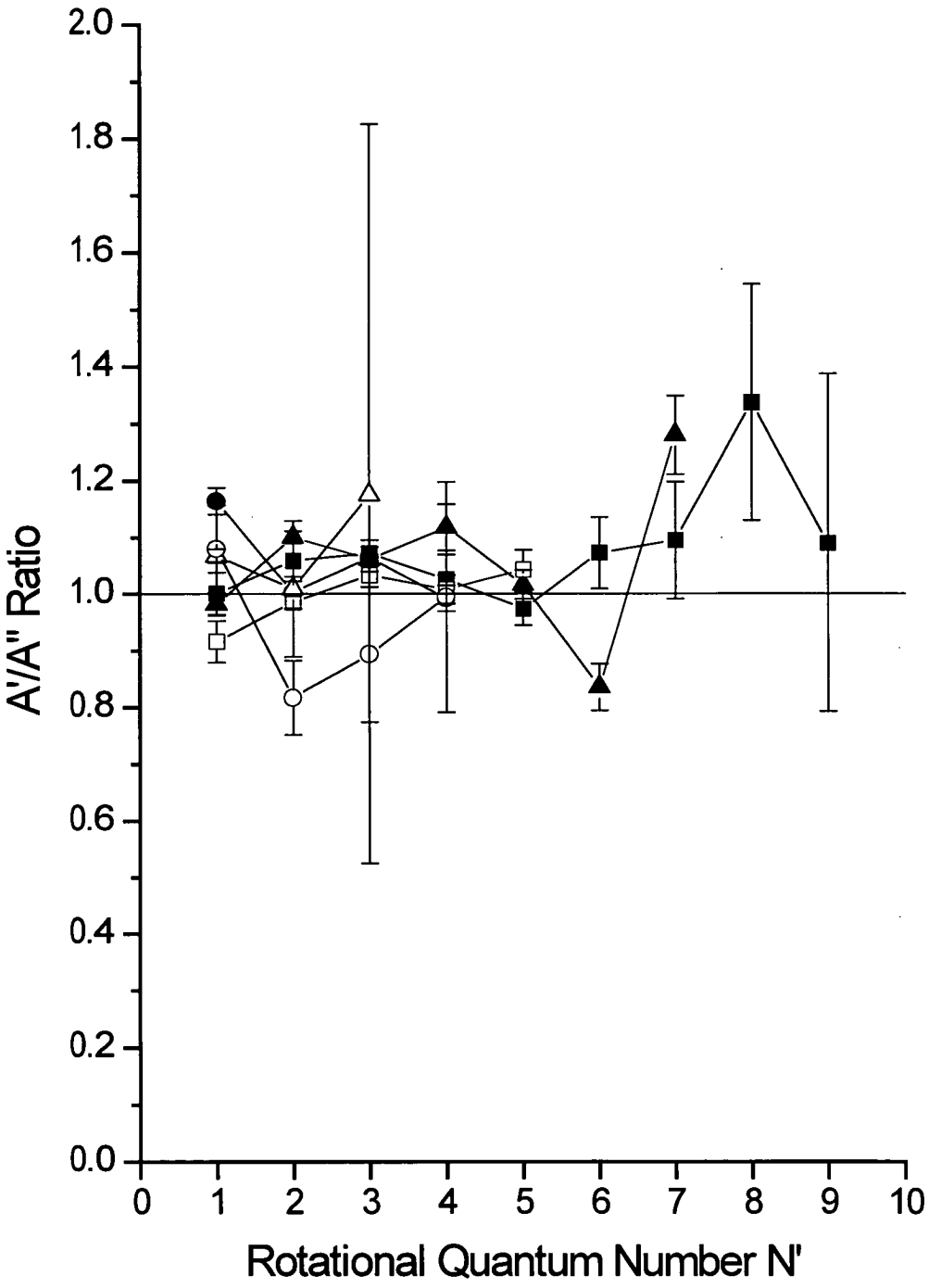

Figure 4.17: Measured Λ-doublet population in the OH/OD product of the investigated reactions. Symbols as in figure 4.15.

4.5.3 Vibrational branching

LIF is a notoriously unreliable method to determine vibrational distributions. But since this is the first systematic study of reactions of $O(^3P)$ with deuterated compounds, it is worth trying to derive some additional information, admittedly approximate, on these reactions.

The relative signal-to-noise ratio in the spectra, as defined above, can be used to evaluate approximately the relative populations in different vibrational levels in the OH and OD product. Together with measurements from previous molecular beam studies [14] on cyclohexane, relative vibrational branching ratios for the reaction of $O(^3P)$ with CH_4 and CD_4 can be established for the first time. The experimental signal-to-noise ratios for the different reactions and the corresponding vibrational branching ratios are given in table 4.4.

Reaction	*Product*	*Signal-to-Noise*	*Ratio of Signal-to-Noise (v'=1) / (v'=0)*	*Adjusted ratio of populations (v'=1) / (v'=0)*
$O(^3P)$+*cyclo*-C_6H_{12}	OH(v=1)	14.2±1.9	0.20	0.24[a]
	OH(v=0)	74.1±18.2		
$O(^3P)$+*cyclo*-C_6D_{12}	OD(v=1)	40.3±11.5	0.83	0.7[a]
	OD(v=0)	48.4±4.7		
$O(^3P)+CH_4$	OH(v=1)	<1[b]	≤0.03	≤0.03
	OH(v=0)	38.1±7.2		
$O(^3P)+CD_4$	OD(v=1)	0.9±0.7	0.08	≤0.07
	OD(v=0)	11.5±1.2		

Table 4.4: Vibrational branching ratios. The errors quoted are the standard error of the mean. The value for CH_4 is less than unity by definition, since no signal above the level of noise could be established under these conditions. Using longer times and higher pressures, the OH LIF signal was found to grow in. [a] Fixed to previously reported value by Andresen and Luntz [14]. [b] Less than unity by definition, since no signal above the level of noise could be established under these conditions.

In addition, different proportional populations in the N'=1 level in the different vibrational levels have to be taken into account to evaluate the vibrational partitioning over the whole rotational envelope and not only for the lowest rotational level. The rotational distributions in the first vibrationally excited state of OH and OD(v'=1) produced by reactions (4.2) and (4.4) are significantly colder than the respective populations in the vibrational ground state OH/OD (v'=0) as demonstrated in section 4.5.1.4. No reactive populations for the excited vibrational level from reactions (4.6) and (4.8) were measured.

The conditions of the signal-to-noise measurements for cyclohexane were sufficiently nascent to avoid significant rotational relaxation and the different relative populations for the lowest rotational level in both vibrational levels are known.

The situation for methane is different. The hydroxyl radicals have undergone about 3 collisions on average before being detected. While this is unlikely to completely thermalised the rotational populations, it does not represent the (unknown) nascent rotational distribution. This introduces an error which always leads to an overestimation of the vibrational branching ratios for the methane reaction. This error will be no more than a factor of two. The results in table 4.4 therefore represent upper limits on the production of OH/OD(v'=1) from reactions (4.6) and (4.8).

While no indication for the production of OH(v'=1) from reaction (4.6) was found, the OD(v'=1) product from reaction (4.8) was positively identified.

4.6 Attempt to observe the reaction of $O(^3P)$ with methane in a supersonic beam

The experiments using jet-expansion of NO_2 with CH_4, through a supersonic nozzle produced a dramatically increased signal with respect to the bulk-phase. Closer investigation of the resulting OH spectra showed large population in very high lines of N'. An example is shown below in figure 4.18, upper panel, which is compared with the result of a normal bulk experiment, lower panel.

Even though the distribution of collision energies in a jet-expansion are quite different from a bulk experiment, it is unlikely that this is the explanation of the difference in the result. If anything, it is more likely that a "colder" nascent distribution would be observed due to channelling of energy from internal degrees of motion into the group translation in the beam of molecules as well as a reduction of the width of the collision energy distribution.

Although the presence of both gases and the firing of both lasers were necessary to produce the signal it may not necessarily be $O(^3P)$ which is responsible for the observation of the highly rotationally excited OH product. The spectra obtained look suspiciously similar to those measured for reaction of $O(^1D)$ and CH_4.

The photolysis of NO_2 with 266 nm lies well below the threshold for production of $O(^1D)$ by a one-photon process. But the number density of NO_2 in the supersonic jet will be rather high and the cooling significant.

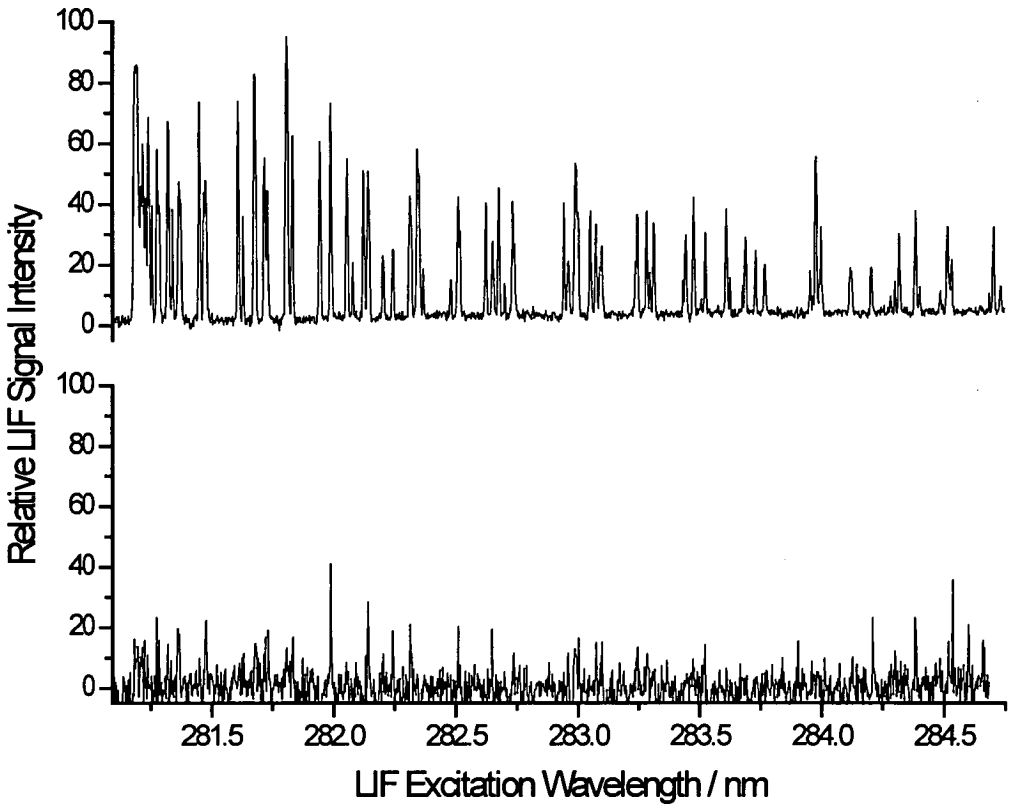

Figure 4.18: Nascent OH(v'=0) spectra from the reaction with CH_4. Supersonic nozzle expansion (upper panel) with a total backing pressure of 700 Torr behind the nozzle, 350 Torr NO_2 and 350 Torr CH_4. Standard bulk experiment (lower panel) with total pressure of 500 mTorr, 250 mTorr NO_2 and 250 mTorr CH_4. Photolysis-probe delay in both cases 200 ns.

The backing pressure behind the nozzle was about 1 bar of which half was made up of NO_2. To roughly estimate the amount of N_2O_4 present relative to NO_2 a simple calculation of the degree of dissociation α can be carried out.

The equilibrium constant for the chemical dissociation of N_2O_4

$$N_2O_4 \rightleftharpoons 2\ NO_2 \qquad \text{reaction (4.12)}$$

can be calculated knowing the difference in the standard Gibbs energy $\Delta G°$ as

$$K_P = \exp\left(-\frac{\Delta G°}{RT}\right) \qquad \text{equation (4.20)}$$

The values for $\Delta G_f°$ as taken out of a standard compilation [69] are $\Delta G_f°(298.15\ K)$ (NO_2)=51.3 and $\Delta G_f°$ (298.15 K)(N_2O_4)=97.9 kJ mol^{-1} in the gas phase. Therefore equation (4.20) yields a value for K_p of 0.150. The degree, α of dissociation can be calculated as

$$\alpha = \left(\frac{K_P}{4p + K_P}\right)^{1/2} \qquad \text{equation (4.21)}$$

with p, the pressure, in units of standard pressure. If the backing pressure behind the nozzle is 1 bar, the degree of dissociation, α, is calculated to be 0.26, that means only 26% of the N_2O_4 molecules are dissociated. This calculation does not take any cooling into account and therefore the amount of undissociated N_2O_4 in the nozzle expansion will be even larger.

Most of the NO_2 will in effect be present as N_2O_4 which lies 57.2 kJ mol^{-1} lower in energy than two NO_2 molecules [111]. N_2O_4 has a much larger absorption cross section than NO_2 at 266 nm [112]. On energetic grounds, it can dissociate into NO_2 plus $O(^3P)$ and NO in its electronic ground state but also into a pair of NO_2

molecules, at least one of which may be electronically excited [113].

The low-lying electronically excited states of NO_2 are the $\tilde{A}\ ^2B_2$ and the $\tilde{B}\ ^2B_1$ states which are known to have lifetimes in the order of several tens of microseconds [114]. They are therefore quite likely to absorb a second photon at 266 nm. Energetically they are now quite comfortably above the threshold to produce $O(^1D)$.

Due to the much higher reactivity of $O(^1D)$ atoms any signal due to $O(^3P)$ will be completely swamped under the OH produced by the reaction of $O(^1D)$ with CH_4. Since it can be assumed that it is impossible to conduct a supersonic nozzle experiment without having a large concentration of N_2O_4 present and therefore it is impossible to avoid the unwanted presence of $O(^1D)$, further experiments with the supersonic jet were abandoned. Even though the amount of cooling can be varied by heating the nozzle or adding different gases to the reaction it was judged to be infeasible since it would be impossible to be sure of the selectivity of only seeing the product of the $O(^3P)$ reactions.

In contrast for the experimental standard bulk conditions the N_2O_4 pressure was at most 0.25 Torr, and the analogue calculation yield a degree of dissociation of α=99.6%. The production of $O(^1D)$ atoms out of the bulk mixture is therefore not of practical significance.

4.7 Results of CH_4 absorption and opto-acoustic measurements

Measurements of the IR spectrum of CH_4 in the range of 2850 cm^{-1} up to 3150 cm^{-1} were made to ensure that the experimental setup would be able to pump CH_4 (ν_3, v=1). Spectra were obtained both as pure absorption spectra as well as opto-acoustic spectra. It should be noted again that using a pulsed laser system without correction for shot-to-shot variation in pulse energy does not constitute a good method to measure an absorption spectrum. For the purpose of the latter experiment only questions about the line position and optical density effects needed to be addressed. For these purposes a cosmetically perfect absorption spectrum is not necessary.

A typical absorption spectrum is shown together with the corresponding opto-acoustic spectrum is shown in figure 4.19. The opto-acoustic spectrum is much less sensitive to the variations in pulse energy and its features are nicely resolved. The system was not found to be optically dense for a CH_4 pressure up to 10 Torr. An opto-acoustic CH4 spectrum could always be recorded, independent of the pressure and absorption in the reaction chamber.

In the actual IR pumping experiments the pump laser wavelength is tuned to the strongest line in the Q-head. Although it may be unclear to which set of lines this strongest feature corresponds it can be assumed that the number of molecules pumped is proportional to the signal strength. This can be directly compared to the strength of the strongest line in the R-branch, which is the R(5) line. Due, in part to

spin statistics [76], J=5 has the highest number of molecules in the F state. Its relative population in a thermal sample is known. The size of the observed signal is directly proportional to the number of molecules pumped, unless the conversion of the CH_4 internal excitation into translation of the bath gas, i.e. the soundwave recorded is J depend. The number of molecules pumped on the feature in the Q-head can be estimated by comparing its relative size with the R(5) line. The spectra in figure 4.19 can be compared with the Hitran [106] simulation of the same spectral range. The simulated spectrum was already presented in figure 2.9.

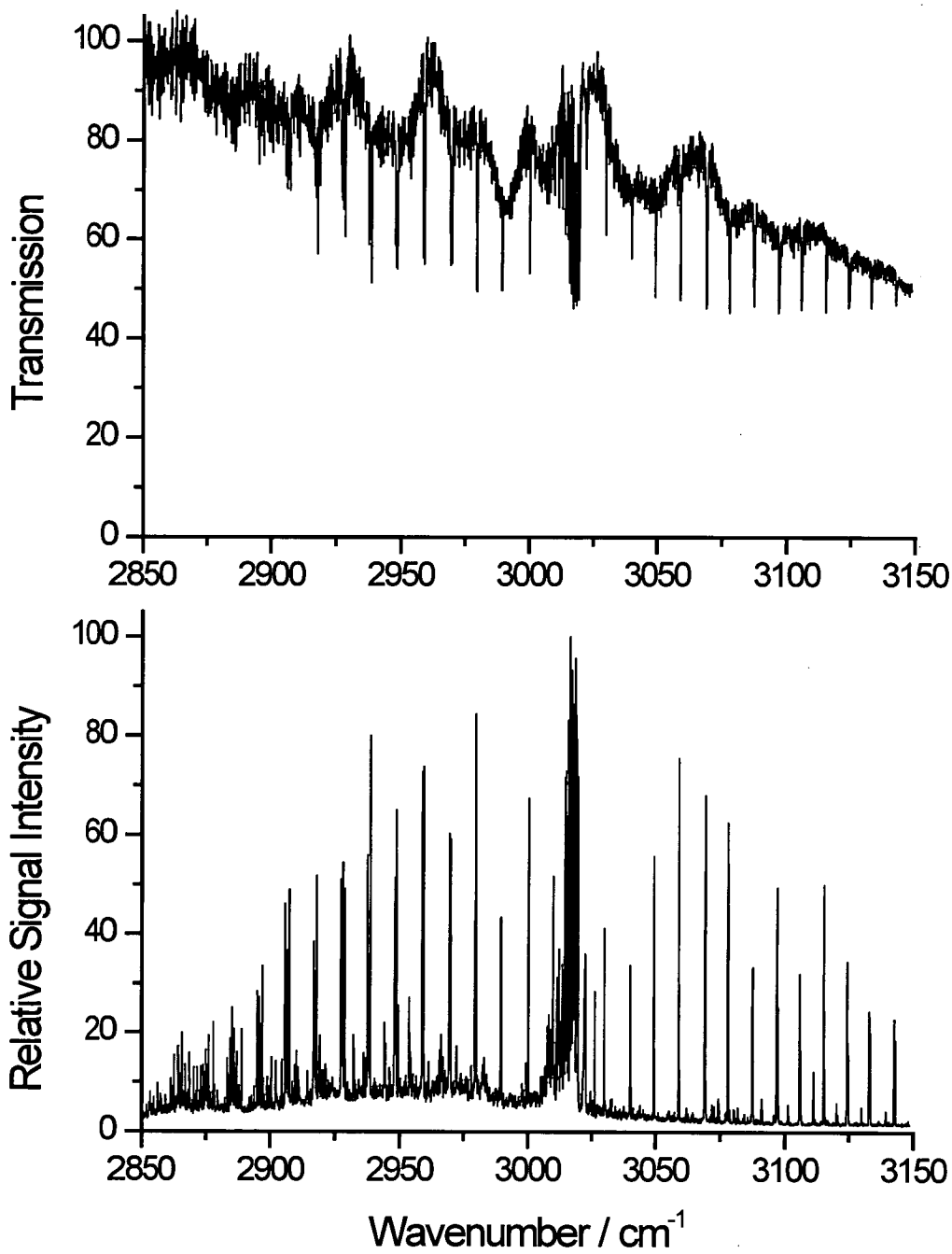

Figure 4.19: Absorption (upper) and opto-acoustic spectrum (lower) of CH_4 (ν_3, v=1). Pressure: 7.5 Torr (CH_4). Absorption pathlength: 40 cm, IR pulse energy 0.6 mJ.

4.8 Results of IR pumping of the methane (OH-LIF)

As explained in section 4.3.2.1 the aim was to observe an enhanced signal level if the IR pump laser was fired in coincidence with the photolysis laser, thereby producing a fraction of vibrationally excited CH_4 molecules. The relative OH-LIF signal level with and without the use of the IR pump laser set on the highest feature in the Q-branch (see previous section) needed to be compared. No obvious increase in the LIF signal level was recorded on the screen.

Spectra of the R_1 branch of the OH A-X (1,0) band were measured with the IR laser switched on and off in order to observe any not as obvious enhancement by vibrational excitation of the CH_4 reactant.

Initially a small signal enhancement in the order of 2 percent was observed. This initial effect remained present even when the IR-pump laser was blocked. The suspicion of it being an experimental artefact was confirmed when the dependence on the number of averaged shots was investigated. While it diminished with increased number of shots, it decreased in a linear fashion. It turned out to be an artefact of the data acquisition programme.

Luckily, the experimental procedure could be adjusted to avoid this problem. Tests were conducted to prove that the observed LIF signals, at a given photolysis-probe delay, were independent on the firing of the IR pump laser if it was physically blocked from entering the reaction chamber.

The real measurements were set to produce three data sets. The first set contained a short photolysis-probe delay, usually about 500 ns, with the IR-pump laser firing in conjunction with the photolysis laser, thereby vibrationally exciting CH_4 molecules. The second data set contained the same photolysis-probe delay, but the IR pump laser was delayed with respect to the probe laser by 10 μs. The third data set contained a long time delay spectrum for normalisation purposes.

Subtraction of the second data set from the first should contain only the contribution from the reaction of the vibrationally excited CH_4, reaction (1.9). A typical result with the spectrum from the pumped reaction, the non-pumped reaction and the subtraction is shown in figure 4.20. An analysis of the underlying oscillation is consistent with a beat frequency of about 48 Hz indicating that it is most likely caused by variations in power supply of the lasers, or the detection electronics rather than an experimental effect.

Integration over areas of OH A-X (1,0) R_1 transitions never produced statistically significant positive numbers, indicating that no enhancement was observed. Therefore any possibly existing enhancement is of the order or less than the level of noise which was less than 1% as measured by one standard deviation of the baseline with respect to the signal level in the unpumped reaction. This negative result allows an estimate on the upper limit of enhanced reactivity of the pumped methane which will be treated quantitatively in section 5.6.2 below.

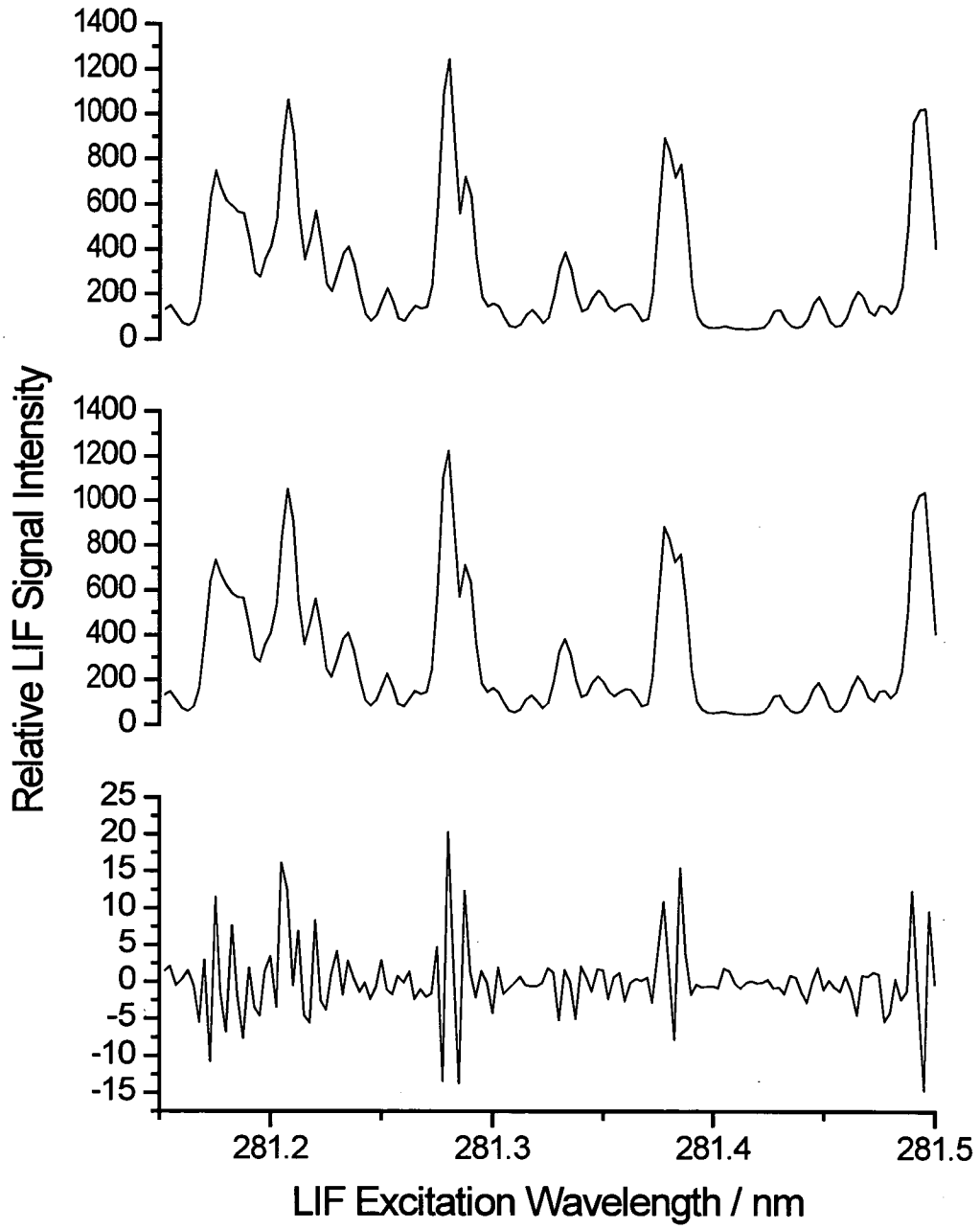

Figure 4.20: Results of pumping the ν_3 vibration in CH_4 with an IR laser on the Q-head at 3016.5 cm^{-1} with 0.6 mJ. OH A-X (1,0) R_1 branch with pumping (upper panel), without pumping (centre panel), subtraction (lower panel). Pressure 500 mTorr of a equal mixture of CH_4 and NO_2. Photolysis-Probe delay 500 ns. Energy of the IR beam.

Chapter 5: Discussion of the reaction of ground state oxygen atoms with deuterated and non-deuterated saturated hydrocarbons

5.1 OH / OD rotational distribution

5.1.1 Previous experimental results and their interpretation

In all previous measurements, the rotational distributions for the OH product were found to be characteristically "cold" for the reaction of $O(^3P)$ with hydrocarbons [7]. The absolute amount of available energy, as well as the fraction of it channelled into OH rotation, f_{rot}, increased in the order tertiary < secondary < primary < methane, which is notably the opposite order of exothermicity of the reactions but the direction anticipated if the differences in degrees of freedom is taken into account. In addition, if the OH(v'=1) was investigated, it was found to be much less rotationally excited than the corresponding OH(v'=0) product

As has been discussed in the introduction, the low OH product rotational excitation was interpreted as a strong experimental indication of a preferred collinear geometry since this mass combination (H + L-H) should be very sensitive to any torque in the "transition state".

Taking up this argument further, if the interaction of $O(^3P)$ with the H-C bond is fast with respect to a rotational period of the hydrocarbon reagent, its rotation is not expected to contribute significantly to OH rotation. This assumption would break

down if a collisional complex would be formed. The observed tendency towards more energy in OH rotation as function of the hydrocarbon opposite to the trend of $<E_{av}>$ has been therefore concluded to be a dynamical effect, corresponding to variations in the degree of deviation from collinearity at the point of energy release [14,23].

This has previously been explained by the increase in steric hindrance experienced by the attacking $O(^3P)$ atom, i.e. a shrinking of the cone of acceptance, enforcing a more collinear transition state and therefore less rotation. This argument is only valid if the product rotation is due to a bent geometry in the "transition state". The "colder" rotational distribution for the vibrational excited product OH/OD(v'=1) [14,16,22,23] is also consistent with this view. It can be interpreted in this picture as a further narrowing of the constraint towards a collinear transition state geometry to ensure the product is formed in the excited vibrational level, therefore restricting the amount of rotation possible.

It should be noted though, that the nascent rotational distribution is a function of the collision energy. As the cone of acceptance widens with increasing collision energy, more energy gets channelled into rotation, though only in an absolute sense, because the relative amount of rotational energy decreases with increasing collision energy. Translational energy is therefore a very inefficient way to introduce product rotation in these reactions. This is expected since the kinematic mass combination of Heavy + Light-Heavy implies that the total angular momentum is roughly given by

the orbital motion of the reactants. It is mostly converted into the orbital motion of the products and not internal rotational motion of the product.

$$J \approx l \rightarrow l' \approx J' \qquad \text{equation (5.1)}$$

This means that the rotation of the product states is mostly uncoupled from the orbital motion of the reactants and products. Any amount of angular momentum, which could end in the product rotation can easily be accommodated in the orbital motion of the partners due to the much heavier masses.

5.1.2 Previous theoretical work on the OH product rotation

The first attempts to underpin the observed "cold" rotational OH distributions theoretically were carried out by Luntz and Andresen [39] in their LEPS study, treating the hydrocarbon as a "pseudo-diatomic". The OH product was found to be universally rotationally cold for all the hydrocarbons, with OH(v'=1, N') distributions considerably narrower than the OH(v'=0, N') distributions. The distributions broadened only slightly with increasing collision energy.

The calculations therefore successfully reproduced the main features of the experimental observations, although at least the secondary hydrocarbon PES has been designed specifically to produce a cold OH(v'=0, N') distribution.

In addition, Luntz and Andresen [39] identified the correlation between the "cold" rotational distributions and a strong constraint to collinearity at the mid-point of the reaction. The effect was not only due to the variation of the barrier height with

bending angle, but also of active steering of an initially non-collinear approach geometries by reorientation of the H-R diatomic. This conclusion should be treated with caution, since the treatment of the hydrocarbon as a structureless particle introduces an artificially low moment of inertia for the H-R pseudo-diatomic which may lead to an overestimation of this effect.

As introduced in section 1.3, the main theoretical work on OH product rotation was done by González and coworkers [55], who carried out a QCT calculation to match the experimental conditions of the experimental work on the $O(^3P)$ with CH_4 reaction done by McKendrick and coworkers [23]. Elaborating on this in more detail, as shown in figure 5.1 the QCT calculation was able to reproduce the experimental OH(v'=0) rotational population distribution quite accurately. Very little OH(v'=1) was predicted, which is consistent with the failure to detect it experimentally [23], although it was not pursued any further. This represents the state-of-the-art comparison between experiment and theory at the moment.

Only a small fraction (7-8%) of the energy available was calculated to appear in OH(v'=0) product rotation and the fraction does not increase significantly with E_T. Most of the additionally available energy at higher E_T is converted into the translation of the products, consistent with the expected $l \rightarrow l'$ propensity, noted above, for H+LH systems. While no detailed differential cross-sections were reported, the angular scattering was stated to be clearly backward. With increasing E_T the cross-sections broadened and shifted towards more forward scattering.

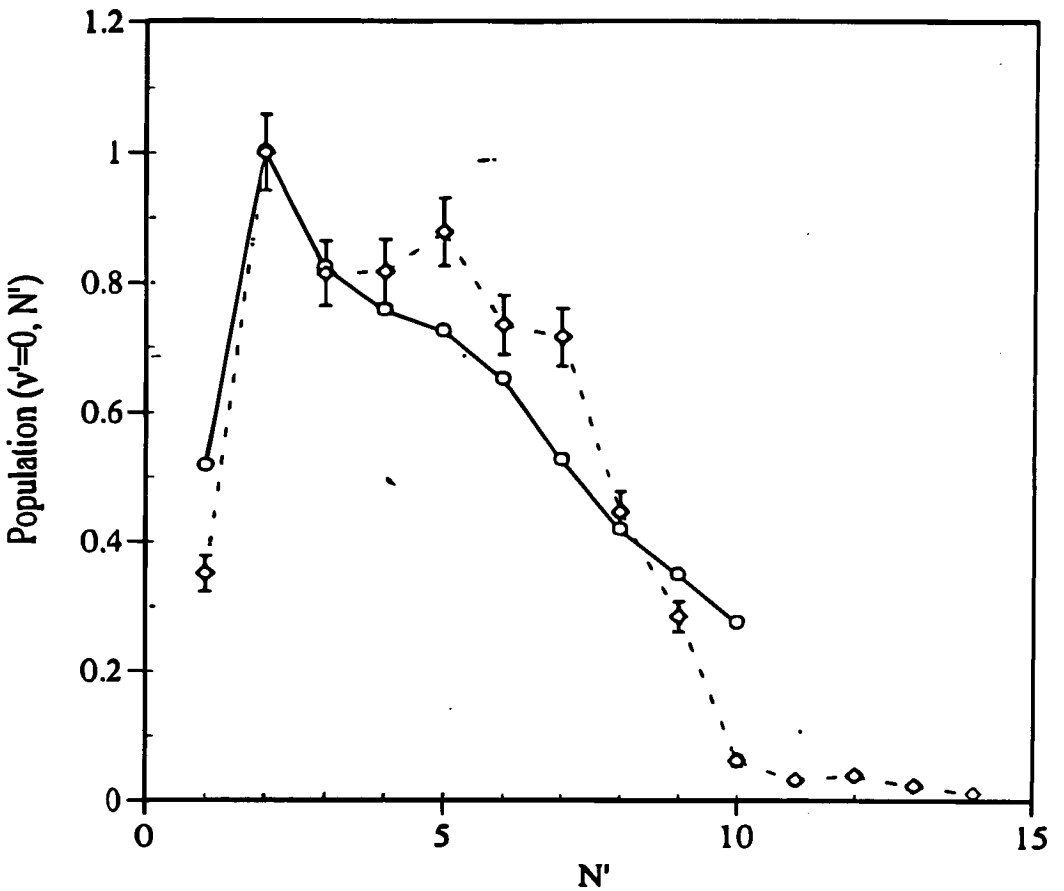

Figure 5.1: Comparison of the measured OH(v'=0) rotational distribution (○ and solid line) from O(^{3}P) + CH_4 and the predictions of QCT calculations (◊ with error bars and dashed line) on a O-H-(CH_3) surface. Taken from [55] with experimental data from [23].

The alignment of the OH product ***j'*** was found to be preferentially perpendicular to the ***kk'*** plane, in agreement with the results of the early VADW model [40].

González *et al.* [55] tried to identify the origin of the "cold" OH rotational distributions in more detail than the previous qualitative conclusions. They forwarded an argument first developed by McKendrick, Rakestraw, Zhang and Zare [19]. They had attempted to explain the dramatic differences in the "cold" rotational distributions produced by $O(^3P)$ with hydrocarbons and the much "hotter" rotational $OH(v'=0)$ distributions from the related reaction $O(^3P)$ with HBr [19,115].

The OH product rotational distribution from the $O(^3P)$ with HBr reaction was quite well reproduced in QCT calculations [19] on an LEPS surface developed independently by Broida *et al.* [116]. All model surfaces have a preferred collinear pathway. McKendrick *et al.* [19] noted that the deviation from collinarity described by the bending angle α, was much more broadly distributed for reactive trajectories for the HBr reaction than for the hydrocarbon reaction, as shown in figure 5.2.

This behaviour was correlated with the angular dependence of the barrier height on the two surfaces. González *et al.* [55] observed a much steeper rise of the barrier as a function of the deviation from collinearity for the tertiary $O(^3P)$ with HR barrier with respect to $O(^3P)$ with HBr even though the collinear barrier heights themselves are very similar. González and coworkers [55] support the earlier conclusion that this constitutes the main reason for the difference in OH rotation for these two systems.

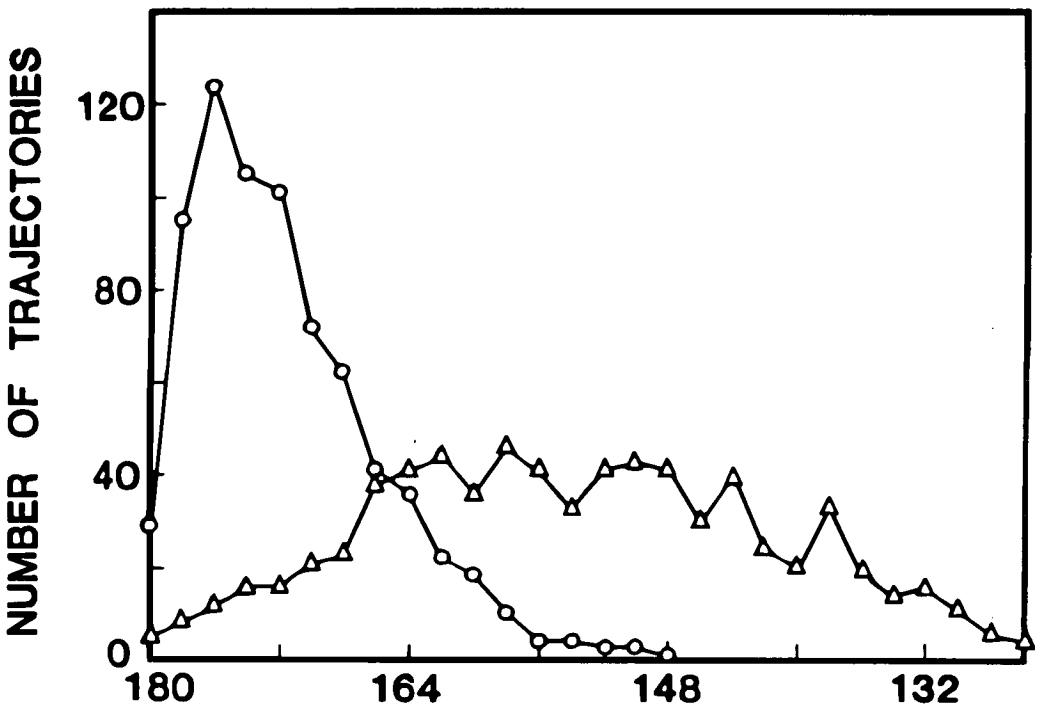

Figure 5.2: Distribution of O-H-X angles of attack α for reactive trajectories in QCT studies of the reactions O + HBr (△) and O + tertiary HR (○) on model LEPS surfaces. Adapted slightly from figure 14 in [19].

However, the $O(^3P)$ with H-(CH_3) curve is shallower and nearly parallel to that for $O(^3P)$ with HBr, just displaced to higher energy. Therefore the increase of the fraction of energy channelled into OH product rotation from tertiary H-R (2%) to nearly 8% for methane fits into the picture. This does, however, not answer why a much larger fraction (22%) of $<E_{av}>$ appears in OH rotation in the reaction with HBr. Interestingly, a closer analysis [55] of the $O(^3P)$ with H-(CH_3) trajectories at a collision energy of 0.65 eV (63 kJ mol^{-1}) showed that they covered a wide range of angles, with an average value of α=146°. But f_{rot} was found to be independent of $<\alpha>$, having essentially the same value for trajectories sampled at different angles in 180-160, 160-140 and 140-120° intervals. This surprising result was not explained any further.

González and coworkers [55] suggested, however, a new argument to explain the differences between the HBr and H-(CH_3) reactions, which is the position of the saddle-point. While, as explained above, see section 1.4.1.3, the saddle-point in the case of methane is located centrally, with both the C-H and O-H bond roughly equally extended, the $O(^3P)$ with HBr system has an earlier saddle-point with a considerably larger extension of the O-H distance. González *et al.* argue that, assuming similar forces acting in both systems, the longer O-H lever arm for HBr results in a larger torque and hence greater OH rotational excitation.

5.1.3 Confirmation of previous studies

The observed OH(v'=0), (v'=1) rotational distributions in this study, as shown in section 4.5.1.2, for the reactions of O(^{3}P) with non-deuterated hydrocarbons fit well into the general observed scheme [7]. The rotational distributions are found to be characteristically "cold" with respect to the total energy available, which is consistent with previous observations as discussed in detail in section 1.3.1.2.2. The "hottest" distribution is observed for methane, with "colder" distributions for higher substituted hydrocarbons.

Since this is the only study so far carried out at a photolysis wavelength of 266 nm a perfect agreement with previous data is not expected. Interestingly enough, the observed rotational distributions are "cold" relative to the closest similar experiment by McKendrick *et al.* [23]. They measured the rotational distributions as a function of the photolysis wavelength at 248, 308 and 351 nm and observed an increase in the energy channelled into rotation in the inverse order. Assuming that because the current wavelength of 266 nm lies in the same absorption band, the result should lie between the results obtained at 248 nm and 308 nm. The results of this study are all colder than the 308 nm data of McKendrick *et al.* However, this does not necessarily imply a discontinuity in the partitioning of energy of rotation, but is most likely due to different methods of analysis.

More importantly, the distributions show a very good qualitative agreement with respect to those reported by McKendrick and coworkers, but also, at a given

wavelength, between the different hydrocarbons. All distributions look rather "Boltzmann-like", peaking early and falling monotonically thereafter. They are all "cold" with respect to the total energy available and always less than 10% of the total energy ends up in rotational motion of the hydroxyl products.

They can, however, be significantly "hotter" than room temperature in the case of OH/OD(v'=0) from methane, or significantly "colder" for OH/OD(v'=1) from cyclohexane. As explained above, the concept of temperature is not strictly valid in this study, but it is a qualitatively useful indication of the amount of energy channelled into rotation.

5.1.4 New results and conclusions

The most important new result of this study, with respect to the rotational motion of the hydroxyl radical, is that the amount of energy channelled into rotation is independent on the H/D isotopic substitution. This is best demonstrated in figure 4.13. There are no previous systematic measurements of this effect. It should be stressed that this means that the distributions differ in terms of angular momentum.

The highest energetic difference between deuterated and non-deuterated hydrocarbons is the position of the OD(v'=1) product state levels compared to the OH (v'=1) level. No distinct effect in the rotational energy distribution due to this change of vibrational energy was observed. The changes in exothermicity and barrier height are small compared to the total energy available in this system, refer to figure 4.8.

Since the total collision energies do not change significantly for the deuterated hydrocarbons with respect to the non-deuterated ones, as demonstrated in figure 4.7, it is safe to assume that the relative fraction of the total energy channelled into product rotation is also H/D isotope independent.

A crude model can be deployed to check if the apparent isotope independence of the rotational energy release is consistent with an abstraction mechanism, at least for classically behaving particles. The basis of this model is that the rotational excitation is due to a bent geometry at the "transition state", i.e. the point of maximum repulsive energy release. The H atom experiences a repulsive force due to the breaking of the CH bond, which is determined by energy and linear momentum conservation, and which results in a velocity of the hydrogen atom, v_H, of

$$v_H = \left(\frac{2 m_R E}{m_H m_{HR}} \right)^{1/2} \qquad \text{equation (5.2)}$$

where m denotes the mass of the hydrogen (m_H), of the hydrocarbon (m_{HR}) or the hydrocarbon radical fragment (m_R) and E is the energy being released repulsively.

It is worth keeping in mind that the mass of the hydrogen atom, or even of the deuterium atom, is much smaller than the mass of the hydrocarbon. In the case of a non-collinear approach the resulting OH molecule experiences a angular acceleration due to the repulsive motion of the hydrogen atom. This gives rise to an angular momentum j_{OH} for the OH molecule which is given (classically) as

$$j_{OH} = \mu_{OH} v_H b_{eff} = \frac{m_H m_O}{m_{OH}} \left(\frac{2 m_R E}{m_H m_{HR}} \right)^{1/2} b_{eff} \qquad \text{equation (5.3)}$$

where μ is the reduced mass and b_{eff} is the effective impact parameter or lever arm that depends only on O-H-R angle. It is the extrapolated distance between the recoiling H atom and the centre-of-mass of the OH if the H atom moves along a straight line. Since rotational energy is given classically as

$$E_{rot}=\frac{j^2}{2I} \qquad \text{equation (5.4)}$$

with I being the moment of inertia, the rotational energy E^{rot} for the OH molecule is therefore

$$E_{OH}^{rot}=\frac{j_{OH}^2}{2\mu_{OH}r_{OH}^2}=\frac{m_O m_R}{m_{OH} m_{HR}}\left(\frac{E b_{eff}^2}{r_{OH}^2}\right) \qquad \text{equation (5.5)}$$

with r denoting the internuclear distance, and accordingly for OD

$$E_{OD}^{rot}=\frac{j_{OD}^2}{2\mu_{OD}r_{OD}^2}=\frac{m_O m_R}{m_{OD} m_{DR}}\left(\frac{E b_{eff}^2}{r_{OD}^2}\right) \qquad \text{equation (5.6)}$$

To compare the two isotopes for a given hydrocarbon, it can safely be assumed that the released energy E, the effective impact parameter b_{eff} and the internuclear distance r are essentially independent of the isotope. It therefore follows that the ratio of energy channelled into rotation of the non-deuterated to the deuterated reaction is predicted by the model to be

$$\frac{E_{OH}^{rot}}{E_{OD}^{rot}}=\frac{m_{CH_3} m_{OD} m_{CD_4}}{m_{OH} m_{CH_4} m_{CD_3}}\approx 1.10 \qquad \text{equation (5.7)}$$

for methane and

$$\frac{E_{OH}^{rot}}{E_{OD}^{rot}}=\frac{m_{C_6H_{11}} m_{OD} m_{C_6D_{12}}}{m_{OH} m_{C_6H_{12}} m_{C_6D_{11}}}\approx 1.07 \qquad \text{equation (5.8)}$$

for cyclohexane.

The difference between the different isotopically substituted hydrocarbons, even for the least favourable case of methane, is only about 10 %. This difference decreases with increasing size of the hydrocarbon.

This crude classical model therefore predicts a near isotope-independence of the OH/OD rotational energy which is in accordance with the experimental results. The low rotational excitation in the OH/OD products has always been interpreted as evidence of a collinear abstraction mechanism. The fact that this very crude model reproduces adequately the experimental outcome supports the idea of the mechanism as a direct abstraction.

It is necessary to stress that not all conceivable mechanisms would be isotope independent. A stripping mechanism, where a fixed proportion of reactant orbital angular momentum, l, would be transferred to the OH/OD product angular momentum, j', would clearly not be isotope independent.

It is worth making a comparison with the Cl (^{2}P) with methane reaction, for which extensive measurements have been made and were recently been reviewed by Valentini [117]. There is considerably more information available for this reaction than for the O(^{3}P) reactions, including, measurements with CD_4. The bulk of this evidence leads also to the conclusion that this reaction is dominated by direct abstraction via low-impact parameter collisions, with a close to collinear geometry at the transition state. The energy channelled into rotation was found to be very similar for the deuterated and non-deuterated reaction [118]. All these conclusions therefore

support the interpretation of the more limited, but similar in respect to what has been measured, results for $O(^3P)$ with hydrocarbons as evidence for a direct abstraction.

This perception for this class of reactions was also strengthened by calculations at various levels of theory [7]. The latest study by González and coworkers [56], tried to illuminate a larger part of the microscopic reaction mechanism by explicitly investigating the reaction $O(^3P)$ with CH_4 at different collision energies of E_T=0.65, 1.0 and 1.5 eV.

They found a decrease of the average fraction of energy channelled into vibration with increasing collision energy. Instead, the loss in the relative vibrational energy appears mostly in the product translation and to a much smaller extent in product rotation. This is supposed to be responsible for the slight broadening of the rotational distribution as a function of the available energy, consistent with observations by McKendrick and coworkers [23]. For the highest collision energy González *et al.* [56] even calculated a bimodal OH rotational distribution with a significant high N' component for very high collision energies.

In addition, they calculated a set of two-vector properties. As could be expected for H+L-H kinematics, the total angular momentum of the system was found to be dominated by the orbital motion of the two partners on both the reactant and product side of the reaction. The calculation of the $\boldsymbol{kk'}$ correlation revealed it to be predominantly backscattering for low E_T. With increasing E_T, though, a stronger sidewards scattering component gains importance and finally takes over for the

highest calculated energy. Only trajectories with high impact parameters were found to produce scattering in the forward hemisphere. The product rotation $\boldsymbol{j'}$ was found to be quite strongly aligned with the orbital motion of the products ($\boldsymbol{l'j'}$) and found to be perpendicular to the $\boldsymbol{kk'}$ plane.

In order to analyse the microscopic mechanism, González and coworkers [56] divided the trajectories as being either "rebound" or "non-rebound". The "rebound" trajectories tend to be predominantly backscattered and are dominant at low E_T. They are usually formed by low impact parameters and may form relatively highly rotationally excited products. This is due to the fact that low impact parameters allow a significant fraction of E_T be used to reach a more repulsive part of the potential, converting reactant translation into product rotation. The "non-rebound" trajectories, on the other hand, tend to be more forward scattering and less rotationally excited.

No similar trajectory information is available for CD_4. All currently available information seem to agree that the observed isotope independence of the energy channelled into hydroxyl rotation from the reaction of $O(^3P)$ with hydrocarbons is fully consistent with the proposed collinear abstraction mechanism.

5.2 OH / OD fine-structure distribution

5.2.1 Previous results and interpretation

The "cold" OH rotational distribution is not the only characteristic feature of the reactions of O(^{3}P) with alkanes. Also universally [7], a strong preference for the population of the lower lying F_1 spin-orbit manifold, of the OH product is observed. A systematic study of this effect was carried out by McKendrick and coworkers [23,66], who also presented a model, to explain this behaviour, which will be discussed in detail below in section 5.2.1.2.

If the ratio of the spin-orbit manifolds were purely controlled by degeneracy it would have a value of unity after correcting for the spatial degeneracy as explained in section 4.5.2. Experimentally there is still a residual preference for the F_1 states of slightly less than a factor of 2, which is approximately independent of N'.

Andresen and Luntz [14] had already proposed that the preference may be the result of adiabatic correlations with the corresponding O(^{3}P$_j$) fine-structure states. If the reactant fine-structure states are unequally populated and the reaction behaves at least partially adiabatically, so that non-adiabatic transitions do not equilibrate the fine-structure populations, then a non-statistical product state distribution could result. This approach had already been deployed successfully on some other systems [119].

However, the specific correlations proposed for O(^{3}P) with hydrocarbon reactions by Andresen and Luntz [14] were later shown to be incorrect by Sweeney

and McKendrick [66]. They proposed a new correlation based on the extensive work of Aquilanti and coworkers [28,29,30,120,121], who had discussed in considerable detail how the couplings between the different forms of angular momentum evolve as a function of intermolecular distance for open shell reacting with closed shell systems.

5.2.1.1 Fully adiabatic electronic coupling model

A new, fully adiabatic correlation diagram was derived by Sweeney and McKendrick [66]. It represents a collinear reaction of $O(^3P)$ with a cylindrically-symmetric $^1\Sigma$ H-R molecule. On the reactants' side, to a first approximation neglecting spin-orbit splitting, the oxygen atom can collinearly attack the hydrogen bonded to the carbon in two different ways. The p orbital approaching can either be filled with two electrons, resulting in an unreactive $^3\Sigma^-$ symmetry or it can be one of the two p orbitals filled with only one electron producing the doubly degenerate $^3\Pi$ surface. These $^3\Pi$ surfaces correspond to the reactive ^3E surface identified for $O(^3P)$ + CH_4 in C_{3v} geometry [41] and are displayed in figure 1.12, and correlate between reactants and products. They split into $^3A'$ and $^3A''$ surfaces on bending. In addition, the $^3\Sigma^-$ surface is the corresponding unreactive $^3A_2$ surface.

On the product side, the $^2\Pi$ OH and $^2\Sigma$ R radicals give rise to the $^3\Pi$ surfaces that connect to $O(^3P)$ and HR reactants. The $^1\Pi$ surfaces do not correlate to the reactant side.

The correlation between the different surfaces depends on the balance of three factors. The dominating interaction, if the partners are far apart, will be the spin-orbit interaction. That is l, the orbital angular momentum of the collision pair O + HR and j, the total electronic angular momentum will be good quantum numbers to describe the system. In terms of Hund's coupling cases, this would correspond to Hund's coupling case (e).

The centrifugal energy, defined via the orbital angular momentum l, can be neglected in a collinear approach. At short range, the dominant interaction will be the electrostatic interaction. It has been worked out in considerable detail by Aquilanti and co-workers [28,29,120,121] that Hund's case (c), where j and Ω are good quantum numbers, describes the intermediate range well. Hund's case (a) predicts the behaviour at short range, where the electrostatic interaction is responsible for the relative energies of the levels involved.

Sweeney and McKendrick derived the new fully adiabatic correlation diagram shown in figure 5.3 [66]. In addition to obeying Ω conservation, the parity of the surfaces has to be taken into account to connect the surfaces from reactants' side through to the products' side.

It can clearly be seen in figure 5.3 that the $O(^3P_2)$ atoms are the most connected to the product side, producing predominantly OH $^2\Pi_{3/2}$ (F_1), while only one connecting surface can be found for the $O(^3P_1)$ atoms, producing OH $^2\Pi_{1/2}$, and the $O(^3P_0)$ atoms remain unreactive. To predict the F_1/F_2 ratio for a particular experiment,

the outcomes for the individual $O(^3P_j)$ states have to be weighted by their relative initial populations. The j =2, 1, and 0 states lie at energies of 0, 158 and 226 cm^{-1}, respectively. The thermal distribution, as would be present, for example in a molecular beam experiment [14,16], turns out to be only slightly different from the photolytically produced distributions at a range of wavelengths in the same electronic band for NO_2 [22,23]. In all cases, the lowest-lying $O(^3P_2)$ state dominates the distribution due to its highest degeneracy. Therefore a preferential production of the lower F_1 state is predicted from the fully adiabatic model, which agrees qualitatively with the experimental observations.

This fully adiabatic model [66] predicts a $^2\Pi_{3/2}$: $^2\Pi_{1/2}$ ratio of approximately 3 if the distribution of oxygen atoms in the photolysis process is taken into account [122]. This value is considerably off the mark for all previously reported data [7].

If tested on a quantitative level, however, a value of F_1/F_2 ~3 is derived from the model which is a serious overestimate of the observed effect. Similar overestimates were found for the other experiments [66].

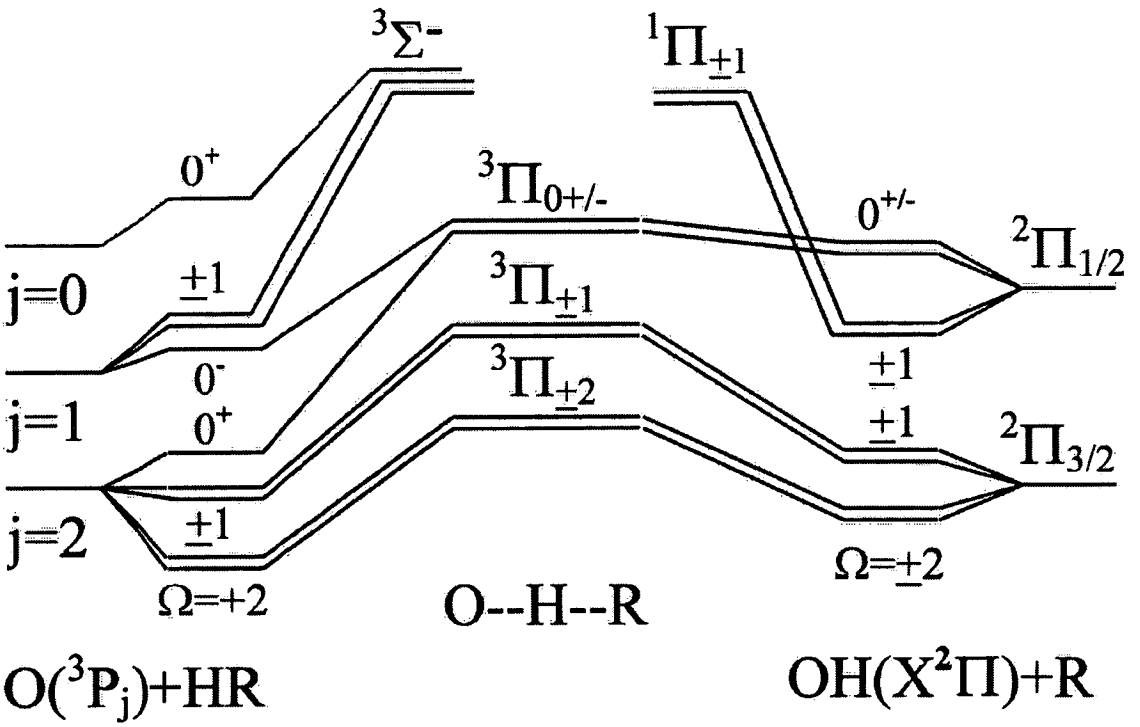

Figure 5.3: Fully adiabatic correlation diagram for a collinear $O(^3P)$ + hydrocarbon reaction taken from reference [66].

5.2.1.2 Non-adiabatic Mixing

Consequently, Sweeney and McKendrick [66] developed a new model which kept its Ω and parity conserving characteristics, but allowed coupling between channels of the same value of Ω in the entrance and the exit side. This model is displayed graphically in figure 5.4.

Now all reactant surfaces are at least partially reactive. The coupling is assumed to be sufficiently strong to cause equalisation of population on the coupled surfaces. This assumption was underpinned by a first-order perturbation calculation showing inelastic transition probabilities between $^3P_2$ and $^3P_1$ states to be large and essentially independent of the collision energy, at least for collision energies sufficient to cross the substantial barrier to the reaction. This scrambling itself is a function of the collision energy, but for the energies of this study it is well into the "totally scrambled" region. The coupling strengths used in the perturbation calculation were independently derived by Aquilanti and coworkers [29] from their studies of elastic scattering of magnetically selected atoms.

Additional independent evidence of a different type comes from experimental work of Ma and Liu [123], who studied the inelastic conversion of $O(^3P_2)$ to $O(^3P_{1,0})$ states. Their studies suggest that the $O(^3P_2)$ collisionally scrambles into $O(^3P_1)$ and $O(^3P_0)$ in a ratio of 2 : 1 at high collision energies. This corresponds to the same as treating the entrance channels as completely scrambled. This result survives in more rigourous close-coupling calculations [124,125] for collisions with He and H_2.

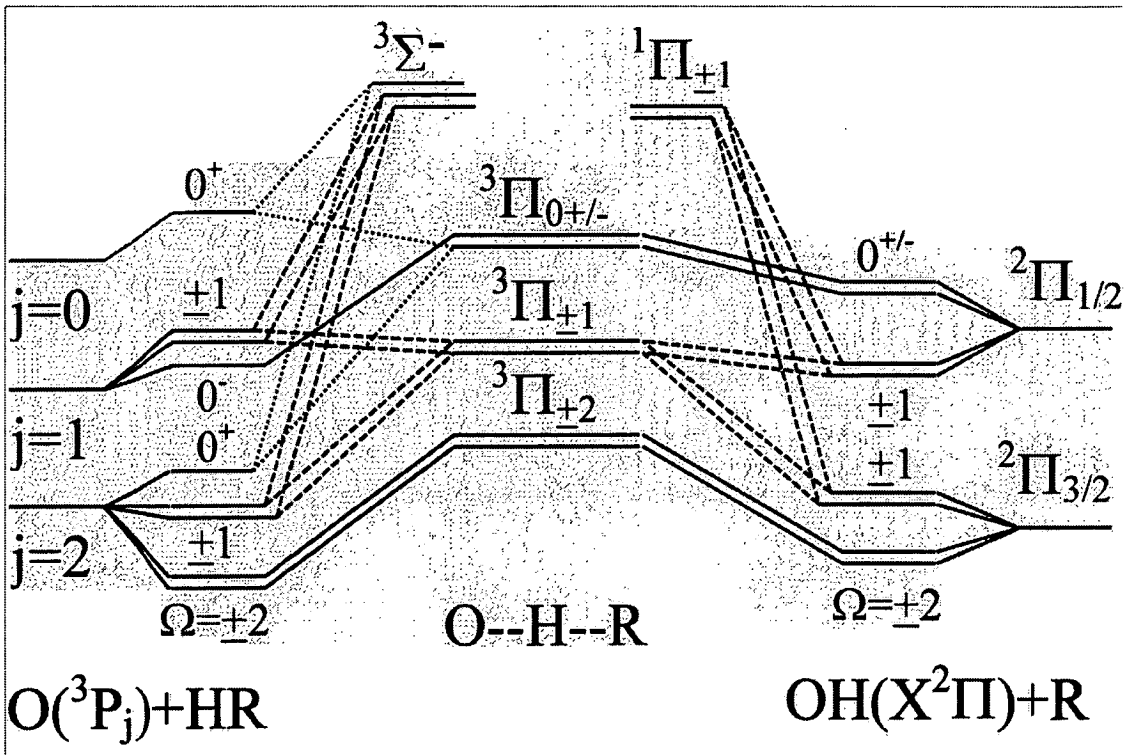

Figure 5.4: Correlation diagram allowing for mixing in entrance and exit channel under conservation of Ω and parity taken from [66].

Additionally, as experimental observation to support the assumption of scrambled surfaces, any attempts to measure *J*-specific rates of reactions of $O(^3P_J)$ + hydrocarbons have been thwarted by the rapid interconversion between the fine-structure states [11].

McKendrick and Sweeney [66] applied the non-adiabatic mixing model to their experimental data to predict the OH product F_1/F_2 spin-orbit fine-structure ratio. This coupling model predicts a $^2\Pi_{3/2}$: $^2\Pi_{1/2}$ ratio for the $O(^3P_J)$-state distribution produced by photolysis [122] of 1.72, which is in good agreement with the experimental results of McKendrick and coworkers [23].

5.2.2 Confirmation of previous studies

The most striking feature of the measured F_1/F_2 ratios, as shown in section 4.5.3 above, is that there is no significant difference between the OH and OD product fine-structure population produced by any of the following reactions (4.1)-(4.5) and (4.7).

$O(^3P) + cyclo\text{-}C_6H_{12} \rightarrow OH\ X\ ^2\Pi_i\ (v'=0) + cyclo\text{-}C_6H_{11}$ reaction (4.1)

$O(^3P) + cyclo\text{-}C_6H_{12} \rightarrow OH\ X\ ^2\Pi_i\ (v'=1) + cyclo\text{-}C_6H_{11}$ reaction (4.2)

$O(^3P) + cyclo\text{-}C_6D_{12} \rightarrow OD\ X\ ^2\Pi_i\ (v'=0) + cyclo\text{-}C_6D_{11}$ reaction (4.3)

$O(^3P) + cyclo\text{-}C_6D_{12} \rightarrow OD\ X\ ^2\Pi_i\ (v'=1) + cyclo\text{-}C_6D_{11}$ reaction (4.4)

$O(^3P) + CH_4 \rightarrow OH\ X\ ^2\Pi_i\ (v'=0) + CH_3$ reaction (4.5)

$O(^3P) + CD_4 \rightarrow OD\ X\ ^2\Pi_i\ (v'=0) + CD_3$ reaction (4.7)

All reactions produced preferentially the OH/OD product in the F_1 spin-orbit manifold, which is consistent with observations in all previous studies. [7]. After adjusting for degeneracy, as shown in figure 4.16, the value drops slowly and monotonically with N' from a maximum value at N'=1. This behaviour is qualitatively similar to the reports by McKendrick and coworkers [23].

The F_1/F_2 product spin-orbit manifold preference established in this work, 1.53±0.17, with one standard error of the mean, compares favourably within the overlapping error bars with most of the previous experimental results [7] including the only measurement of OD(v'=0) by Andresen and Luntz [14] which was reported to be 1.4 (with no indication of uncertainty). It is just outside the value predicted by Sweeney and McKendrick's model of 1.72 [66].

5.2.2.1 Interpretation

The main assumption of the proposed models is that the F_1 preferences is entirely an electronic effect. While the non-adiabatic coupling model seems to predict the experimental values rather well, it could be fortuitous.

The data obtained in this study suggest that the F_1 preference is independent of the hydrocarbon, in agreement with McKendrick *et al.* [23,66]. In addition, this investigation establishes for the first time the independence of the hydroxyl F_1/F_2 spin-orbit ratio of the isotopic substitution and vibrational level.

Initially, it was hoped that isotopic substitution of the hydrocarbon would test any possible influence of rotation on the product spin-orbit ratio. As discussed above in section 5.1.4, however, the energy channelled into OH or OD rotation turns out to be identical for a given hydrocarbon and product vibrational level. No statement about an energetic influence can therefore be made on the basis of the isotopic substitution alone. Instead, since OH and OD products do not differ in energy but in product angular momentum of which no indication of influence on the spin-orbit ratio was found.

The observed independence on the rotational level yields more information. Changing the product vibrational level has a significant influence on the total energy available, as can be seen in figure 4.8. Since no difference between different product vibrational levels in the F_1/F_2 preference has been observed, neither the energetic change makes a difference nor seems the vibrational motion to be coupled to the

electronic motion.

Additionally, the rotational distributions for the various reactions can be reasonably well assigned a "temperature", or an average amount of energy channelled into rotation, as discussed in section 4.5.1.4 and listed in table 4.2. The results are rather independent of the isotope, but depend on the hydrocarbon as well as the OH/ OD vibrational product level v'. While the reaction of $O(^3P)$ with methane produces a "temperature" which is significantly "hotter" than room temperature, cyclohexane produces roughly a room temperature distribution for the ground vibrational level of the OH / OD product and a significantly "colder" distribution for the $v'=1$ product level. A given "temperature" on the other hand also predicts a specific F_1/F_2 spin-orbit ratio. In a thermal sample the F_1/F_2 spin-orbit manifolds would be populated according to Boltzmann statistics given by

$$\frac{^2\Pi_{3/2}}{^2\Pi_{1/2}}(N)=\frac{F_1}{F_2}(N)=\frac{N+1}{N}\times\exp\frac{E_{F_2}(N)-E_{F_1}(N)}{kT} \qquad \text{equation (5.9)}$$

with N being the rotational quantum number, E (N) the respective energy levels in each spin-orbit manifold, k the Boltzmann constant, T the temperature and $^2\Pi_{3/2}$ and $^2\Pi_{1/2}$ the spectroscopic states of the OH / OD product. The ratio can be corrected for the different spatial degeneracy in the F_1 and F_2 manifold and given as

$$\frac{^2\Pi_{3/2}}{^2\Pi_{1/2}}(N)\times\frac{N}{N+1}=\frac{F_1}{F_2}(N)\times\frac{N}{N+1}=\exp\frac{E_{F_2}(N)-E_{F_1}(N)}{kT} \qquad \text{equation (5.10)}$$

The spin-orbit ratio predicted by the rotational "temperature" is displayed together with the experimental results for the OH / OD ($v'=0,1$) products from the reaction of $O(^3P)$ with cyclohexane in figure 5.5.

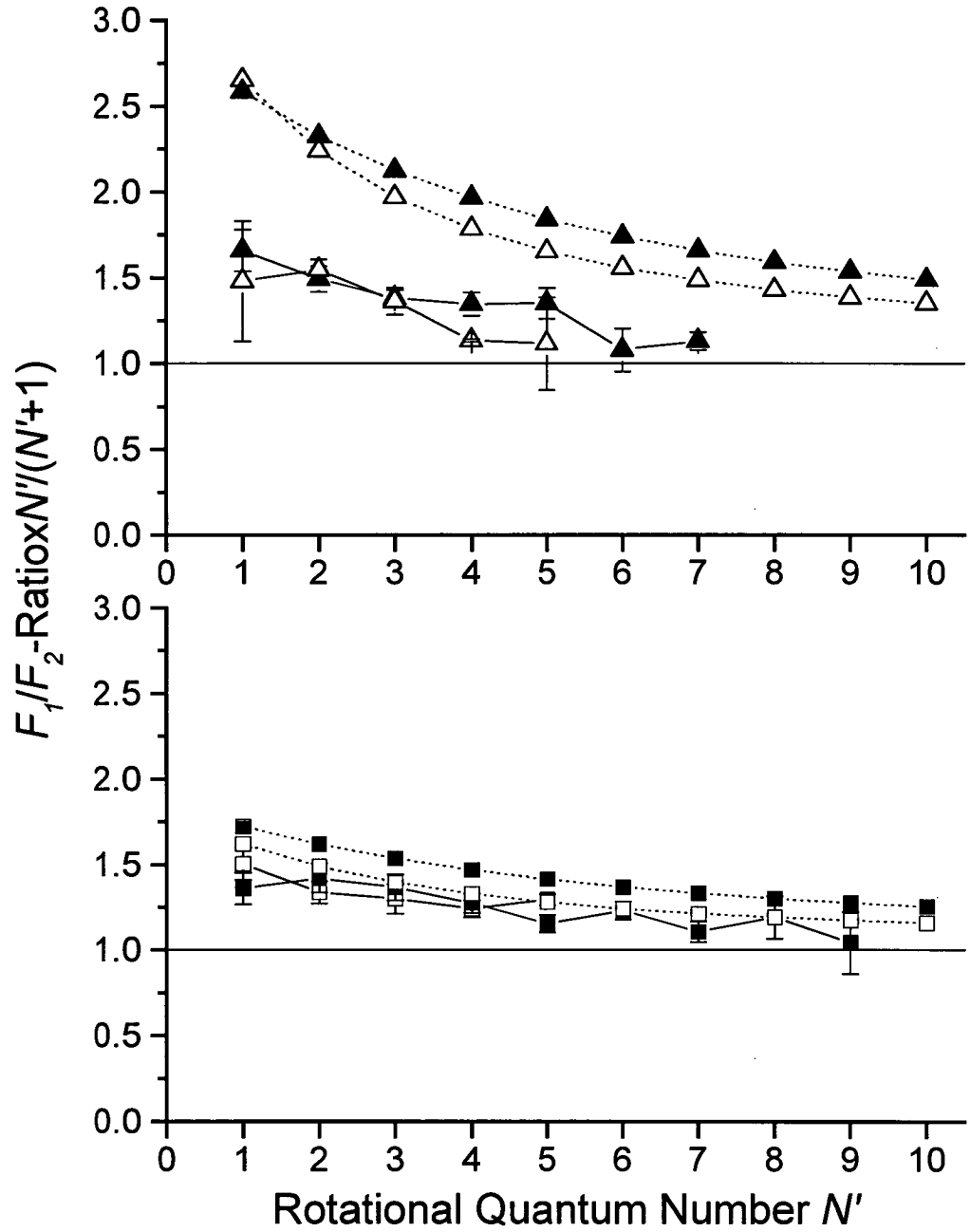

Figure 5.5: Degeneracy adjusted OH and OD fine-structure state distributions from $O(^3P)$ + cyclohexane. Upper panel OH and OD (v'=1) from *cyclo*-C_6H_{12}, open triangles, and *cyclo*-C_6D_{12}, solid triangles. Lower panel OH and OD (v'=0) from *cyclo*-C_6H_{12}, open squares, and *cyclo*-C_6D_{12}, solid squares. The experimental results (with error bars) are joined by solid lines. Predictions on the basis of the equivalent Boltzmann rotational "temperatures", as discussed in the main text are joined by dotted lines.

If the F_1/F_2 product spin-orbit distribution were be coupled to the movement of the nuclear framework, a dependence on the hydrocarbon, the product vibrational level or even the isotope would be expected. This is not observed and it can therefore be concluded that the observed F_1/F_2 spin-orbit distribution is to a good approximation independent of the movement of the nuclear framework. This is an important new observation which supports the conclusion that the spin-orbit branching is a truly electronic effect.

More important than the perfect quantitative agreement with the predicted value by McKendrick *et al.*'s model [66] is the fact that the model is only based on the electronic characteristics of the reaction. These should be independent of the hydrocarbon, isotope substitution or vibrational level of the OH / OD product. This is in full agreement with the observed experimental data. Data for different isotopes and product vibrational levels present therefore a very sensitive test if the observed effect is truly electronic in nature or if the nuclear motion is coupled to the spin-orbit states on the product side.

While the proposed model would predict the same value for the spin-orbit ratio independently of the product rotation, previous studies [23] as well as the results of this work suggest a monotonic decrease for this value with increasing product rotation. There are several reasons which would lead to a lower spin-orbit ratio with increasing N'.

Equation (5.10) predicts the maximum value of this ratio is the lowest value of N, which is the non-rotating molecule, with the highest spin-orbit splitting. With increasing N the ratio decreases along with the drop of the spin-orbit splitting for two levels with the same value of N.

A related effect is the the transition between Hund's case (a), for a non-rotating molecule, to Hund's case (b), for a fast rotating molecule where Ω is no longer a good quantum number and therefore can't be conserved as it is in the proposed coupling scheme. A breakdown of the Ω conservation would allow mixing between levels with different Ω and equilibrate any spin-orbit preference.

In addition, the basic assumption of a collinear approach gets more difficult to sustain for higher values of N in the OH/OD product state, for according to the discussion in section 5.1 this corresponds to passage via a more bent geometry [56] for which the correlation diagram is no longer valid.

Furthermore the correction for the spatial degeneracy is based on the assumption that all m_J' product levels are equally populated, the $(N'/N'+1)$ factor becomes void if the product is strongly aligned or becomes more aligned with higher rotation. Admittedly, the factor also becomes less important with higher rotation because it approaches unity with increasing N.

Another fundamental question to be asked is whether the observed spin-orbit product state distribution is indeed controlled by an entrance or exit channel effect. The model described above assumes controlled scrambling on both sides. Sweeney

and McKendrick also predicted a spin-orbit ratio for the case of exit channel scrambling only [66]. The prediction agreed less well with their data than the model presented above.

It is, however, interesting to look into reactions which do not have a splitting in the entrance channel but still have one in the exit channel. This class of reactions was recently investigated by Brouard and coworkers [126]. Examples include H atom reactions with N_2O, H_2O and CO_2 for which OH is also a product. While there is clearly no fine-structure splitting in the entrance channel, a similar preference to that observed for $O(^3P)$ + hydrocarbons is found in the OH products of these reactions. By definition, those have to be controlled by exit channel effects. Brouard and coworkers concluded a situation of partially non-adiabatic behaviour for the H atom reactions in between the two extremes of completely scrambled (suddenly recoupled [127]) and fully adiabatic behaviour.

The final conclusion on the observed product spin-orbit preference for the class of $O(^3P)$ with hydrocarbon reactions is that the observed effect appears to be electronic in nature and independent of the nuclear motion. It is impossible to decide, whether it is predominantly an entrance or exit channel effect. Nevertheless, it seems reasonable to propose that both entrance and exit channel effects do play a role. Only rigourous *ab initio* calculations or an experimental method that specifically perturbs the entrance channel j distribution may provide the definite answer. But the computational methods are still in early stages of development and have only

recently started to be applied to simple three atom systems like F and Cl with H_2 [128,129].

5.3 OH / OD Λ-doublet distribution

No significant variations from unity in the OH / OD Λ-doublet populations were found. This is in very good agreement with nearly all previous measurements [7]. There is no preference for either Λ-doublet, which correspond, at least in the limit of high rotation to the electron being either in (A') or out of the plane (A") of rotation of the OH / OD molecule. The relative population of the two Λ-doublets in a thermal sample of OH or OD is essentially unity. The energy difference between those two levels is negligible with respect to the thermal energy. This ratio describes the motion of the π electrons around the rotating nuclei. In the limiting case of high rotation, this corresponds to the two different π orbitals, say π_x and π_y, being in or perpendicular to the plane of rotation defined by the rotating nuclei.

For a filled π shell molecule no splitting occurs since there is no distinction between the two orbitals. In the case of OH and OD one electron is missing and therefore the two orbitals are no longer necessarily equally populated. The π orbital containing only one electron may lie in the plane of rotation (A') or perpendicular to it (A").

In the limiting case of no rotation, no energy splitting occurs since there is no physical distinction. As rotation occurs the orbitals become more clearly defined which is described by the degree of electron alignment [130,131]. It has a value of 0

for no rotation and approaches 1 in the case of very fast rotation. It is a function of the molecule and determined by its rotational constants.

The ratio A'/A" is usually not unity for dynamical reasons if the reaction involved takes place in a preferred plane. Depending on where the breaking bond in a given reaction lies with respect to the plane of reaction, the unpaired electron may have a preference for the one or the other Λ-doublet. For a reaction along a line of symmetry this argument does not predict any Λ-doublet preference.

It should be noted though that any possible preference is fundamentally limited by the degree of electron alignment [131], which will not be significant at very low levels of rotational excitation. Any preference could imply a transition state with the electron in an orbital confined preferentially to a specific plane.

To be noted in passing, in principle, a value of unity would also be achieved for a completely statistical process, e.g. a long-lived complex. There are, however, no indications for a statistical behaviour neither in previous work nor in this study.

The only picture on the reaction of $O(^3P)$ with hydrocarbons consistent with a Λ-doublet ratio of unity as well all other available information is the established picture of a predominantly collinear abstraction mechanism.

5.4 OH / OD vibrational branching

5.4.1 Previous work

In general [7], the relative ratio of the OH(v'=1) to OH(v'=0) was observed to increase along with the reaction exothermicity in the order primary < secondary < tertiary. In the case of tertiary hydrocarbons an inversion was observed [14,22] and calculated [39]. There have only been selective measurements for deuterated hydrocarbons along the line of measurements of non-deuterated hydrocarbons [14], and one calculation [39].

The main energetic difference between the possible OH and OD products is the lower energy of the excited vibrational states in OD, making the vibrationally excited states energetically more accessible.

Andresen and Luntz [14] measured the excitation function for primary, secondary and tertiary hydrocarbons. The excitation functions are displayed in figure 1.3. For both the secondary and tertiary hydrocarbons the excitation function rose to a maximum and fell slightly afterwards. This was interpreted as the opening of other product channels, probably including vibrational excitation of the hydrocarbon fragment. The onset of the excitation function OH/OD(v'=0) and OH/OD(v'=1) for cyclohexane are the same, see figure 1.3, which was interpreted as both product states lying below the barrier.

This behaviour is readily explained by the "Polanyi-rules" for direct reactions [36]. In the limiting kinematic case of Heavy + Light-Heavy mass combination, the

expectation is a larger vibration in the product for a more repulsive exit channel. The vibrational branching for a given hydrocarbon is found to be dependent on the collision energy [14,55,56]. Therefore the comparison of vibrational branching ratios derived from different experiments can only be expected to agree qualitatively. The values of Andresen and Luntz [14] have been obtained at a different, lower, collision energy than the one present in this study.

No data are available for the reaction of $O(^3P)$ with CD_4. There are, however, two classical scattering calculations on reaction of $O(^3P)$ with CH_4, reaction (1.5), that predict the vibrational branching ratio. The earlier calculation [55] predicts a branching ratio of 0.04 for a energy of 0.55 eV.

The latest calculation [56] predicts a branching of about 8% of the product into the OH (v'=1) product for reaction (1.5) at a collision energy of 0.65 eV. There is a substantial increase in the vibrational branching with increasing collision energy. For energies equal and higher than 1 eV the calculation even predicts population in the (v'=2) vibrational level of the hydroxyl product. The calculation for a collision energy of 0.65 eV is the closest to those present in this experimental study.

5.4.2 Own results and interpretation

The results of this study are given in table 4.4 and imply a hydroxyl (v'=1)/ (v'=0) branching ratio of ≤0.03 and ≤0.07 for the reactions of $O(^3P)$ with CH_4 and CD_4, reactions (1.5) and (1.7), respectively. These results, estimated from the

experimental signal-to-noise level, for the vibrational branching are only valid in combination with the results for the vibrational branching for $O(^3P)$ with cyclohexane, reaction (1.6) and (1.8), obtained by Andresen and Luntz [14] at much lower collision energies. There is much uncertainty about the accuracy of the results of this study and they are rather an indication of the branching ratio than a correct numerical value.

Although, there is a considerable spread of collision energies, see figure 4.7, collision partners which lie above the barrier for reaction (1.5) have an average energy of about 0.55 eV. The experimental result of an upper limit of 3% branching is therefore considered to be in qualitative agreement with the calculated values of 4% (E_{coll}=55 eV) and 8% (E_{coll}=65 eV) respectively [55,56].

These are the first experimental measurements of this property for the reactions (1.5) and (1.7). All these observations are in agreement with a direct abstraction.

While this conclusion does not constitute a dynamical surprise, it is interesting to compare it with data on other hydrides of the same main group in the periodic table. The reactions of $O(^3P)$ with the parent silane

$$O(^3P) + SiH_4 \rightarrow OH + SiH_3 \qquad \text{reaction (5.1)}$$

was studied by Wiesenfeld's group [20]. This was one of the first studies which used photolytic production of $O(^3P)$ in combination with LIF detection of the OH. Wiesenfeld and co-workers' were aware of the earlier work on $O(^3P)$ + larger hydrocarbon reactions [14], but no data on CH_4 was available then.

Reaction (5.1) is significantly more exothermic than the analogous methane reaction (1.5) by about –50 kJ mol^{-1}. The vibrational populations were found [20] to be heavily inverted, with OH(v'=1)/(v'=0)=3.4±0.4. This agreed reasonably well with an almost contemporaneous result of 4.2±0.6 obtained by Agrawalla and Setser [132] using LIF in a flowing-afterglow reactor. The latter group interpreted the result as an evidence for a direct abstraction mechanism.

However, the complicated nature of the OH rotational and fine-structure state distributions led Wiesenfeld and coworkers [20] to propose a less straightforward interpretation. The internal state distribution for the majority OH(v'=1) product, i.e. rotational distribution, spin-orbit preference and Λ-doublet propensity, resembled very much the OH product as observed from the reactions of O(^{3}P) with hydrocarbons.

Therefore they concluded that the OH(v'=1) product was formed in a similar way for SiH_4 as for hydrocarbons, namely by a direct abstraction mechanism. The rotational distribution for the OH(v'=0) product showed distinct bimodal behaviour. It consisted of a low-N' component, roughly characterised by a temperature of 750 K, which inverted at higher N' to form a broad distribution extending towards the energetic limit. There was no preference in OH(v'=0) for either spin-orbit state but there was a level-dependent propensity, surprisingly largest at low N', for the Π (A') Λ-doublet. This behaviour is very similar to what is observed from reactions with O(^{1}D) and hydrocarbons, where the OH(v'=0) was proposed to be produced via a

competitive insertion mechanism. It was suggested that the involvement of a triplet silanol intermediate was energetically feasible in this case, unlike the hydrocarbon reactions where the lowest-lying triplet ROH state was assumed to lie to high in energy above the reactants.

Park and Wiesenfeld followed up the work on SiH_4 with a similar study [133] of the more heavily substituted trimethylsilane:

$$O(^3P) + (CH_3)_3SiH \rightarrow OH + (CH_3)_3Si \qquad \text{reaction (5.2)}$$

Unlike substituted alkanes, the Si-H bondstrength in $(CH_3)_3SiH$ does not differ significantly from that in SiH_4 [69]. Conveniently enough, the available energy was not sufficient to promote abstraction from the primary CH_3 groups. The main difference between reactions (5.1) and (5.2) was therefore the degree of steric hindrance encountered by the attacking $O(^3P)$ atom.

As for reaction (5.1), both $OH(v'=0)$ and $OH(v'=1)$ were observed from reaction (5.2) and found to be inverted in the ratio 2.3±0.2 [133]. No Λ-doublet preference was found for either vibrational level. The respective rotational distributions could be fitted to Boltzmann temperatures of ~770 K and ~173 K, respectively. This corresponds to only ~5% of the available energy being channelled into OH rotation. As for the $OH(v'=1)$ product from reaction (5.1) it closely resembled those from alkanes, with no sign of the unusual component found in $OH(v'=0)$ from SiH_4.

Park and Wiesenfeld [133] concluded that the mechanism of reaction (5.2) was therefore a simple direct abstraction. In order to explain the anomalous OH(v'=0) component from reaction (5.1) its rotational distribution was investigated with a simple classical repulsive model, similar to that discussed above in section 5.1.4. The main question of interest is the maximum possible degree of bending angle in the transition state. Not surprisingly, this suggested that the transition state for $(CH_3)_3SiH$ suffers from a much tighter steric constraint than for SiH_4, and is more similar to that for alkanes. It was suggested that bending in O–H–SiH_3 might be encouraged by the tendency of Si towards pentavalent bonding. The corresponding five-centred collision complex could act as a long-lived intermediate leading to the more O(^{1}D)-like behaviour of the OH(v'=0) product population.

The reaction with the next heavier homologue, germane,

$$O(^3P) + GeH_4 \rightarrow OH + GeH_3 \qquad \text{reaction (5.3)}$$

is yet more exothermic (~-80 kJ mol^{-1}) than reaction (1.5) because of the progressively weaker Ge–H bond [69]. It was first studied by Setser's group [134] in a flowing afterglow experiment with infrared chemiluminescence (IRCL) detection. This was followed up by the same group using both IRCL and LIF as part of the comparative study with SiH_4 introduced above [132]. As in the case of reaction (5.1), the OH vibrational distribution from reaction (5.3) is strongly inverted but extends to higher levels (v'=3) consistent with the extra energy available. The vibrational inversion of OH(v'=1) over OH(v'=0) from reaction (5.3) was subsequently

confirmed by Whitehead's group [21] using laser photolysis-LIF probe techniques.

They also derived nascent rotational and fine-structure distributions in these levels. The populations extended to the relatively high levels N'=17 and 14, respectively. The low-N' components of the rotational distributions could be approximated by temperatures of 400 ± 70 K and 560 ± 160 K in OH(v'=0) and (v'=1), respectively. The populations in higher N' levels were strongly inverted in both vibrational states. No preference for either spin-orbit manifold was found in either case. In contrast, the Π(A') Λ-doublet component was favoured strongly (by a factor of ~2.3) in OH(v'=0). The preference was in the same sense for OH(v'=1), but appeared to decline with N'.

Drawing on similar arguments to those advanced by Wiesenfeld *et al.* [20] to explain their results for $O(^3P)$ + SiH_4, and the already noted analogy with $O(^1D)$ + hydrocarbon reactions, Whitehead and Winterbottom [21] proposed that the majority of the OH(v'=0, and 1) was formed via a complex-forming mechanism. The Λ-doublet preference certainly seems to be inconsistent with a collinear abstraction. They speculated that the complex might be a triplet state of germanol, H–O–GeH_3, or a related bridged structure, or could also involve a crossing to a lower-lying singlet surface.

They concluded that it was not possible to distinguish between these possibilities on the basis of their results. It was suggested that the small fraction of OH(v'=0 and 1) populations in low N' states might have been formed by direct

abstraction. No rotational state distributions have been measured for the higher OH vibrational levels. It therefore remains unknown whether a larger component of the population in these levels might come via this alternative route, continuing the trend inferred by Wiesenfeld's group [20] from their results on SiH_4.

In conclusion it seems, as if the collinear abstraction as observed for alkanes is a limiting case of a mechanism in this series of hydrides of group 14. The more energy that is available by the fission of the X-H bond, i.e. the more exothermic the reactions become, the more these characteristics are inconsistent with the general picture of a collinear abstraction are observed. In addition to the energetic argument the steric conditions of the reactions have to be considered. The OH product from the reaction with $(CH_3)_3SiH$ (5.2) looks more "abstraction-like" than the product from the reaction with SiH_4 (5.1) even though the Si-H bond strength are the same.

The hydrocarbon reaction with the highest exothermicity, but also with the highest steric constraints is the tertiary bond in $(H_3C)_3CH$. No unusual distributions have been observed from OH(v'=0), indicating that there is no change in the reaction mechanism. While the steric requirements for the $O(^3P)$ attack might limit the cone of acceptance down to an extent that abstraction is the only possibility, in methane which arguably might have the largest cone of acceptance, the energetics are much more unfavourable. In addition, silane and especially germane are significantly larger than methane which may lead to a shallower potential as function of the bending angle, allowing higher rotational states to be accessed.

It seems therefore that the reactions of hydrides of group 14 with $O(^3P)$ atoms may proceed via different channels, of which the collinear H atom abstraction is a limiting case. In the case of hydrocarbons, this channel seems to be uniquely present, at least at experimentally accessible collision energies, while at least one other channel comes into play for the hydrides of the lower elements of group 14. The relative importance of the different channels depends on energy but also on steric constraints.

5.5 Information on the hydrocarbon radical fragment

No additional information was derived on the fate of the hydrocarbon radical coproduct. The amount of information which could be interfered from the observation of the OH / OD product is limited.

The amount of energy going into rotation for the OH and OD product was found to be constant, but due to the relative mass situation the hydrocarbon fragment can easily absorb a wide range of rotational energy without showing up as a significant difference in the OH/OD fragment.

In all of the theoretical calculations [7] the hydrocarbon is treated simplified either in the treatment of the potential energy surface or in the actual trajectory calculation. Nevertheless the theoretical calculations show good agreement with the experimental results. This implies that regarding the hydrocarbon residue as a spectator seems in large to be justified. No calculation has been carried out with deuterated hydrocarbons to predict the OD product distributions. This might now be

a worthwhile task to establish that isotopic substitutions lead to similar results as now observed experimentally.

5.6 IR-pumping of methane

The experimental attempt of measuring the relative enhancement of the reaction of $O(^3P)$ with vibrationally excited methane $CH_4(\nu_3, v=1)$, reaction (1.9) with respect to reaction (1.5),

$$O(^3P) + CH_4 \rightarrow OH\ X\ ^2\Pi_i\ (v'=0/1) + CH_3 \qquad \text{reaction (1.5)}$$

$$O(^3P) + CH_4\ (\nu_3, v=1) \rightarrow OH\ X\ ^2\Pi_i\ (v'=0/1) + CH_3 \qquad \text{reaction (1.9)}$$

did not produce any significant enhancement above the level of noise. The level of noise was estimated, in section 4.8, to be less than 1% of the signal level of the unpumped reaction. Therefore, by definition, no change in the nascent rotational population due to vibrational excitation could be observed either. Any possible enhancement of the reactivity is below the level of the noise.

5.6.1 Estimation of experimental parameters

In order to understand this negative result it is worth quantifying a few of the conditions involved in the experiment. In a linear absorption regime, it can be assumed that the main contribution to the width of the absorption line is the Doppler broadening, that is the line broadening due to the component of the CH_4 parallel or antiparallel with respect to the propagation direction of the laser beam. Both, the spectral profile of the laser beam and the absorption line can be expressed as gaussian

in shape which is, when converted to $\Delta\nu$, the full-width-half-maximum (FWHM), given as

$$f(\nu)=\frac{2\sqrt{ln2}}{\sqrt{\pi}\Delta\nu}\exp\left(-4ln2\frac{(\nu-\nu_0)^2}{\Delta\nu^2}\right) \qquad \text{equation (5.11)}$$

with the frequency ν and the centre frequency ν_0. The linewidth of the Doppler-broadened absorption line can then be expressed as

$$\frac{\Delta\nu}{\nu_0}=\frac{2}{c}\left(\frac{2ln2RT}{M}\right)^{1/2} \qquad \text{equation (5.12)}$$

with ν_0 being the centre frequency, c being the speed of light, R the universal gas constant, T the temperature of the gas and M its mass. For the following illustrative calculation the R(5) transition in the CH_4 (ν_3, v=1) band at 3067.3 cm^{-1} [106] was chosen because it is a nicely isolated line. In addition, this transition has the maximum pumpable population at room temperature [76] in its lower quantum state as was discussed in more detail in section 4.8. Equation (5.12) predicts a Doppler-broadened bandwidth of less than 0.01 cm^{-1}. The laser system was quoted to have a bandwidth of 0.1 cm^{-1}, see section 3.1.3, in the infrared region after the mixing process [108].

If the laser is set with the centre wavelength ν_0 matching the frequency of the transition, only a small part of the laser line profile can actually be used to excite the transition because the linewidth is about a factor of 10 narrower than the laser bandwidth function. The convolution integral of the absorption line profile $g(\nu)$ and the spectral line profile of the laser $f(\nu)$, expressed in probability per unit frequency,

is given as

$$\int g(\nu)f(\nu)d\nu \approx f(\nu_0)\int g(\nu)d\nu = f(\nu_0) = \frac{2\sqrt{ln2}}{\sqrt{\pi}\,\Delta\nu_{Laser}} \approx \frac{1}{\Delta\nu_{Laser}}$$

equation (5.13)

In the case of linear absorption, the total number of photons absorbed per molecule can be calculated as

$$-\int \frac{dI}{N}d\nu = \sigma_0 \frac{I_0}{A}\int g(\nu)f(\nu)d\nu = \sigma_0 \frac{I_0}{A}\frac{1}{\Delta\nu_{Laser}} \quad \text{equation (5.14)}$$

with dI being the change in the number of photons, N the number of molecules per unit volume, I_0 the initial number of photons, A the area of the beam. The integrated absorption strength, σ_0, is taken from the Hitran database [106]. If the calculation is carried out on the R(5) line, with σ_0 = 2.115x10^{-19} cm molecule^{-1} and, the area as above, of 0.54 cm^2, the laser bandwidth as 0.1 cm^{-1} and I_0 as 1x10^{16} photons the result is 0.039 photons per methane molecule. This corresponds to 3.9% of *all* the CH_4 molecules in the sample absorbing a photon. But due to spin and Boltzmann statistics, as explained in section 2.2.8.3 and 2.2.8.4, there are only 0.78% of the molecules in the right quantum state.

A completely optically saturated system would populate the levels involved in the transitions according to their relative degeneracies. In the case of the R(5) transition this corresponds to 121/290 in the lower to 169/290 in the upper state. Therefore, complete optical saturation on the R(5) branch can at most only excite 0.45% of the molecules present in the sample.

That would correspond to an absorption of nearly 9 photons per molecule. Therefore the principal assumption on which this calculation is based, i.e. linear absorption, is no longer valid and the system is optically heavily saturated.

Equation (5.13) represents the fraction of photons which are capable of exciting the transition of interest in the laser beam. The mixed infrared laser beam had an energy of 0.6 mJ per pulse and irradiated an area of 0.54 cm^2. The total number of photons in a pulse are

$$I_0 = \frac{E_{pulse}}{hc\tilde{\nu}} \approx 1 \times 10^{16} \qquad \text{equation (5.15)}$$

with E_{pulse} as the energy of one pulse, h is Planck's constant, c the speed of light and $\tilde{\nu}$ the wavenumber of the pulse. Under the present experimental conditions, the beam passes through the reaction chamber in cylinder of 0.50 m length and 5.4×10^{-5} m^2 base until it reaches the centre of the chamber. The resulting volume is 2.7×10^{-5} m^3. The number of CH_4 molecules present in this volume at a pressure of 250 mTorr, which is about 32.9 Pa can straightforwardly be worked out using the perfect gas law and assuming room temperature

$$n = \frac{pV}{kT} = 2.15 \times 10^{17}\, molecules \qquad \text{equation (5.16)}$$

with p being the pressure, V the volume, k the Boltzmann constant and T the temperature present in the system. This is the total number of CH_4 molecules in gas volume passed by the laser beam before it reaches the observation zone.

The fraction of CH_4 molecules in the single quantum state (J=5, f) and the right spin statistical state is 0.0078 [76]. In the limit of total optical saturation only a

169/290 of the molecules can absorb a photon, that is at most $9.7x10^{14}$ CH_4 molecules can be excited under these conditions. There are about 10 times more photons of the correct wavelength in the beam than molecules which can absorb them.

Therefore the beam does not get significantly depleted when passing through the sample even if total optical saturation is achieved. This means, that the sample will be optically saturated, but not optically dense. The light capable of exciting the transition of interest will therefore be present in the interaction region. This result is consistent with the experimental observation reported in section 4.8 that an opto-acoustic signal was always observed after the IR pump beam passed through the reaction chamber, independent of the CH_4 pressure present in the reaction chamber. The opto-acoustic signal was reduced to about half of its original size, if passed through the reaction chamber filled with 500 mTorr of CH_4, compared to the empty chamber.

5.6.2 Estimate of the expected vibrational enhancement

This section aims to quantify the size any effect of vibrational excitation of the CH_4 on the reaction with $O(^3P)$ atoms with the experimental conditions present. The relative reactivity, R_{pump}, of the pumped reaction (1.9) can be expressed as multiple of the reactivity of the standard reaction (1.5). The observed OH LIF signals will be proportional to the number of OH molecules produced. In case of the unpumped

reaction, all OH A-X fluorescence is originating from reaction (1.5). As discussed above, only a small fraction of the CH_4 molecules present can be excited if the IR pulse is fired. Therefore the LIF signals will come from OH produced by both the reaction with vibrationally excited methane (1.9) and the normal, not excited methane (1.5). The relative signal enhancement, Y is given as the sum of the relative reactivity of the non-pumped reaction (1.5) times the fraction of methane molecules in the vibrational ground state and the fraction of vibrationally excited methane times its relative reactivity, R_{pump}

$$\frac{CH_4(\nu_3, v=0)}{(CH_4)_{tot}} \times 1 + \frac{CH_4(\nu_3, v=1)}{(CH_4)_{tot}} \times R_{pump} = Y \qquad \text{equation (5.17)}$$

This equation can be rearranged to express the relative reactivity of the excited methane as a function of the observed signal enhancement

$$\frac{Y - \frac{CH_4(\nu_3, v=0)}{(CH_4)_{tot}} \times 1}{\frac{CH_4(\nu_3, v=1)}{(CH_4)_{tot}}} = R_{pump} \qquad \text{equation (5.18)}$$

Equation 5.17 allows the calculation of the enhanced relative signal intensity if it is known how much more reactive the vibrationally excited methane is compared to the ground state. Equation 5.18 on the other hand allows the determination of the relative reactivity from an observed enhancement. More specifically, in this work it allows an upper limit to be put on the relative reactivity from the observed signal-to-noise ratio in the experiment.

5.6.3 Theoretical predictions of relative reactivity

The motivation for the attempt to measure vibrational enhancement came from a series of quantum scattering calculations carried out by David Clary with and without his coworker Juliana Palma on the system $O(^3P)$ with methane [48,49,50,51]. The main aim was to develop reduced dimensional models (RD) to treat the complex 6-atom reaction approximately and to identify the degrees of freedom most important in the reaction.

The first study of interest was the RBA study [48], see also section 1.4.1.4. Clary calculated state specific cross sections as function of excitation of the umbrella and the symmetric stretch mode of methane. His calculations predicted not only a significantly larger cross section for the vibrationally excited molecules but it also led him to the conclusion that the thermal rate constant of reaction (1.5) is dominated by the small fraction of CH_4 molecules which are in the first excited vibrational umbrella state. Additionally his calculation predicted an odd/even rotational propensity for the CH_3 coproduct of the OH (v'=0) product.

When this work was published it seemed to indicate a very promising route for further experimental studies since the signal-to-noise ratio would increase dramatically if the methane reactivity would increase as could be expected from the calculated cross section, see below for the estimates calculated.

The second study in this series, published one year later [49] together with Palma replaced the, somehow *ad-hoc*, Hamiltonian of the previous study with a more

rigorous one (3DF). The subsequent quantum scattering calculation produced again relative cross sections which turned out to be essentially the same for the reaction of the vibrational ground state of methane, but increased for stretching mode excitation and decreased for the umbrella mode excitation relative to the RBA results.

These two earliest studies, while surely representing much progress from the theoreticians point of view, were lacking information which could be tested against an experiment. Most of the calculated properties concerned the CH_3 fragment for which only one study had been carried out [24]. Essentially, no information about the OH fragment was derived. The treatment of the vibrational states of the methane reactant was at lower dimension and did not correspond to the real spectroscopic states of the molecule.

The subsequent study by Clary and Palma [50] treated an additional degree of freedom, an asymmetric stretch, in methane, making it a 4-dimensional model (4DF). This asymmetric stretch itself was not a spectroscopic reality, but was supposed to mimic the molecular motion of the ν_3 vibration, see also section 2.2.8.3, of methane. They found that the previous stretching motion in reference [49] was in fact the sum of the now distinguished symmetric and asymmetric stretch. The asymmetric stretch was found to increase the reaction probability less than the symmetric one but at least a similar motion is spectroscopic reality. There is however, an unknown effect associated with the fact that the asymmetric stretch in the calculation is treated as non-degenerate, while the real spectroscopic state is triply degenerate.

The latest study [51], continued the use of the 4DF Hamiltonian but extended the work to calculations of the deuterated reaction (1.7) with CD_4. CH_4 and CD_4 showed distinctly different dynamical behaviour, especially in the enhancement of the reaction probability due to excitation of the umbrella mode. While the umbrella mode was found, as before, to significantly enhance the reactivity for CH_4, it actually inhibits the reactivity for CD_4. This would have a profound influence on the thermal rate constant if, as discussed above, the umbrella mode contributes significantly to it.

One significant restriction was common to all theoretical studies. The calculated reaction probabilities or cross sections were all calculated for a direct collinear approach with the condition of total angular momentum J=0.

5.6.3.1 Predicted increased reactivity on the basis of the theoretical work

It is possible to estimate the relative enhancement of the vibrationally excited reaction (1.9) with respect to the CH_4 ground state reaction (1.5). While the absolute numbers for the calculated cross sections and reaction probabilities may not be trusted, they should be consistent in themselves and their relative values trustworthy.

The calculated vibration which comes closest to the real spectroscopic behaviour of the ν_3 vibrational mode is the treatment of the asymmetric C-H stretch as treated in the two latest studies [50,51].

The data for the reaction probability, which is proportional to the reaction cross section, for the calculated vibrational ground state reaction and the asymmetric

stretch excited reaction are plotted in figure 5.6.

In order to convert the reaction probability to something similar to a rate of reaction, the corresponding reaction probability, RP, has to be convoluted with the distribution of collision energies, $P(E_{coll})$ and multiplied by the square root of the collision energy. The calculated reaction probabilities did not cover the whole range of collision energies as present in the collision energy distribution in the experiment and was linearly extrapolated towards the higher energies. This may introduce a significant error depending on how and when the reaction probabilities actually tail off. The quantity obtained from the convolution is proportional to the rate of reaction for the vibrational ground and excited state. The predicted relative reactivity, R_{pred} can then be determined by dividing the latter by the former.

$$R_{pred} = \frac{RP(v=1) \times P(E_{coll}) \times \sqrt{E_{coll}}}{RP(v=0) \times P(E_{coll}) \times \sqrt{E_{coll}}} \qquad \text{equation (5.19)}$$

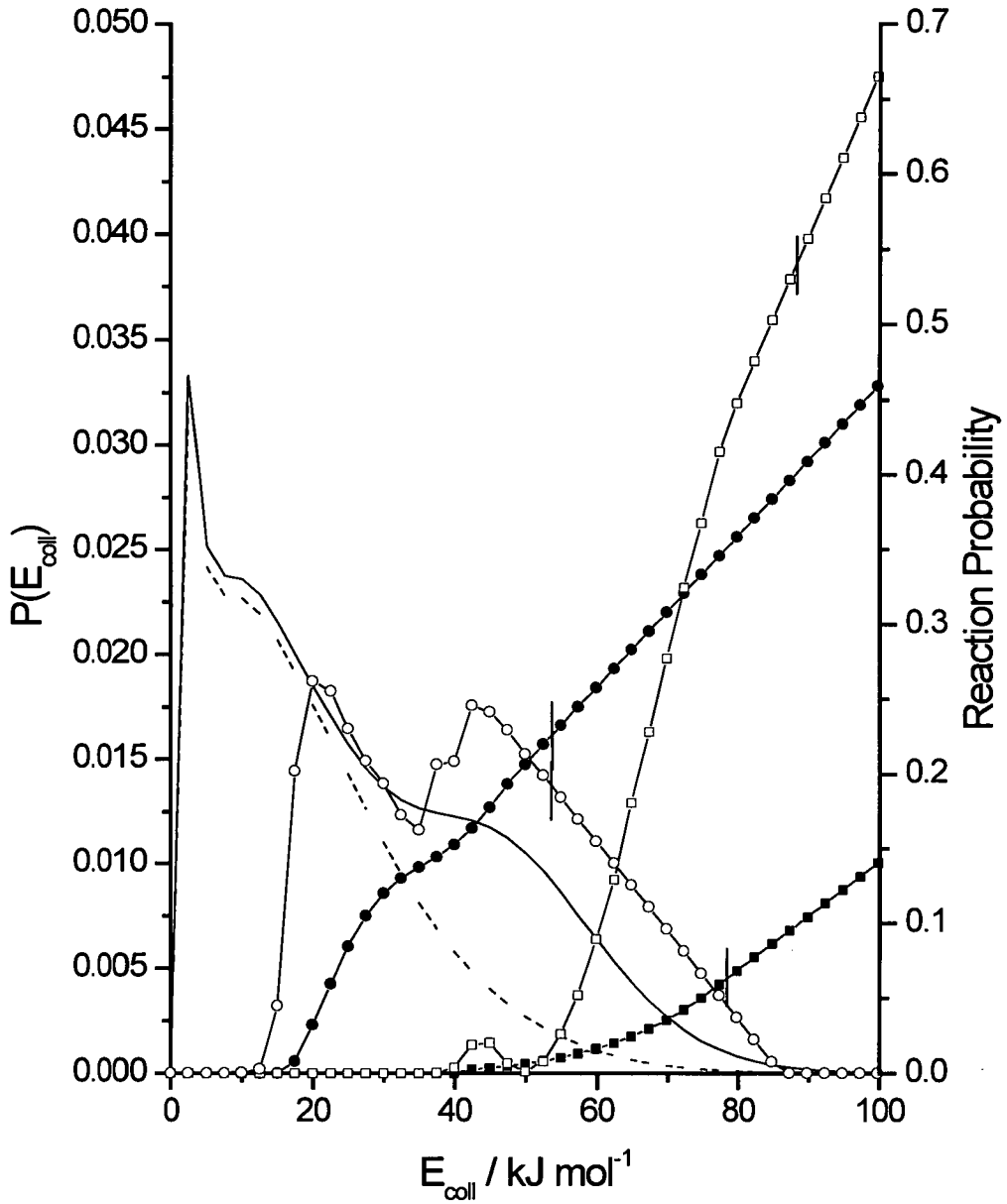

Figure 5.6:Calculated reaction probabilities for CH_4 vibrational ground state. Distributions of collsion energies as measured [97] (solid line) and adjusted (dashed line). Reaction probabilities as calculated by the RBA study [48], vibrational ground state (solid squares) and stretching mode excited (solid circles). Reaction probabilities as calculated by the latest 4DF study provided by Palma [135] and published in [51], vibrational ground state (open squares) and excitation in the non-degenerate asymmetric stretch (open circles). The sharp peak in the asymmetric stretch curve is supposed by the authors to be an artefact of the calculation. The vertical lines indicate the last published data point on the low energy side. The high energy side was extrapolated linearly.

5.6.3.2 Comparison of predicted vibrational enhancement and experimental data

It is now possible to make a comparison between the experimental results of this investigation and the theoretical predictions of Clary and Palma's [48,51] calculations.

The negative result of experimental data, i.e. no positive identification of any signal enhancement, provides an upper limit on the largest possible relative reactivity of the reaction of vibrationally excited CH_4 with $O(^3P)$ with respect to the ground state reactant. On the other hand, the calculated reaction probabilities supply an estimate on the size of the effect that could be expected.

Some assumptions have to be made to describe the experimental conditions. The number of molecules present in the excited state depend critically on the assumed degree of optical saturation of the sample. As discussed in section 5.6.1, there are good reasons to assume a significant optical saturation in the sample. The fraction of excited CH_4 molecules are estimated by comparing the size of the pumped feature in the Q-branch with the size of the R(5) line for which the thermal population is known. The pumped feature was 1.33 times more intense than the R(5) line. Another critical parameter of the calculation is the distribution of collision energies. Both of the ones calculated in section 4.4, as measured by [97] and the one adjusted to less population in the $NO(v'=0)$ fragment of the NO_2 photolysis will be used.

Starting from equation (5.19) a predicted signal enhancement, Y_{pred}, can be calculated for the experimental conditions by taking the fraction of the populations in the vibrational ground and excited state into account.

$$\frac{CH_4(\nu_{asym.\,stretch}, v=0)}{(CH_4)_{tot}} \times 1 + \frac{CH_4(\nu_{asym.\,stretch}, v=1)}{(CH_4)_{tot}} \times R_{pred} = Y_{pred} \qquad \text{equation (5.20)}$$

On the other hand, equation 5.18 allows the calculation of the relative reactivity R_{pump} from the observed relative signal enhancement. The calculations were carried out and the results for different conditions are summarised in table 5.1 for the experimental observations and in table 5.2 for the predictions based on the Clary and Palma's scattering calculations.

A closer look on table 5.2 reveals a lower value of R_{pred} and Y_{pred} for the more advanced 4DF [51] calculation compared to the RBA [48] calculation throughout all simulated conditions. This is mainly due to the explicit treatment of the symmetric and asymmetric stretch in the 4DF calculation, while the RBA calculation treated an average stretch, including the later distinguished symmetric and asymmetric stretch. The RBA data therefore predicts a much more friendly scenario to experimentally observe the predicted enhancement. The RBA results formed the basis from which the experiment was originally judged to be feasible.

Assumed degree of optical saturation	$CH_4(\nu_3, v=1) / (CH_4)_{tot}$	$CH_4(\nu_3, v=0) / (CH_4)_{tot}$	[a] $Y_{S/N}$	[b] R_{pump}
100%	0.00605	0.99395	1.01	2.7
50%	0.00302	0.99698	1.01	4.3

Table 5.1: Estimates of the relative reactivity of vibrationally excited CH_4 (ν_3, v=1) compared to CH_4 in the vibrational ground state reacting with $O(^3P)$. [a] The relative signal enhancement was set to 1.01 which corresponds to the upper limit of any enhancement disappearing under the level of noise. [b] This number represents the maximum value for the relative reactivity of the pumped reaction to the non-pumped one which would just disappear below the level of noise observed in the experiment.

[a] *Set of reaction probabilities*	[b] *P(Ecoll)*	*Assumed degree of optical saturation*	[c] $CH_4(v=1) / (CH_4)_{tot}$	[c] $CH_4(v=0) / (CH_4)_{tot}$	R_{pred}	Y_{pred}
RBA	1	100%	0.00605	0.99395	48.4	1.29
4DF	1	100%	0.00605	0.99395	17.2	1.10
RBA	2	100%	0.00605	0.99395	22.0	1.13
4DF	2	100%	0.00605	0.99395	4.7	1.02
RBA	1	50%	0.00302	0.99698	48.4	1.14
4DF	1	50%	0.00302	0.99698	17.2	1.05
RBA	2	50%	0.00302	0.99698	22.0	1.06
4DF	2	50%	0.00302	0.99698	4.7	1.01

Table 5.2: Estimates of the relative reactivity of vibrationally excited CH_4. compared to the vibrational ground state based on the reaction probabilities of the scattering calculations. [a] reaction probabilities taken from [48] RBA, or from [51] 4DF, linearly extrapolated for high E_{coll} as described in the main text. [b] $P(E_{coll})$ as calculated in section 4.4, 2 indicates the measured distribution from [97], 1 indicates the adjusted distribution. [c] the vibration indicated corresponds to the stretching vibration in case of the RBA study [48] and the asymmetric stretch in the DF study [51].

Only the conditions of the last row in table 5.2 yield results that are compatible with the experimental results. It is therefore unlikely that experimental results and theoretical predictions agree except in the extreme case of the assumptions leading to the results in the last row of table 5.2 are correct. In order to classify this apparent disagreement between experimental observations and theoretical predictions it is

worth summarising the unknown factors in both cases.

On the experimental side, the largest unknown quantity is the number of CH_4 molecules excited into the first vibrational state CH_4 (ν_3, v=1). This number critically affects the additional level of signal to be observed. The other largely unknown experimental quantity is the shape of the collision energy distribution, which is not known. Both of these quantities were rationalised on the basis of available information. Since no better information is available, the approximations and assumptions made to derive these quantities have to be judged to be reasonable in the light of the experimental setup.

Since the IR laser beam is vertically polarised, it can be expected that only superposition states of the threefold degenerate ν_3 vibration which have an electric field vector component in the vertical plane can interact with the IR laser beam and therefore be excited. This lowers the number of molecules which can be pumped and the observable signal enhancement even more. This effect has not been included in the estimates in table 5.1.

The main assumptions made in the theoretical calculations, beside fundamental problems of the accuracy of the PES and computational details, is the validity of the Hamiltonian, especially the lack of proper treatment of the motion associated with the ν_3 vibration. All calculations are still of reduced dimensionality and none describes the true spectroscopic states, the normal vibrations of the CH_4 molecule, properly. While the RBA calculation does not treat the different stretching vibrations

separately, the newer 4DF calculation treats it as a non-degenerate motion which is not the same as the motion of the accessible spectroscopic states. Furthermore, the calculations were only carried out for a total angular momentum of J=0. A lot of the "bumps" displayed by the reaction probabilities in figure 5.6 can be expected to vanish if a proper distribution over all J values would be carried out. An unknown error is included by assuming this J=0 reaction probability to be representative for all J in the distribution present. Additionally, it is not known how significant the error introduced by the linear extrapolation for higher E_{coll} *is*.

The latest calculation by Palma and Clary [51] also predicts the effect of vibrational enhancement in the CD_4 asymmetric stretch which seems to have a much higher reaction probability for the vibrational ground state. Any pumping experiment with CD_4 is likely to be even more difficult due to even more unfavourable Boltzmann statistics.

No significant enhancement of the reaction of $O(^3P)$ with CH_4 due to excitation of the CH_4 (ν_3, v=1) vibrational mode was observed in the experiment. Despite some uncertainty in the number of molecules pumped, the lack of enhancement was found not to be compatible with the various generations of theoretical predictions [48-51] in all but one extreme case which is unlikely to be correct.

5.7 Summary

The aim of expanding the knowledge of the class of reactions of $O(^3P)$ with hydrocarbons to the area of deuterated hydrocarbons has been achieved. Using photolysis of NO_2 at 266 nm, fast oxygen atoms were created to react with the deuterated or non-deuterated hydrocarbons. These produce either OD or OH which were probed by LIF.

For the first time the OD(v'=0) was observed from the reaction of $O(^3P)$ with CD_4, and the reaction of $O(^3P)$ with *cyclo*-C_6D_{12} was studied in unprecedented detail. Reactions of $O(^3P)$ with methane, reactions (4.5)-(4.8), were studied comparatively and for the first time information about the OH/OD product vibrational branching ratio for the parent reactions of CH_4 and CD_4 could be established. In both cases the production of the vibrationally excited OH/OD product could be confirmed as being a minor channel accounting for no more than 3% or 7% of the total yield respectively.

Rotational product state distributions were measured from reactions (4.1)-(4.5) and (4.7). These results agree well with previous measurements, producing the "hottest" distribution for the methane reaction, a "colder" distribution for the vibrational ground state product from cyclohexane and a "very cold" distribution for the vibrationally excited product from cyclohexane. Those trends must be stereochemical in origin, because they are opposite to those expected on the basis of reaction exothermicity. The amount of energy channelled into OH/OD product

rotation was found to be independent of isotopic substitution. This fits in well with a direct abstraction mechanism as assessed through a simple classical model.

The data derived on the F_1/F_2 spin-orbit finestructure of the OH/OD product provided a sensitive test to a recently proposed electronic coupling model [66] for these reactions. The reactive F_1/F_2 population was found to be independent of the isotope, the hydrocarbon or the product vibrational level produced, strongly indicating an electronic effect uncoupled to the nuclear motion.

The measurement of the Λ-doublet values did not show a significant variation from unity in accordance with previous measurements [7].

All this information strengthened the perception of this class of reactions as proceeding via a collinear abstraction.

Attempts were made to measure the relative enhancement of reaction (1.5) due to vibrational excitation of the CH_4 (ν_3, v=1) vibration. No enhancement was observed and upper limits to the increase in reactivity of the pumped molecules were estimated for various cases of optical saturation. This result could not be reproduced by comparison with predictions based on the most recent quantum scattering calculations.

Chapter 6: Additional work attempted

6.1 Reaction of ground state oxygen atoms with acetonitrile

The reactions of ground state oxygen atoms with saturated hydrocarbons have only one available product channel, which leads to the production of the hydroxyl and the corresponding hydrocarbon radical. However, switching the attention to unsaturated and functionalised hydrocarbons other reactions, leading to different products, might occur. In reactions where several product channels are open one might expect simultaneous appearance of the possible products and a competition between the different channels.

As presented in section 1.6.1, the reaction of $O(^3P)$ with unsaturated hydrocarbons may produce a whole range of product channels. The OH product is not observed for reactions with C_2H_4 [72]. It is produced by larger unsaturated hydrocarbons in competition with other products and displays very similar characteristics as the OH product from saturated hydrocarbons. The hydrogen seems to come preferably from an allylic position but always from a saturated chain [70,71].

The case of the reaction of $O(^3P)$ atoms with acetonitrile might be considered as a good test case for observing different competing channels. While the nitrile function at the end of the molecule may react similar to an unsaturated hydrocarbon bond system, the methyl group of the molecule might essentially behave like an alkane.

The thermodynamic data from a standard compilation [69] shows that the C-H bondstrength in H_3CCN, 389.0±10.5 kJ mol^{-1} is comparable with the C-H (tertiary) bondstrength in $(H_3C)_3CH$ with 390.2±2.0 kJ mol^{-1} [69]. Therefore the reaction enthalpy for the OH producing channels of both reactions (6.1) and (6.2) should also be very similar

$O(^3P) + (H_3C)_3CH \rightarrow OH + (H_3C)_3C \quad \Delta H^0_{298} = -37.3\ kJ\ mol^{-1}$ reaction (6.1)

$O(^3P) + H_3CCN \rightarrow OH + H_2CCN \quad \Delta H^0_{298} = -38.5\ kJ\ mol^{-1}$ reaction (6.2)

The available data are limited to kinetic experiments, see section 1.6.2, measuring the disappearance of the $O(^3P)$ reactant [73] and mass spectrometric end product analysis [74]. So far, no attempt has been made to identify the nascent products.

However, reaction (6.2) forms only one of the three possible main channels as identified in the previous studies, namely

$O(^3P) + H_3CCN \rightarrow OH + H_2CCN$ reaction (1.13)

$O(^3P) + H_3CCN \rightarrow CH_3 + NCO$ reaction (1.14)

$O(^3P) + H_3CCN \rightarrow HCN + H_2CO$ reaction (1.15)

The previous studies agree on the major channel being reaction (1.14) via an addition of the $O(^3P)$ atom to the triple bond, but there is some evidence, especially for higher temperatures, that channel (1.13) becomes an important pathway [73].

From a simple dynamical view, there is no obvious reason, why a hydrogen abstraction in analogy to the alkanes should not take place if the $O(^3P)$ approaches the alkyl end of the acetonitrile molecule.

The thermal rate constant of reaction of $O(^3P)$ with H_3CCN (1.12) is given as $1.06x10^{-13}$ cm^3 $molecule^{-1}$ s^{-1} [73] or $1.48x10^{-13}$ cm^3 $molecule^{-1}$ s^{-1} [74] and is about a factor of 2 or 3 faster than the thermal rate constant for the reaction of $O(^3P)$ with isobutane which is quoted to be $5.8x10^{-14}$ cm^3 $molecule^{-1}$ s^{-1} [8]. The rate coefficients for acetonitrile were extrapolated from the the general form given in the respective literature since the measured temperature range did not include 298 K.

In addition the activation energies are of comparable size with 5 [73] and 17 kJ mol^{-1} [74] for reaction (1.12), as derived from an Arrhenius plot of the rate coefficients, and about 21 kJ mol^{-1} for reaction (6.1). This indicates that the barrier heights are of similar size.

6.2 Attempts to detect OH from the reaction of ground state oxygen atoms with acetonitrile

As mentioned in section 1.6.2 above no positive identification of a nascent product from reaction 1.12 currently exists. The previous work with saturated hydrocarbons, as discussed above, has shown that OH could be detected well as a product from a bimolecular reaction. The same experimental approach, section 3.2.1 was therefore deployed in an attempt to find OH from the reaction of $O(^3P)$ with acetonitrile.

The conditions were essentially the same as for the reactions with cyclohexane, as listed in table 4.4, namely a combined pressure of 80 mTorr of equal amounts of NO_2 and acetonitrile. Delay times of 75, 200 and 20000 ns between photolysis and probe pulse were used in order to detect nascent OH distributions. Surprisingly, even

after numerous attempts no nascent OH(v'=0) could be detected.

The absence of any observable OH(v'=0) product was further confirmed by alternating experiments with cyclohexane and acetonitrile to identify any systematic experimental errors. Mistakes in the experimental setup could be excluded due to the positive detection of OH(v'=0) from the reaction with cyclohexane.

On the basis of the signal-to-noise level achieved for the reactions with acetonitrile, a comparison with cyclohexane can be made. The production of OH(v'=0) from the reaction of O(^{3}P) atoms with acetonitrile, reaction (1.13), was found to be no more than 0.7% ±0.7% of the reaction with cyclohexane, reaction (4.1), after correction for OH signal produced by the photolysis of the rogue H-containing compound in the NO_2.

6.3 Attempts to detect NCO from the reaction of ground state oxygen atoms with acetonitrile

The lack of nascent OH(v'=0) product was surprising and prompted further questions about the nature of the main products. Consequently, the work was extended to try to detect NCO which may be produced following reaction (1.14).

First, attempts were made to detect NCO on the $\tilde{A}-\tilde{X}$ band near 390 nm by LIF. No NCO $\tilde{A}-\tilde{X}$ excitation spectra could be recorded or any signal unequivocally identified as originating from NCO fluorescence.

To check independently for NCO, the experimental setup was changed to enable $\tilde{B}-\tilde{X}$ excitation scans at 315 nm. The spectroscopy of the NCO $\tilde{B}-\tilde{X}$ bands was discussed in section 2.2.7.4. Again, no nascent NCO signal was detected.

While extensive experience had been developed to detect nascent OH as a product of a bimolecular reaction in the laboratory, the same was not true for NCO. In order to optimise the detection of NCO and to gain necessary experience, the experimental setup was changed to study the reaction of oxygen molecules with CN radicals

$$O_2 + CN \rightarrow NCO + O \qquad \text{reaction (6.3)}$$

which is known to produce NCO [102,136,137,138]. The changes to the experimental setup were minor. CN radicals were produced by photolysing ICN at 266 nm, a solid compound which is known to have a reasonable vapour pressure at room temperature. The detection of NCO from reaction (6.3) was successful as demonstrated in figure 6.1. It shows a $\tilde{B}-\tilde{X}$ LIF excitation spectrum which can be assumed to be completely thermalised since the photolysis-probe delay was large enough to ensure several tens of collisions. It is almost identical to the one reported by Dagdigian and coworkers [139].

After confirming the capability to detect NCO as a reaction product the attention switched back to the reaction of $O(^3P)$ with acetonitrile. Now, NCO was indeed detected successfully by $\tilde{B}-\tilde{X}$ LIF excitation spectra under thermalised conditions with 100 mTorr total pressure, 50 mTorr NO_2 and 50 mTorr H_3CCN, and 100 μs delay between photolysis and probe pulse. To obtain the NCO LIF excitation spectrum both lasers needed to be fired in the right order and the signal grew in with time. It might therefore be concluded that the NCO observed was indeed produced by the reaction (1.14).

In order to double check the results, measurements were carried out without the acetonitrile flowing, i.e. only NO_2 was presumably present in the reaction chamber. Unfortunately, NCO was still detected.

Therefore, it was concluded that a likely reason was the presence of residual absorbed ICN on the surfaces of the gas lines and the chamber.

To check this assumption, the experimental setup was switched to CN detection on the B-X (0,0) band. The photolysis of ICN at 266 nm is well studied [140,141,142] and positive identification of the CN product from this process would be easy.

In order to have some gas flow, only cyclohexane was allowed into the chamber, which also eliminates any unexpected multiphoton processes in acetonitrile which may produce CN radicals. Even though this was judged not to be a very likely explanation for the ultimate source of NCO, using cyclohexane provided an additional safeguard.

CN radicals were successfully detected under these conditions as demonstrated in figure 6.2. NCO could be detected when either O_2 or NO_2 was also present. Therefore, it was concluded that the chamber was indeed contaminated with residual ICN. NCO would always be detected simply by reaction of CN radicals produced by photolysis of the residual ICN with NO_2 [143]. Further attempts to investigate the NCO producing channel were suspended.

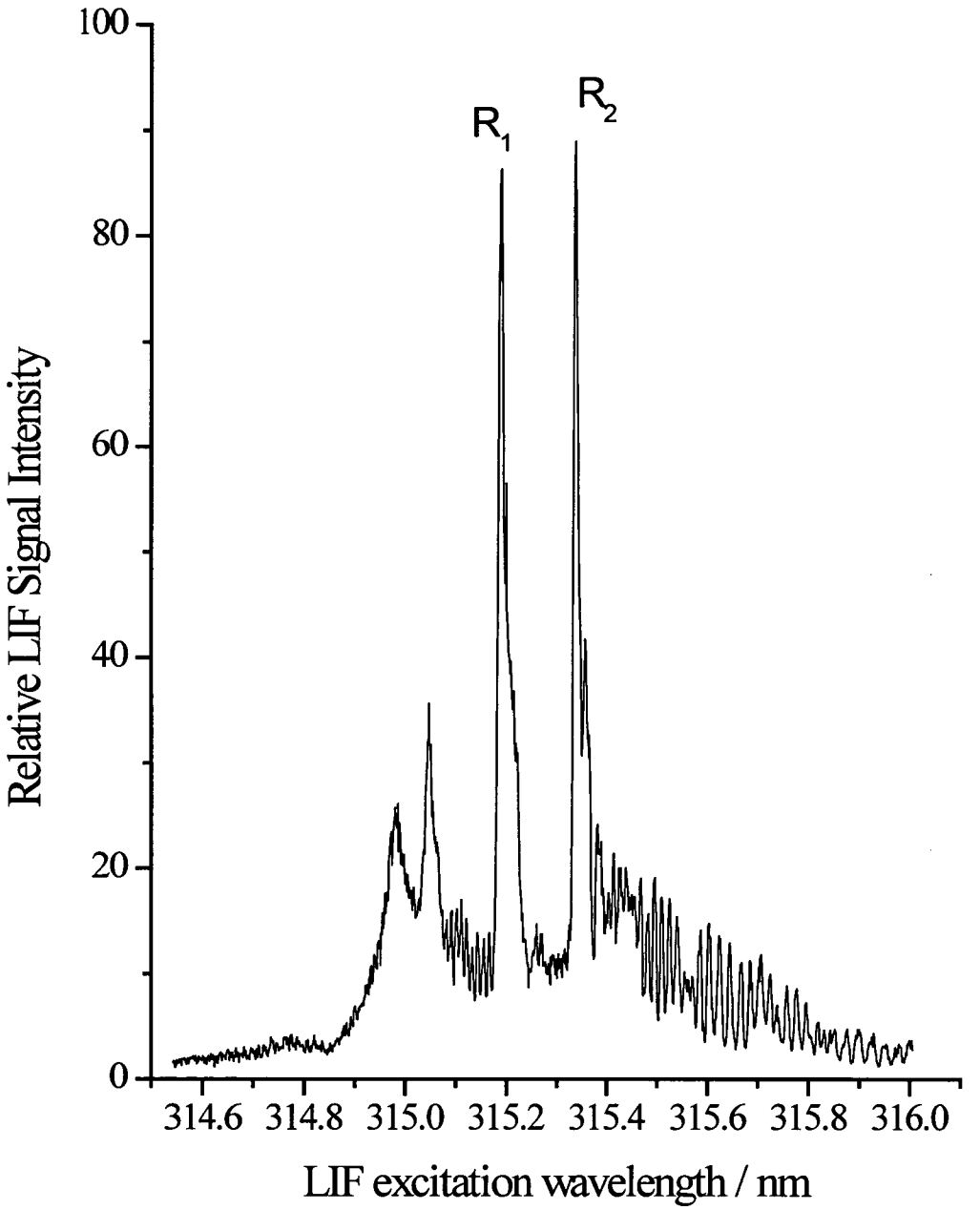

Figure 6.1: Thermalised NCO $\tilde{B}$ (0,0,0) - $\tilde{X}$ (0,0,0) LIF excitation spectrum. The R_1 and R_2 heads are marked. $P(O_2)$=60 mTorr, P(ICN)=20 mTorr, photolysis-probe time delay: 100 μs, photolysis wavelength 266 nm.

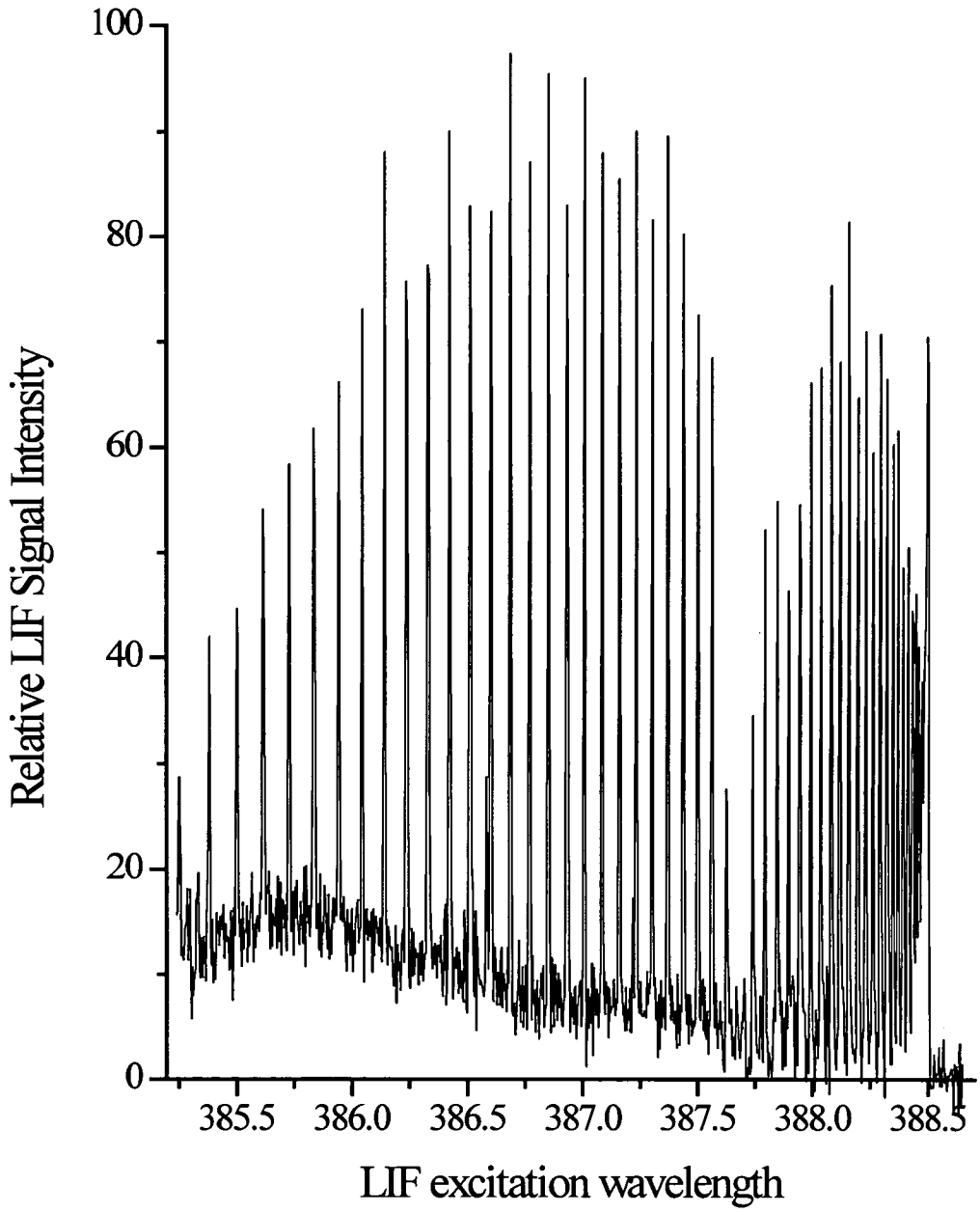

Figure 6.2: CN B-X (0,0) excitation spectrum. P(*cyclo*-C_6H_{12}): 100 mTorr, photolysis-probe delay: 300 ns.

6.4 Discussion and conclusion

Until the present time there is no positive identification of the main channel of the reaction of ground state oxygen atoms with acetonitrile. It was surprising that no OH (v'=0) was found on the basis of previous kinetic work, which identified it as a major channel at higher temperatures [73]. This is also true on the basis of comparison with saturated hydrocarbons.

The reaction of O(^{3}P) with H_3CCN is about as fast thermally as the reaction of O(^{3}P) with cyclohexane, see above section 6.1, and has a lower barrier than any of the O(^{3}P) + saturated hydrocarbon reactions. Furthermore, the C-H bondstrength in acetonitrile is roughly comparable with that of a tertiary hydrocarbon. It is therefore implausible that the failure to detect any OH(v'=0) at a yield above 0.7%±0.7% of that of cyclohexane, reaction (4.1), could be the result of anything other than reaction (1.13) not being a major channel of the reaction of O(^{3}P) with H_3CCN.

It is worth mentioning that no detection of any possible OH (v'=1) product was attempted, which should perhaps be the main, but unlikely to be the exclusive, product of an H abstraction channel on the basis of energetic arguments.

No NCO was detected either, but since the reaction chamber was contaminated with a spurious indirect source of NCO, while trying to optimise the NCO detection sensitivity, no conclusive statement about this channel can be made.

Being aware of the limited data, it could be speculated that the molecular channel, producing HCN and H_2CO, reaction (1.15), may be the most dominant route of reaction (1.12). However, no positive identification has been reported kinetically

or even attempted spectroscopically.

Chapter 7: Outlook

A large amount of knowledge about reactions of $O(^3P)$ atoms with hydrocarbons in the gas phase is now available. Essentially all the available experimental data are consistent with a collinear H-atom abstraction mechanism. On the other hand, nearly all this data are limited to information about the OH/OD product and close to nothing is known about the fate of the hydrocarbon radical product.

A logical extension of this work would therefore be to look into the internal energy distribution of the hydrocarbon fragment. Probably the best candidates would be CH_3 and CD_3 from the reactions (1.5) and (1.7) of $O(^3P)$ with CH_4 and CD_4 respectively. They have been observed as products of the equivalent reactions with $O(^1D)$ by REMPI [25,26,27].

The main experimental problem would be to find a suitable precursor to produce $O(^3P)$ for REMPI experiments. Jet-expansion of NO_2 seems to be doomed to failure because it inevitably produces $O(^1D)$ as shown in section 4.6, which makes it impossible to extract the contribution due to $O(^3P)$. The experimental limitations would be revolutionised if another photolytic precursor for the production of $O(^3P)$ could be found.

The best scenario would be a diatomic precursor that would produce only $O(^3P)$ with a very high and well defined velocity, with a high spatial anisotropy at an easily accessible wavelength. Ideally it could be used in jet-expansions. If it would also be possible to easily perturb the $O(^3P_J)$ distribution, for example by changing the

photolysis wavelength, the *J*-state dependent dynamics could be investigated. This would allow the surface coupling model proposed to explain the spin-orbit branching ratios to be evaluated.

While all theoretical calculations and nearly all experimental information suggest that the hydrocarbon fragment remains a spectator in the process of the reaction, this has not yet been experimentally verified.

Of considerable interest would also be an extension of Tsurumaki *et al.*'s work [18] on translational energy release of the OH product and extraction of product differential cross sections. Furthermore, measurements of the m_j' state distributions of the OH fragment would identify the validity of the theoretical predictions [40,56] on the product alignment. This would again be preferably done with methane. While this may prove to be impossible due to low signal-to-noise level, ethane might present a feasible candidate to obtain this kind of information.

The current work was the first to confirm the presence of OD (v'=1) from the reaction of O(^{3}P) with CD_4 and to report some indication for the presence of OH (v'=1) from the reaction of O(^{3}P) with CH_4. If the level of noise could be lowered enough, the internal state distribution of this product could be measured.

In addition, the experiments on specific enhancement of CH_4 vibrational modes may be extended to overtones and combination bands. The fundamental problems of low numbers of molecules present in the lower states to be excited might be overcome if, with a suitable precursor for O(^{3}P), a jet-expansion setup might be used. This may yield a greater enhancement which may then be detectable.

This would also present an opportunity to test the latest scattering calculations. These are still not of full dimensionality and need to be validated against experimental data. On this theoretical side, the major outstanding challenges are to achieve a full quantum scattering calculation in full dimensionality and to a level of detail which would include the electronic fine-structure. This would provide a very sensitive test on the potential energy surfaces and the assumptions made in the proposed surface coupling model [66]. It would also help to establish what effect any excitation of the true spectroscopically accessible vibrational states of the CH_4 has in reaction with $O(^3P)$ and how it could be experimentally verified.

The gas phase reactions are now well studied and one possible development of the work is to extend it to the gas-liquid interface. One study has already been carried out by a molecular beam scattering method and translational and spatial information on the OH product obtained [144]. The techniques presented here have been proven to be reliable to obtain internal state distributions of the OH product and therefore might be used with a proper experimental setup to probe the OH product ejected from a hydrocarbon surface after reaction with $O(^3P)$ atoms.

Of special interest would be the establishment of differences between the pure gas-phase mechanism, i.e. collinear abstraction, and any mechanism involving the liquid surface, e.g. trapping-desorption. Partial deuteration may yield information on the structure of the hydrocarbon surface formed by long-chain molecules, where either end-groups or the centre of the chains may preferentially be present. These are the major routes which may be seen as natural progressions of this work.

Bibliography

1 P. H. Wine and A. R. Ravishankara; *Chem. Phys.*; **69** (1982) 365.

2 P. Michaud, G. Paraskevopoulos and R. J. Cvetanovic; *J. Phys. Chem.*; **78** (1974) 1457.

3 J. A. Davidson, H. I. Schiff, G. E. Streit, J. R. McAfee, A. L. Schmeltekopf and C. J. Howard; *J. Chem. Phys.*; **67** (1977) 5021.

4 S. T. Amimoto, A. P. Force, R. G. Gulotty Jr. and R. J. Wiesenfeld; *J. Chem. Phys.*; **71** (1979) 3640

5 R. Atkinson, D. L. Baulch, R. A. Cox, R. F. Hampson, J. A. Kerr, M. J. Rossi and J. Troe; *J. Phys. Chem. Ref. Data*; **26** (1997) 521.

6 J. R. Wiesenfeld; *Acc. Chem. Res.;* **15** (1982) 110.

7 F. Ausfelder and K. G. McKendrick; *Prog. Reac. Kin.*; **25**, (2000), 299.

8 J. T. Herron and R. E. Huie; *J. Phys. Chem. Ref. Data*; **2** (1973) 467.

9 J. T. Herron; *J. Phys. Chem. Ref. Data*; **17** (1988) 967.

10 N. Cohen and K. R. Westberg; *J. Phys. Chem. Ref. Data*; **20** (1991) 1211.

11 A. Miyoshi, K Tsuchiya, N. Yamauchi and H. Matsui; *J. Phys. Chem.*; **98** (1994) 11452.

12 R. Grice; *Acc. Chem. Res.*; **14** (1981) 37.

13 P. Casavecchia, N. Balucani, M. Alagia, L. Cartechini and G. G. Volpi; *Acc. Chem. Res.*; **32** (1999) 503.

14 P. Andresen and A. C. Luntz; *J. Chem. Phys.*; **72** (1980) 5842.

15 G. H. Dieke and H. M. Crosswhite; *J. Quant. Spectrosc. Radiat. Transf.*; **2** (1962) 97.

16 N. J. Dutton, I. W. Fletcher, J. C. Whitehead; *Mol. Phys.*; **52** (1984) 475.

17 W. J. van der Zande, R. Zhang, R. N. Zare, K. G. McKendrick and J. J. Valentini; *J. Phys. Chem.*; **95** (1991) 8205.

18 H. Tsurumaki, Y. Fujimara and O. Kajimoto; *J. Chem. Phys.*; **112** (2000) 8338.

19 K. G. McKendrick, D. J. Rakestraw, R. Zhang and R. N. Zare; *J. Phys. Chem.*; **92** (1988) 5530.

20 C. R. Park, G. D. White and J. R. Wiesenfeld; *J. Phys. Chem.*; **92** (1988) 152.

21 J. C. Whitehead and F. Winterbottom; *Chem. Phys. Lett.*; **177** (1991) 207.

22 N. M. Ferber, J. C. Whitehead, F. Winterbottom; *Arabian Journal for Science and Engineering*; **17** (1992) 321.

23 G. M. Sweeney, A. Watson and K. G. McKendrick; *J. Chem. Phys.*; **106** (1997) 9172.

24 T. Suzuki and E. Hirota; *J. Chem. Phys.*; **98** (1993) 2387.

25 R. Schott, J. Schlütter, M. Olzmann and K. Kleinermanns; *J. Chem. Phys.*; **102** (1995) 8371.

26 J. Schlütter, R. Schott, M. Olzmann and K. Kleinermanns; *Zeit. Phys. Chem.*; **188** (1995) 143.

27 J. Schlütter, R. Schott and K. Kleinermanns; *Chem. Phys. Lett.*; **213** (1993) 262.

28 G. Liuti and F. Pirani; *J. Chem. Phys.*; **87** (1987) 1987.

29 V. Aquilanti, R. Candori, L. Mariani, F. Pirani and G. Liuiti; *J. Phys. Chem.*; **93** (1989) 130.

30 V. Aquilanti, E. Luzzatti, F. Pirani and G. G. Volpi; *J. Chem. Phys.*; **73** (1980) 1181.

31 P. M. Arker, J. J. A. Obrien and J. J. Sloan; *J. Chem. Phys.*; **84** (1986) 745.

32 C. R. Park, J. R. Wiesenfeld; *J. Chem. Phys.*; **95** (1991) 8166.

33 S. G. Cheskis, A. A. Iogansen, P. V. Kulakov, I. Y. Razuvaev, O. M. Sarkisov and A. A. Titov; *Chem. Phys. Lett.*; **155** (1989) 37.

34 M. Brouard, H. M. Lambert, J. Short and J. P. Simons; *J. Phys. Chem.*; 99 (1995) 13571.

35 M. Brouard, S. Duxon, P. A. Enriquez, J. P. Simons; *J. Chem. Soc. Faraday Trans.*; **89** (1993) 1427.

36 J. C. Polanyi, *Acc. Chem. Res.*; **5** (1972) 161.

37 C. A. Parr, J. C. Polanyi and W.H. Wong; *J. Chem. Phys.*; **58** (1973) 5.

38 A. M. G. Ding, L. J. Kirsch, D. S. Perry, J. C. Polanyi and J. L. Schreiber; *Faraday Disc. Chem. Soc.*; **55** (1973) 252.

39 A. C. Luntz and P. Andresen; *J. Chem. Phys.;* **72** (1980) 5851.

40 D. C. Clary, J. N. L. Connor and W. J. E. Southall; *J. Chem. Phys.*; **84** (1986) 2620.

41 S. P. Walch and T. H. Dunning, Jr.; *J. Chem. Phys.*; **72** (1980) 3221.

42 E. P. Wigner; *Z. Phys.Chem.*; **19** (1932) 203.

43 C. Gonzalez, J. J. W. McDouall and H. B. Schlegel; *J. Phys. Chem.;* **94** (1990) 7467.

44 B. S. Jursic; *Int. J. Quantum Chem.*; **65** (1997) 75.

45 J. C. Corchado, J. Espinosa-García, O. Roberto-Neto, Y.-Y. Chuang and D. G. Truhlar; *J. Phys. Chem. A*; **102** (1998) 4899.

46 J. Espinosa-García and J. C. Corchado; *J. Phys. Chem.*; **100** (1996), 16561.

47 J. Espinosa-García and J. C. García-Bernáldez, *Phys. Chem. Chem. Phys.*; **2** (2000) 2345.

48 D. C. Clary; *Phys. Chem. Chem. Phys.*; **1** (1999) 1173.

49 J. Palma and D. C. Clary; *J. Chem. Phys.*; **112** (2000) 1859.

50 J. Palma and D. C. Clary; *Phys. Chem. Chem. Phys.*; **2** (2000) 4105.

51 J. Palma and D. C. Clary; *J. Chem. Phys.*; **115** (2001) 2188.

52 H.-G. Yu and G. Nyman; *J. Chem. Phys.;* **112** (2000) 238.

53 M.-L. Wang, Y.-M. Li and J. Z. H. Zhang; *J. Phys. Chem. A*; **105** (2001) 2530.

54 M. J. T. Jordan and R. G. Gilbert; *J. Chem. Phys.*; **112** (2000) 238.

55 M. González, J. Hernando, J. Millán and R. Sayós; *J. Chem. Phys.*; **110** (1999) 7326.

56 R. Sayós, J. Hernando, M. P. Puyuelo, P. A. Enríquez and M. Gonzáles; *Chem. Phys. Lett.*; **341** (2001) 608.

57 H. Arai, S. Kato and S. Koda; *J. Phys. Chem.*; **98** (1994) 12.

58 M. González, J. Hernando, I. Baños and R. Sayos; *J. Chem. Phys.*; **111** (1999) 8913.

59 M. González, M. P. Puyuelo, J. Hernando, R. Sayos, P. A. Enriquez, J. Guallar and I. Baños; *J. Phys. Chem. A*; **104** (2000) 521.

60 S. Wada and K. Obi; *J. Phys. Chem.*; **102** (1998) 3481.

61 C.-L. Lin and W. B. DeMore; *J. Phys. Chem.*; **77** (1973) 863.

62 R. D. van Zee and J. C. Stevenson; *J. Chem. Phys.*; **102** (1995) 6946.

63 C. C. Miller; R. D. van Zee, J. C. Stevenson; *J. Chem. Phys.*; **114** (2001) 1214.

64 M. Oltzmann; *Ber. Bunsenges. Phys. Chem.*; **101** (1997) 533.

65 M. González, J. Hernando, M. P. Puyuelo and R. Sayos; *J. Chem. Phys.*;**113** (2000) 6748.

66 G. M. Sweeney and K. G. McKendrick; *J. Chem. Phys.*; **106** (1997) 9182.

67 A. M. Schmoltner, P. M. Chu, R. J. Brudzynski and Y. T. Lee; *J. Chem. Phys.*; **91** (1989) 6926.

68 R. Quandt, Z. Min, X. Wang and R. Bersohn; *J. Phys. Chem. A*; **102** (1998) 60.

69 Handbook of Chemistry and Physics; ed. D. R. Lide; CRC Press, Boca Raton; 73rd edition; 1992.

70 K. Kleinermanns and A. C. Luntz; *J. Phys. Chem.*; **85** (1981) 1966.

71 K. Kleinermanns and A. C. Luntz; *J. Chem. Phys.*; **77** (1982) 3533.

72 A. M. Schmoltner, P. M. Chu, and Y. T. Lee; *J. Chem. Phys.*; **91** (1989) 5365.

73 R. J. Bonanno, R. B. Timmons, L. J. Stief and R. B. Klemm; *J. Chem. Phys.*; **66** (1977) 92.

74 S. Budge and J. M. Roscoe; *Can. J. Chem.*; **73** (1995) 666.

75 G. Herzberg; Molecular Spectra and Molecular Structure; I. Spectra of Diatomic Molecules; Reprint 1989; Krieger; Florida, USA.

76 G. Herzberg; Molecular Spectra and Molecular Structure; II. Infrared and Raman Spectra of Polyatomic Molecules; Reprint 1991; Krieger; Florida, USA.

77 G. Herzberg; Molecular Spectra and Molecular Structure; III. Electronic Spectra and Electronic Structure of Polyatomic Molecules; Reprint 1991; Krieger; Florida, USA.

78 K. Kohse-Hoinighaus; *Prog. Energy Combust. Sci.*; **20** (1994) 203.

79 G. Grunefeld, M. Schutte and P. Andresen: *Appl. Phys. B*; **70** (2000) 309.

80 W. R. Simpson, A. J. Orr-Ewing, R. N. Zare; *Chem. Phys. Lett.*; **212** (1983) 163.

81 W. R. Simpson, A. J. Orr-Ewing, T. P. Rakitzis, S. A. Kandel and R. N. Zare; *J. Chem. Phys.*; **103** (1995) 7299.

82 W. R. Simpson, T. P. Rakitzis, S. A. Kandel, A. J. Orr-Ewing and R. N. Zare; *J. Chem. Phys.*; **103** (1995) 7313.

83 W. R. Simpson, T. P. Rakitzis, S. A. Kandel, T. Lev-On and R. N. Zare; *J. Phys. Chem.*; **100** (1996) 7938.

84 A. J. Orr-Ewing, W. R. Simpson, T. P. Rakitzis, S. A. Kandel and R. N. Zare; *J. Chem. Phys.*; **106** (1997) 5961.

85 E. J. Llewellyn and B. H. Long; *Can. J. Phys.*; **56** (1978) 581.

86 D. J. W. Kendall and T. A. Clark; *J. Quant. Spectrosc. Radiat. Transfer*; **21** (1979) 511.

87 J. A. Coxon and S. C. Foster; *Can.J.Phys.*; **60** (1982) 41.

88 W. J. Wilson and A. H. Battett; *Science*; **161** (1968) 778.

89 D. J Rakestraw, K. G. McKendrick and R. N. Zare; *J. Chem. Phys.*; **87** (1987) 7341.

90 M. Brouard and J. O'Mahony; *Chem. Phys. Lett.*; **149** (1988) 45.

91 J. August, M. Brouard and J. P. Simons; *J. Chem. Soc. Faraday Trans. 2*; **84** (1988) 587.

92 M. Brouard, S. Duxon, P. A. Enriquez and J. P. Simons; *J. Chem. Soc. Faraday Trans.*; **89** (1993) 1435.

93 M. A. A. Clyne, J. A. Coxon and A. R. Woon Fat; *J. Mol. Spec.*; **46** (1973) 146.

94 J. Luque and D. Crosley, LIFbase: Database and Spectral Simulation Program (Version 1.45); SRI International Report MP 98-021 (1998).

95 H. Okabe, Photochemistry of small molecules; Wiley-Interscience; New York; 1978.

96 T. G. Slanger, W. K. Bischel and M.J. Dyer; *J. Chem. Phys.*; **79** (1983) 2231.

97 St. J. Dixon-Warren, R. C. Jackson, J. C. Polanyi, H. Rieley, J. G. Shapter and H. Weiss; *J. Phys. Chem.*; **96** (1992) 10983.

98 R. P. Wayne; Chemistry of the Atmospheres; 2nd edition; Oxford, UK; 1994

99 J. A. Miller, C. T. Bowman; *Prog. Energy Combust. Sci.*; **15** (1989) 287.

100 R. N. Dixon; *Trans. R. Soc. London, Ser A*; **252** (1960) 165.

101 C. Jungen and A. J. Merer in Modern Spectroscopy: Modern Research edited by K. N. Rao (Academic, New York 1976) Vol II, Chapter 2.

102 S. A. Wright and P. J. Dagdigian; *J. Chem. Phys.*; **104** (1996) 8279.

103 G. Herzberg and E. Teller; *Z. phys. Chem.*; **B21** (1933) 410.

104 R. Renner; *Z. Physik*; **92** (1934) 172.

105 R. N. Dixon, M. J. Trenouth and C. M. Western, *Mol. Phys.*; **60** (1987) 779.

106 The Hitran Molecular Spectroscopic Database and Hawks (Hitran Atmospheric Workstation): 1996 Edition; L. S. Rothman *et al.*; *J. Quant. Spectrosc. Radiat. Transfer*; **60** (1998) 665

107 Gillian Michelle Sweeney; Thesis; The University of Edinburgh; 1995.

108 Mike Towry, personal communication.

109 G. Maitland; Thesis; The University of Edinburgh; 1993..

110 P. J. Chantry; *J. Chem. Phys.*; **55** (1971) 2746.

111 M. Kawasaki, K. Kasatani, H. Sato, H. Shinohara and N. Nishi; *Chem. Phys.*; **78** (1983) 65.

112 A. Bass, A. E. Ledford Jr. andA. H. Laufer; *J. Res. Natl. Bureau Stands.*; **80** (1975) 143.

113 W. N. Sisk, C. E. Miller and H. S. Johnson; *J. Phys. Chem.*; **97** (1993) 9916.

114 K. O. Patten Jr., J. D. Burley and H. S. Johnson; *J. Phys. Chem.*; **94** (1990) 7960.

115 K. G. McKendrick, D. J. Rakestraw and R. N. Zare; *Faraday Discuss. Chem. Soc.*; **84** (1987) 3.

116 M. Broida, M. Tamir and A. Persky, *Chem. Phys.*; **110** (1986) 83.

117 J. J. Valentini; *Annu. Rev. Phys. Chem.*; **52** (2001) 15.

118 W. R. Simpson, T. P. Rakitzis, S. A. Kandel, T. Lev-On and R. N. Zare; *J. Phys. Chem.*; **100** (1996) 7938.

119 P. J. Dagdigian and M. L. Campell; *Chem. Rev.* ; **87** (1987) 1.

120 V. Aquilanti and G. Grossi, *J. Chem. Phys.*; **73** (1980) 1165.

121 V. Aquilanti, P. Casavecchia, G. Grossi and A. Laganà; *J. Chem. Phys.*; **73** (1980) 1173.

122 J. Miyawaki, T. Tsuchizawa, K. Yamanouchi and S. Tsuchiya; *Chem. Phys. Lett.* **165** (1990) 168.

123 Z. Ma and K. Liu; *Chem. Phys. Lett.*; **213** (1993) 269.

124 R. Jaquet, V. Staemmler, M. D. Smith and D. R. Flower; *J. Phys. B*; **25** (1992) 28.

125 T. S. Monteiro and D. R. Flower; *Mon. Not. R. Astron. Soc.*; **228** (1987) 101.

126 M. Brouard, I. Burak and S. D. Gatenby; *Phys. Chem. Chem. Phys.*; **2** (2000) 715.

127 R. N. Dixon; *J. Chem. Phys.*; **102** (1995) 301.

128 M. H. Alexander, H.-J. Werner and D. E. Manolopoulos; *J. Chem. Phys.*; **109** (1998) 5710.

129 M. H. Alexander, D. E. Manolopoulos, and H.-J. Werner; *J. Chem. Phys.*; **113** (2000) 11084.

130 M. H. Alexander *et al.*; *J. Chem. Phys.*; **89** (1988)1749.

131 P. Andresen and E. W. Rothe; *J. Chem. Phys.*; **82** (1985) 3634.

132 B. S. Agrawalla and D. W. Setzer; *J. Chem. Phys.*; **86** (1987) 5421.

133 C. R. Park and J. R. Wiesenfeld; *J. Phys. Chem.*; **93** (1989) 1365.

134 B. S. Agrawalla, A. S. Manocha and D. W. Setzer; *J. Phys. Chem.*; **85** (1981) 2873.

135 Juliana Palma, personal communication.

136 D. Patel-Misra, D. G. Sauder and P. J. Dagdigian; *J. Chem. Phys.*; **93** (1990) 5448 and references therein.

137 S. A. Wright and P. J. Dagdigian; *J. Chem. Phys.*; **103** (1995) 6479.

138 L. F. Phillips, I. W. M. Smith, R. P. Tuckett, and C. J. Whitham; *Chem. Phys. Lett.*; **183** (1991) 254.

139 D. G. Sauder, D. Patel-Misra and P. J. Dagdigian; *J. Chem. Phys.*; **95** (1991) 1696.

140 A. P. Baronavski; *Chem. Phys.*; **66** (1982) 217.

141 A. P. Baronavski and J. R. McDonald; *Chem. Phys. Lett.*; **45** (1977) 172.

142 W. Krieger, J. Häger and J. Pfab; *Chem. Phys. Lett.*; **85** (1982) 69.

143 Y. Y. You, N. S. Wang and J. Chin.; *Chem. Soc.*; **40** (1993) 337.

144 D. J. Garton, T. K. Minton, M. Alagia, N. Balucani, P. Casavecchia and G. G. Volpi; *Faraday Disc. Chem. Soc.*; **108** (1997) 387.

Appendices

A Courses attended

Inelastic and Reactive Scattering Theory

Laser Physics

Atmospheric Dynamics

Atmospheric Physics

Modern Optics

Introduction to the European Union

European Institutions

French for Scientists II

French Elective III

B Conferences attended

Royal Society of Chemistry, Faraday Division, Gas Kinetics Discussion Group, January Meeting, University of York, January 1999

16th International Symposium on Gas Kinetics, Cambridge, July 2000

XVIIIth Conference on the Dynamics of Molecular Collisions, Copper Mountain, USA, July 2001

C Published Papers

F. Ausfelder and K. G. McKendrick; *Prog. Reac. Kin.*; **25**, (2000), 299-370.

F. Ausfelder, H. Kelso and K. G. McKendrick; *Phys. Chem. Chem. Phys.*; **4** (2002) 473-481.